

WALTER SCHOTTKY INSTITUTE
DEPARTMENT OF PHYSICS

**Two dimensional electron systems
in atomically precise periodic potentials**

Ph.D. Dissertation

Rainer Alexander Deutschmann

July 27, 2001

UNIVERSITY OF TECHNOLOGY MUNICH

Walter Schottky Institut
Zentralinstitut für Physikalische Grundlagen der Halbleiterelektronik
der
Technischen Universität München

**Two dimensional electron systems
in atomically precise periodic potentials**

Rainer Alexander Deutschmann

Vollständiger Abdruck der von der Fakultät für Physik der Technischen Universität
München zur Erlangung des akademischen Grades eines

Doktors der Naturwissenschaften

genehmigten Dissertation.

Vorsitzender: Univ.-Prof. Dr. M. Kleber
Prüfer der Dissertation: 1. Univ.-Prof. Dr. G. Abstreiter
2. Univ.-Prof. Dr. R. L. Gross
3. Prof. Dr. H. L. Stormer,
Columbia Universität, New York/USA
(schriftliche Beurteilung)

Die Dissertation wurde am 04.07.2001 bei der Technischen Universität München
eingereicht und durch die Fakultät für Physik am 27.07.2001 angenommen.

to Annike

But with a little effort, you can still find the good stuff.

K&D

Contents

Summary	1
1 Introduction	3
1.1 Physics in two dimensions	4
1.2 Superlattices	7
1.3 Superlattice field effect transistor	9
1.4 Outline of this thesis	11
2 Magnetotransport in the Lowest Miniband	15
2.1 Review	16
2.2 Qualitative model using the zero-field band structure	17
2.2.1 Sample structure	17
2.2.2 Kronig-Penney band structure calculation	18
2.2.3 Self-consistent band structure calculation	20
2.2.4 Calculation of the zero-field density of states	22
2.2.5 Electron trajectories in the artificial band structure	25
2.2.6 Closed electron orbits	27
2.2.7 Open electron orbits	29
2.2.8 Magnetic breakdown	32
2.3 Experimental results	32
2.3.1 Magnetoresistance for $E_F < \Delta$	33
2.3.2 Magnetoresistance for $E_F > \Delta$	35
2.3.3 Gate voltage to electron density relation	37
2.3.4 Magnetoresistance maxima and minima in the (U_g, B) plane	38
2.3.5 Transport model for $E_F < \Delta$	41
2.3.6 Comparison of theoretical and experimental magnetoresistance	44

2.3.7	Magnetic breakdown	46
2.3.8	Spin-polarized state at high magnetic fields	49
2.3.9	Density dependence of the zero-field resistance	50
2.3.10	High frequency magnetoresistance oscillations	53
2.4	Quantum mechanical model	54
2.4.1	Formulation of the problem	54
2.4.2	Qualitative discussion of the energy spectrum	56
2.4.3	Energy bands and density of states	56
2.4.4	Density of states in the (U_g, B) plane	59
2.5	Conclusion	60
3	High Field Miniband Transport	63
3.1	Superlattice transport: Review	64
3.1.1	Esaki-Tsu model	64
3.1.2	Bloch oscillations	66
3.1.3	Beyond the Esaki-Tsu model	68
3.1.4	Experimental work	70
3.2	Self consistent band structure calculation	71
3.3	Experimental results: $q=0$ nm SLFET	74
3.3.1	Current-voltage relation: Overview	76
3.3.2	Comparison to the Esaki-Tsu model	79
3.3.3	Bloch - phonon resonances	81
3.4	Experimental results: All SLFETs	84
3.4.1	Current-voltage relation of SLFETs and CEOFETs	84
3.4.2	Peak current and transconductance	86
3.4.3	Ruling out other mechanisms for negative differential resistance	89
3.4.4	Stabilization of the charge distribution	90
3.4.5	Electron mobility	92
3.5	Transport in magnetic field	94
3.5.1	Experiment	94
3.5.2	Theory: Miniband transport	95
3.5.3	Theory: Resonant tunneling	98
3.5.4	Discussion	100
3.6	Towards ultra short channel vertical transistors	101

3.6.1	Heterobarrier CEOFET	103
3.6.2	Planar doped CEOFET	105
3.7	Conclusion	106
4	Transport in the Resonant Tunneling Regime	107
4.1	Review on low dimensional resonant tunneling	108
4.2	Sample design and band structure calculation	110
4.3	Resonant tunneling in zero magnetic field	112
4.3.1	Experimental current-voltage traces	112
4.3.2	Resonant tunneling model	114
4.4	Resonant tunneling in a perpendicular magnetic field	116
4.4.1	Experimental current-voltage traces	118
4.4.2	Theory for the ground state to ground state resonance shift	118
4.4.3	Theory for the tunneling current increase	121
4.5	Resonant tunneling in a parallel magnetic field	122
4.5.1	Experimental current-voltage traces	123
4.5.2	Qualitative model	123
4.6	Conclusion	125
5	Quantum interference in artificial band structures	127
5.1	Artificial band structures	128
5.2	Self-consistent calculation	131
5.2.1	SLFET structure and electron density	132
5.2.2	Potential modulation	133
5.2.3	Potential modulation amplitude	134
5.3	Magnetotransport experiments	136
5.3.1	Magnetoresistance traces	137
5.3.2	Density dependent study	139
5.3.3	Electron orbits in a multi-band structure, magnetic breakdown	140
5.3.4	Probability of electron orbits	145
5.3.5	Quantum interference in closed orbits	147
5.3.6	Quantum interference between open orbits	149
5.3.7	Commensurability oscillations	151
5.3.8	Temperature dependence	152

5.3.9	Quantum interference in metal physics	154
5.3.10	Quantum interference in organic superconductors	155
5.4	Commensurability effects in focused laser beam diffused structures	156
5.4.1	Method of fabrication	156
5.4.2	Self-consistent calculation	157
5.4.3	One-dimensional surface lateral superlattice	159
5.4.4	Two-dimensional antidot superlattice	159
5.4.5	Magnetic focussing structure	159
5.4.6	Summary	160
5.5	Conclusion	162
6	Phase Transition at Fractional Filling	163
6.1	Review	164
6.2	Overview	166
6.3	Temperature dependence	169
6.4	Hysteresis at filling factor $\nu=2/3$	171
6.5	Resistance time dependence	171
6.6	Nuclear magnetic resonance	174
6.7	Conclusion	176
7	Conclusion	179
	Acknowledgements	183
	List of Figures	187
	References	191
	List of Publications	209

Summary

In this work we introduce the superlattice field-effect transistor (SLFET), a new three-terminal semiconductor device that combines a two-dimensional electron system with a superlattice, and thus allows us to explore hitherto undisclosed low-dimensional regimes. The SLFET is fabricated with atomic precision in two spatial dimensions by molecular beam epitaxy (MBE) in the GaAs/AlGaAs lattice matched material system using the cleaved-edge overgrowth technique. In a first MBE growth step along the (001) direction, an undoped superlattice is sandwiched between the source and drain contacts. After *in situ* cleaving the sample, a GaAs set-back layer and a gate barrier and contact is grown in (110) direction. We have perfect control over all relevant layer thicknesses and compositions, thus by band-structure engineering we can design any system between an array of weakly coupled quantum wires, to a two-dimensional electron system with wide minibands and narrow minigaps. We investigate these systems in low temperature electronic transport experiments, either by equilibrium magnetotransport, or non-equilibrium current-voltage measurements. Theoretical models are developed using semi-classical and quantum mechanical methods.

The artificial band structures, obtained with the SLFETs, represent energy scales (e.g. miniband width or subband spacing), that are of comparable magnitude to other experimentally controllable energy scales, such as the Fermi energy, the magnetic and potential energy, and temperature. This sets us in a position to explore band structure effects in a variety of systems over a wide parameter space. We have sectioned this work according to the miniband width of the SLFET under study.

Magnetotransport in the lowest miniband of width $\Delta = 3.3$ meV reveals a cross-over from a two-dimensional behavior, characterized by closed electron orbits and magnetoresistance oscillations, to a one-dimensional behavior, manifested by open electron orbits and quenching of magneto-quantum oscillations, as the Fermi energy is raised from within the miniband into the band gap. For large magnetic fields, closed electron orbits are recovered due to magnetic breakdown. For the first time we directly confirm the theoretically expected breakdown field. We can explain all experimental data within a semiclassical model, and gain additional insight with a new quantum mechanical description by directly calculating

the density of states in a non-perturbative way.

For a series of SLFETs with miniband widths between $\Delta = 3.3$ meV and $\Delta = 21.2$ meV, in **high field miniband transport** experiments we discover negative differential resistance in qualitative agreement with the Esaki-Tsu model. Additional current maxima are explained by resonant emission of folded acoustic phonons through Bloch-oscillating electrons. The two-dimensionality of the electron system together with the presence of a metallic gate serve to stabilize the charge density in the negative differential velocity regime.

In weakly coupled quantum wires we observe **transport in the resonant tunneling regime** involving the wire ground and first excited states. Magnetic fields applied perpendicular to the wires, either parallel or perpendicular to the current direction, change the position of the resonance peaks as well as the tunneling current. Our model is based on the simultaneous conservation of electron energy and momentum in the tunneling process, the magnetically induced spatial separation of forward and reverse moving electrons within each wire and the distortion of the tunneling path in a magnetic field, and the formation of wire Landau levels at high magnetic fields.

In weakly modulated two-dimensional electron systems, for the first time we directly visualize the text-book case of a one-dimensional band structure. Our observation is explained semiclassically as **quantum interference in artificial band structures**. The first type of quantum interference effect occurs in closed electron orbits, in part made possible by magnetic breakdown of the small energy gaps separating formerly unconnected electron trajectories. The second type of quantum interference effect relates two different open electron orbits and results in a magnetic field dependent back-scattering probability. This process corresponds to the Aharonov-Bohm effect in reciprocal space. The known Weiss (commensurability) oscillations appear as a special case of our theory, and are thus, for the first time, explained by the topology of the artificial band structure.

Owing to the unparalleled combination of high electron mobility and density tunability in very weakly modulated SLFETs, we are able to discover hitherto undisclosed aspects of a ferromagnetic **phase transition at fractional filling**. As there exist two degenerate $\nu = 2/3$ fractional quantum Hall states with different spin orientations at low electron densities, hysteresis in magnetoresistance, a non-monotonic time dependence reminiscent of the Barkhausen effect, and peculiar features in resistively detected nuclear magnetic resonance experiments are ascribed to a ferromagnetic ordering and domain morphology. Even though our results generally apply to two-dimensional electron systems, we have evidence that the potential modulation in the SLFET intensifies domain formation.

Chapter 1

Introduction

Two of the great achievements in solid state physics are the fabrication of low dimensional systems, and the fabrication of artificial crystals with periodicity larger than that of natural crystals. Examples of low dimensional systems are two-dimensional electron gases, which led to the discovery of the integer and fractional quantum Hall effects, and one-dimensional electron quantum wires. By 'artificial crystals' we mean superlattices, i.e. man made periodic potentials superimposed on the natural periodic crystal potential.

These man-made structures become theoretically tractable with a quasi-particle description. In a periodic potential, the relevant quasi-particles are electrons that are assigned an effective mass, and in the case of the fractional quantum Hall effect we deal with composite fermions. The beauty of artificial crystals is that they allow the design of man made band structures, and give thus control over the properties of these quasi-particles.

In this work we combine both these great achievements of solid state physics into one semiconductor device, the superlattice field effect transistor. We explore the landscape that opens up between the one- and the two-dimensional world, that is furthermore enhanced by the effect of a magnetic field. This introductory chapter is supposed to give a first impression of this world. All necessary tools for understanding it will be provided in the subsequent chapters.

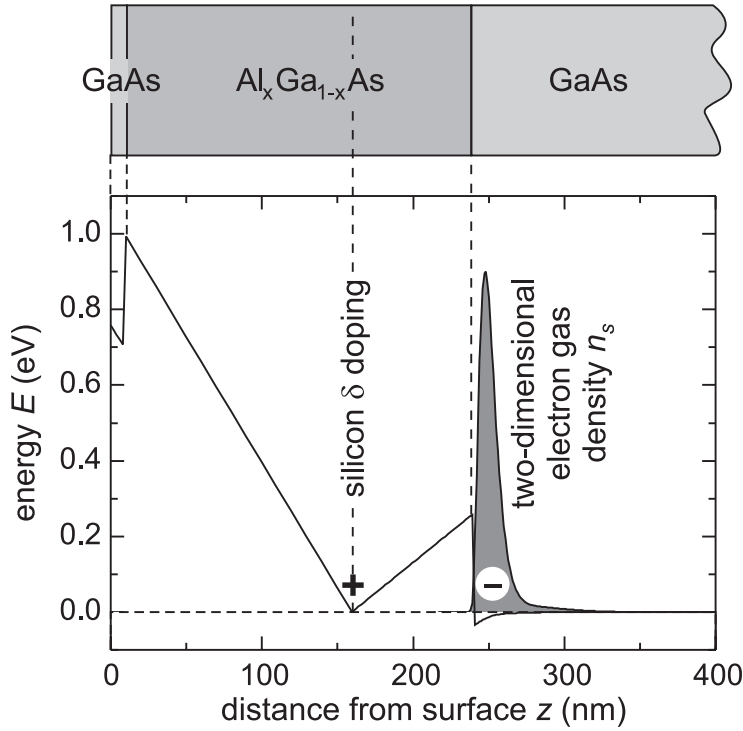


Figure 1.1: Modulation doped heterostructure.

1.1 Physics in two dimensions

Historically, first experiments on two-dimensional electron systems were performed in an n -channel inversion layer on the Si(100) surface [And82]. In 1966 Fowler, Fang, Howard, and Stiles first observed Shubnikov-de Haas oscillations [Fow66a][Fow66b]. The most prominent vehicle nowadays for studying two-dimensional electrons is the modulation doped heterostructure, for highest quality best fabricated in the lattice matched gallium-arsenide/aluminum-gallium-arsenide (GaAs/AlGaAs) material system. As shown in Figure 1.1, using the technique of molecular beam epitaxy (MBE) on a semi-insulating GaAs substrate, the layer sequence GaAs - AlGaAs - δ silicon doping - AlGaAs - GaAs is grown. Because silicon on (001) GaAs acts as a donor, and AlGaAs has a larger band gap than GaAs, in thermodynamical equilibrium electrons are transferred from the δ doping site to the AlGaAs/GaAs interface. There they form a two-dimensional electron system (2DES) of density n_s , electrostatically bound to the interface. The electron energy spectrum is

$$E_i(k_x, k_y) = E_i^0 + \hbar^2 \frac{k_x^2 + k_y^2}{2m^*}, \quad (1.1)$$

where E_i^0 is the subband energy of the quantizing triangular shaped potential in z direction, $\vec{k} = (k_x, k_y)$ is the electron momentum, and $m^* = 0.067m_0$ is the electron effective mass in GaAs. This parabolic energy spectrum causes a constant density of states per subband

$$D_0 = \frac{m^*}{\pi\hbar^2}. \quad (1.2)$$

In a magnetic field perpendicular to the electron system, the electronic states condense into spin-split Landau levels

$$E_{n,s} = \hbar\omega_c(n - 1/2) + sg^*\mu_B B; \quad n = 1, 2, \dots; \quad s = \pm \frac{1}{2}, \quad (1.3)$$

where $\omega_c = eB/m^*$ is the electron cyclotron frequency, $\mu_B = e\hbar/(2m_0)$ is the Bohr magneton, and g^* is the effective g factor, accounting for the Zeeman effect and the electron-electron exchange interaction. g^* is magnetic field dependent and can significantly differ from the Landé factor g_0 in GaAs. The constant zero-field density of states changes into a series of delta functions

$$D(E) = n_L \sum_{n,s} \delta(E - E_{n,s}), \quad (1.4)$$

where the amount of states per spin-split Landau level $n_L = eB/h$ is magnetic field dependent. The filling factor $\nu = n_s/n_L$ counts the amount of occupied levels.

Magnetotransport experiments are conducted by measuring the longitudinal or transverse magnetic field dependent resistance of the electron system, thus probing the electron states at the Fermi energy. For small magnetic fields $\omega_c\tau < 1$ the classical Hall effect for the transverse resistance, and a magnetic field independent longitudinal resistance is found. A unique feature of these two-dimensional electron systems is their high perfection, manifest in a large electron transport scattering time τ , or electron mobility $\mu = e\tau/m^*$. In the molecular beam epitaxy machine used for fabricating the SLFET in this work, on (001) GaAs we routinely obtained low-temperature mobilities of $\mu = 10 \times 10^6 \text{ cm}^2/\text{Vs}$, equivalent to a scattering time of $\tau = 0.4 \text{ ns}$, or a mean free path of $\lambda = v_F\tau = 25 \mu\text{m}$ at an electron density of $n_s = 2 \times 10^{11} \text{ cm}^{-2}$, where $v_F = \hbar k_F/m^*$ is the Fermi velocity, and $k_F = \sqrt{2\pi n_s}$ is the Fermi wave vector.

At low temperatures and high mobilities the condition $\omega_c\tau \gg 1$ is readily achieved. Electrons complete their cyclotron orbits, and the semiclassical quantization condition (Bohr-Sommerfeld condition) for stationary states requires that an integer number of magnetic flux quanta $\Phi_0 = h/e$ threads the enclosed real space area πr_c^2 , where $r_c = v_F/\omega_c$ is the cyclotron

radius. As the magnetic field is raised, this condition is met periodically in $1/B$, and the longitudinal resistance oscillates with a frequency

$$\Delta^{-1} \equiv (\Delta(1/B))^{-1} = \Phi_0 n_s \quad (1.5)$$

when the spin is resolved (Shubnikov-de Haas oscillations). This semiclassical picture will be discussed and extended to more complex electron trajectories than circles in Chapter 5. In the self-consistent Born approximation, short range scatterers result in a broadening of the delta-function like density of states (1.4), and the scattering time depends on the density of states $D(E_F)$ at the Fermi edge, $\tau \propto 1/D^2(E_F)$. When the Fermi energy lies between two Landau levels, the density of states vanishes, and the scattering time is large. This results in a minimal longitudinal resistance and, via tensor inversion, minimal longitudinal conductivity. At these integer filling factors, a plateau like Hall resistance with exact quantization

$$\rho_{xy} = \frac{h}{\nu e^2}, \quad \nu = 1, 2, \dots \quad (1.6)$$

has first been observed (in a silicon inversion layer) by von Klitzing, Dorda, and Pepper [vK80]. The vanishing longitudinal resistance with a quantized transverse resistance is called the integer quantum Hall effect. More realistic models of the density of states consider extended states in the center of the Landau levels, framed by localized states. In the edge-channel picture the quantized Hall plateaus are explained by one-dimensional channels at the sample boundaries, with conductance e^2/h each, separated by insulating regions. Around integer filling factors, backscattering is inhibited because the bulk two-dimensional electron system is isolating. We will encounter a similar transport model in Section 5.3.

In exceptionally clean two-dimensional electron systems, minima in the longitudinal resistance and quantized Hall resistances are observed also at fractional filling factors [Tsu82]. As in the integer quantum Hall effect, which results from an energy gap in the density of states within which no electrons are able to carry current, the fractional quantum Hall effect also results from an energy gap. This gap, however, is caused by the interaction of electrons with each other in the presence of a magnetic field. The ground state is characterized by a minimal Coulomb energy of all participating electrons. At certain values of the magnetic field, a highly symmetric many-particle solution, called the 'Laughlin state' [Lau83], satisfies this criterion by putting $1/m^{\text{th}}$ of an electron on average at each magnetic flux quantum site ($m = 1, 3, 5, \dots$ is an odd number). To find the minimum excited state we note that the minimum displacement distance by which we can vacate a site in the two-dimensional electron gas is characterized by the extent of a wave function, $l_B = \hbar/(eB)$, the magnetic

length [Gra98]. This discrete minimum distance results in a discrete increase in the Coulomb energy of the system, defining a gap.

The fractional quantum Hall effect is a correlated electron phenomenon since electron interactions define the gap, making it critically different in character from the non-interacting integer quantum Hall effect. In the last two decades the fractional quantum Hall effect has become an intensely studied field of correlated electron physics, joining the only handful strongly correlated many-particle phenomena known to date, including superconductivity, superfluidity, and magnetism. In Chapter 6 we report on ferromagnetic phenomena observed in the fractional quantum Hall regime.

1.2 Superlattices

In natural crystals, the periodicity of the atomic lattice leads to an energy spectrum characterized by energy bands [Blo28], instead of discrete levels as in atoms and molecules. The corresponding quantum mechanical states are characterized by a band index v , and the Bloch vector \vec{k} . Their energy is given by the dispersion relation $E^v(\vec{k})$. An example of a natural crystal and its corresponding electronic band structure is shown in Figure 1.2(a). Gallium-arsenide (GaAs) crystallizes in the zincblende structure with a lattice constant $a = 5.65 \text{ \AA}$, and the energy scale of the bands and of the band gap is electron volts.

A superlattice is a periodic potential within the natural crystal potential, and many of the properties encountered in natural crystals are also found in these artificial crystals, but on a different scale (see Figure 1.2(b)). Typical period lengths d in superlattices are tens of nanometers, and energies are best plotted on a meV-axis. As in natural crystals, the periodicity of the potential leads to a continuous energy spectrum, and in analogy to the bands here we speak about minibands. The Brillouin zone boundary $k_0 = \pi/d$ in superlattices is reduced by a factor $d/a \approx 30$ to 150 with respect to natural crystals. These reductions of the energy and reciprocal space scales allow one to explore previously inaccessible regimes in the parameter space spanned by magnetic field, electric field, temperature, scattering time, and Fermi energy.

The theoretical proposal of the semiconductor superlattice by Esaki and Tsu [Esa70] was only a beginning. Significant advances in material sciences were necessary for its successful realization using epitaxial growth methods. As with the fabrication of two-dimensional systems, molecular beam epitaxy of ultra-pure source material in ultra-high vacuum is the method of choice for fabricating atomically precise GaAs/AlGaAs superlattices. The alu-

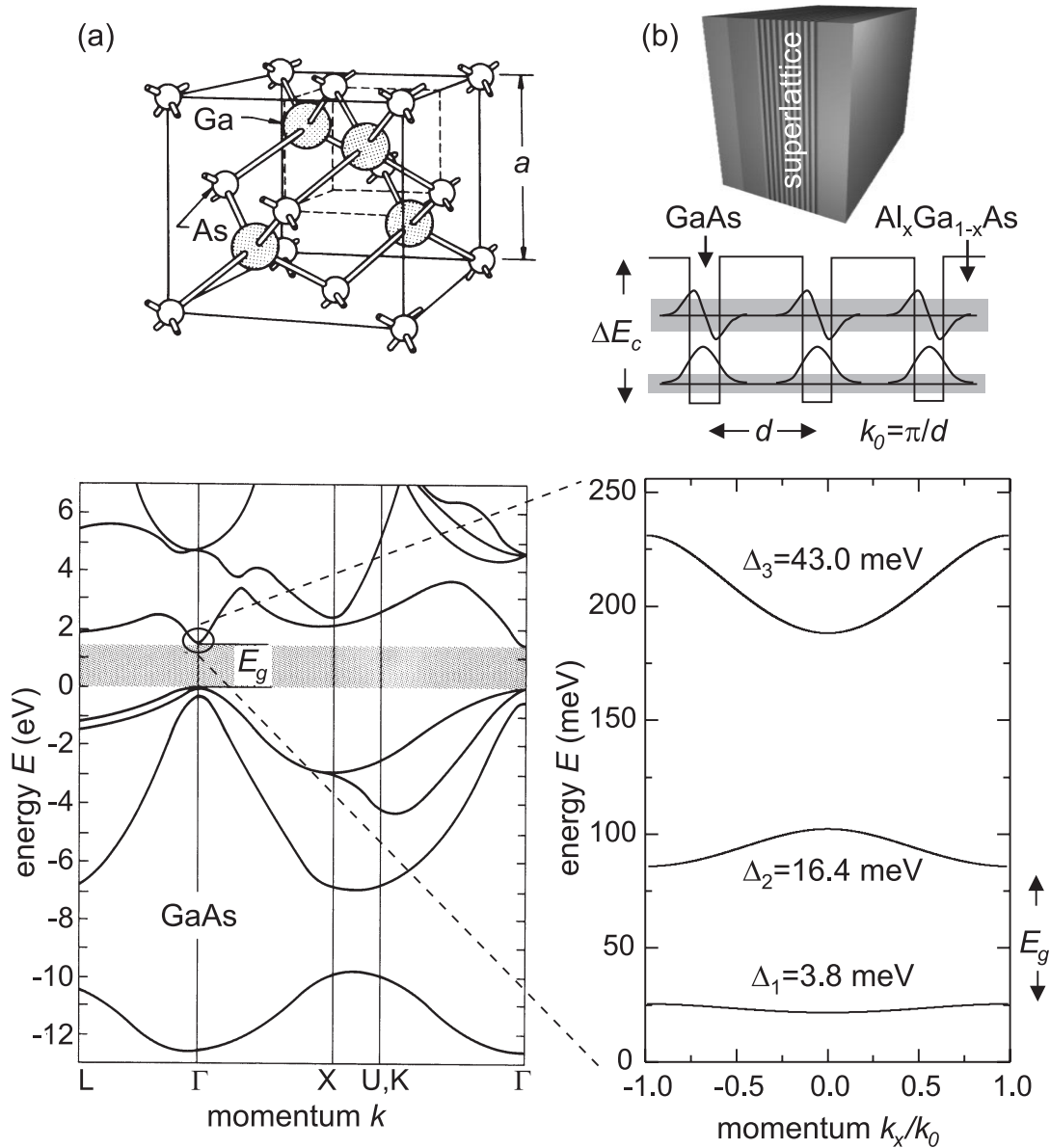


Figure 1.2: Natural (a) and artificial (b) crystals and band structures.

minimum content x defines the larger $\text{Al}_x\text{Ga}_{1-x}\text{As}$ band gap, which translates in part to a conduction band offset $\Delta E_c = 0.8 * x$ (eV) between GaAs and $\text{Al}_x\text{Ga}_{1-x}\text{As}$ at the Γ -point [Ins93]. Band structure engineering in the parameter space of well thickness l_w , barrier thickness l_b ($l_w + l_b = d$), and barrier energy ΔE_c allows us to custom design artificial band structures.

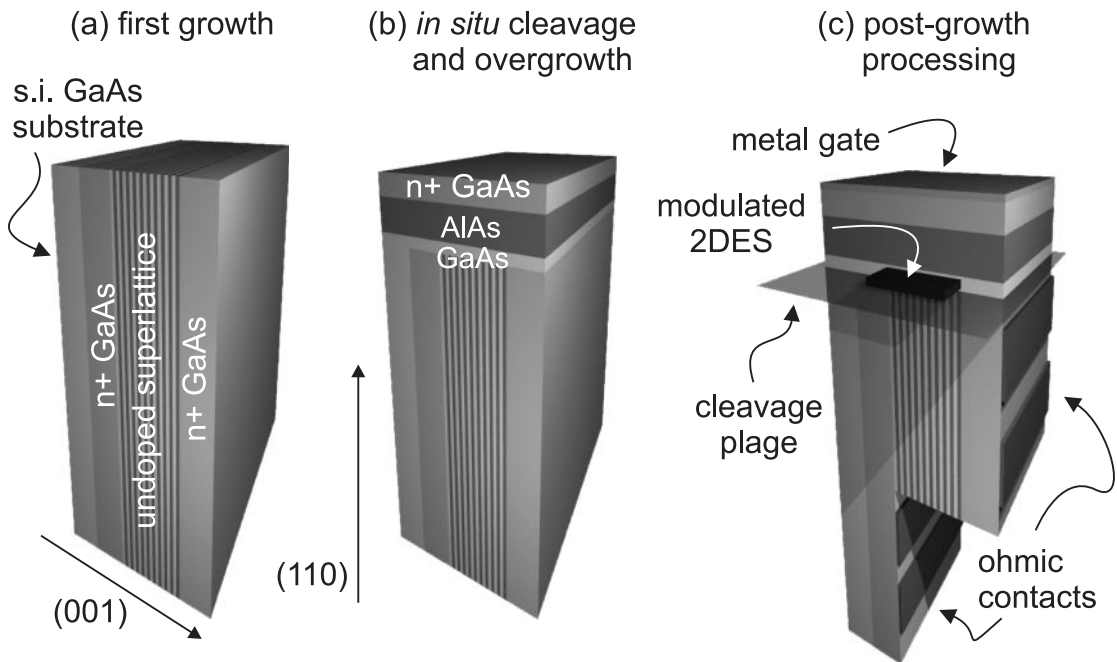


Figure 1.3: Fabrication of the superlattice field-effect transistor. (a) First growth step on (001) semi-insulating GaAs substrate: Undoped superlattice between two n+ GaAs contacts. (b) *In-situ* cleavage and second growth step on the freshly exposed (110) GaAs surface: GaAs layer, AlAs barrier, and n+ GaAs gate contact. (c) Sample processing after the growth: Etching to lower n+ GaAs contact, metallization of source, drain and gate, sample cutting into pieces of 250 μm width, and wire bonding.

1.3 Superlattice field effect transistor

Both two-dimensional systems and superlattices have been at the heart of semiconductor physics during the last thirty years. In this thesis we explore the world created by combining both in a single semiconductor device, called the superlattice field effect transistor (SLFET). The SLFET is fabricated by the cleaved-edge overgrowth (CEO) technique, invented at Bell laboratories by L. Pfeiffer and coworkers [Pfe90]. The uniqueness of the CEO technique lies in the fact that low-dimensional electronic systems can be fabricated to atomic precision not only in one, but in two, or even three perpendicular spatial directions, and that this system is buried in the bulk of the semiconductor, unaffected by surface effects, such as surface depletion. Examples of previously fabricated devices include ballistic one-dimensional systems (quantum wires) [Yac96] [Rot00] and zero-dimensional systems (quantum dots) [Weg97].

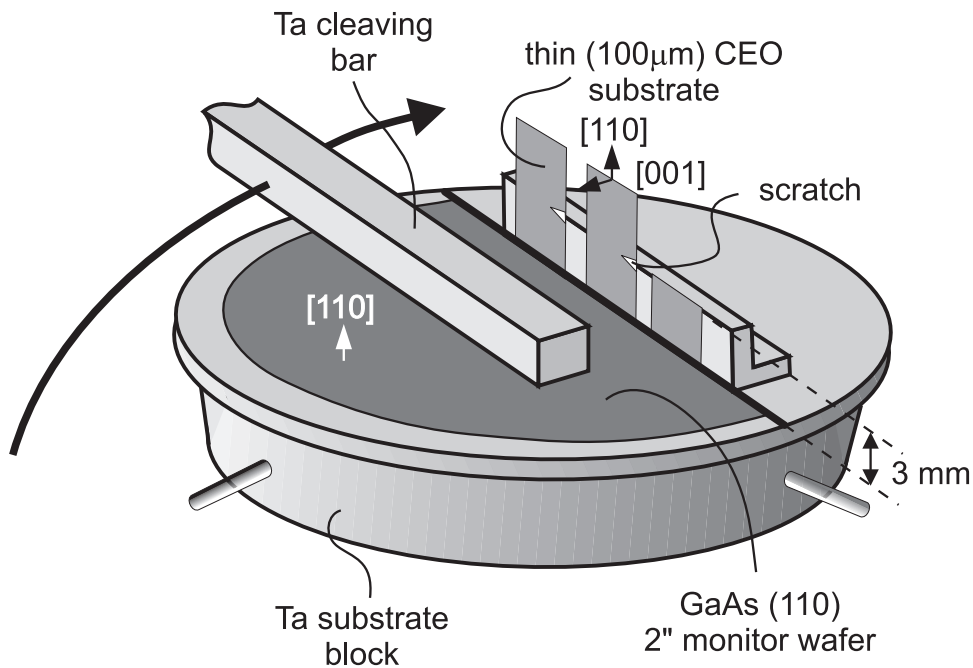


Figure 1.4: Cleaved-edge overgrowth technique (drawing by W. Wegscheider).

Details on the latter system, and about the CEO technology, can be found in [Sch98a]. The SLFET is based on a design by Stormer [Sto91b].

The fabrication scheme of the SLFET is shown in Figure 1.3. In the first MBE step, on a semi-insulating two-inch (001) GaAs wafer an undoped GaAs/AlGaAs superlattice is grown between two 1 μm thick n+ GaAs contacts, silicon doped to $2 \times 10^{18} \text{ cm}^{-3}$. Standard (001) growth parameters are used. The specific parameters of the superlattices investigated in the work are given in the respective chapters. In reference samples the superlattice is replaced by bulk AlGaAs. The resulting devices are called cleaved-edge overgrowth field-effect transistors (CEOFETs). The wafer is taken out the MBE, chemically thinned down to a thickness of 100 μm using a solution of 12% bromine in methanol, and cut into pieces of 7 mm by 7 mm. The position of the CEO cleave is scribed into the sample surface with a diamond tip, the samples are cleaned, and reinserted into the MBE, using a custom made tantalum sample holder (see Figure 1.4). After desorption of surface oxygen, when ultra-high vacuum conditions are met again, the samples are cleaved *in situ* by a tantalum bar, and the growth commences immediately thereafter on the freshly exposed (110) surface. At a lower growth temperature, smaller growth rate, and higher arsenic pressure, the layer sequence q nm GaAs, 100 nm AlAs, and 200 nm n+ GaAs (silicon doped to $2 \times 10^{18} \text{ cm}^{-3}$) is grown,

where q varies between zero and a few tens of nm depending on the SLFET design.

With standard optical lithography, wet chemical etching and PdGeAu metallization processing steps both (001) n+ GaAs layers are contacted, to serve as source and drain. The (110) n+ GaAs layer is contacted to serve as a gate. Finally the 7 mm wide samples are cut into pieces of 250 μm width, glued with conductive silver onto the gold coated surface of a GaAs wafer piece, and wire bonded into a ceramic chip carrier.

The transistor is operated by applying a positive gate voltage with respect to source and drain, and measuring the source-drain current in dependence of the source-drain voltage. What we have achieved with the SLFET is a hybrid superlattice two-dimensional electron system. The field-induced electron gas resides at the interface between the superlattice and the gate barrier, and the thickness q of the (110) GaAs layer determines the overlap of this electron gas with the superlattice, and thus the modulation strength. Details on this system and self-consistent calculations will be presented in subsequent chapters.

Our SLFET differs from the original device invented by Stormer *et al.* [Sto91b] in three important ways. First we use n+ GaAs source and drain contacts instead of n+ SL contacts, which is crucial to avoid leakage currents through the bulk superlattice at finite source-drain bias. Second we use an n+ GaAs gate instead of a fixed doping to obtain tunable electron density and higher electron mobility due to the absence of remote ionized impurity scattering. Third, a new degree of freedom in band structure design is introduced since by proper choice of the (110) GaAs layer thickness q , the strength of the potential modulation can be tuned without changing the superlattice itself.

1.4 Outline of this thesis

The SLFET represents the intersection of a superlattice with a two-dimensional electron system, and can be considered as an array of coupled quantum wires. Depending on the modulation amplitude, or the coupling between the wires, very different regimes can be investigated. In Figure 1.5 the chapters of this thesis are put in relation to these regimes. For weakly coupled wires, the SLFET has one-dimensional character, electronic states are discrete, and transport between the wires is expected to occur via resonant tunneling. The system is best described by a tight-binding model, which considers the coupling between the wires as a perturbation. For intermediate coupling, the overlap between the wire states becomes significant, and we will be able to investigate miniband transport. The regime of strong coupling is best described by a two-dimensional electron system with weak periodic

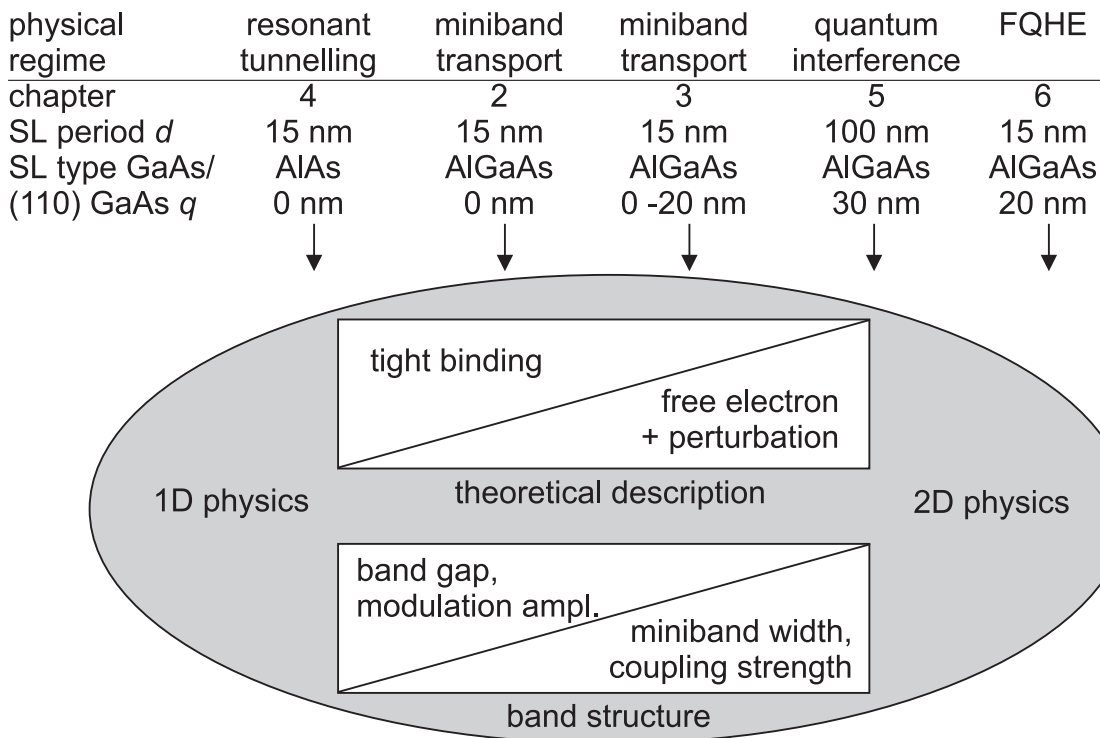


Figure 1.5: Graphical outline of this thesis. The different chapters investigate the different regimes observable between one-dimensional and two-dimensional systems.

perturbation. Electron systems in this regime are often referred to as lateral superlattices. The gaps between the minibands become narrow, and magnetotransport experiments will reveal two-dimensional electron orbits. Finally, for the case of very strong coupling, thanks to unparalleled high electron mobility and electron density tunability, the SLFET represents an ideal vehicle for electron density dependent studies in the fractional quantum Hall regime.

Chapter 2 is concerned with magnetotransport in the intermediate coupling regime. The unparalleled situation investigated in this chapter is characterized by a commensurability of the miniband width, the Fermi energy, and the magnetic energy. In the first part of the chapter we calculate the zero-magnetic field band structure by a Kronig-Penney model, and more sophisticated, by self-consistently solving the coupled Schrödinger/Poisson equations. These calculations give insight into the electron distribution in the SLFET at equilibrium. Based on this band structure, and on the semi-classical equations of motion, we discuss the electron orbits under the application of a magnetic field. Different types of orbits are found, that are expected to leave characteristic fingerprints in the magnetoresistance. In

the second part of this chapter, we find indeed striking signs of these qualitatively different orbits in magnetotransport experiments. In the third part of the chapter we present fully quantum mechanical results for the electron energy spectrum and the density of states, suited to explain not only the limiting cases tractable with the semiclassical model, but also the transition region of comparable miniband and magnetic energy.

Chapter 3 revolves around non-equilibrium electrons in artificial band structures and contributes to the quest for the electrically driven Bloch oscillator. We show clear signatures of the fact, that the miniband width represents an upper limit to the energy that conduction electrons can acquire in an applied electric field. Following a discussion of transport models and self-consistent band structure calculations, current-voltage data of SLFETs with different miniband widths are presented, compared to reference samples, and explained. In the SLFET the electric field is stabilized owing to the presence of a metallic gate, and to its lower dimensionality with respect to bulk superlattices. Folded superlattice phonons appear to critically influence electron transport. The observed negative differential resistance peak is found to characteristically shift in a perpendicular magnetic field. In the last part of this chapter we demonstrate ultra-short channel vertical field effect transistors.

In **Chapter 4** we study the tunneling transport across an array of quantum wires, corresponding to a weakly coupled superlattice. In non-equilibrium transport, source-drain current peaks result from resonant tunneling between wire states, governed by the simultaneous conservation of energy and momentum. These resonances are found to depend characteristically on the magnetic field strength and orientation.

Chapter 5 will most certainly appeal to anybody excited by multi-band structures, electron orbits therein, and semiclassical models. Central results of this work on weakly modulated electron systems are a direct visualization of different closed electron orbits in a multiply connected band structure, the proof of a quantum interference effect between different electron orbits, reminiscent to the Aharonov-Bohm effect, and, deduced from this effect, the first explanation, based on the artificial band structure, of the previously observed commensurability oscillations. We begin this chapter with self-consistent calculations of the electron density distribution in the SLFET. Then we present magnetotransport experiments, which are subsequently explained in a semiclassical model entirely from the artificial band structure. A relation is established to results in metal physics and other two-dimensional conductors. An extra section in this chapter is dedicated to a technique developed to fabricate lateral surface doped superlattices. We demonstrate its flexible use by a variety of commensurability effects, both in one- and two-dimensionally modulated systems.

Chapter 6 contributes to our current understanding of the fractional quantum Hall effect, and quantum phase transitions between spin-polarized and spin-unpolarized states. This ferromagnetic phase transition is observed at the fractional filling factor $\nu = 2/3$ as a hysteresis in the sample resistance, and is studied in dependence of electron density, magnetic field, temperature, time, and radio-frequency irradiation. In this chapter we exploit the unparalleled combination of high electron mobility and density tunability in the SLFET, and our results generally apply to two-dimensional electron systems. Additionally, we have evidence of an intensifying effect to the domain formation due to the underlying superlattice.

We conclude in **Chapter 7** with a summary and an outlook.

Chapter 2

Magnetotransport in the Lowest Miniband

We are interested in the electronic structure of a two-dimensional system in a regime, where the magnetic energy and the zero-field band width are of comparable magnitude. Thus neither the magnetic field nor the periodic potential giving rise to the band structure can be treated as a perturbation. Experimentally this regime can be explored either by using bulk crystals and very high magnetic fields, or, at more comfortable magnetic field strengths of a few Tesla, by reducing the band width to the meV range in an artificial crystal, namely a superlattice. Theoretically, we gain insight to this problem by semiclassical and quantum mechanical calculations.

Following a short review of relevant work in Section 2.1, we discuss the motion of electrons in an artificial band structure and a perpendicular magnetic field semiclassically in Section 2.2. Low temperature magnetoresistance data is presented in Section 2.3, which can in part be understood with the tools developed so far. A detailed insight to the problem is elaborated in Section 2.4 by a full quantum mechanical calculation of the density of states, which allows to draw conclusions for the electronic transport.

2.1 Review

In this chapter we study equilibrium magnetotransport in the lowest miniband, which has a band width Δ comparable to the magnetic energy $\hbar\omega_c$ at a field of a few tesla. Due to the large band gap, the next miniband does not play any role here. Experimentally, this regime is inherently difficult to achieve, because for narrow minibands in combination with wide gaps short period superlattices are required, which at the same time must host a two-dimensional electron gas of sufficient mobility to allow for magneto-quantum oscillations.

In the literature we find two main classes of lateral superlattices. On the one side, the so-called surface lateral superlattices are based on semiconductor heterostructures, which are modulated by changing the surface properties. These superlattices are suited for generating weakly modulated electron systems with rather long period lengths (on the order of 100 nm). As a result, many minibands are occupied at electron densities $n_s > 1 \times 10^{11} \text{ cm}^{-2}$, and minigaps are narrow. These superlattices will be reviewed in Chapter 5. On the other side, short period superlattices have been fabricated using self-organizing mechanisms rather than lithography. One exploits the corrugated growth on high-index surfaces and the fact that atomic steps modify the electrostatic potential in a two-dimensional electron gas. On vicinal (111)B GaAs surfaces multi-atomic steps with a periodicity of a few tens of nanometers were generated [Nak98] [Sak99], similar devices were fabricated on GaAs (001) vicinal planes [Fuk88] [Mot89] [Tsu90]. All these structures have the advantage of small period modulations, but due to the self-organized growth, the superlattices are irregular and mobilities are generally low.

With the cleaved-edge overgrowth technique, the fabrication of short-period, highly regular and high mobility lateral superlattices is possible. Stormer *et al.* [Sto91b] have demonstrated magnetoresistance oscillations in high-mobility lateral superlattices with period $d = 10 \text{ nm}$. The width of their miniband $\Delta = 22 \text{ meV}$, however, was too large for shifting the Fermi energy into the minigap. Thus they observed only two-dimensional behavior. The other extreme was reported by Ohno *et al.* [Ohn95], who measured a few periods of magnetoresistance oscillations in a sample of almost uncoupled parallel quantum wires, thus probing one-dimensional subbands. In a recent paper [Maj00], the Tsui group at Princeton measured an effective mass enhancement of two-dimensional electrons in a miniband by temperature dependent magnetoresistance measurements. Even though they were able to change the electron density by means of a metal gate, they observed purely two-dimensional behavior.

In this chapter we demonstrate for the first time the drastic changes that accompany the shifting of the Fermi energy from within the miniband into the minigap. In magneto-transport we witness the transition from a two-dimensional to a one-dimensional behavior, and we are able to explain the experimental data in semiclassical and quantum mechanical terms. A good source of information for the general understanding of conduction electrons in band structures, written for metals, include the short introduction by Pippard [Pip65], the excellent review by Shoenberg [Sho84], and the tutorials by Chambers [Cha90] and Brauer [Bra72]. Superlattice electron motion in magnetic fields has been reviewed by Jan-Kees Maan [Maa87]. Some results of this chapter have previously been published in [Deu00a].

2.2 Qualitative model using the zero-field band structure

In this section we lay the foundation to understanding the physics of conduction electrons in a band structure of a one-dimensionally modulated system. After a description of the SLFET used for this chapter, we calculate its overall band structure in a Kronig-Penney model, and its detailed band structure self-consistently, including minibands that occur due to the two-dimensionality of the electron gas. We analytically calculate the zero-field density of states, and highlight the electron trajectories in real and reciprocal space. The interplay between the three energy scales miniband width Δ , magnetic energy $\hbar\omega_c$, and Fermi energy E_F is then found to result in a intricate phase diagram, with prevalence of closed orbits, open orbits, and magnetic breakdown orbits. This phase diagram will then be explored experimentally in the following section.

2.2.1 Sample structure

The structure of the sample investigated in this chapter is shown in Figure 2.1. The undoped superlattice with period $d = 15$ nm consists of 3 nm $\text{Al}_{0.32}\text{Ga}_{0.68}\text{As}$ and 12 nm GaAs repeated 100 times. The superlattice is sandwiched between two n+ GaAs contacts, doped to $2 \times 10^{18} \text{ cm}^{-3}$, and grown on a semi-insulating (001) GaAs wafer. After cleaving the sample along the (110) plane the regrowth in (110) direction consists of a 100 nm $\text{Al}_{0.32}\text{Ga}_{0.68}\text{As}$ barrier and another n+ GaAs contact layer. Ohmic contacts are evaporated to the upper and the lower n+ GaAs layer, serving as source and drain contacts, as well as to the (110) n+ GaAs layer, which serves as a gate. By positively biasing the gate with respect to source

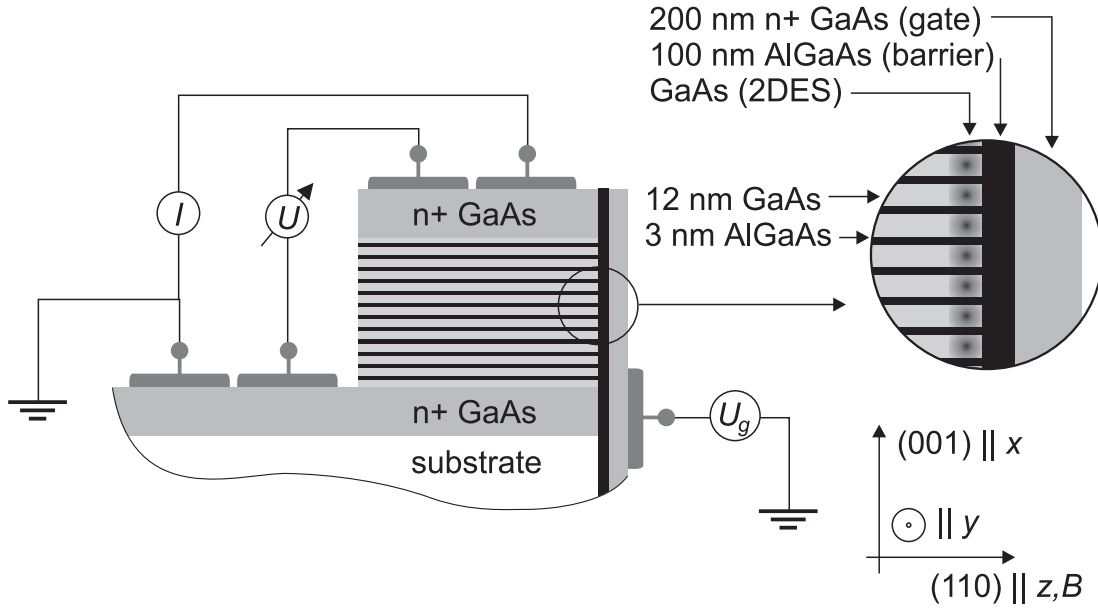


Figure 2.1: SLFET sample structure and definition of the coordinate system and magnetic field direction.

and drain, a two-dimensional electron gas is field induced at the superlattice-AlGaAs barrier. The length of the electron channel is given by the thickness $L = 1.5 \mu\text{m}$ of the superlattice, the channel width is $W = 250 \mu\text{m}$. The equilibrium electric properties of this modulated two-dimensional electron system in the presence of a perpendicular magnetic field are the focus of this chapter.

2.2.2 Kronig-Penney band structure calculation

In the Kronig-Penney model [dLK31] the Schrödinger equation

$$H\Psi \equiv \left(\frac{p_x^2(x)}{2m^*(x)} + V(x) \right) \Psi = E\Psi \quad (2.1)$$

is solved with a potential $V(x)$ that consists of periodically repeated square wells of depth V_0 , width l_w separated by barriers of thickness l_b . The superlattice period is $d = l_w + l_b$. The band structure is obtained by matching propagating or evanescent envelope functions at the boundary of consecutive layers. The envelope functions are the solutions of the effective Hamiltonian in Equation (2.1) in which both band edges *and* effective masses [Bas81] are position dependent. The effective mass jumps modify the boundary conditions imposed to

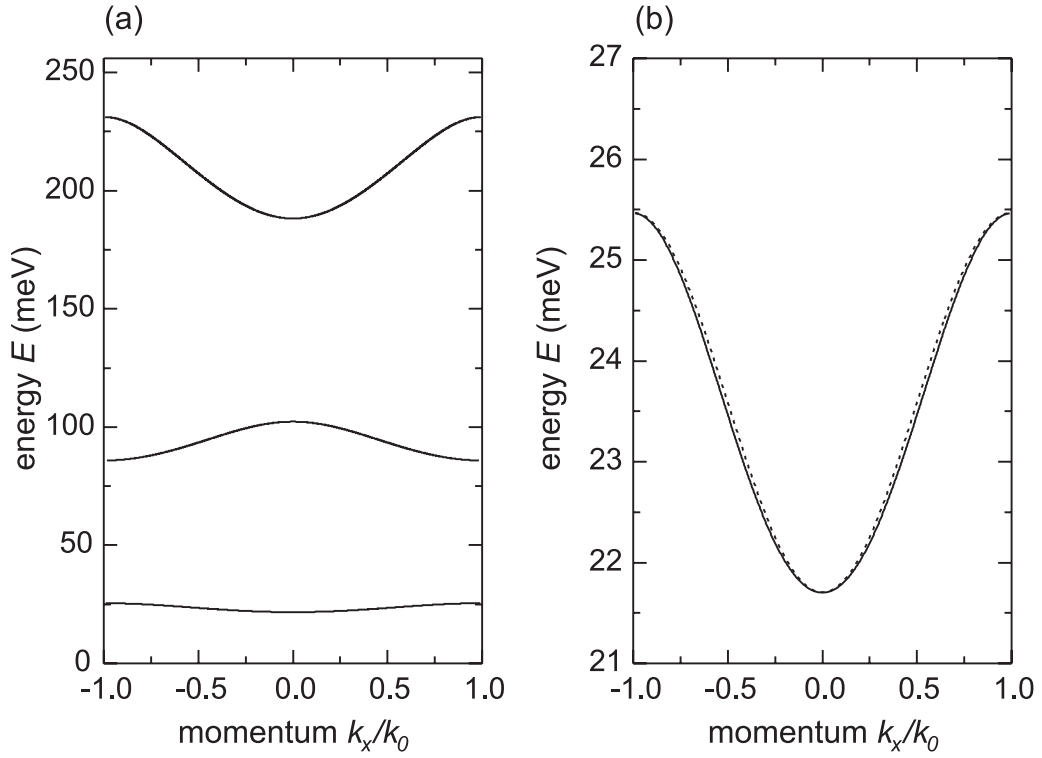


Figure 2.2: (a) Calculated band structure in the Kronig-Penney model. (b) Enlargement of the lowest subband. The dotted line represents a cosine function. The electron momentum is normalized to the Brillouin zone boundary $k_0 = \pi/d$.

the eigenstates of the effective-mass Hamiltonian. The energy-momentum dispersion relation $E(k_x)$ is obtained by solving the implicit equation

$$\cos(k_x d) = \cos(k_w l_w) \cosh(k_b l_b) - \frac{1}{2} \left(\chi - \frac{1}{\chi} \right) \sin(k_w l_w) \sinh(k_b l_b) \quad (2.2)$$

where

$$k_w = \frac{1}{\hbar} \sqrt{2m_{GaAs} E(k_x)} \quad (2.3)$$

$$k_b = \frac{1}{\hbar} \sqrt{2m_{AlGaAs} (V_0 - E(k_x))} \quad (2.4)$$

$$\chi = \frac{m_{AlGaAs} k_w}{m_{GaAs} k_b}. \quad (2.5)$$

The parameters used in our calculation are: $m_{GaAs} = 0.067 m_0$, $m_{AlGaAs} = m_{GaAs} + 0.083 x m_0$ [Ins93] where $x = 0.32$ is the Al-content in the barriers, $V_0 = 0.8x$ (eV) [Ins93].

The resulting dispersion relation is shown in Figure 2.2(a). The lowest miniband has a width of $\Delta=3.7$ meV, and a ground state energy with respect to the GaAs conduction band of 21.7 meV. This energy difference between the superlattice and the GaAs conduction band is crucial to avoid leakage currents through the bulk superlattice away from the cleavage plane. The second miniband is separated from the first miniband by a quasi-gap of 60 meV. Due to this large energy gap this and the third miniband will not be occupied in the present study and can therefore be neglected.

In Figure 2.2(b) we demonstrate that the lowest miniband can be well approximated by a cosine function (dotted line). A cosine function is indeed obtained when the right hand side of Equation (2.2) is expanded in the vicinity of the quantization energy E_0 of the isolated quantum well [Bas88]

$$E(k_x) = E_0 + \frac{\Delta}{2} (1 - \cos(k_x d)) \quad (2.6)$$

This is the result also found in the *tight-binding model* [Ash76].

One has to be aware of the assumptions and approximations involved with using the Kronig-Penney model. First, this model is strictly one-dimensional, and excited states in the z -direction are therefore not considered. Second, the Kronig-Penney model is based on a single-particle theory, any self-consistent effects are neglected. Both of these limitations are cured by a full two-dimensional and self-consistent quantum mechanical calculation.

2.2.3 Self-consistent band structure calculation

The quantum-mechanical states in the SLFET are self-consistently calculated using a computer program developed by M. Rother [Rot99a][Rot00]. Input parameters to the program are the material parameters in the (x, z) plane, and appropriate boundary conditions. In the case of the SLFET we model 16 periods of the superlattice, plus the gate dielectric and the gate contact. The two-dimensional electron gas and the gate contact represent two different Fermi systems. The difference in their chemical potential is defined as the gate voltage U_g . A total of 100 subbands are calculated for different gate voltages. In Figure 2.3 we show the resulting electron density distribution $n(x, z)$ for a mean two-dimensional electron density of $n_s = 1.7 \times 10^{11} \text{ cm}^{-2}$. The density $n(x, z)$ is obtained by summing all occupied electron states up to the Fermi energy using the Fermi distribution at $T = 300$ mK. The electrons are localized at a distance of about 10 nm from the interface between superlattice and gate barrier, and the electron density almost vanishes in the region of the superlattice barriers. To

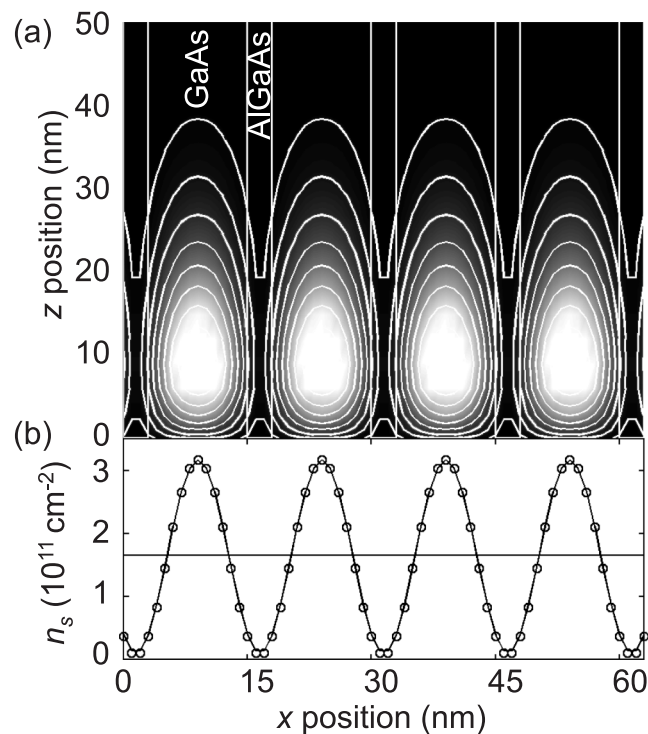


Figure 2.3: Self-consistently calculated electron density distribution. (a) Gray-scale coded electron density distribution in the (x, z) plane. The line $z = 0$ marks the interface between the superlattice and the gate barrier. One superlattice quantum well is marked by *GaAs*, and one barrier by *AlGaAs*. (b) sheet electron density integrated over z . The circles mark the calculated density, while the solid line is a cosine function approximation to the integrated electron density. The mean two-dimensional electron density is $n_s = 1.7 \times 10^{11} \text{ cm}^{-2}$.

a very good approximation the integrated two-dimensional electron density is described by a cosine function.

The band structure in the SLFET is readily obtained by plotting the energy of the calculated electronic states versus the corresponding momentum, as shown in Figure 2.4. Interestingly, energetically above the lowest miniband further bands of the same symmetry appear. These bands stem from excited electronic states in the z direction. For all electron densities obtainable with the SLFET these bands are unoccupied in equilibrium transport and can therefore be neglected. Our calculation further shows that for the lowest quantum well state all minibands have the same band width of $\Delta = 3.3 \text{ meV}$, and that Δ is only very weakly dependent on the electron density. Only the offset between the minibands increases with in-

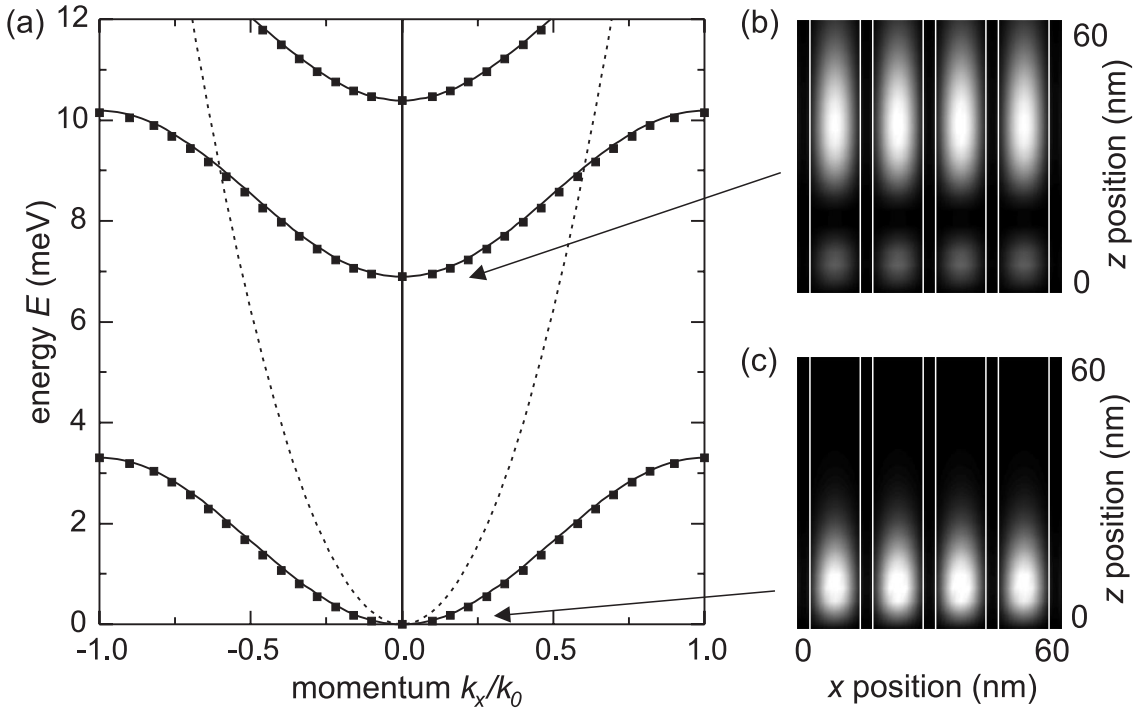


Figure 2.4: (a) Self-consistently calculated band structure for an electron density of $n_s = 1.7 \times 10^{11} \text{ cm}^{-2}$. The squares are the calculated points, the solid lines are a cosine function approximation to the calculated bands, and the dotted line is the free electron dispersion relation. (b) Real space plot of the lowest electronic state to the first excited miniband (unoccupied). (c) Lowest electronic state of the ground miniband (occupied).

creasing electron density. The band width obtained here is very close to the Kronig-Penney result.

2.2.4 Calculation of the zero-field density of states

In a one-dimensional superlattice the electron energy spectrum is given by

$$E(\vec{k}) = E_x(k_x) + \frac{\hbar^2 k_y^2}{2m^*}. \quad (2.7)$$

The first term is a periodic function with period $2\pi/d$, while the second term describes the free electron motion in y direction. We have shown in Sections 2.2.2 and 2.2.3 that for the SLFET at hand using the Kronig-Penney model, or the tight-binding approximation,

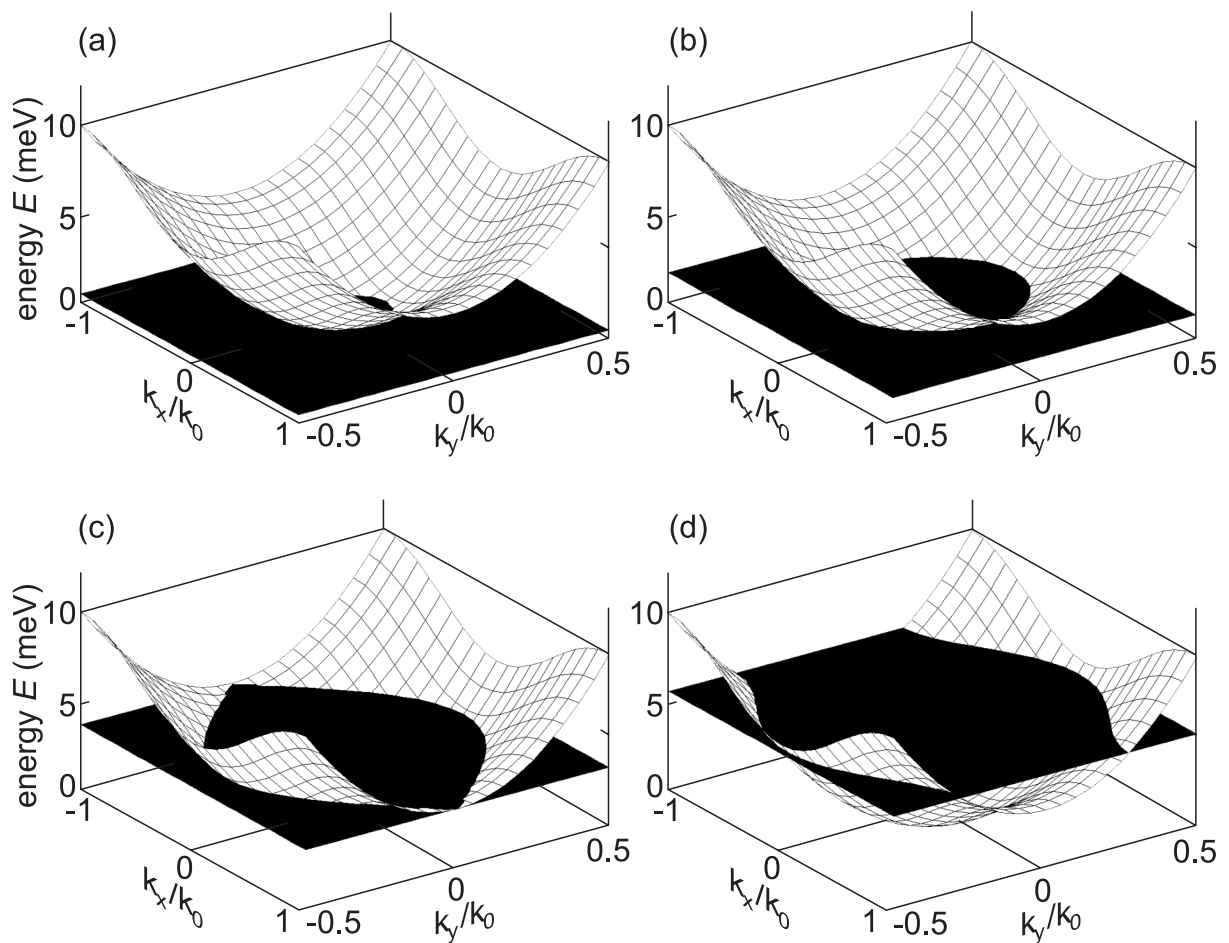


Figure 2.5: Fermi contours for different Fermi energies. (a) and (b) $E_F < \Delta$. (c) $E_F = \Delta$. (d) $E_F > \Delta$.

the dispersion in superlattice direction $E_x(k_x)$ is well described by a cosine function. We therefore write

$$E(\vec{k}) = \frac{\Delta}{2}(1 - \cos(k_x d)) + \frac{\hbar^2 k_y^2}{2m^*}. \quad (2.8)$$

In Figure 2.5 we plot the energy surface $E(k_x, k_y)$, and additionally different Fermi energies as horizontal planes. In x direction the cosine shape appears, while parabolas mark the dispersion along the y direction. The electrons relevant for electronic transport populate the intersection between the energy surface $E(k_x, k_y)$ and the Fermi plane E_F .

Given the dispersion relation (2.8) the density of states $D(E)$ can analytically be calcu-

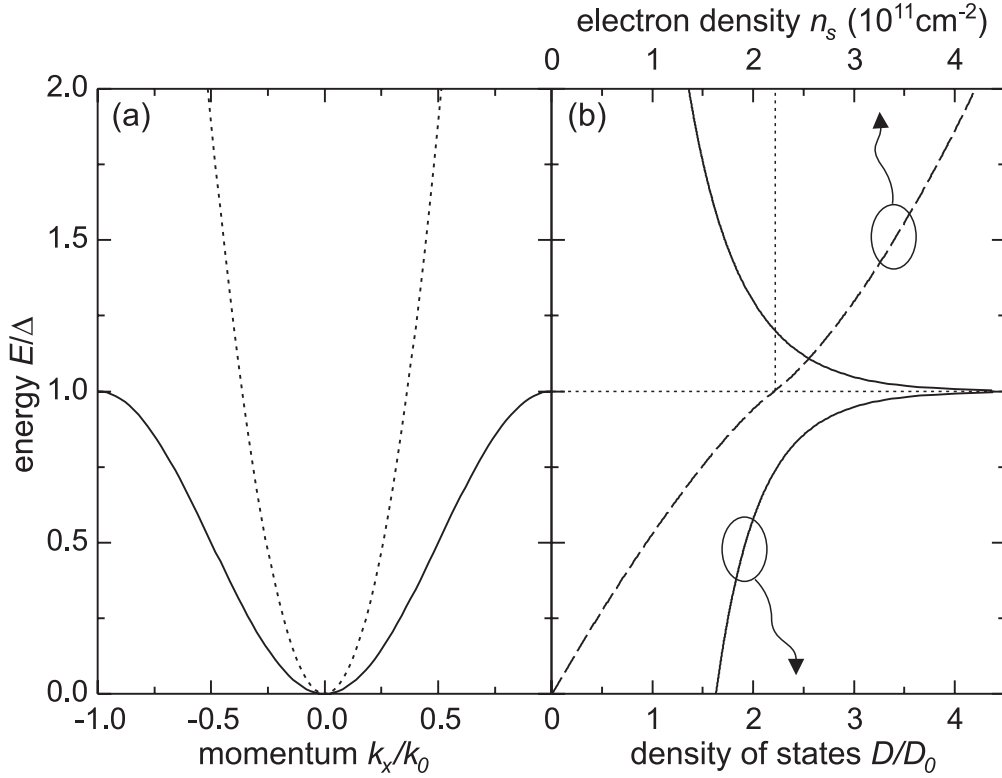


Figure 2.6: (a) Dispersion relation in superlattice direction (solid line) and in the free electron direction (dotted line). The energy is normalized to the band width Δ . (b) Calculated density of states normalized to the two-dimensional density of states D_0 (solid line, bottom axis) and integrated density of states yielding the electron density (dashed line, top axis).

lated using

$$D(E) = \frac{2}{(2\pi)^2} \int \delta(E - E(\vec{k})) dk_x dk_y = \frac{1}{2\pi^2} \oint_{E(\vec{k})=E} \frac{dk}{|\nabla_{\vec{k}} E(\vec{k})|} \quad (2.9)$$

and we find after integration

$$\frac{D(E)}{D_0} = \begin{cases} \frac{2}{\pi} \sqrt{\frac{m_x^*}{m_y^*}} K\left(\frac{E}{\Delta}\right), & \text{for } 0 < E < \Delta, \\ \frac{2}{\pi} \sqrt{\frac{m_x^*}{m_y^*}} \sqrt{\frac{\Delta}{E}} K\left(\frac{\Delta}{E}\right), & \text{for } \Delta < E, \end{cases} \quad (2.10)$$

where $K(m) = \int_0^{\pi/2} (1 - m^2 \sin^2 \varphi)^{1/2} d\varphi$ is the complete elliptic integral [Abr65], and D_0 is

the density of states of the free two-dimensional electron gas

$$D_0 = \frac{m^*}{\pi\hbar^2}. \quad (2.11)$$

The two electron masses

$$m_x^* = \hbar^2 \left(\frac{\partial^2 E}{\partial k_x^2} \right)_{k_x=0}^{-1} = \frac{2\hbar^2}{\Delta d^2} \quad (2.12)$$

$$m_y^* = m^* = 0.067 m_0 \quad (2.13)$$

are defined by the band curvature at zero energy along the x and the y direction, respectively. Recall that $K(0) = \pi/2$ and $K(1) = \infty$.

The calculated density of states is shown in Figure 2.6. At the miniband minimum $D(0)/D_0 = \sqrt{m_x^*/m_y^*} > 1$ reflects the increased electron mass in superlattice direction. At the band edge $E = \Delta$ the density of states has a logarithmic singularity, and in the quasi gap for $E > \Delta$ it decreases proportional to the square root of E , as expected for a one-dimensional system.

We integrate the calculated density of states (2.10) to obtain the relation between Fermi energy and electron density n_s , also shown in Figure 2.6. For $n_s < 2.2 \times 10^{11} \text{ cm}^{-2}$ the Fermi energy lies within the miniband, while for $n_s > 2.2 \times 10^{11} \text{ cm}^{-2}$ the miniband is completely filled and the quasi gap is occupied. We expect a drastic change in the magnetotransport as the Fermi energy is raised from the miniband into the quasi-gap as the physics changes from a two-dimensional to a one-dimensional behavior.

2.2.5 Electron trajectories in the artificial band structure

We discuss the electron motion semiclassically in the presence of a perpendicular magnetic field using the zero-field band structure. This approximation should only be valid as long as the magnetic energy is smaller than the band width $\hbar\omega_c < \Delta$, which implies for the SLFET at hand $B < 2 \text{ T}$. The semiclassical electron motion in a magnetic field $\vec{B} = (0, 0, B)$ is described by

$$\vec{v}(\vec{k}) = \frac{1}{\hbar} \nabla_{\vec{k}} E(\vec{k}) \quad (2.14)$$

$$\hbar \frac{d\vec{k}}{dt} = -e\vec{v}(\vec{k}) \times \vec{B}. \quad (2.15)$$

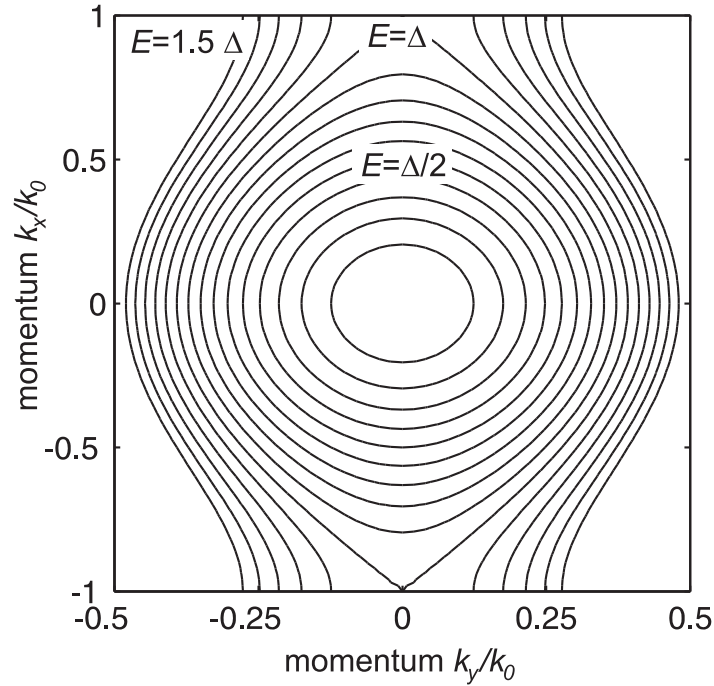


Figure 2.7: Fermi contours for different Fermi energies in k space. For Fermi energies within the miniband $E_F < \Delta$ electrons perform closed orbits within one Brillouin zone, while for larger Fermi energies electrons can only travel along open orbits across Brillouin zone boundaries.

Electron motion proceeds along contours of constant energy (Fermi contour). After integration we find

$$\vec{k}(t) - \vec{k}(0) = -\frac{e}{\hbar} (\vec{r}(t) - \vec{r}(0)) \times \vec{B}, \quad (2.16)$$

which states that orbits in reciprocal space correspond to orbits in real space, rotated by $-\pi/2$ and scaled by l_B^{-2} , where

$$l_B^2 = \frac{\hbar}{eB} \quad (2.17)$$

is the magnetic length.

In Figure 2.7 we show k space orbits for different Fermi energies. These Fermi contours correspond to the lines of intersection between the electron energy surface and the Fermi plane, as was shown in Figure 2.5. Two different types of orbits can be distinguished. First, for Fermi energies within the miniband $E_F < \Delta$ electrons perform closed orbits. Second, for larger Fermi energies, contours join across the Brillouin zone boundaries $k_x = k_0 = \pm\pi/d$

and electrons can only perform open orbits along snake shaped lines. This transition from closed to open orbits has drastic implications for the magnetoresistance, as discussed in the following.

2.2.6 Closed electron orbits

For $E_F < \Delta$ the electron motion is periodic with a period t_c given by

$$t_c = \frac{2\pi}{\omega_c} = \frac{\hbar^2}{eB} \oint_{E(\vec{k})=E} \frac{dk}{|\nabla_k E(\vec{k})|} = \frac{\hbar^2}{eB} \frac{\partial A_k(E)}{\partial E}, \quad (2.18)$$

where ω_c is the cyclotron frequency and $A_k(E)$ the k space area enclosed by the electron orbit. For the special case of a free electron, using $E = \hbar^2 k^2 / (2m^*)$ we find $A(E) = 2\pi m^* E / \hbar^2$ and $\omega_c = eB/m^*$ as expected. For the general case it is therefore customary to define a field independent electron cyclotron effective mass m_c by $\omega_c = eB/m_c$. Using this definition and comparing Equations (2.10) and (2.18), the density of states can be written as

$$D(E) = \frac{m_c(E)}{\pi \hbar^2}. \quad (2.19)$$

Thus the cyclotron effective mass is directly proportional to the density of states. It equals $m_c = \sqrt{m_x m_y}$ at the miniband minimum (cf. Equation (2.10)), and has a logarithmic singularity at the miniband edge. Experimentally the cyclotron effective mass can be determined by the temperature dependence of the magnetoresistance oscillations.

The semiclassical quantization condition imposed on stationary states corresponding to closed orbits (Bohr-Sommerfeld quantization rule) reads

$$\oint \vec{p} d\vec{r} = (n + \gamma)h, \quad (2.20)$$

where n is an integer, γ a phase factor, and the integration of the momentum $\vec{p} = \hbar \vec{k} + e\vec{A}$ is along the classical cyclotron orbit. Using the equation of motion (2.15) and Stoke's theorem we find

$$\Phi = BA_r = (n + \gamma)\Phi_0 \quad (2.21)$$

stating that the enclosed real space area is threaded by an integer number of magnetic flux quanta $\Phi_0 = h/e$, give or take a phase factor. Using the conversion between real space and k space areas $A_r = l_B^4 A_k$ derives Onsager's expression

$$\Delta \left(\frac{1}{B} \right) = \frac{2\pi e}{\hbar A_k} = 2 \frac{e}{\hbar n_s} \quad (2.22)$$

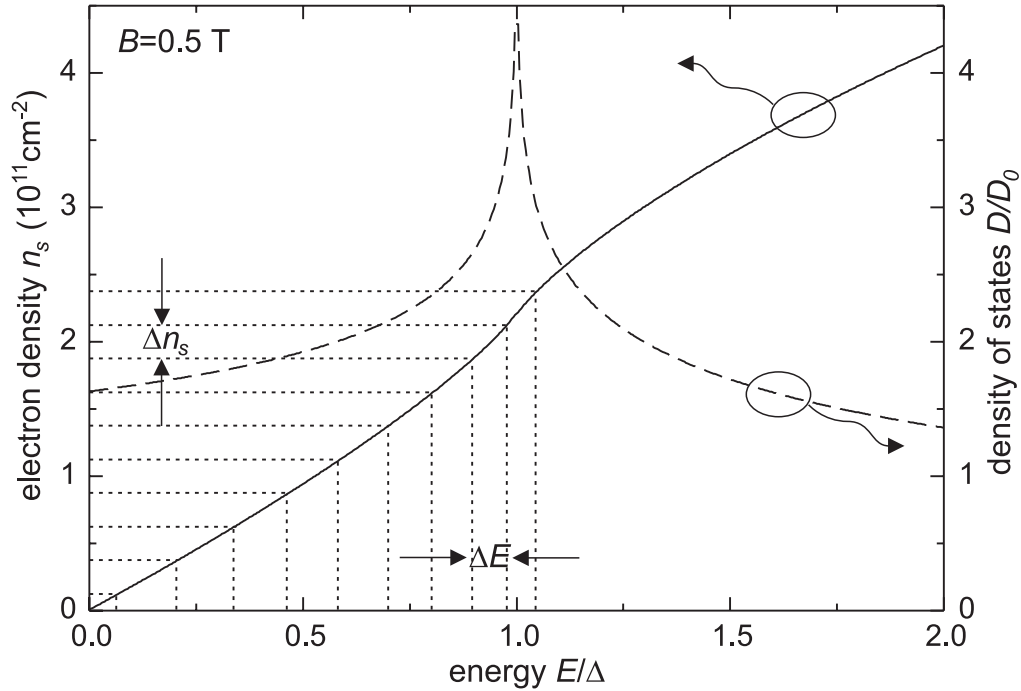


Figure 2.8: Landau level spacing vs. energy and electron density. As the effective mass depends on the density of states (dashed line), the spacing of the Landau levels (dotted lines) $\hbar\omega_c$ on the energy axis is not equidistant. In contrast, the Landau level spacing is equidistant on the electron density axis, which is proportional to the gate voltage. The electron density dependence on the energy is plotted as solid line.

relating the distance between the stationary states on the inverse magnetic field axis, and the enclosed k space area, or equivalently the electron density. This expression will be used to determine the electron density n_s from the measured magnetoresistance, which directly reflects the position of the stationary states (the Landau levels) on the magnetic field axis.

The Landau level spacing at fixed magnetic field is $\Delta E = \hbar\omega_c$ and thus inversely proportional to the cyclotron effective mass m_c . When plotted on an energy scale, as shown in Figure 2.8, the Landau level spacing therefore depends on energy, the spacing for example decreases with increasing m_c , corresponding to an increasing density of states. This is unlike two-dimensional systems with parabolic energy dispersion and constant density of states, where the Landau level spacing is constant. Interestingly, the Landau level spacing

on an electron density scale Δn is independent of energy, as graphically demonstrated in Figure 2.8. The reason lies in the proportionality between the cyclotron effective mass and the density of states. Mathematically we prove

$$\Delta n_s = \frac{dn_s}{dE} \Delta E = D(E) \frac{\hbar e B}{m_c(E)} = \frac{eB}{\pi \hbar}. \quad (2.23)$$

The independence of the Landau level spacing on the electron density is of great importance for the experimental situation, where via the gate voltage the electron density is directly controlled.

In order to resolve single Landau levels, their spacing should exceed their width. In other words, the electron must perform at least one closed cycle before a phase breaking scattering event occurs. If τ_q is the relevant quantum scattering time, the condition for the observability of quantum oscillations reads

$$\omega_c \tau_q > 1 \quad (2.24)$$

This reasoning can be used to estimate the electron quantum scattering time from the experimentally determined onset of the magnetoresistance oscillations, see Chapter 6.

In the classical Hall regime, where $\omega_c \tau < 1$, electron motion in crossed electric E_x and magnetic B_z fields is a superposition of a circular motion with frequency ω_c and a uniform drift perpendicular to E_x with a drift velocity $\vec{v} = (0, E_x/B_z)$. The resulting orbit is a trochoid as a consequence of the Lorentz force. Electron scattering is modelled by adding a term proportional to \vec{v}/τ to the equation of motion, where τ is the Drude scattering time. The resulting conductivity tensor is

$$\sigma = \frac{\sigma_0}{1 + \omega_c^2 \tau^2} \begin{pmatrix} 1 & -\omega_c \tau \\ \omega_c \tau & 1 \end{pmatrix} \quad (2.25)$$

where σ_0 is the zero-field conductance. This result is useful to determine the Drude scattering time and the electron mobility from the low field magnetoresistance.

2.2.7 Open electron orbits

In Figure 2.9 we have calculated the real space orbits corresponding to the k space orbits shown in Figure 2.7 for two different magnetic fields. For closed orbits, we have seen in Equation (2.25) that the diagonal elements σ_{xx} and σ_{yy} tend to zero as B^{-2} for large fields. This is intuitively clear, because the diagonal elements must be even functions of the magnetic field, and the electron orbits shrink with increasing field, localizing the electron more

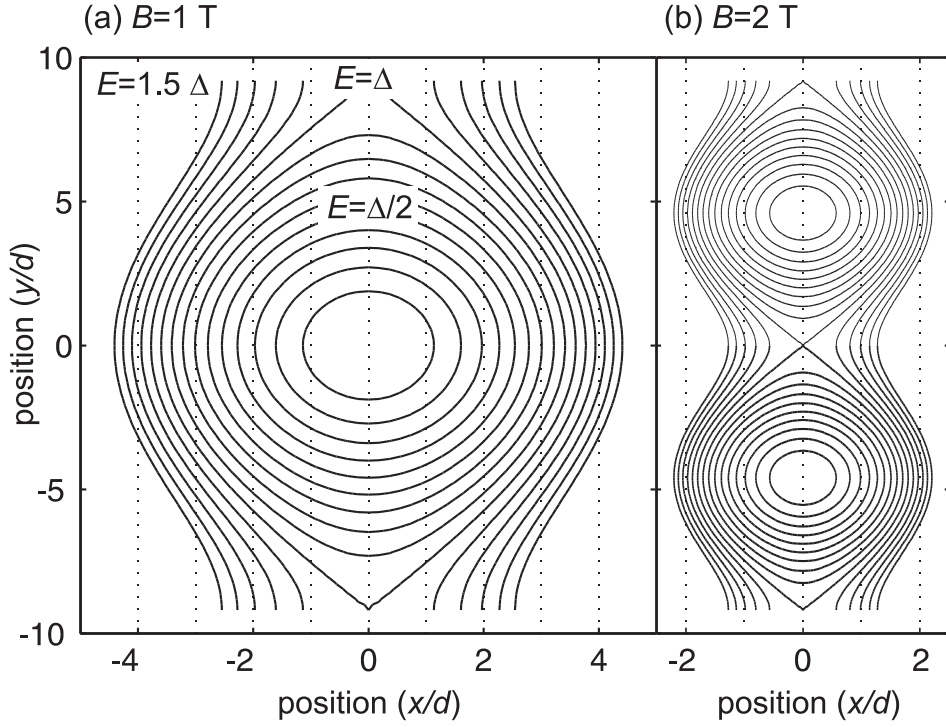


Figure 2.9: Fermi contours for different Fermi energies in real space. (a) Orbits calculated for $B = 1$ T. (b) Orbits calculated for $B = 2$ T. For $E_F > \Delta$ the presence of open orbits leads to a non-vanishing electron drift velocity in y direction even at high magnetic fields, while electron motion in x direction is quenched. This results in a strong quadratic increase of the magnetoresistance in x direction.

and more. However, this argument does not hold for the case of open orbits. The k space orbit is still of limited width in the k_y direction, but it now extends indefinitely in the k_x direction. Correspondingly, the real space orbit is of limited width in the x direction, and this width gets smaller and smaller as B increases, but it extends indefinitely in y direction. It follows, as above, that σ_{xx} falls as B^{-2} , but the electron has a finite, non-vanishing average velocity in y direction. This means that σ_{yy} tends to a finite limit at high fields, rather than vanishing as B^{-2} . The conductivity tensor for open orbits in the 'high field limit' $\omega_c\tau > 1$ therefore reads

$$\sigma \propto \begin{pmatrix} (\omega_c\tau)^{-2} & -(\omega_c\tau)^{-1} \\ (\omega_c\tau)^{-1} & c \end{pmatrix}, \quad (2.26)$$

where c is a constant. A rigorous treatment of the transport theory at the presence of open orbits leads to the same result, and can be found in historical papers by Lif-

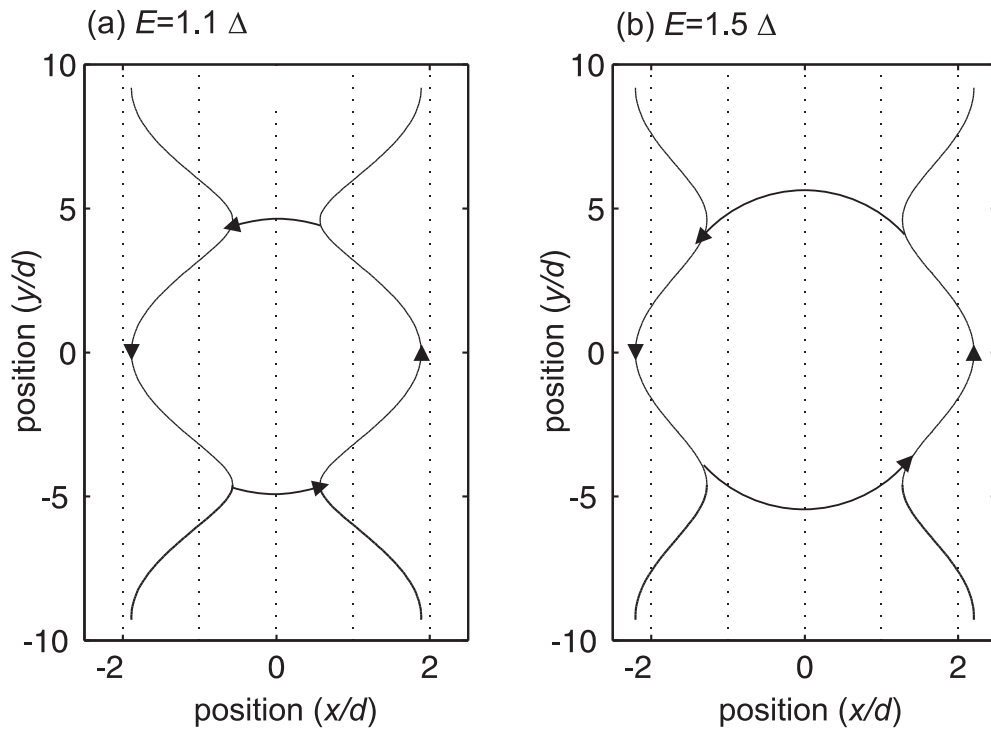


Figure 2.10: Electron orbits in the regime of magnetic breakdown calculated for a magnetic field of 2 T and for two different Fermi energies in the band gap. (a) $E = 1.1 \Delta$, (b) $E = 1.5 \Delta$

shitz [Lif56][Lif57][Lif59][Lif60]. It is straightforward to derive the measured resistivity tensor ρ

$$\rho = \sigma^{-1} \propto \begin{pmatrix} c(\omega_c \tau)^2 & \omega_c \tau \\ -\omega_c \tau & 1 \end{pmatrix}. \quad (2.27)$$

The quadratically increasing magnetoresistance in x direction will be clearly evident in the transport measurement in Section 2.3.2.

In the regime of open orbits, magnetoresistance oscillations are expected to disappear. This is because the quantization condition (2.20) only applies to closed orbits. The energy spectrum is therefore continuous, and experimentally we expect a quenching of the magnetoresistance oscillations as soon as the band gap is occupied. This will experimentally be shown in Section 2.3.2.

2.2.8 Magnetic breakdown

Our description so far was entirely based on the zero magnetic field band structure. In the low-field regime the magnetic field is a small perturbation to the given band structure, and we have seen that when the Fermi energy is above the miniband, electron orbits open up at the Brillouin zone boundaries, and magnetoresistance oscillations quench. In the limit of high magnetic fields, however, conversely the modulation due to the superlattice can be treated as a perturbation to the magnetic energy levels, and electrons will move in free particle orbits, namely the cyclotron orbits. In this regime, due to electrons performing *closed* orbits, quantum oscillations are recovered. Historically, after the discovery of magneto-oscillations by Priestley in 1960 with a frequency too high to be explained by known Fermi surface extremal areas, Cohen and Falicov [Coh61] and Blount [Blo62] introduced the notion of *magnetic breakdown* as a quantum mechanical tunneling of electrons between different electron trajectories of equal energy, but separated in k space by a potential barrier. Two examples for this process are shown in Figure 2.10. The condition for magnetic breakdown is [Blo62][Sta67]

$$\hbar\omega_c E_F > E_g^2, \quad (2.28)$$

where E_g is the potential energy the electrons have to overcome from one trajectory to the other. This condition is milder than $\hbar\omega_c > E_g$, which one would think intuitively. Essentially by the introduction of a quantum mechanical tunneling process the deficiency of using the zero-field band structure is healed.

In summary, using the zero-field band structure and semiclassical arguments, we have developed a fundamental understanding of the physics of a modulated two-dimensional electron system in a perpendicular magnetic field. In Figure 2.11 we summarize our main findings. At low electron densities, we expect to find magnetoresistance oscillations, that quench when the Fermi energy is shifted into the band gap. Further we expect the magnetoresistance oscillations to reappear in this electron density regime at sufficiently high magnetic fields due to magnetic breakdown.

2.3 Experimental results

Magnetotransport data was obtained in a ^3He bath cryostat at $T = 330$ mK unless otherwise indicated. An AC measurement current of $I = 10$ nA (rms) was sourced to one of the top contacts, keeping one of the bottom contacts grounded, while the AC voltage drop U was

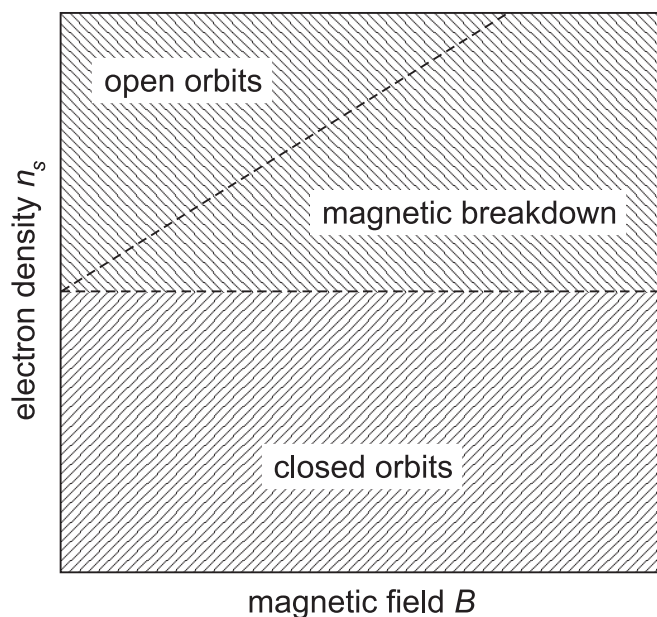


Figure 2.11: Electron trajectory 'phase diagram' in the (n_s, B) plane.

measured between the other pair of contacts, see Figure 2.1. The sample resistance $R(B)$ is directly obtained by lock-in technique. The magnetic field was oriented perpendicular to the two-dimensional electron system, and was swept at a rate of 264 mT/min with a maximum field of 14 T. In the following we present magnetoresistance traces obtained at different fixed gate voltages. A phenomenological description is given, clear periodicity over inverse magnetic field is found, and from Landau plots the relation between electron density and gate voltage is deduced.

2.3.1 Magnetoresistance for $E_F < \Delta$

Clear magnetoresistance oscillations can be observed for gate voltages above $U_g = 0.15$ V. With increasing gate voltage the zero field resistance drops drastically until $U_g = 0.45$ V. Figure 2.12 shows data obtained at $U_g = 0.25$ V. For low magnetic fields R is constant at about $R = 9.6$ k Ω , and magnetoresistance oscillations start at $B = 300$ mT. We have indexed the maxima of R (indicated by upward triangles) and plotted them versus the inverse of their position in magnetic field. The resulting Landau plot is shown in the inset. Clearly the observed maxima are $1/B$ periodic, and the linear fit intercepts at zero. This indicates that the labelling corresponds to the filling factor, and that indeed the indexing of the *maxima*

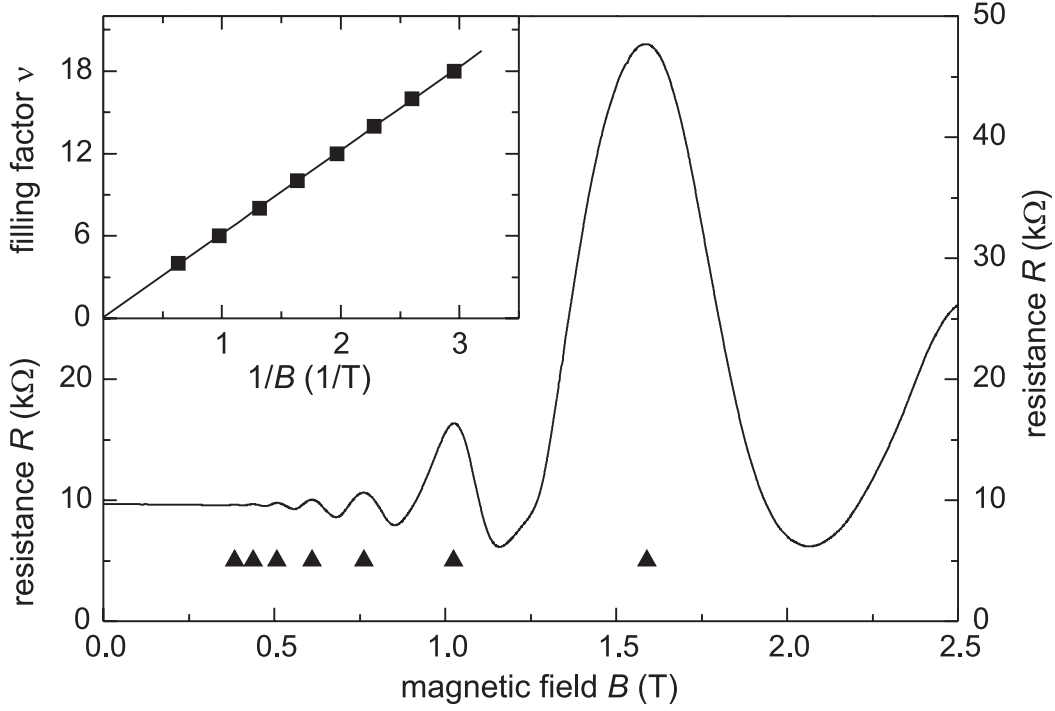


Figure 2.12: Magnetoconductance for gate voltage $U_g = 0.25$ V. In the inset the resistance maxima are indexed and plotted versus inverse magnetic field.

(vs. the minima) is correct. At filling factor 2 the resistance has a maximum at $R = 48$ k Ω , and for $B > 2$ T the sample becomes insulating. The electron density n_s is calculated from the slope of the linear fit to the Landau plot Δ^{-1} multiplied by e/h (all states, including the spin-split states, are counted)

$$n_s = \frac{e}{h} \Delta^{-1} \quad (2.29)$$

We find with $\Delta^{-1} = 6$ T a density of $n_s = 1.4 \times 10^{11}$ cm $^{-2}$.

At $U_g = 0.4$ V the zero field resistance has dropped to $R = 370$ Ω , as shown in Figure 2.13. At low magnetic fields R is increasing quadratically, until at around $B = 300$ mT first magnetoconductance oscillations are observed. For larger magnetic fields R shows pronounced maxima, and at $B = 4.5$ T a clear plateau of $R = 12.9$ k $\Omega \approx h/(2e^2)$ appears. The Landau plot, drawn from the resistance maxima, again intercepts zero, and we obtain an electron density of $n_s = 2.3 \times 10^{11}$ cm $^{-2}$.

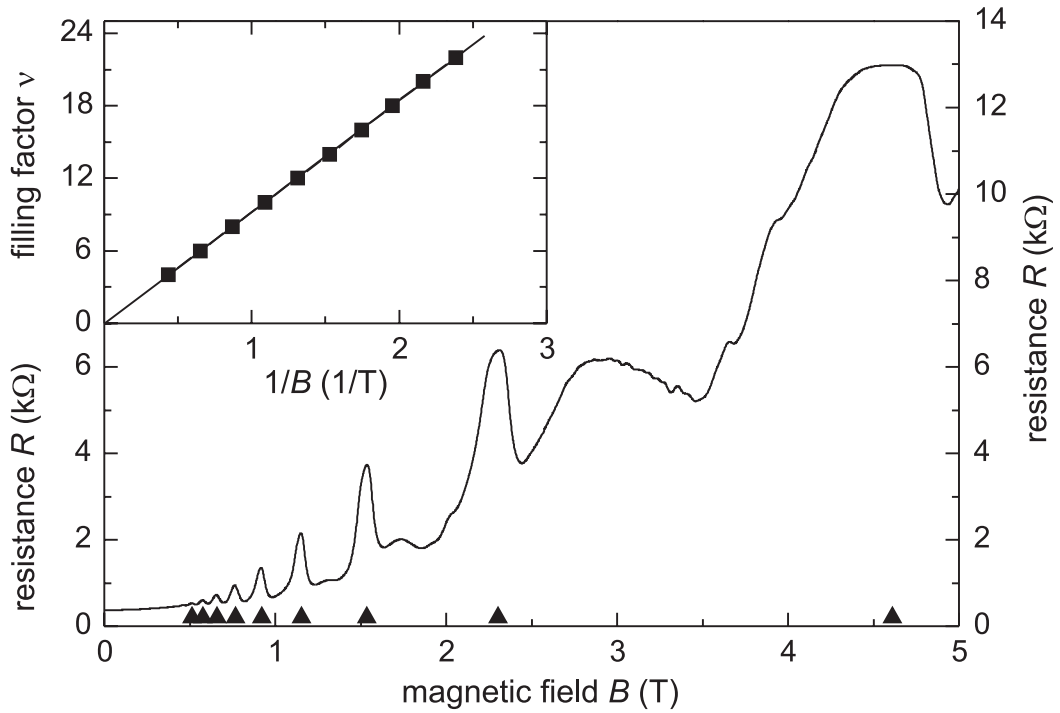


Figure 2.13: Magnetoconductance for gate voltage $U_g = 0.4$ V.

2.3.2 Magnetoconductance for $E_F > \Delta$

For gate voltages larger than $U_g = 0.45$ V we observe a drastic change in the magnetoconductance, regarding the position of the resistance maxima and minima, and regarding the low field magnetoconductance. An example for $U_g = 0.5$ V is given in Figure 2.14. Although the zero field resistance has dropped further to $R = 210 \Omega$ as compared to the $U_g = 0.4$ V trace, the quadratic magnetoconductance increase is much stronger. At the same time the onset of the oscillations has shifted to a higher magnetic field of $B = 440$ mT. Most strikingly, however, a Landau plot with zero intercept is only obtained when the magnetoconductance *minima* are considered for $B < 1.5$ T, as indicated by downward pointing triangles. Only filling factors 8 and below are associated with resistance *maxima*. An electron density of $n_s = 2.8 \times 10^{11} \text{ cm}^{-2}$ is found.

This transition from maximum resistance to minimum resistance at integer filling factors, the quadratically increasing magnetoconductance, and the shift of the onset of the magnetoconductance oscillations to larger magnetic fields are even more developed for larger gate voltages, as seen in Figure 2.15 for $U_g = 0.6$ V. The low field resistance is very well ap-

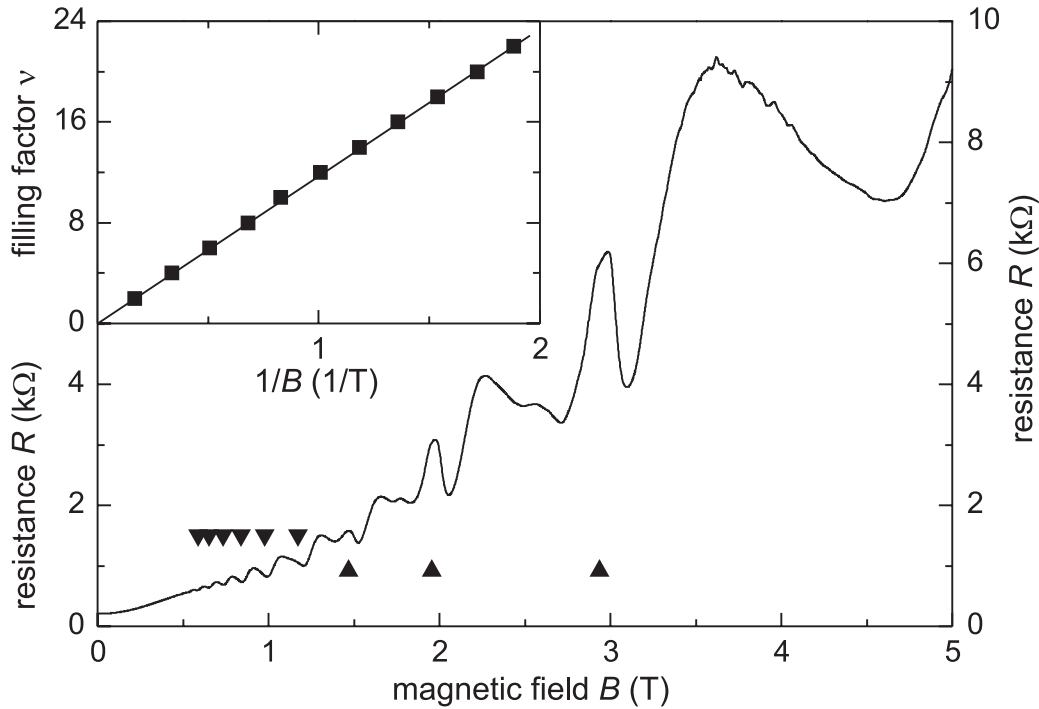


Figure 2.14: Magnetoconductance for gate voltage $U_g = 0.5$ V.

proximated by a parabola, as indicated by the dashed line. The onset now occurs only at $B = 0.9$ T, and the resistance *minima*, cast into a Landau plot with zero intercept, yield an electron density of $n_s = 3.4 \times 10^{11} \text{ cm}^{-2}$.

The striking increase of the magnetoconductance is summarized in Figure 2.16. Here we plot magnetoconductance data for gate voltages between $U_g = 0.425$ V and $U_g = 0.9$ V versus magnetic field normalized by the electron density, such that regardless of the electron density all filling factors lie at the same x-axis position. As discussed before, at integer filling factors the resistance maxima present for low gate voltages evolve into resistance minima for large gate voltages. From a different point of view it rather seems that the resistance minima between integer filling factors evolve into maxima for increasing gate voltages. We point out the rather large resistance values of above $R = 100 \text{ k}\Omega$ obtained for large gate voltages.

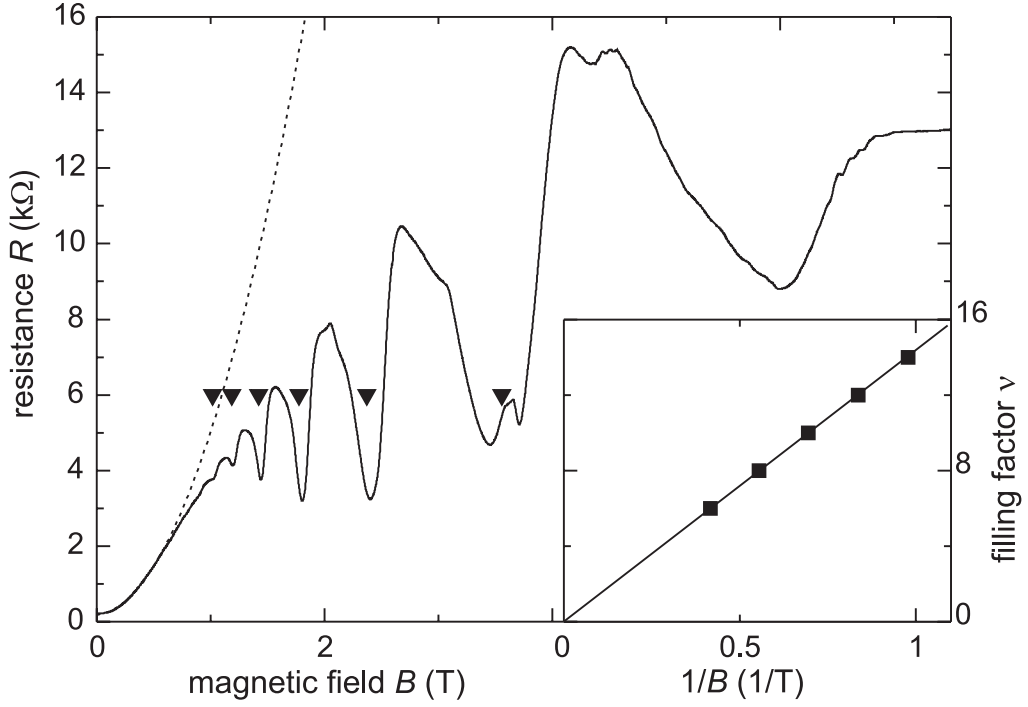


Figure 2.15: Magnetoconductance for gate voltage $U_g = 0.6$ V.

2.3.3 Gate voltage to electron density relation

We summarize the electron densities obtained from the Landau plots for gate voltages between $U_g = 0.15$ V and $U_g = 0.9$ V in Figure 2.17. The $n_s(U_g)$ relation is well approximated by the linear relationship

$$n_s = (5.7 \pm 0.1) \times 10^{11} U_g [\text{cm}^2/\text{Vs}] \quad (2.30)$$

In a simple approximation the SLFET can be considered as a parallel plate capacitor, with the two-dimensional electron system on the one side, and the n+ GaAs gate contact on the other side, separated by the insulator AlGaAs of thickness $d = 100$ nm. Using the dielectric constant for AlGaAs with 33% Al content $\epsilon = 11.6$ [Ins93], the following relation is expected

$$n_s^{(theo)} = \frac{\epsilon_0 \epsilon}{d e} U_g = 6.4 \times 10^{11} U_g [\text{cm}^2/\text{Vs}]. \quad (2.31)$$

In this calculation quantum mechanical effects have been neglected. For example d should

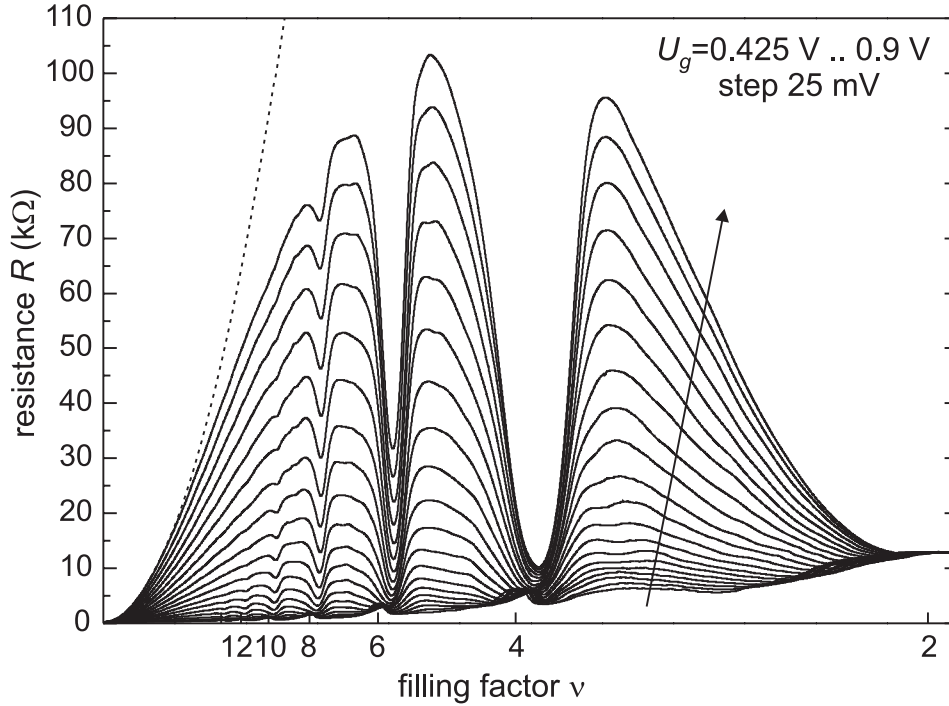


Figure 2.16: Overview of magnetoresistance traces for $E_F > \Delta$, plotted versus filling factor.

be assumed larger since the charge distribution in the two-dimensional electron system will be located a distance away from the GaAs/AlGaAs interface.

2.3.4 Magnetoresistance maxima and minima in the (U_g, B) plane

It is instructive (and esthetic) to assume a bird's perspective to view the magnetotransport data in its entity. Since the magnetoresistance varies, depending on the gate voltage and the magnetic field, over orders of magnitudes, we extract a value V indicating the magnetoresistance maxima and minima using the following recipe

$$V = -\frac{\partial^2 R(U_g, B) / \partial U_g^2}{|\partial R(U_g, B) / \partial U_g|}. \quad (2.32)$$

Effectively the second derivative distinguishes, by means of the sign, between maximum and minimum, while the first derivative in the denominator vanishes at maxima and minima, thus emphasizing these points. In Figure 2.18 we plot the resulting $V(U_g, B)$ color coded,

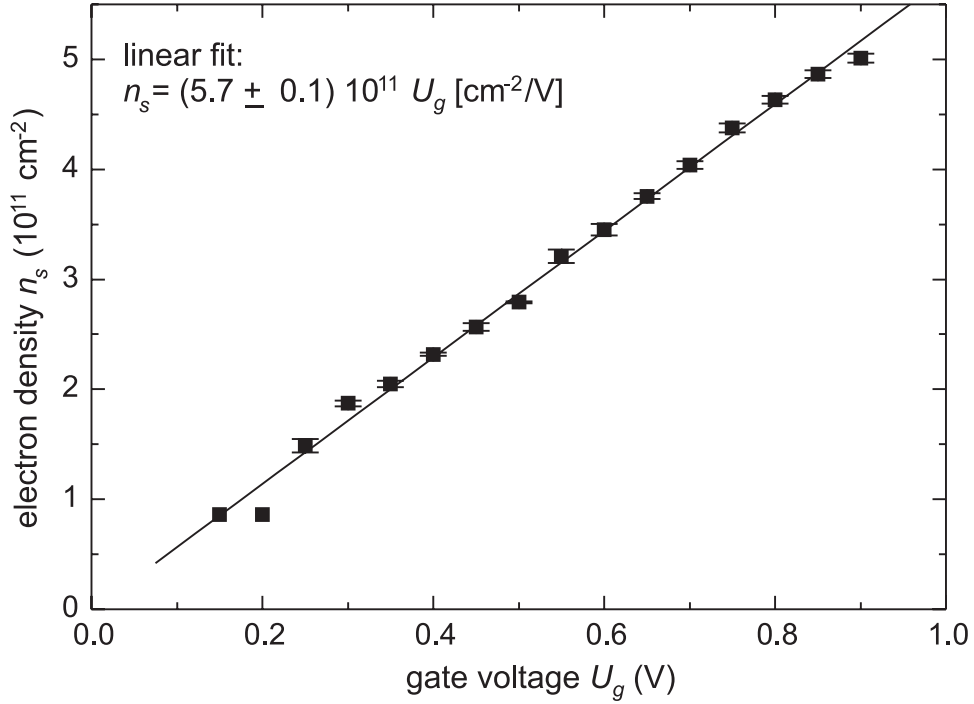


Figure 2.17: Experimentally deduced relation between the applied gate voltage and the electron density.

marking maxima red and minima blue. We overlay the integer filling factors ν according to

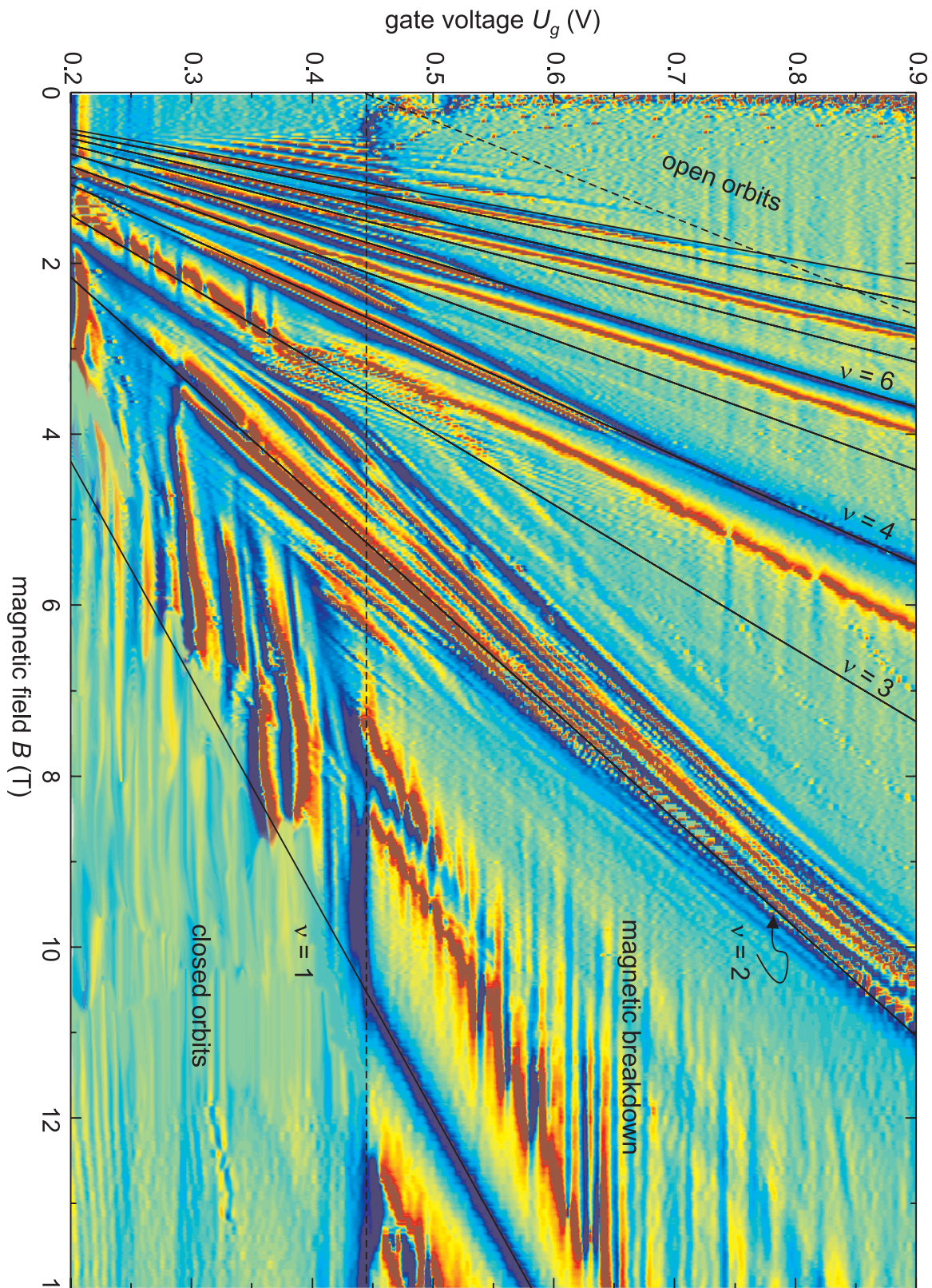
$$E_F = n_s / D(E_F) = \hbar \omega_c \nu. \quad (2.33)$$

Using the zero field density of states $D(E_F) = m^* / (\pi \hbar^2)$ we obtain

$$n_s = \frac{eB}{\pi \hbar} \nu \quad (2.34)$$

and the $n_s(U_g)$ relation is known from Figure 2.17.

The Landau fan appears as the most obvious pattern, and a closer look reveals the formerly discussed transition from maxima to minima along integer filling factors as the electron density and the magnetic field are increased. At odd filling factors for $U_g < 0.45$ V maxima are found. The fine structure within the $\nu = 2$ filling factor is due to the presence of a plateau, to which our evaluation method for V reacts sensitive.



R. A. Deutschmann *Two dimensional electron systems in atomically precise periodic potentials* (2001)
Ph.D. Dissertation. Selected Topics of Semiconductor Physics and Technology, ISBN 3-932749-42-1

Figure 2.18: Magnetoresistance maxima and minima in the (U_g, B) plane.

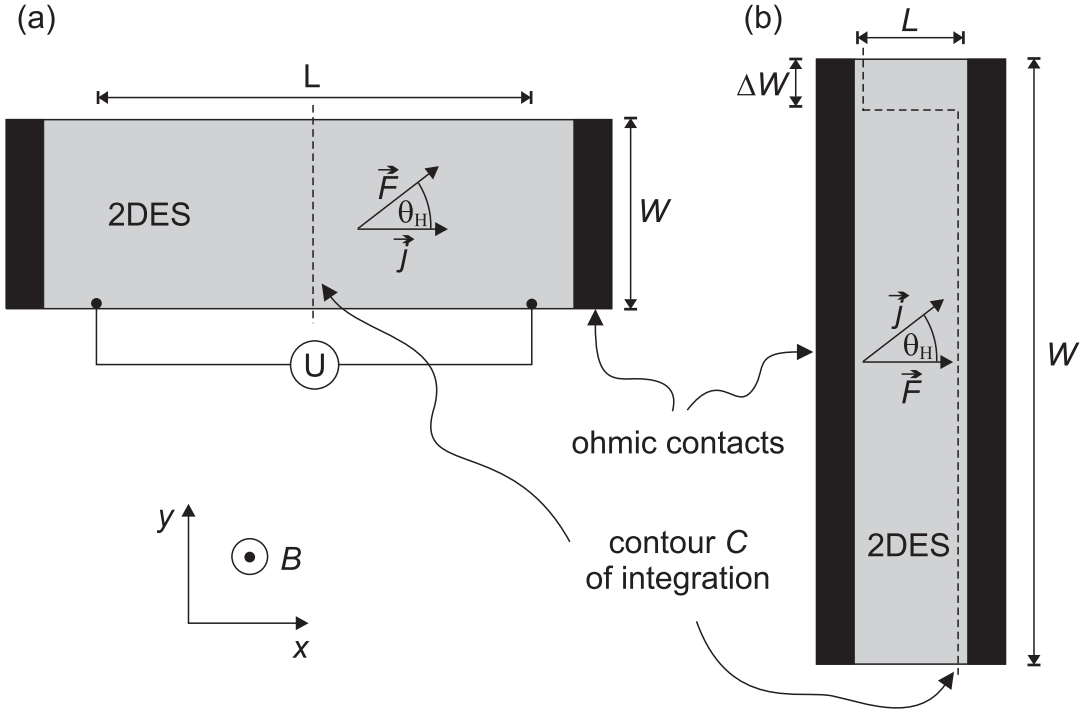


Figure 2.19: Two different sample geometries and definitions for calculating the magnetoresistance. (a) Long and narrow sample, normally used for Hall bars. (b) Short and wide sample, as is the case for the SLFET.

2.3.5 Transport model for $E_F < \Delta$

We calculate the magnetoresistance of a 2DES from intrinsic properties of the 2DES in magnetic field, given by the longitudinal conductivity σ_{xx} and the transverse conductivity σ_{xy} . We consider two extreme cases for the sample geometry, namely a long and narrow sample, as used for standard Hall measurements, and a short and wide sample as for the SLFETs. Both geometries are shown in Figure 2.19, and for the calculation differ in their respective boundary conditions.

The Hall angle Θ_H is defined by the angle between the current density $\vec{j} = (j_x, j_y)$ and the electric field $\vec{F} = (F_x, F_y)$

$$\cos \Theta_H = \frac{\vec{j} \cdot \vec{F}}{jF} \quad (2.35)$$

and we assume an ohmic relation between current density and electric field

$$\begin{pmatrix} j_x \\ j_y \end{pmatrix} = \begin{pmatrix} \sigma_{xx} & \sigma_{xy} \\ -\sigma_{xy} & \sigma_{xx} \end{pmatrix} \cdot \begin{pmatrix} F_x \\ F_y \end{pmatrix}. \quad (2.36)$$

(A) Magnetoresistance of a long and narrow sample

When the length of the sample is much larger than its width W , sufficiently far away from the contacts the current density $|\vec{j}| = j_x$ only has a component in the x direction, and $j_y = 0$. Therefore relation (2.36) reads

$$\begin{pmatrix} j_x \\ 0 \end{pmatrix} = \begin{pmatrix} \sigma_{xx} & \sigma_{xy} \\ -\sigma_{xy} & \sigma_{xx} \end{pmatrix} \cdot \begin{pmatrix} F_x \\ F_y \end{pmatrix}. \quad (2.37)$$

and the Hall angle

$$\cos \Theta_H = \frac{\vec{j} \cdot \vec{F}}{jF} = \frac{j_x F_x}{j_x F} = \frac{F_x}{\sqrt{F_x^2 + F_y^2}} = \frac{1}{\sqrt{1 + F_y^2/F_x^2}} \quad (2.38)$$

simplifies to

$$\tan \Theta_H = \frac{F_y}{F_x} = \frac{\sigma_{xy}}{\sigma_{xx}}. \quad (2.39)$$

As can immediately be seen in the quantum Hall regime as $\sigma_{xx} \rightarrow 0$ the Hall angle $\Theta_H \rightarrow \pi/2$ and the electric field component in x direction vanishes.

From the voltage drop U between the voltage probes spaced a distance L apart and the current $I = \int_C \vec{j} \cdot d\vec{r} = j_x W$ integrated over contour C , using Equations (2.38) and (2.39), the measured resistance is given by

$$R = \frac{U}{I} = \frac{L}{W} \frac{F_x}{j_x} = \frac{L}{W} \frac{\sigma_{xx}}{\sigma_{xx}^2 + \sigma_{xy}^2}. \quad (2.40)$$

This is the well known result, stating that in the quantum Hall regime the measured four-point resistance vanishes.

(B) Magnetoresistance of a short and wide sample

When the sample is much wider than long, clear boundary conditions are imposed by the presence of the pair of wide and parallel metallic contacts. Sufficiently far away from the edges equipotential lines are parallel to the contacts the electric field $|\vec{F}| = F_x$ only has a component in x direction with $F_y = 0$. Ohm's law (2.36) in this case reads

$$\begin{pmatrix} j_x \\ j_y \end{pmatrix} = \begin{pmatrix} \sigma_{xx} F_x \\ -\sigma_{xy} F_x \end{pmatrix}. \quad (2.41)$$

and the Hall angle

$$\cos \Theta_H = \frac{\vec{j} \cdot \vec{F}}{jF} = \frac{j_x F_x}{j F_x} = \frac{j_x}{\sqrt{j_x^2 + j_y^2}} = \frac{1}{\sqrt{1 + j_y^2/j_x^2}} \quad (2.42)$$

simplifies to

$$\tan \Theta_H = \frac{j_y}{j_x} = \frac{-\sigma_{xy}}{\sigma_{xx}}. \quad (2.43)$$

As before in the quantum Hall regime as $\sigma_{xx} \rightarrow 0$ the Hall angle $\Theta_H \rightarrow \pi/2$, but in this geometry the current density in x direction vanishes.

The macroscopic current is obtained by integrating the current density along contour C as shown in Figure 2.19, neglecting the current across a length $\Delta W \ll W$ at the very edges of the sample:

$$I = \int_C \vec{j} \cdot d\vec{r} = j_x W + j_y L = \sigma_{xx} F_x W + \sigma_{xy} F_x L \quad (2.44)$$

If we assume that the voltage U drops linearly across the sample length L the measured resistance is given by

$$R = \frac{U}{I} = \frac{1}{(W/L)\sigma_{xx} + \sigma_{xy}}. \quad (2.45)$$

This result reminds of the known magnetoresistance for a Corbino geometry (ring shaped 2DES with inner and outer contact). These samples show an infinite resistance in the quantum Hall regime, because transverse currents are not measured. For the SLFETs the resistance also increases in the quantum Hall regime, but will be limited by the current in y direction for large Hall angles $\Theta_H > \arctan(L/W)$. In effect the resistance in the quantum Hall regime is quantized to values of $R = \sigma_{xy}^{-1} = h/(2e^2 i)$ $i = 1, 2, \dots$. This is true for any two-point measurement on a 2DES in a quantizing magnetic field [Fan83].

In a different picture result (2.45) can also be understood when the current between the contacts is divided into two contributions. First to every Landau level below the Fermi energy a conductivity of $\sigma_0 = 2e^2/h$ is assigned. Second, the conduction through the bulk of the 2DES in a simple approximation can be taken as being proportional to the density of states at the Fermi energy $D(E_F)$. Thus the resistance depends inversely on the sum of both contributions

$$R = \frac{1}{cD(E_F) + i\sigma_0}. \quad (2.46)$$

When the Fermi energy is between two Landau levels, current passes through the edge channels, and the resistance is quantized. Additional current is passed through the bulk of the

2DES when the Fermi energy is located within a Landau level, and consequently the resistance decreases.

In this short and wide geometry, an additional contribution to the magnetoresistance, the *geometric magnetoresistance*, originates from the elongation of the current path at non-zero Hall angles. This contribution is accounted for by the transformation [All88]

$$\sigma_{xx} \rightarrow \sigma_{xx}/(1 + \omega_c^2 \tau^2). \quad (2.47)$$

The resulting measured magnetoresistance therefore is given by

$$R = \left(\frac{cD(E_F)}{1 + (\omega_c \tau)^2} + \sigma_{xy} \right)^{-1}, \quad (2.48)$$

where $\sigma_{xy} = i\sigma_0$ is quantized at high fields, and

$$\sigma_{xy} = \frac{\omega_c \tau}{1 + (\omega_c \tau)^2} \quad (2.49)$$

in the classical regime at low fields $\omega_c \tau < 1$.

2.3.6 Comparison of theoretical and experimental magnetoresistance

We calculate the magnetic field dependent magnetoresistance using Equation (2.48). The density of states in dependence of B is calculated by summing Landau levels in form of Gaussians with height $\propto B$ and width $\propto B$. Spin splitting is taken into account by the Zeeman energy $g\mu_B B$. Both conductivity components σ_{xx} and σ_{xy} are shown in Figure 2.20(a). In Figure 2.20(b) the experimental magnetoresistance for gate voltage $U_g = 0.4$ V is compared to the model. The three free parameters are the constant c relating σ_{xx} and the density of states (DOS), the quantum scattering time, which determines the width of the Landau levels, and the electron g-factor, which is expected to be much larger than the bulk value of $g = -0.44$ due to electron-electron interactions. All relevant features of the data are reproduced, most importantly resistance *maxima* at all integer filling factors, and plateaus for low integer filling factors (here $\nu = 2$ and $\nu = 4$).

The reference sample at the same electron density shows similar behavior as the SLFET, and is simulated by the model equally well, as shown in Figure 2.21. This demonstrates that the SLFET in this density regime behaves like a normal 2DES.

The low density traces, where the magnetoresistance is far above the classically expected Hall resistance, can be simulated well using a reduced scattering time. This leads to a reduced

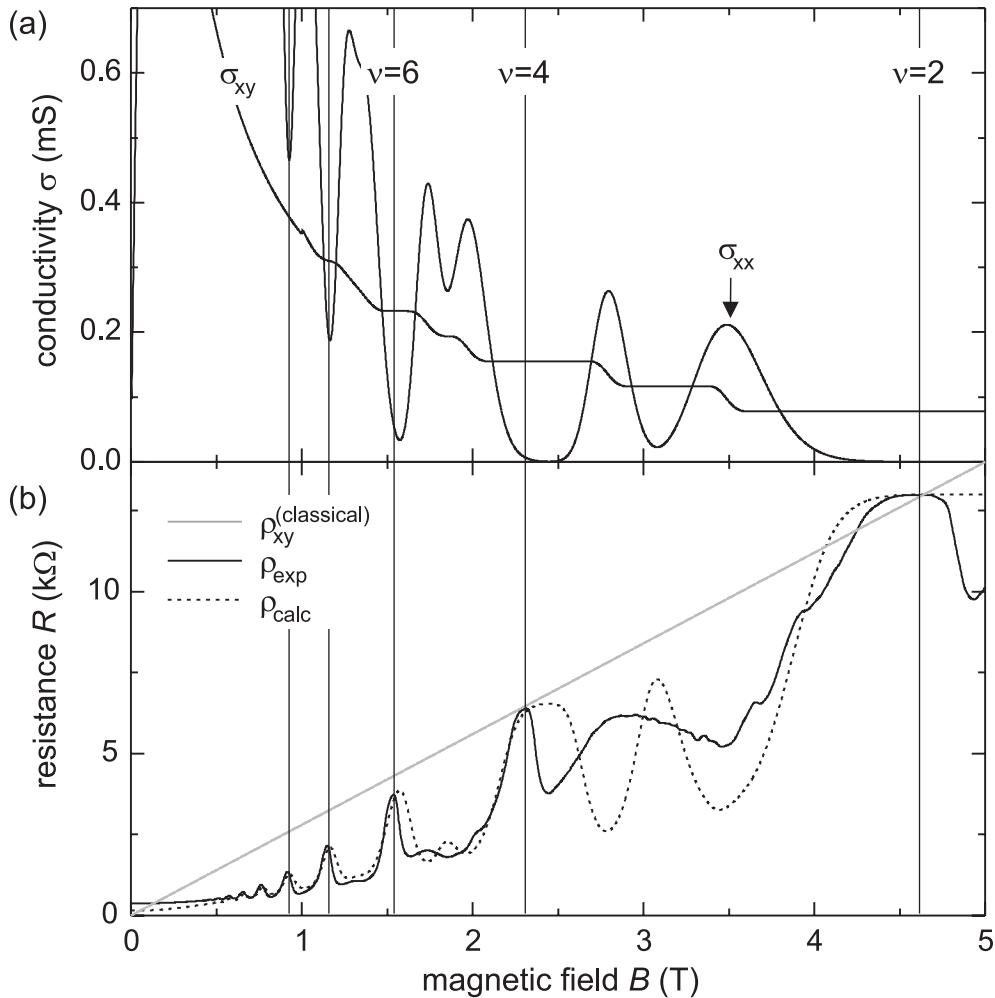


Figure 2.20: Transport model for the SLFET at $U_g = 0.4$ V. (a) Calculated conductivities σ_{xx} and σ_{xy} . (b) Calculated and experimental magnetoresistance.

geometry effect for σ_{xx} , and to a much reduced σ_{xy} . The comparison between experiment and calculation is shown in Figure 2.22.

In summary the SLFET behaves similar to a normal 2DES for Fermi energies within the first miniband $E_F < \Delta$. This is manifested by maxima and plateaus at integer filling factors, and a smaller resistance in between due to maxima in the DOS. In sharp contrast, for $E_F > \Delta$ in the experiment *minima* are observed at integer filling factors. This cannot be explained in this model using the DOS of an unperturbed 2DES.

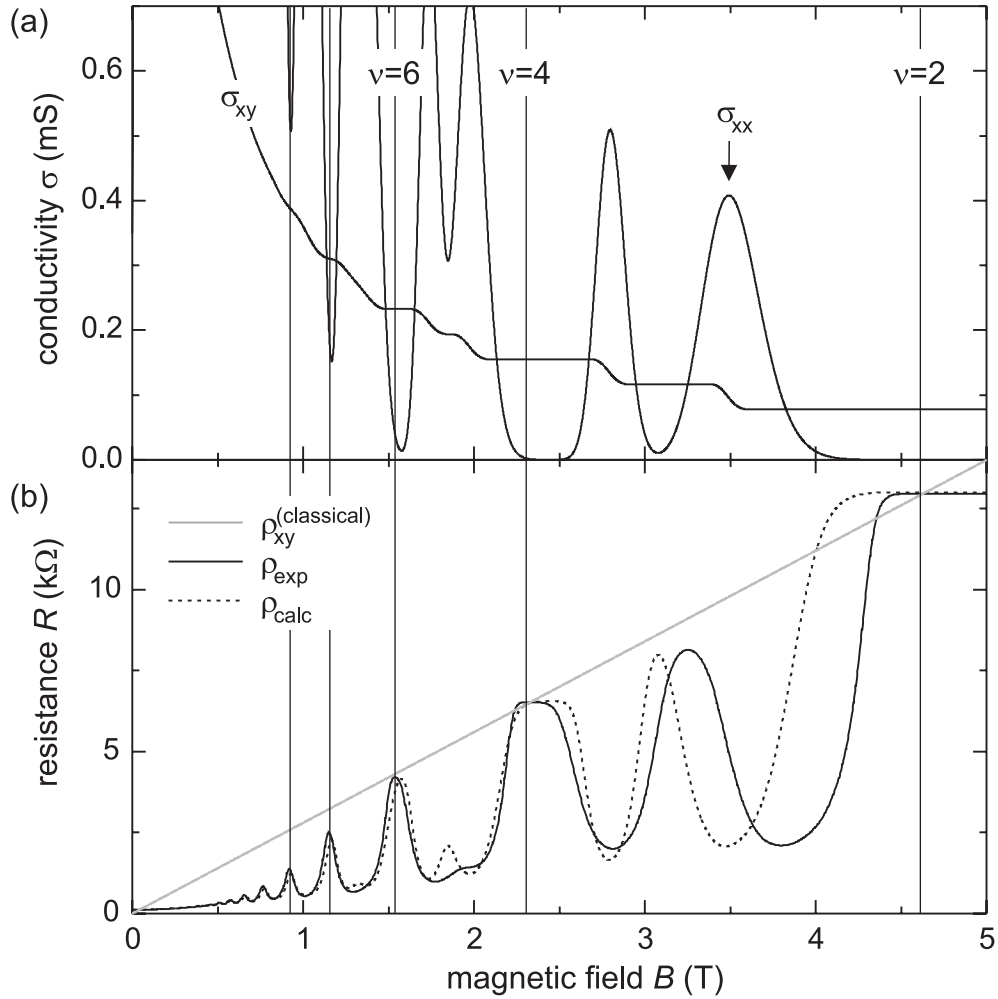


Figure 2.21: Transport model for the reference CEOFET at $U_g = 0.4$ V. (a) Calculated conductivities σ_{xx} and σ_{xy} . (b) Calculated and experimental magnetoresistance.

2.3.7 Magnetic breakdown

From the experimental magnetoresistance we extract the critical magnetic field B_c at which magnetic breakdown occurs and magneto-oscillations recommence. In Figure 2.23 we show the result, the error bars represent the uncertainty in the exact localization of the breakdown field in the magnetoresistance data. The theoretical relation between the Fermi energy, the

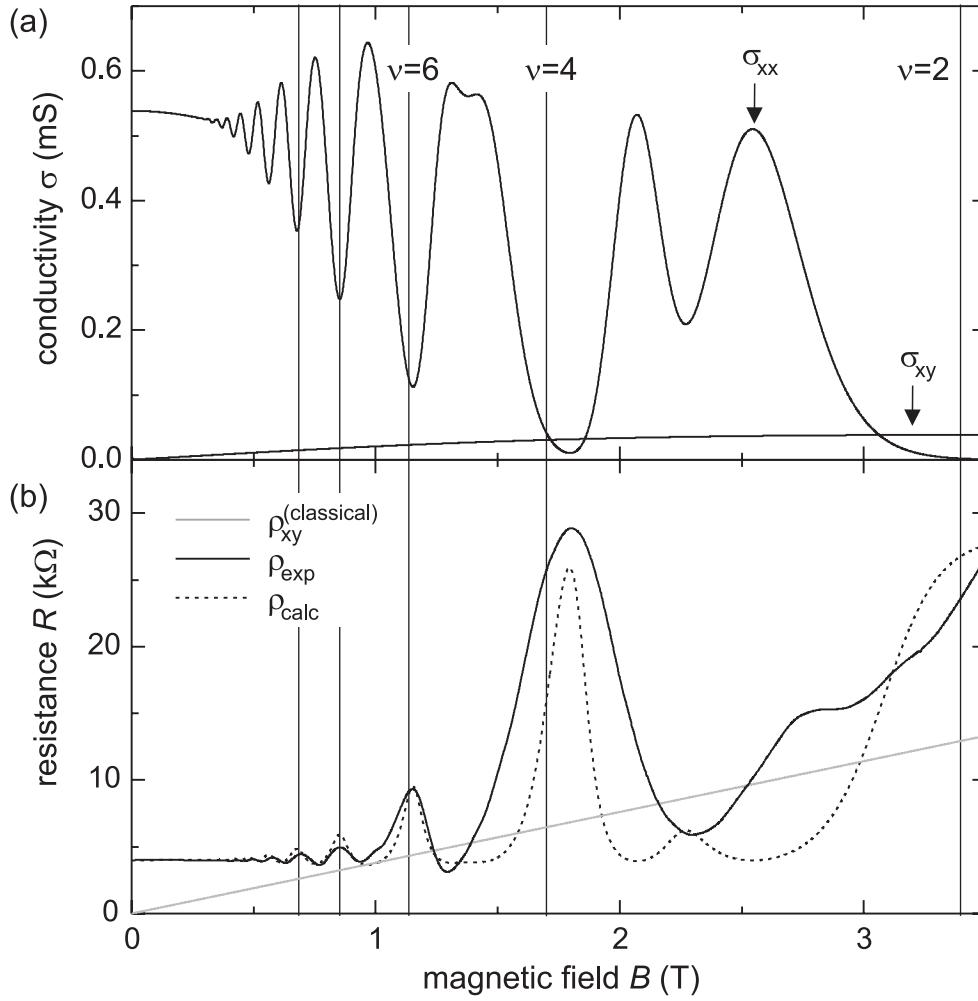


Figure 2.22: Transport model for the SLFET at $U_g = 0.275$ V. (a) Calculated conductivities σ_{xx} and σ_{xy} . (b) Calculated and experimental magnetoresistance.

gap energy, and the magnetic field was given in Section 2.2.8

$$\hbar\omega_c E_F > E_g^2. \quad (2.50)$$

We realize that the gap energy to be overcome by the electron when tunneling between two adjacent trajectories is

$$E_g = E_F - \Delta. \quad (2.51)$$

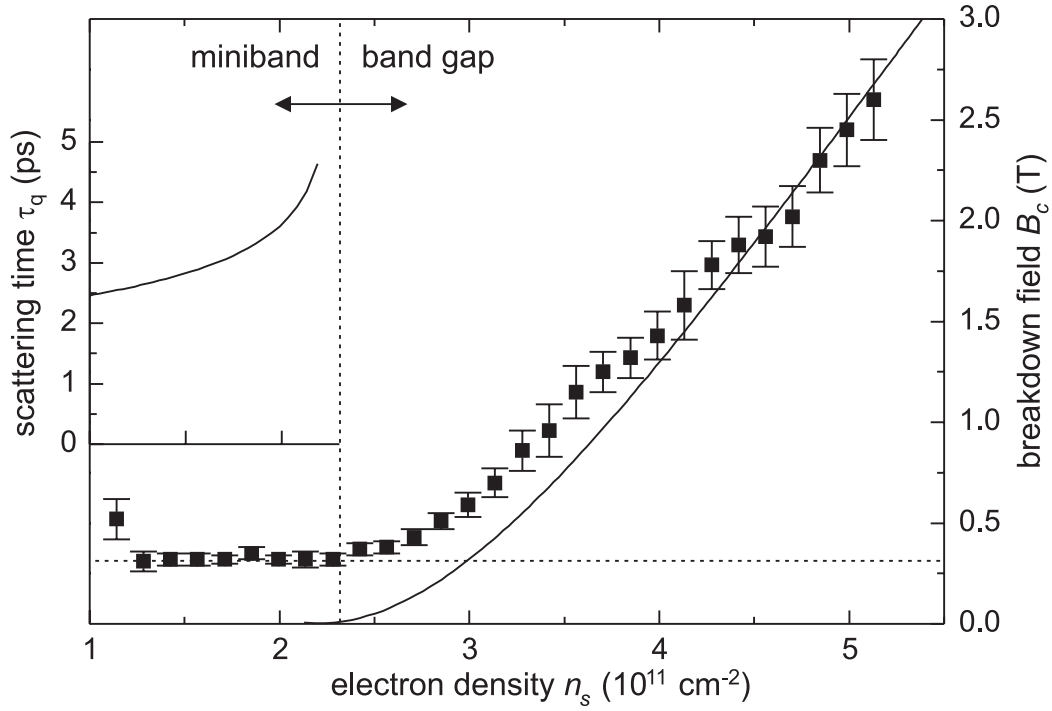


Figure 2.23: Comparison of calculated (solid line) and experimental breakdown magnetic field. In the inset the quantum scattering time τ_q , deduced from the onset of the magnetoresistance oscillations for Fermi energies within the miniband, is shown.

Using $\omega_c = eB_c/m_c$ we can therefore write

$$B_c = \frac{(E_F - \Delta)^2 m_c}{\hbar e E_F}. \quad (2.52)$$

For the conversion between Fermi energy and electron density, as well as the calculation of the electron cyclotron effective mass, we make use of the results of Section 2.2.4. The solid line in Figure 2.23 represents the calculated critical magnetic field. The agreement between theory and experiment is excellent, noting that this theory requires *no* free parameter. At low magnetic fields, and of course for electron densities $n_s < 2.3 \times 10^{11} \text{ cm}^{-2}$, where orbits are closed and no magnetic breakdown can occur, B_c is determined by the quantum scattering time τ_q via $\omega_c \tau \approx 1$. This determines a lower limit for the observable breakdown field.

As can be seen in the Figure, the lower limit for the onset of the magnetoresistance oscillations is $B_c = 300 \text{ mT}$. Using Equation (2.24)

$$\omega_c \tau_q = 1 \quad \Rightarrow \quad \tau_q = \frac{m_c}{eB_c},$$

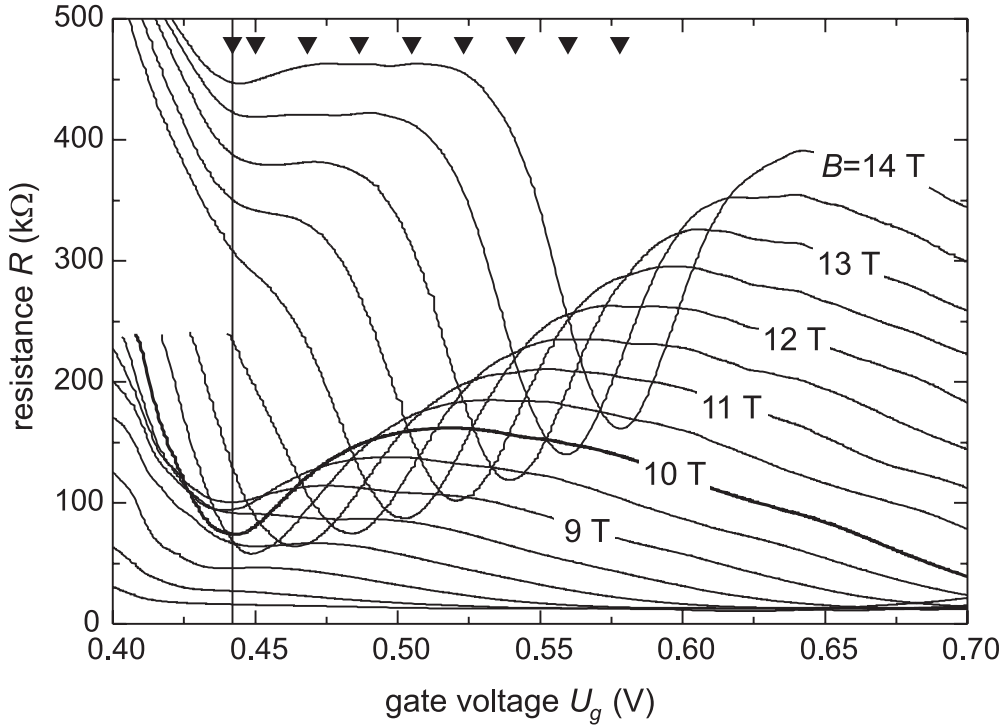


Figure 2.24: Resistance minimum at filling factor $\nu = 1$ occurring only for magnetic fields above $B = 10$ T, possibly indicating the phase transition from a spin-unpolarized to a spin-polarized state at high magnetic fields.

we can estimate the quantum scattering time, using the calculated cyclotron effective mass m_c . As shown in the inset of Figure 2.23, the quantum scattering time τ_q varies between 2 ps and 4 ps depending on the electron density.

2.3.8 Spin-polarized state at high magnetic fields

In our magnetotransport data no unambiguous signature of spin split Landau levels is observed above filling factor $\nu = 2$. In Figure 2.18 at high magnetic fields $B > 10$ T, however, a pronounced magnetoresistance minimum is found exactly at the position of the $\nu = 1$ filling factor. This possibly indicates the presence of a fully spin polarized state. We observe a linear dependence of the magnetic field position of this minimum on the gate voltage only above $B = 10$ T. Below $B = 10$ T, the resistance minimum remains at the constant gate voltage of $U_g = 0.45$ V.

In Figure 2.24 we plot the relevant magnetoresistance traces vs. gate voltage. Downward

pointing triangles indicate the position of the minima, shifting linearly to smaller gate voltages as the magnetic field is decreased as expected for a Landau level. This shift abruptly ceases at $U_g = 0.44$ V, the minimum remains at this gate voltage until $B = 7.5$ T. An additional minimum at exactly the same position $U_g = 0.44$ V is found for the highest magnetic field $B = 14$ T. We note that the gate voltage $U_g = 0.44$ V exactly corresponds to a Fermi energy at the top of the miniband $E_F = \Delta$.

Recently, there has been increasing theoretical interest in the ground state of a two-dimensional electron gas in a short-period lateral potential in magnetic field, with the Coulomb electron-electron interaction included in the Hartree-Fock approximation. It is found that the energy dispersion of the band intersected by the Fermi energy is enhanced [Man95]. Such an effect has been indirectly observed in the magnetoresistance of short-period superlattices as an abrupt onset of the spin-splitting of the Shubnikov-de Haas peaks, occurring only for a sufficiently strong magnetic field [Pet97]. In other words, when the magnetic field increases, the system makes a first-order phase transition from spin-unpolarized to spin-polarized states. The onset of the $\nu = 1$ resistance minimum observed in the SLFET at magnetic fields above $B = 10$ T may be a manifestation of such a phase transition.

2.3.9 Density dependence of the zero-field resistance

For a conventional two-dimensional system at zero magnetic field, as long as only the ground state is occupied, the resistance continuously decreases with increasing electron density. In the SLFET, however, we observe an *increasing* zero-field resistance above a critical electron density, as shown in Figure 2.25 for two different temperatures. The observed minimum resistance is at $U_g = 0.54$ V and shows a shoulder at $U_g = 0.5$ V, which disappears at higher temperatures. The resistance increase above the critical electron density is much pronounced for non-zero magnetic fields. This is yet another sign of the peculiar density of states in the SLFET. In a simple relaxation time approximation model, the conductivity at zero temperature is given by [Ash76]

$$\sigma = e^2 \tau(E_F) \int \frac{d\vec{k}}{2\pi^2} \mathbf{M}^{-1}(\vec{k}), \quad (2.54)$$

where \mathbf{M} is the effective mass tensor. The integration is to be taken over all occupied states. Clearly, for Fermi energies within the band, the \vec{k} -integration results in a proportionality to n_s , which for the free electron case results in the Drude relation $\sigma = n_s e^2 \tau / m^*$. For Fermi energies in the band gap, however, due to the periodicity of the electron effective mass in

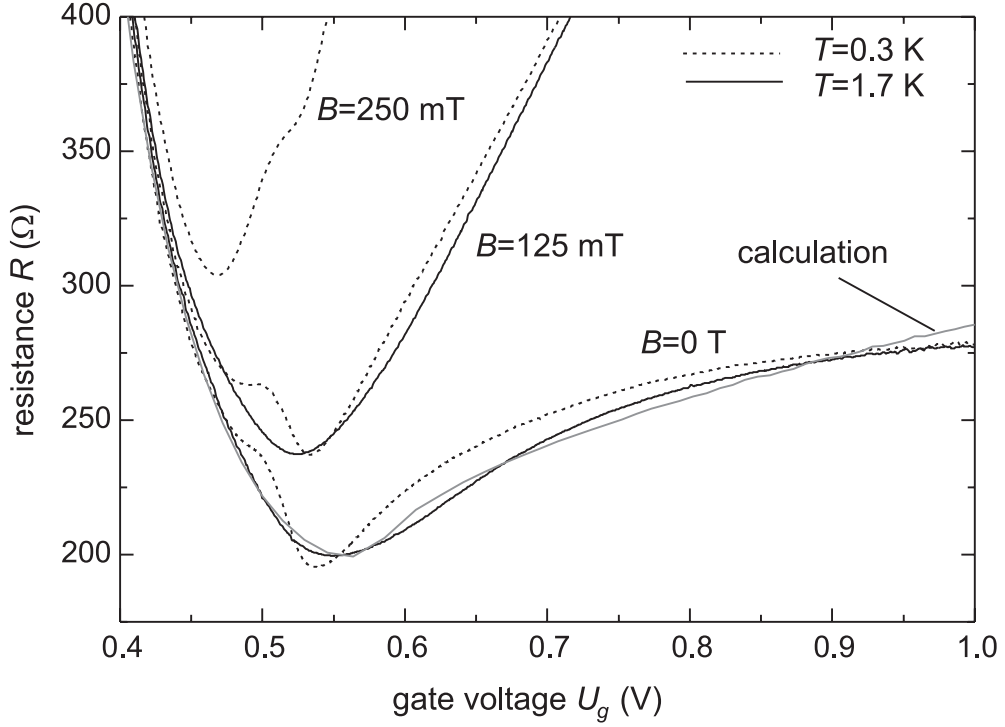


Figure 2.25: Electron density dependence of the zero magnetic field resistance. The solid gray line is calculated.

x direction, the only non-vanishing part in the integral (2.54) has a k space area proportional to the square root of the Fermi energy, just as the density of states for large E_F . This explains the observed increase of the zero-field resistance for large gate voltages. In this model, the shoulder observed at $U_g = 0.5$ V only for the low-temperature trace remains unexplained.

We can directly calculate the zero-field resistance in the following model [Gra01], which assumes only inelastic scattering, see Figure 2.26. Using the energy spectrum (2.8) and the equation of motion (2.15), the x component of the Fermi velocity is given by

$$v_F^{(x)}(k_x) = \frac{\Delta d}{2\hbar} \sin(k_x d). \quad (2.55)$$

The conductivity in x direction is obtained by summing the number of parallel modes of conduction $\Delta k_y/2\pi$ over the Fermi line between k_y^{min} and k_y^{max} , taking into account the spin degeneracy $g_s = 2$

$$\sigma(E_F) = 2g_s \frac{e^2}{h} \frac{1}{2\pi} \int_{k_y^{min}}^{k_y^{max}} l_x(k_y, E_F) dk_y \quad (2.56)$$

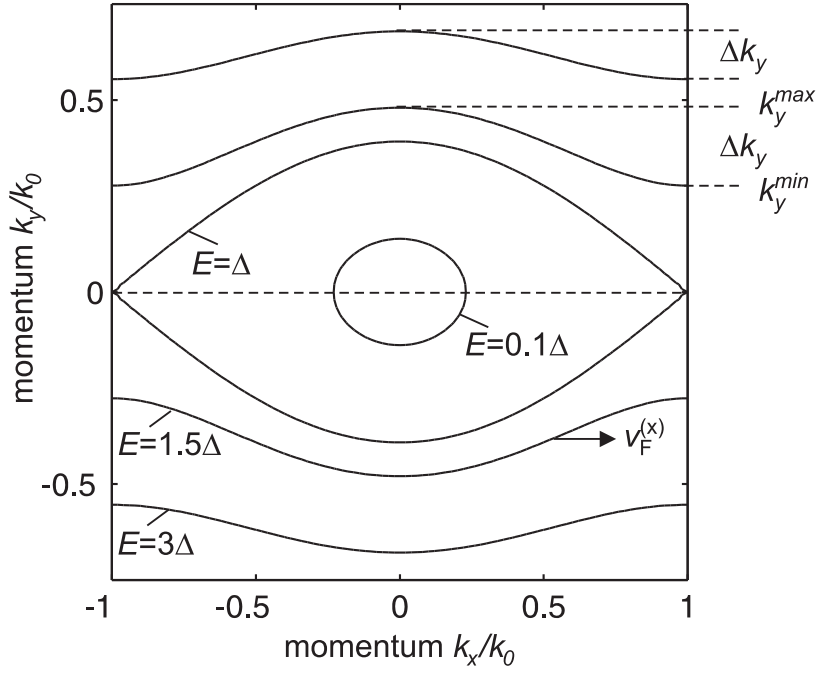


Figure 2.26: Model for explaining the zero-field resistance.

weighted with the scattering length

$$l_x(k_y, E_F) = v_F^{(x)}(k_x(k_y, E_F))\tau(E_F). \quad (2.57)$$

The momentum k_x is expressed in terms of the momentum k_y and the Fermi energy E_F by inverting the energy spectrum (2.8). For the inelastic scattering time we empirically assume an electron density dependence due to screening

$$\tau(n_s) = \tau_0 \left(\frac{n_s}{n_s^\Delta} \right)^c, \quad (2.58)$$

where

$$n_s^\Delta = n_s(E = \Delta), \quad (2.59)$$

is the electron density for a filled miniband, and the relation between the electron density and the Fermi energy is known from Section 2.2.4. The gray line in Figure 2.25 has been calculated in this model with $R = L/(W\sigma)$, using the parameters $\Delta = 3.8$ meV, $d = 15$ nm, $W = 250$ μm , $L = 1.5$ μm , $\tau_0 = 0.5$ ps and $c = 0.7$. The agreement between experiment and theory is excellent, except for a linear offset on the gate voltage axis, which we have accounted for by a linear shift of $\Delta U_g = 0.27$ V.

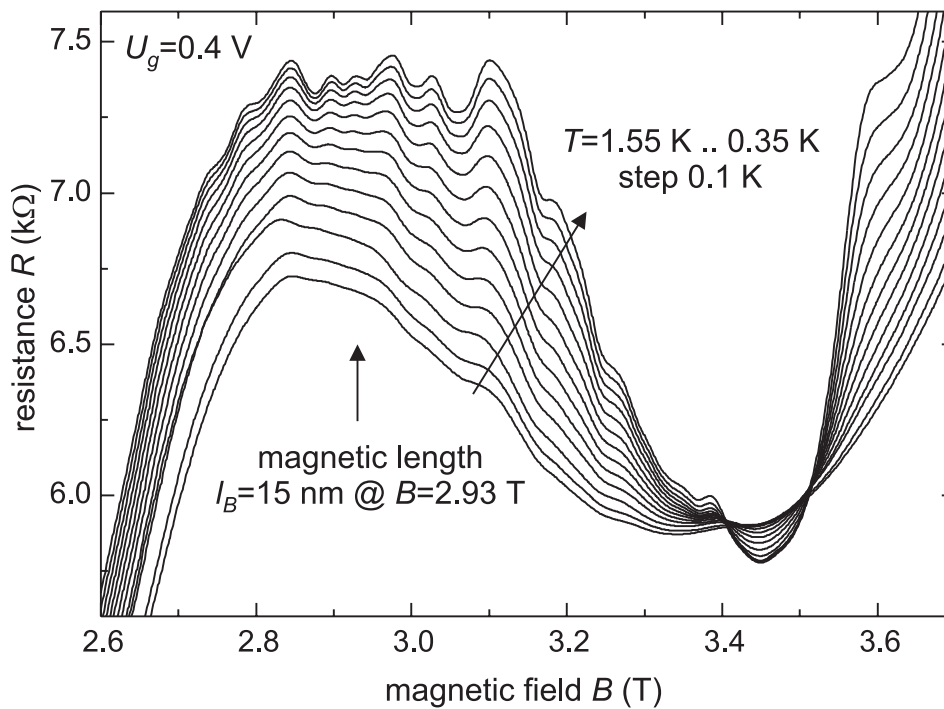


Figure 2.27: High-frequency magnetoresistance oscillations at commensurate superlattice period and magnetic length.

2.3.10 High frequency magnetoresistance oscillations

We want to point out a peculiar resistance oscillation effect observed around filling factor $\nu = 3$, for which we do not have an explanation. As shown in Figure 2.27 between $B = 2.7$ T and $B = 3.3$ T the magnetoresistance exhibits short period oscillations with a mean period of $\Delta B = 57$ mT, although the periodicity is not quite regular. Raising the temperature from $T = 0.35$ K to $T = 1.55$ K almost entirely quenches this effect, pointing to a quantum interference effect as the origin. Signatures of this effect can be found in the (U_g, B) measurement shown in Figure 2.18 in the region $(0.35 \text{ V} \dots 0.55 \text{ V}, 2.5 \text{ T} \dots 4 \text{ T})$ as straight lines, which show a different dependence on magnetic field and electron density than filling factor $\nu = 3$ also crossing this area. We note that the magnetic length $l_B = (\hbar/eB)^{1/2}$ in this magnetic field region matches the period length of the superlattice $d = 15$ nm.

2.4 Quantum mechanical model

Using only semiclassical arguments and the zero-field band structure, we have been able to understand the magnetoresistance data fairly well. Here we are interested in a full quantum mechanical treatment of the problem, where neither the magnetic field nor the potential modulation are treated as a weak perturbation. The results of this calculation yield a better insight into the physics of a strongly modulated electron system in a magnetic field of arbitrary strength. It is found that the Landau levels exhibit an internal band structure. The density of states is calculated explicitly, and allows to understand the hitherto unexplained switching of the magnetoresistance maxima to minima at integer filling factors. The results presented in this section have been obtained in collaboration with K. Vyborny and L. Smrcka, Institute of Physics, Academy of Sciences, Prague, Czech Republic.

2.4.1 Formulation of the problem

The Schrödinger equation reads, in the coordinate system introduced in Figure 2.1, and using the vector potential in the gauge $\vec{A} = (0, Bx, 0)$

$$\begin{aligned} \left(\frac{1}{2m^*} (\vec{p} - e\vec{A})^2 + V(x) \right) \Psi(x, y) &= \quad (2.60) \\ \left(\frac{1}{2m^*} p_x^2 + \frac{1}{2m^*} (-i\hbar \frac{d}{dy} + eBx)^2 + V(x) \right) \Psi(x, y) &= \epsilon \Psi(x, y), \end{aligned}$$

where $V(x)$ is the periodic potential. We exploit the translational invariance in the y direction and make the separation ansatz $\Psi(x, y) = \exp(ik_y y) \psi(x)$ to obtain with

$$\left(\frac{1}{2m^*} p_x^2 + \frac{1}{2m^*} (\hbar k_y + eBx)^2 + V(x) \right) \psi(x) = E(k_y) \psi(x) \quad (2.61)$$

a one-dimensional Schrödinger equation for an electron confined in a parabolic potential with a superimposed periodic modulation. Note that the parabolic potential depends on the momentum in the free electron direction, and increases in strength with increasing magnetic field. The corresponding Hamiltonian H_x is periodic in x direction with period d due to the periodicity of $V(x)$. We solve Equation (2.61) in the tight-binding approximation, assuming that a state $|\varphi(x - jd)\rangle$ is nested in each well, where jd denotes the well center coordinate and j is an integer. In the tight-binding model only neighboring states overlap

$$\langle \varphi(x - jd) | H_x | \varphi(x - kd) \rangle = t \delta_{jk \pm 1} \quad (2.62)$$

with the requirement

$$\langle \varphi(x - jd) | \varphi(x - kd) \rangle = \delta_{jk} \quad (2.63)$$

that the states $|\varphi(x - jd)\rangle$ form an orthonormal basis.

Condition $\langle \varphi(x - jd) | H_x | \varphi(x - jd) \rangle = 0$ defines the zero energy level. In this basis the solutions to Equation (2.61) can be expressed as the linear combination

$$\Psi(x) = \sum_{j=-N}^N a_j \varphi(x - jd), \quad (2.64)$$

and the numerically tractable finite set of equations read

$$\sum_{j=-N}^N H_{jl}(k_y) a_j = E(k_y) a_l \quad (2.65)$$

where the matrix H_{jl} assumes the tridiagonal form

$$H_{jj} = \frac{\hbar^2}{2m^*} (k_y + j\kappa)^2, \quad H_{jj\pm 1} = t, \quad (2.66)$$

with $\kappa = edB/\hbar$. For large N the finite system described in Equation (2.65) is solved by functions periodic in k_y with period κ . Perpendicular to the zero-field periodicity in x direction with a Brillouin zone $k_0 = \pm\pi/d$ a new repeated zone scheme is therefore introduced by the magnetic field with zone boundaries at $k_y = \pm\kappa/2$ that increase with magnetic field strength.

Equation (2.65) is formally similar to the nearly free electron result

$$\left(\frac{\hbar^2}{2m^*} (k_y + j\kappa)^2 - E \right) a_j + \sum_{l=-\infty}^{\infty} V_{l-j} a_l = 0, \quad (2.67)$$

with

$$V_n = \kappa \int_0^d e^{-in\kappa y} V(y) dy. \quad (2.68)$$

This exact equation refers to electrons which are almost free in y direction, and V_n are the Fourier components of the weak perturbing potential V in the y direction. Comparing the Fourier series with Equation (2.65) we realize that $V_{l-j} = t\delta_{l,j\pm 1}$, i.e. $V_{\pm 1} = t$ and $V_{\pm n} = 0$ for $n = 0, 2, 3, \dots$. Therefore $V(y) = t[\exp(i\kappa y) + \exp(-i\kappa y)] = 2t \cos(\kappa y)$, and for $N \rightarrow \infty$ Equation (2.65) is equivalent to

$$\left\{ -\frac{\hbar^2}{2m^*} \frac{d^2}{dy^2} + 2|t| \cos \kappa y \right\} \chi(y) = E\chi(y). \quad (2.69)$$

being solved with the ansatz $\chi(y) = \exp(ik_y y)u(y)$. This is the well known Mathieu problem [Abr65].

2.4.2 Qualitative discussion of the energy spectrum

Using Equation (2.69) we obtain a qualitative idea of the k_y dependence of the energy eigenvalues for the limit of small and large energies with respect to the potential $2|t|\cos\kappa y$. Since the potential in this equation is periodic, we focus on one period $y \in (-\pi/\kappa, \pi/\kappa)$.

For $-2|t| < E < 2|t|$ the eigenstates should be similar to those of a particle confined in a potential well. In particular when $E \ll 2|t|$, the wave function is localized at $|y| \ll \pi/\kappa$, energies supplied by Equation (2.69) are independent of k_y (flat bands), and the potential can be expanded around its minimum

$$2|t|\cos(\kappa y) = -2|t| + \frac{|t|(deB)^2}{\hbar^2}y^2 + O(y^4). \quad (2.70)$$

In this limit the problem corresponds to a harmonic oscillator with potential $\frac{1}{2}m_y\omega_c^2y^2$ with a frequency

$$\omega_c = \frac{eB}{\sqrt{m_x m_y}}, \quad (2.71)$$

that corresponds to the cyclotron frequency at the miniband minimum. The energy spectrum is

$$E = -2|t| + \hbar\omega_c\left(\nu + \frac{1}{2}\right), \quad \nu = 0, 1, \dots \quad (2.72)$$

In the limit of large energies, weak coupling $t \rightarrow 0$, or strong fields, $E \gg 2|t|$, the electron behaves like an almost free one-dimensional particle, only weakly perturbed by the cosine potential. Therefore the spectrum is parabolic with narrow gaps at $k_y = \pm\kappa/2$. Essentially the system separates into decoupled one-dimensional wires with parabolic spectrum and density of states $D(E) \propto 1/\sqrt{E}$.

2.4.3 Energy bands and density of states

We calculate the energy spectrum by numerically diagonalizing the finite linear system in Equation (2.65). The density of states is then calculated from the $E(k_y)$ relation by

$$D(E) = \frac{1}{2\pi} \int_{E'=E} \left| \frac{dk_y}{dE'} \right|. \quad (2.73)$$

We show three examples for different magnetic field strengths for energies between $E = 0$ and $E = 2\Delta$. We have shifted the energy axis for the Figures up by $2|t|$ to define the energy minimum to $E = 0$, and we use $\Delta = 4|t|$. In order to draw a relation to the transport

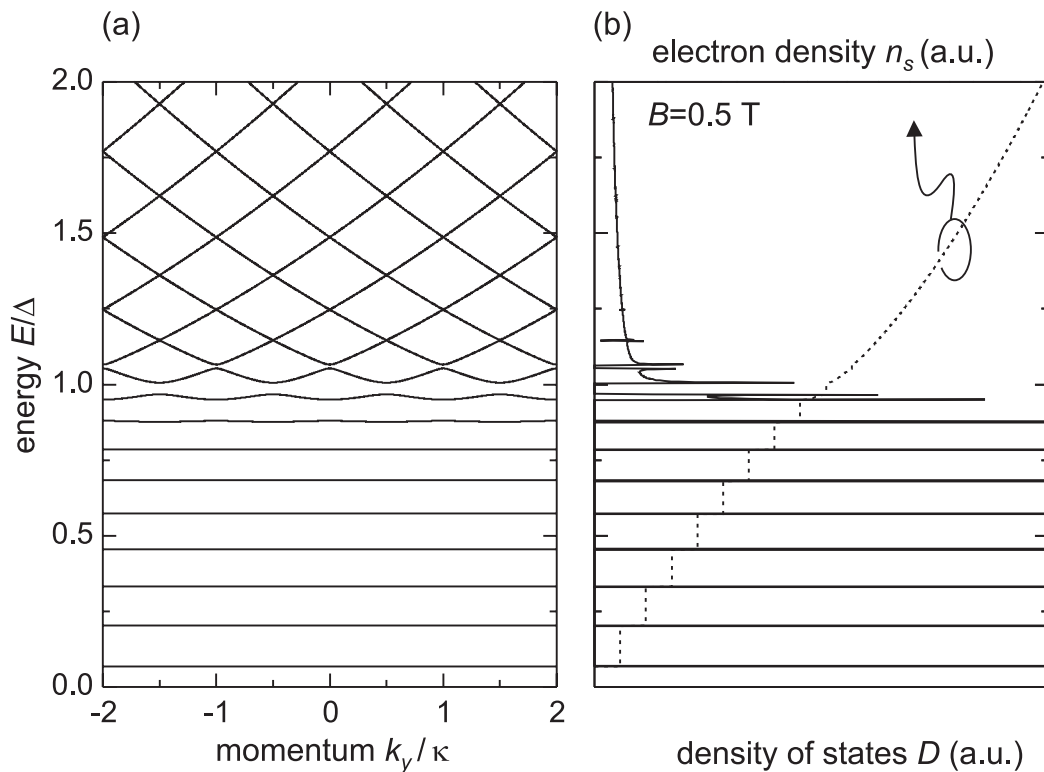


Figure 2.28: Calculated band structure (a), density of states and electron density (b) for $B = 0.5$ T

experiment we assume that extrema in the density of states correspond to extrema of the conductivity.

In Figure 2.28 the low-field case is shown for $B = 0.5$ T. As discussed qualitatively in the last section, for low energies the bands are flat, almost equidistant as expected from regular Landau levels, and the density of states consists of delta functions. The system behaves like a two-dimensional electron gas, in a semiclassical picture electrons perform closed orbits. At the band edge the system undergoes a sharp transition. The Landau levels exhibit an internal dispersion, and for larger energies bands are parabolic with vanishing gaps, while the density of states decreases like one over square root of energy. Semiclassically this situation corresponds to open electron orbits, no quantum oscillations are expected due to the continuity of the density of states.

The intermediate regime $\hbar\omega_c \approx \Delta$ is shown in Figure 2.29 for $B = 1.75$ T. Only two Landau levels are located below $E = \Delta$, both show some dispersion, and higher Landau levels

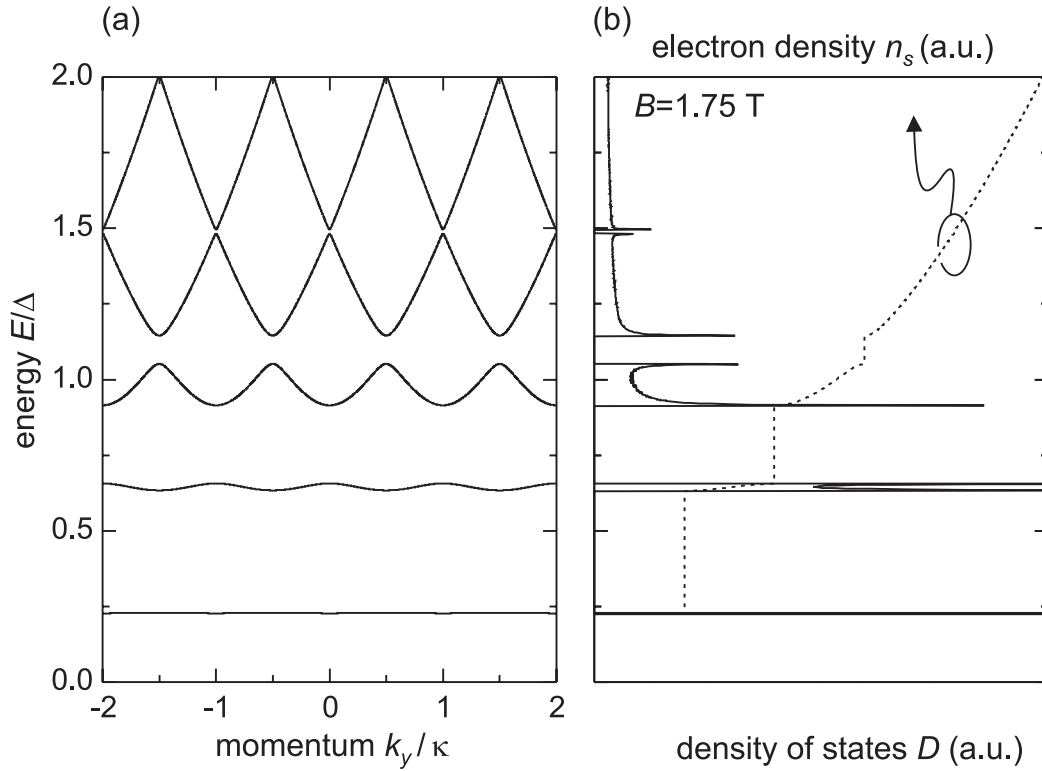


Figure 2.29: Calculated band structure (a), density of states and electron density (b) for $B = 1.75$ T

are strongly modulated. Most importantly, even for $E > \Delta$ the density of states exhibits an internal structure with maxima at the flat band energies, and clear gaps are visible, which will leave signature in the magnetoresistance. This corresponds to the magnetic breakdown. Electrons perform closed orbits even for energies in the band gap.

The high field case is displayed in Figure 2.30, calculated for $B = 10$ T. Here, only one single highly dispersive Landau level is visible below $E = 2\Delta$, and no magnetoresistance oscillations are expected. The density of states is continuous, and in the energy range shown no breakdown occurs. We note that the increasing breakdown field with increasing Fermi energy has already been discussed semiclassically in Section 2.2.8. Since we have not included the spin degree of freedom in the quantum mechanical calculation, the observed spin-split Landau level (see Section 2.3.8) cannot be explained in this model.

The quantum mechanical calculation yields results similar to the semiclassical model for both high ($E > \Delta$) and low ($E \approx 0$) energies. In the latter case narrow peaks in the DOS

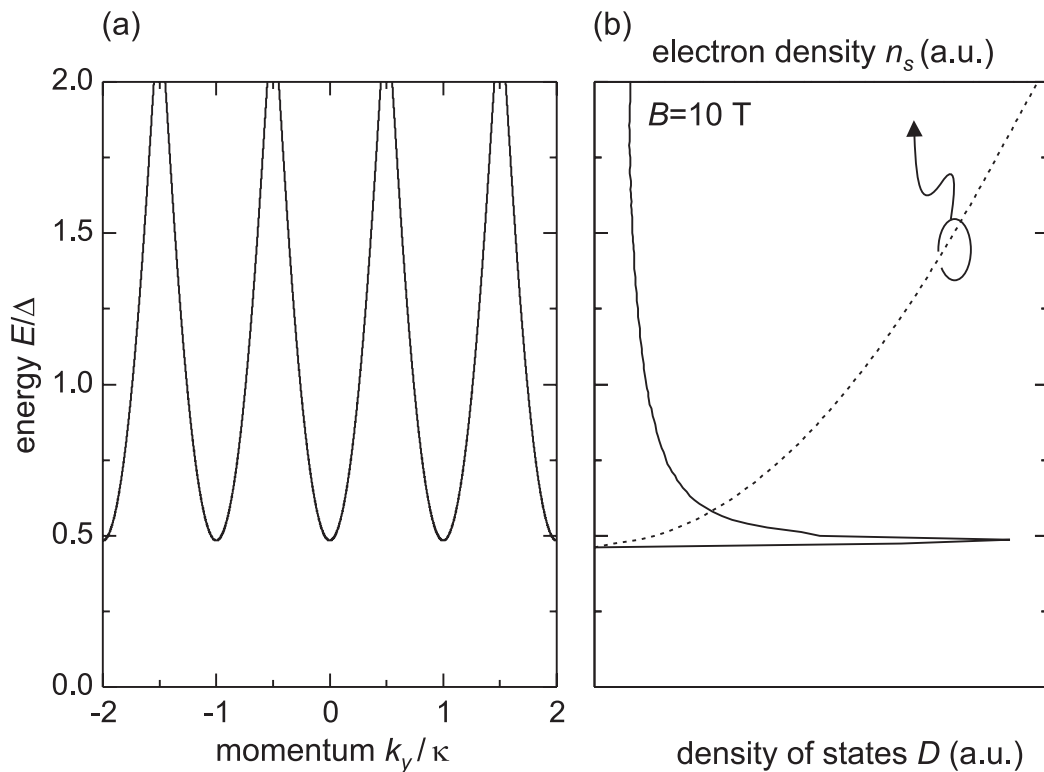


Figure 2.30: Calculated band structure (a), density of states and electron density (b) for $B = 10$ T.

can be interpreted as closed orbits on the Fermi surface. The almost parabolic bands present for large energies correspond, up to the narrow gaps, to open orbits. However, according to the semiclassical model, the transition between these two regimes should be sharp. The difference between semiclassical and quantum mechanical model is the presence, first, of gaps in the parabolic part and, second, of wide bands in the transition region $E \approx \Delta$.

2.4.4 Density of states in the (U_g, B) plane

In Figure 2.31 we show the calculated density of states in the parameter space (U_g, B) and compare it to the measurement. The electron density is obtained by integrating the density of states, and the relation between electron density and gate voltage is linear, and known from the experiment. A high density of states is shown in dark, while zero density of states is displayed in white. For gate voltages $U_g < 0.45$ V sharp Landau levels are recognized, that broaden for larger gate voltages. As can be seen, the sharp Landau levels correspond

to magnetoresistance maxima in the experiment, while magnetoresistance minima for larger gate voltages appear at the density of state gaps, and large resistance maxima correspond to the local density of states minima between the gaps. Given this density of states, it is straightforward to calculate the conductivity tensor for arbitrary magnetic field strengths using the Kubo formula. This calculation is beyond the scope of this work.

2.5 Conclusion

In this chapter we have presented an electronic system that took us on a tour starting from a two-dimensional world and ending in a one-dimensional micro-cosmos, the location dictated by the magnetic field. The experimental method used to probe the system was magnetotransport, and we gained understanding of the system by semiclassical considerations, and by a full quantum mechanical calculation.

In the two-dimensional world, electrons perform closed orbits, magnetoresistance oscillations periodic in inverse magnetic field are measured, and the electron states are condensed on sharp Landau levels. In the one-dimensional regime we observe a strong increase of the magnetoresistance at low fields, explained by the presence of open orbits, or by Landau levels with an internal band structure. For larger fields magnetoresistance oscillations are recovered, explained semiclassically by magnetic breakdown, i.e. electron tunneling in k space between open orbits, or quantum-mechanically by the presence of gaps in the density of states even for energies in the gap.

We supply a full experimental mapping of the phase diagram, presented in Figure 2.11, comprising these regimes. This is a unique demonstration of a transition from a two-dimensional electron system to a one-dimensional behavior in a single sample, and may be the first proof of the magnetic breakdown relation (2.28) between Fermi energy, energy gap and magnetic field.

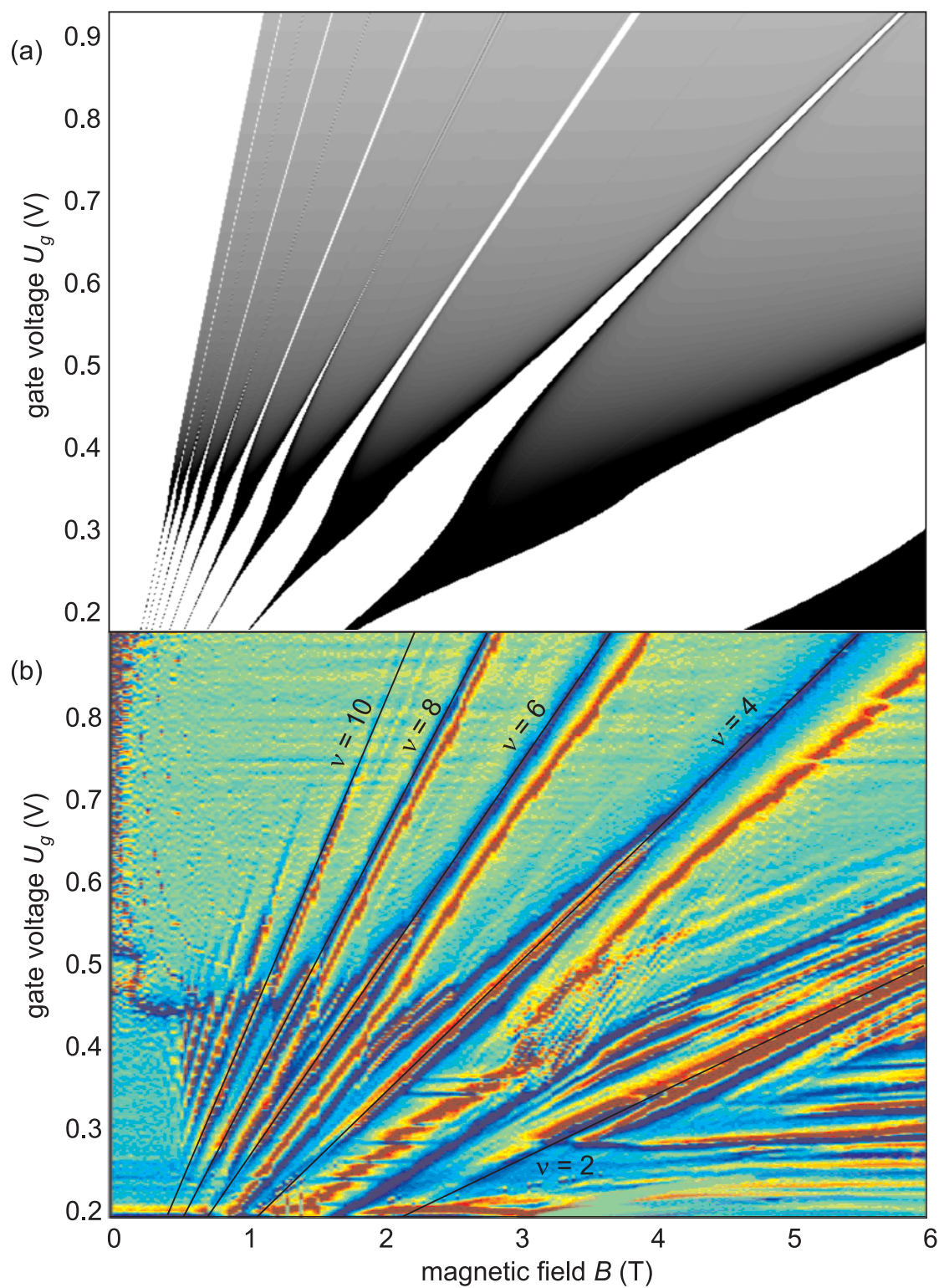


Figure 2.31: (a) Calculated density of states, gray scale coded (white=zero). (b) Experimental longitudinal resistance maxima (red) and minima (blue) as a function of gate voltage U_g (V) and magnetic field B (T). Adapted from *Phys. Rev. Lett.* 86, 126801 (2001) by precise periodic potentials (2001) Ph.D. Dissertation. Selected Topics of Semiconductor Physics and Technology, ISBN 3-932749-42-1

Chapter 3

High Field Miniband Transport

The fundamental effect of the existence of a miniband on charged carrier conduction is related to an upper limit of the energy, which can be acquired from the electric field applied along the superlattice growth axis. As opposed to other scattering mechanisms commonly known in bulk semiconductors, this limit strongly influences the high field transport for moderate miniband widths Δ .

In this chapter we experimentally and theoretically study the non-equilibrium transport of electrons through SLFET devices with different miniband widths. After a review of miniband transport, we present self-consistent calculations of the miniband structures of the SLFETs. Current-voltage traces are then discussed in the framework of the Esaki-Tsu miniband conduction. The possibility of the observation of Bloch-phonon resonances is discussed, as well as advantages of SLFETs with respect to bulk superlattices in regard of charge instabilities.

Further insight to miniband conduction is gained by transport studies in crossed electric and magnetic fields. We conclude this chapter with a variant of the SLFET in the form of two different ultra-short channel transistors and proof their practicability by experimental results.

3.1 Superlattice transport: Review

Superlattice systems have been a very active research area in solid state physics. A simple search for the term 'superlattice' in the INSPEC database yields 15000 hits, over 9000 of these published papers relate to semiconductor superlattices. A review of the field is therefore bound to be incomplete. Here we concentrate on seminal papers investigating high-field superlattice transport, briefly discuss the history of Bloch oscillations, and then focus on device structures similar to the SLFET, i.e. modulated two-dimensional electron systems. An excellent recent overview of transport and optical experiments in bulk superlattices, written by several leading authors in the fields, has been collected in a textbook style by H. Grahn [Gra95]. Some results of this chapter have previously been published in [Deu00c] and [Deu01b].

3.1.1 Esaki-Tsu model

In their seminal paper [Esa70], Leo Esaki and Raphael Tsu not only introduced the concept of the superlattice, but they also indicated that the fabrication of the Bloch oscillator device should become feasible by making use of the obtained reduced band width. The essential features of the so called Esaki-Tsu model have been proven correct since their proposal.

The semiclassical equation of electron motion in a one-dimensional solid under the application of an electric field F are

$$\hbar \frac{dk}{dt} = eF \quad \text{and} \quad v = \frac{1}{\hbar} \frac{\partial E}{\partial k}. \quad (3.1)$$

Even though, by means of the first equation, the momentum k is increasing linearly in time

$$k(t) = \frac{eFt}{\hbar}, \quad \text{assuming} \quad k(0) = 0, \quad (3.2)$$

in a periodic potential, for example a sinusoidal miniband structure in a superlattice with period d , the group velocity $v(t)$ is not increasing without bounds, but oscillating in time

$$E(k) = \frac{\Delta}{2} (1 - \cos(kd)) \quad \Rightarrow \quad v(t) = \frac{\Delta d}{2\hbar} \sin(\omega_B t). \quad (3.3)$$

The relevant frequency, the Bloch frequency ω_B ,

$$\omega_B = \frac{eFd}{\hbar} \quad (3.4)$$

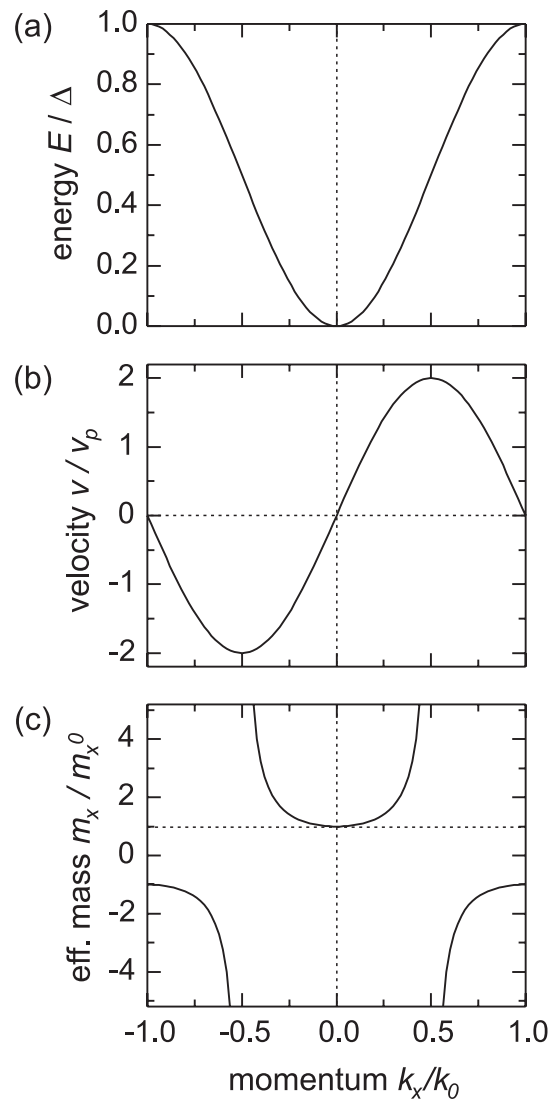


Figure 3.1: Electron velocity (b) and electron effective mass (c) in the Esaki-Tsu model, when a sinusoidal energy dispersion is assumed (a). The Brillouin zone boundary is at $k_0 = \pi/d$, where d is the superlattice period.

is nothing but the potential energy the electron gains when travelling one period of the superlattice in the electric field F . The relation between $E(k)$, $v(k)$ and $m(k) = \hbar(\partial v(k)/\partial k)^{-1}$ is shown in Figure 3.1.

Scattering is introduced to the model by a mean time between collisions τ through an assumed exponential temporal decay of the probability of collisionless (ballistic) transport

at time t . The net velocity computed as an average over the whole electron gas then reads

$$v_m = \int_0^\infty \exp(-t/\tau) dv = \frac{eF}{\hbar^2} \int_0^\infty \frac{\partial^2 E}{\partial k^2} \exp(-t/\tau) dt. \quad (3.5)$$

Integration, using the sinusoidal dispersion, yields the important result

$$v_m = \frac{\mu F}{1 + (F/F_c)^2}, \quad (3.6)$$

where

$$\mu = \frac{e\tau}{m^*} \quad (3.7)$$

is the low field mobility,

$$m^* = m(k=0) = \frac{2\hbar^2}{\Delta d^2} \quad (3.8)$$

denotes the electron effective mass at the bottom of the miniband, and

$$F_c = \frac{\hbar}{e\tau d} \quad (3.9)$$

is the critical electric field, above which in this model the mean electron velocity v_m is predicted to decrease. This negative differential velocity is indeed a true miniband effect, since the peak velocity v_p

$$v_p = v_m(F = F_c) = \frac{\Delta d}{2\hbar} \quad (3.10)$$

is a value directly proportional to the miniband width. In natural solids band widths usually are on the order of eV, resulting in theoretical peak velocities much too high to be sensible, and other saturation mechanisms, such as phonon emission or intervalley scattering would prevail over miniband negative differential velocity.

3.1.2 Bloch oscillations

Bloch oscillations (BOs) in the semiclassical model of Esaki and Tsu refer to the oscillatory electron motion in a biased periodic potential. The amplitude of this motion is obtained by integration of Equation (3.1) to $\lambda = \Delta/eF$. For low electric fields electrons are scattered before they are significantly accelerated, and a Drude drift current with low field mobility μ results. For sufficiently large electric fields, however, electrons reach the Brillouin zone boundary and are Bragg reflected. The current is therefore expected to decrease, as electrons are localized in space, until they are scattered.

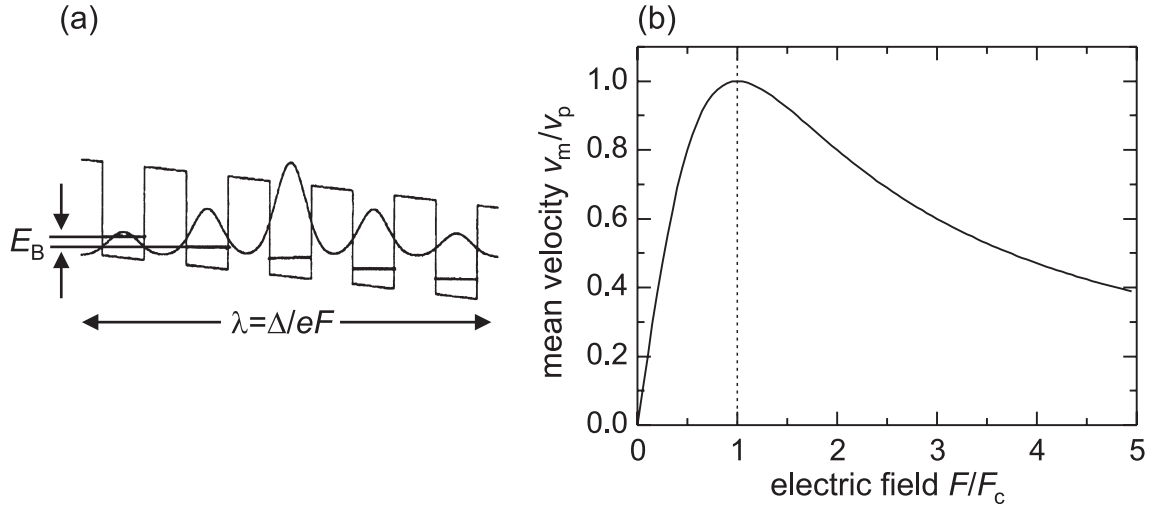


Figure 3.2: (a) Localization of the electron wave packet over a length λ , the Bloch energy E_B is identical to the voltage drop over one period of the superlattice. (b) velocity to electric field relation as predicted by the Esaki-Tsu model.

In fact, within the Esaki-Tsu model, the negative differential velocity is found to occur even earlier than that. The mean electron momentum is given by

$$k_m = \frac{1}{\tau} \int_0^{\infty} \exp(-t/\tau) k(t) dt = \frac{eF\tau}{\hbar}, \quad (3.11)$$

and therefore at the peak electric field $k_m = 1/d$. The average electron momentum acquired from the electric field at the onset of negative differential velocity is below $k_0 = \pi/d$, at which momentum the electrons are Bragg reflected at the Brillouin zone boundary. The origin of negative differential velocity can be understood as originating from the negative effective mass of the electrons above $k = k_0/2$.

In Figure 3.2(a) we schematically show the conduction band of a biased superlattice, which hosts an electron wave packet of lateral extent λ , and with Bloch energy $E_B = \hbar\omega_B$. In Figure 3.2(b) the calculated drift velocity v_m in the Esaki-Tsu model is plotted.

The literature on Bloch oscillations is extensive. Here we can merely recall the history of Bloch oscillations in short terms. Some good review articles that cover the history and physics of Bloch oscillations include the topical review by K. Leo [Leo98], the article by Lysenko [Lys98], and the short review by Dekorsy (in German) [Dek96].

Year	Author	Milestone	Reference
1928	F. Bloch	description of the crystal electron dynamics	[Blo28]
1934	C. Zener	prediction of Bloch oscillations	[Zen34]
1970	L. Esaki and R. Tsu	proposal of the superlattice	[Esa70]
1988	E.E. Mendez <i>et al.</i>	observation of the Wannier Stark ladder	[Men88]
1992	J. Feldmann <i>et al.</i>	observation of BOs by four-wave mixing	[Fel92]
1992	K. Leo <i>et al.</i>	” ”	[Leo92]
1993	C. Waschke <i>et al.</i>	observation of THz emission	[Was93]
1996	K. Unterrainer <i>et al.</i>	Inverse Bloch oscillator	[Unt96]
1996	M. B. Dahan <i>et al.</i>	BOs in ultra-cold cesium atoms	[Dah96]
1997	V. G. Lyssenko <i>et al.</i>	observation of BO real space motion	[Lys97]

Bloch oscillations have been proven to exist using optical excitation. The Bloch oscillator device itself, which would emit tunable high-frequency radiation upon application of a DC voltage, has not yet been proven to exist to date. The reason relates to the fact, that bulk superlattices need to be doped in order to perform transport experiments, as opposed to optical excitation. The first consequence of doping is a great reduction of the electron scattering time τ , shifting the critical electric field up into regions, where miniband transport breaks down. Secondly, doped bulk superlattices are inherently instable against breakdown into high-field and low-field domains. These domains can either be localized in space [Gra91], or travelling [Sch98b], in both cases the Bloch oscillation is quenched. Travelling domains may, however, also be used as high-frequency emitters [Kas97]

3.1.3 Beyond the Esaki-Tsu model

Since the formulation of the Esaki-Tsu model, a great deal of theoretical work has been dedicated to refine it, with the goal in mind to obtain a combined theoretical description for all energy scales involved, namely the zero-field miniband width Δ , the scattering rate Γ/\hbar , and the potential drop per period $E_B = eFd$. Three distinct approaches have been used to describe transport in the parameter space spanned by (Δ, E_B, Γ) , summarized in Figure 3.3:

(A) Miniband conduction [Esa70][Leb70]

For zero electric field the appropriate basis functions are Bloch functions, and the current is numerically calculated using the stationary Boltzmann equation in the relaxation-time approximation. In this approximation the field induced localization is neglected because of

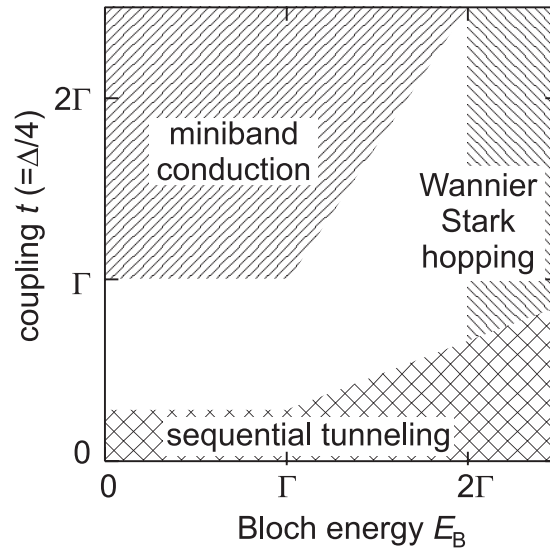


Figure 3.3: Different regimes of superlattice transport (after [Wac98b]). Miniband transport holds for $eFd \ll \Delta/2$ and $\Gamma \ll \Delta/2$; Wannier-Stark hopping holds for $\Gamma \ll eFd$; sequential tunneling holds for $\Delta/2 \ll eFd$ or $\Delta/2 \ll \Gamma$.

its inherent assumption of extended states. The Esaki-Tsu model presented above is a good approximation to the results at $T = 0$ K.

(B) Wannier-Stark hopping [Tsu75]

In the presence of an electric field, the system is best described by localized Wannier states. Scattering causes hopping between the different states, and the current is calculated using Fermi's golden rule. No broadening of the states is assumed.

(C) Sequential tunneling [Tsu73][Esa74][Cho87]

In this approximation the phase information is lost after each tunneling event between adjacent wells, scattering within a well is treated self-consistently, and transition to neighboring wells is explicitly calculated only to lowest order.

A full quantum transport theory, based on non-equilibrium Green functions, is able to treat scattering, electric field, and coupling on an equal footing, and allows an analysis of transitions between the three simplified approaches above [Wac98b][Wac00][Rot99b].

3.1.4 Experimental work

Ever since the proposal by Esaki and Tsu in 1970, the experimental study of transport through superlattices in the miniband regime has proven a difficult task. As mentioned above, for electrical transport the superlattices need to be doped, reducing the electron scattering time, and most importantly, leading to an instability of the electric field in the superlattice in the regime of negative differential velocity. Sibille *et al.* [Sib90] have performed the most extensive study in biased, doped superlattices and observed negative differential velocity only indirectly by a sub-linear current-voltage relation, and fitting by an appropriate model. Transport through undoped superlattices has been studied in a vertical three terminal device by hot electron injection into a superlattice [Rau97].

While Esaki and Tsu [Esa70] have only considered a one-dimensional superlattice, and a Fermi energy at the bottom of the miniband, soon after their paper Lebowitz and Tsu [Leb70] have extended this work to include the two free electron directions of the superlattice, and higher Fermi energies. They show that, contrary to the one-dimensional lattice, in the three-dimensional case the current persists even when the Fermi energy is the the minigap. A modulated two-dimensional system, like the SLFET, has first been considered theoretically in 1976 by Sakaki [Sak76]. He predicts the same field dependence of the velocity as the Esaki-Tsu model, the peak velocity, however, depends on the Fermi energy in such a way that it drops to 33% when increasing the Fermi energy from zero to $E_F = \Delta$. Stiles, working as a Humboldt fellow at the Technische Universität München, was first to theoretically consider three terminal devices, having of course silicon MOSFETs in mind [Sti78]. He suggested to fabricate modulated two-dimensional systems using grid-gates or silicon vicinal surfaces. These devices have subsequently been realized in GaAs MODFETs using one-dimensional metallic stripes [Ism88] and on a GaAs (001) vicinal plane [Mot89]. Negative differential resistance, however, could only be demonstrated using a two-dimensional modulation with square-grid-gate devices [Ber87b] [Ber87a] [Ism88]. The vicinal surface devices, relying on self-organization, hardly achieve regular potential modulations, while the grid-gate devices, although well defined, are limited to periods above 100 nm and weak potential modulations due to the distance between the surface-gates and the two-dimensional electron system. Modulated electron systems fabricated by cleaved-edge overgrowth by Stormer *et al.* [Sto91b] have only been characterized in equilibrium magnetotransport, possibly because they used superlattice contacts which at finite source-drain voltages cause leakage currents through the bulk superlattice. A similar device fabricated by liquid phase epitaxy exhibited

a sub-linear current-voltage relation at the first voltage sweep, which was not reproducible and linear at subsequent sweeps [Kur95].

3.2 Self consistent band structure calculation

The band structure of the $q=0$ nm SLFET can in good approximation be calculated using the one-dimensional Kronig-Penney model. This is because the potential modulation in x direction is known from the growth parameters (aluminum content and layer thicknesses), and because electronic states in x direction and z direction can be treated as separable. For the $q > 0$ nm SLFETs, however, a one-dimensional calculation is insufficient, since here the material parameters vary in x and in z direction. Additionally, from a two-dimensional calculation we can expect to learn about the minibands resulting from excited states in z direction.

We calculate the quantum-mechanical states in the SLFETs self-consistently using a computer program developed by M. Rother [Rot99a][Rot00]. The superlattice, the gate dielectric and the gate contact are modelled as grown, and the chemical potential difference between gate and two-dimensional electron gas is defined as gate voltage U_g . In Figure 3.4(a)-(d) we show the resulting electron density distribution $n(x, z)$ obtained for the four SLFETs under investigation in this chapter. The density $n(x, z)$ is obtained by summing the absolute value of the square of all occupied electron states using the Fermi distribution at $T = 300$ mK. The electrons are localized at a distance of about 10 nm from the interface to the gate barrier, and the electron density almost vanishes in the region of the superlattice barriers. To very good approximation the integrated two-dimensional electron density is described by a cosine function. The mean electron density in this calculation is $n_s \approx 1.1 \times 10^{11} \text{ cm}^{-2}$.

The calculation shows that by insertion of a (110) GaAs layer between the superlattice and the gate barrier the modulation strength of the electron gas can be varied from a relatively weakly coupled one-dimensional wire system to an almost unmodulated two-dimensional system. For $q = 0$ nm the electron density n_s almost drops to zero in the barrier region, whereas for $q > 0$ nm the electron wave function more and more penetrates the barrier regions.

While the electron density n_s was calculated based on all occupied electron states, we now concentrate on single selected electron wave functions, exemplified using the $q = 10$ nm and the $q = 20$ nm SLFETs. In Figure 3.5 we plot the probability distribution of wave functions belonging to $k_x = 0$. States (a) and (c) correspond to the lowest energy state, while (b) and (d) have a higher energy, and correspond to excited states in the z direction.

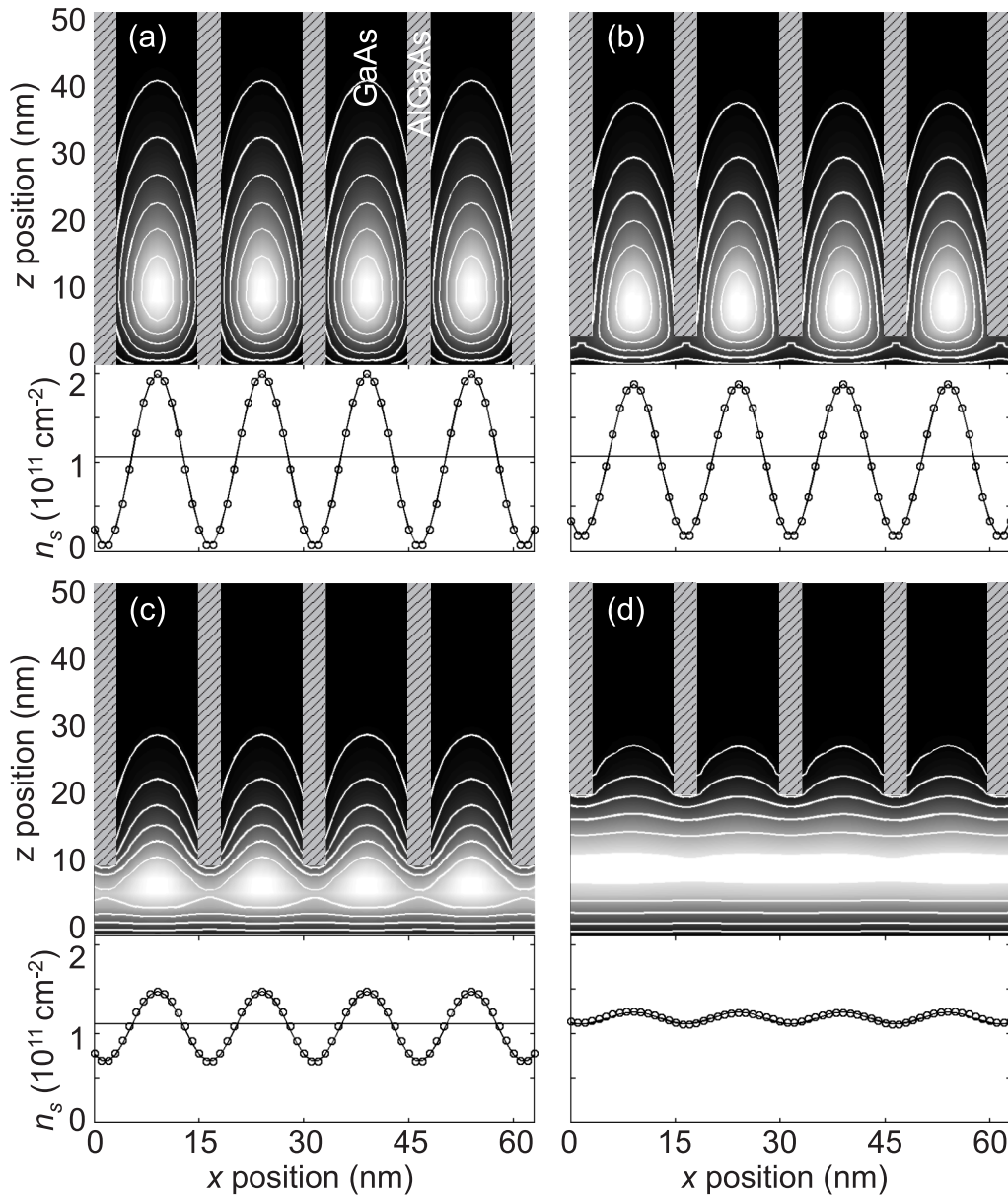


Figure 3.4: Self-consistently calculated electron density distribution for (110) GaAs layer thickness $q=0$ nm (a), 4 nm (b), 10 nm (c) and 20 nm (d). The top part of (a)-(d) shows the gray-scale coded electron density distribution in the (x, z) plane. The gate barrier is situated below the line $z = 0$. The superlattice AlGaAs barriers are hatched. The lower part of (a)-(d) shows the sheet electron density integrated over z . The circles mark the calculated density, while the solid lines are cosine function approximations. The mean two-dimensional electron density is $n_s = 1.1 \times 10^{11} \text{ cm}^{-2}$.

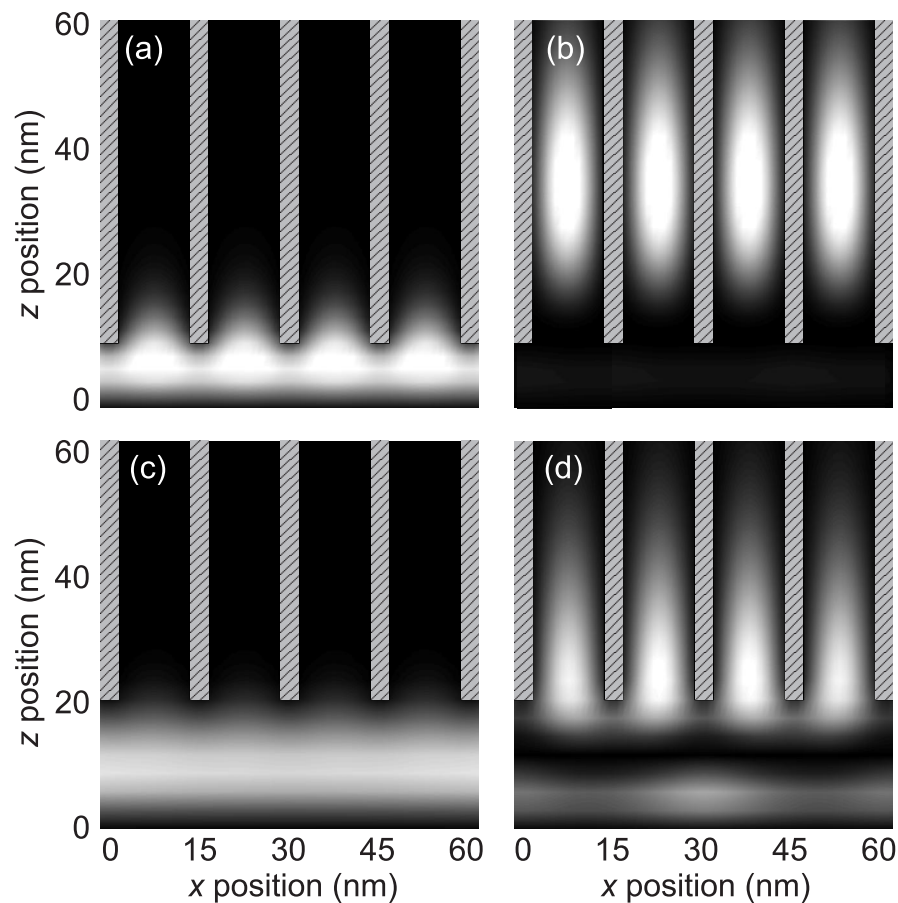


Figure 3.5: Electron wave functions for the $k_x = 0$ state, calculated for the $q = 10$ nm SLFET (a),(b) and the $q = 20$ nm SLFET (c),(d). (a) and (c) represent the ground states of the lowest miniband, (b) and (d) represent the ground state of the first excited miniband.

Two conclusions can be drawn from this observation. First, we expect minibands to emerge from both the z ground states *and* the z excited state, and both bands should have the same symmetry with respect to k_x . Second, the widths of the lower energy miniband is expected to be larger than the higher miniband width. This is because the effective potential modulation depends on the z coordinate, and lower energy electron states are located close to the gate barrier, whereas higher energy electron states are located further inside the superlattice. Thus the lower energy states feel a weaker modulation strength than the higher energy states. For the $q = 10$ nm SLFET therefore the higher miniband is expected to have approximately the same width as the lower miniband width in the $q = 0$ nm SLFET, and the higher miniband width in the $q = 20$ nm SLFET is expected to be increased owing to the decreased modulation

amplitude for the associated electron states.

Based on this reasoning we understand the band structures, calculated from the electronic states for the different SLFETs, and shown in Figure 3.6. For every SLFET the two lowest minibands are shown. As expected, with increasing (110) GaAs layer thickness q from (a) to (d), the width of the lowest band increases correspondingly, as the modulation amplitude decreases. The first excited miniband, however, is only weakly dependent on q , as the corresponding electron states are still embedded in the superlattice. The cosine fit to the data becomes progressively worse as the electron dispersion approaches the almost free GaAs band structure in (d).

The results of the band structure calculation are summarized in Figure 3.7. As the (110) GaAs layer thickness q is increased, the band width of the lowest band increases (a), and the electron density modulation amplitude decreases (b). The band widths are found to be almost independent of the electron density, the energy gap between the minibands, however, increases with increasing electron density.

3.3 Experimental results: $q=0$ nm SLFET

All experimental results in this chapter are obtained at $T = 0.8$ K by applying a voltage to one of the top contacts and draining the source-drain current I_{sd} to ground via one of the bottom contacts, while measuring the source-drain voltage across the superlattice U_{sd} using the other pair of contacts. The plotted source-drain voltage represents the measured source-drain voltage minus the voltage drop from the contacts to the two-dimensional electron system using the sheet resistance of the n+ GaAs contact layers of $\sigma = 25 \Omega/\square$.

All data is analyzed under the assumption of a linear voltage drop across the superlattice $F = U_{sd}/L$, where $L = 1.5 \mu\text{m}$. The source-drain current relates to the carrier velocity as $I_{sd} = n_s e v_m W$, where n_s is the carrier density and $W = 250 \mu\text{m}$ is the sample width. The relation between gate voltage U_g and carrier density n_s is known from the magnetoresistance measurement in Chapter 2. We recall that the top of the lowest miniband in the SLFET with no (110) GaAs layer was reached at an electron density of about $n_s = 2.2 \times 10^{11} \text{ cm}^{-2}$, corresponding to a gate voltage of $U_g = 0.42$ V.

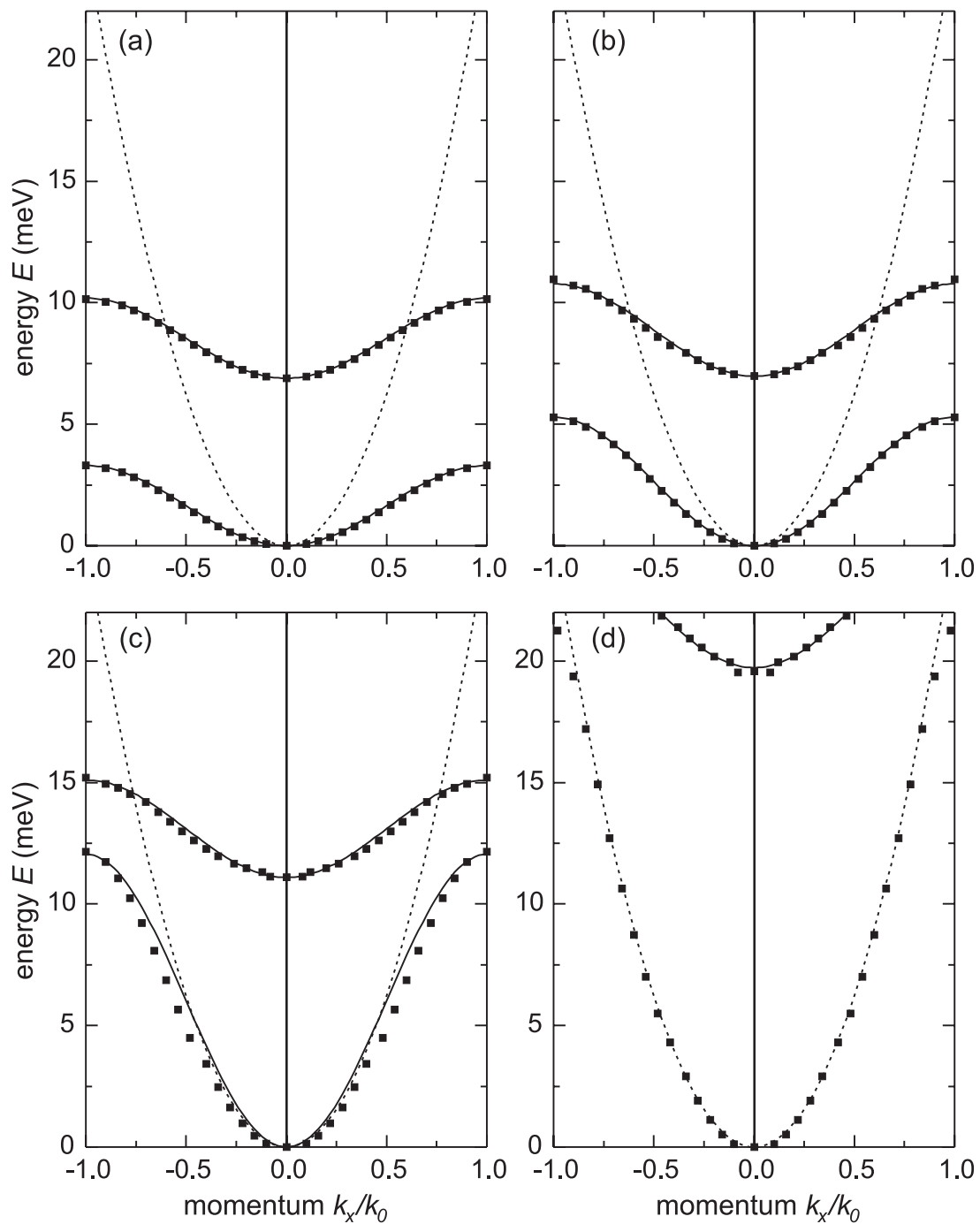


Figure 3.6: Calculated miniband structure for all four SLFETs with different (110) GaAs layer thickness q . The squares are calculated, solid lines are cosine fits to the calculated points, and the dashed lines indicate the free electron dispersion, using the free electron mass in GaAs. (a) $q=0$ nm (b) $q=4$ nm (c) $q=10$ nm (d) $q=20$ nm. The zone-folded minibands associated with the (110) ground state have a minimum energy at $k_x = \pm k_0$ beyond the energy scale of these figures.

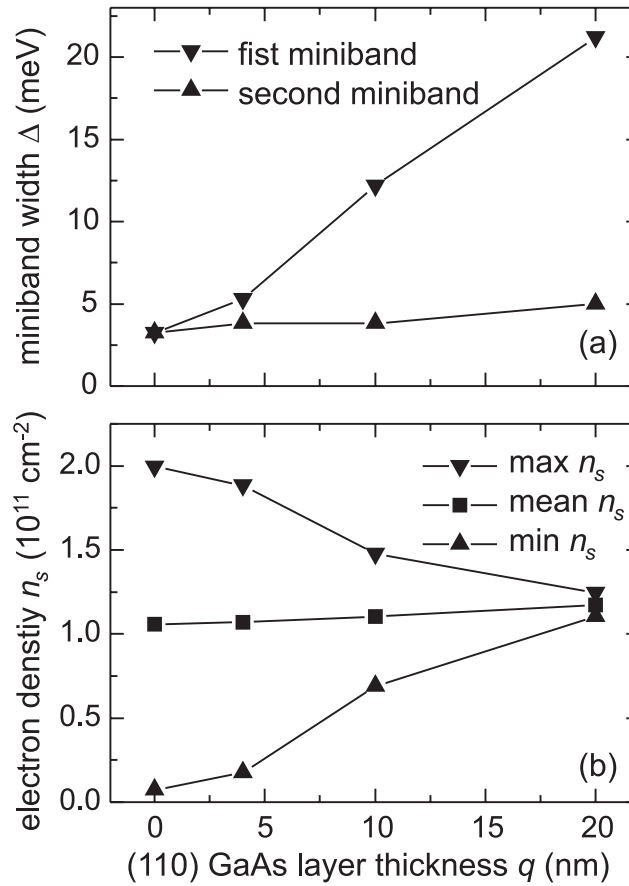


Figure 3.7: (a) Calculated miniband width and (b) electron density variation for different (110) GaAs layer thicknesses q .

3.3.1 Current-voltage relation: Overview

In Figure 3.8 the source-drain current I_{sd} is shown in dependence of the source-drain voltage U_{sd} , for gate voltages between $U_g = 0.1$ V and $U_g = 0.9$ V. At first sight several features can be seen. At small U_{sd} the current exhibits ohmic behavior, with a saturation at larger voltages. The saturation current increases roughly proportional to the gate voltage. These are features expected from a conventional MODFET [Pea90]. In the SLFET, however, at small U_{sd} additionally a region of negative differential resistance appears, followed by oscillations in I_{sd} . The peak to valley ratio increases with increasing gate voltage, and for large U_g the current undergoes a sudden drop. Below $U_g = 0.1$ V the SLFET is completely isolating, apart from a pronounced current maximum and negative differential resistance at source-

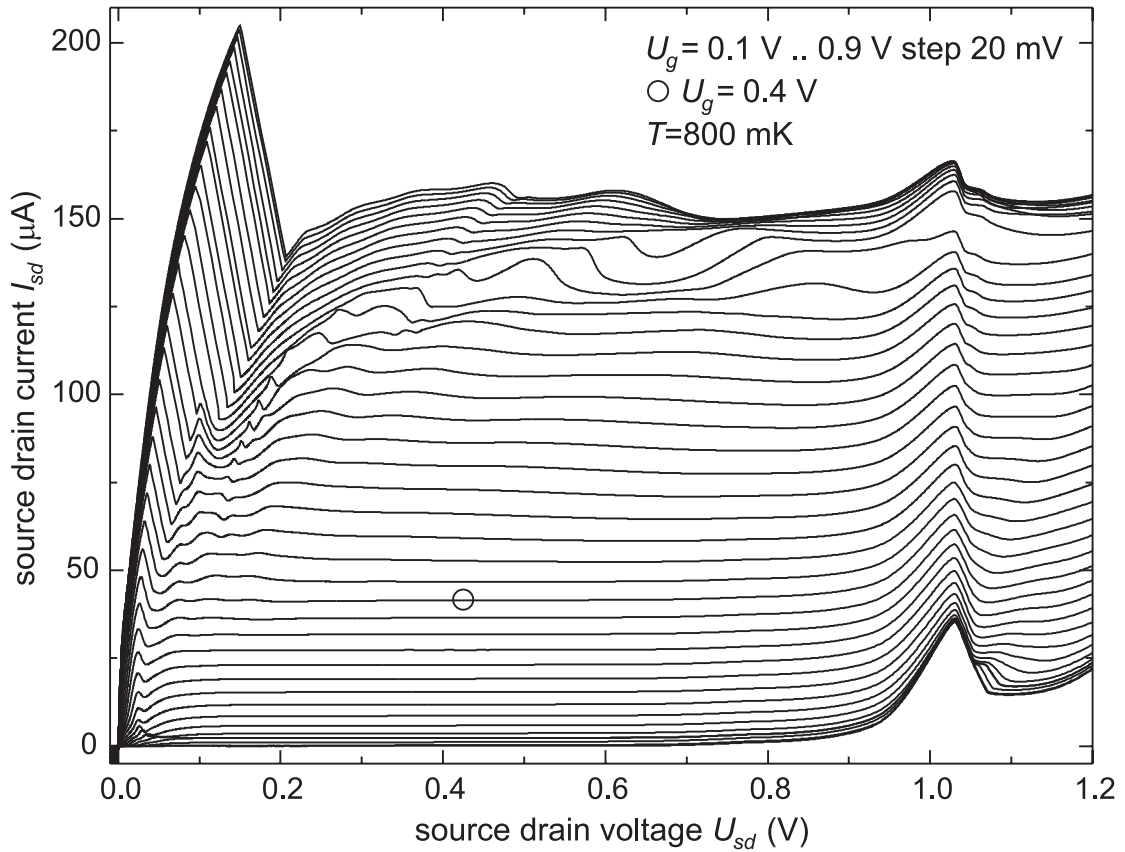


Figure 3.8: Current-voltage relation of the $q = 0$ nm SLFET.

drain voltage $U_{sd} = 1.03$ V, which seems independent of gate voltage.

In the next sections we will discuss the features appearing at small source-drain voltages in relation to the Esaki-Tsu model. The oscillatory features observed at large gate voltages may be due to hot electrons being accelerated from the first to the second miniband. The pronounced peak at $U_{sd} = 1.03$ V is due to a leakage current through the bulk superlattice away from the electron channel. At high source-drain voltages electrons are directly injected into the undoped superlattice, and are accelerated by the electric field. The sudden drop of the source-drain current in the negative differential resistance region at gate voltages above $U_g = 0.42$ V has a slope of $R = 850 \Omega$ identical to the resistance of the external leads. This artefact therefore is determined by the load line of the external circuitry and is not intrinsic to the SLFET.

In Figure 3.9(a) we take a closer look to the low-field regime of the current-voltage

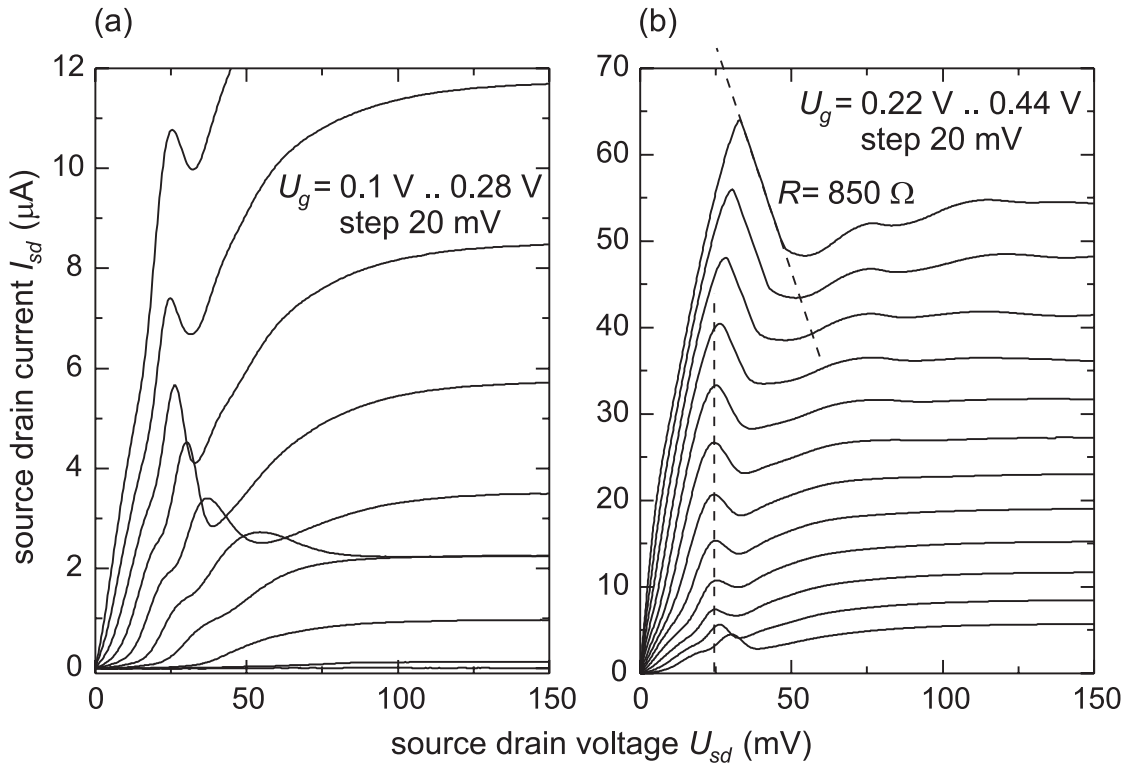


Figure 3.9: Current-voltage relation for small source-drain voltages. (a) $U_g = 0.1 \text{ V} \dots 0.28 \text{ V}$. (b) $U_g = 0.22 \text{ V} \dots 0.44 \text{ V}$.

relation. Beginning with $U_g = 100 \text{ mV}$ a finite source-drain current is observed. From $U_g = 170 \text{ mV}$, the current-voltage behavior is ohmic at zero U_{sd} , coinciding with a negative differential resistance, the peak-voltage of which shifts to $U_{sd} = 25 \text{ mV}$ for larger gate voltages. For $U_g < 0.4 \text{ V}$ the negative differential resistance peak is preceded by a kink. In Figure 3.9(b) the peak position remains constant at $U_{sd} = 25 \text{ mV}$, corresponding to a peak electric field of only $F_p = 166 \text{ V/cm}$, the lowest peak electric field reported in the literature on superlattices. For $U_g > 0.4 \text{ V}$ the peak position shifts to larger source-drain voltages, and, as mentioned above, exhibits a sudden drop, corresponding to the resistance $R = 850 \Omega$ of the external leads.

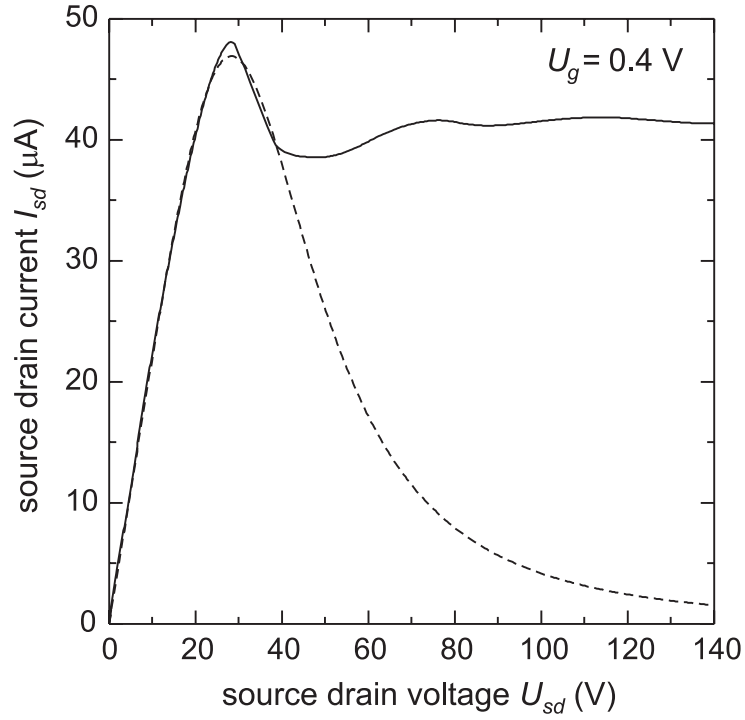


Figure 3.10: Esaki-Tsu fit to the source-drain current.

3.3.2 Comparison to the Esaki-Tsu model

In order to fit the current-voltage data, we use a phenomenological generalization of the Esaki-Tsu formula (3.6) often used in the literature [Sib89]

$$v_m = \frac{\mu F}{1 + (F/F_c)^\eta}. \quad (3.12)$$

For $\eta = 2$ naturally the original Esaki-Tsu form is retrieved, for larger η the velocity-field relation exhibits a steeper negative differential resistance slope, and for $\eta = 1$ the velocity-field relation is just saturating. We further want to make a distinction between the scattering time τ related to the low-field mobility $\mu = e\tau/m^*$ and the scattering time τ_{et} which determines the peak of the velocity-field relation

$$F_c = \frac{\hbar}{ed\tau_{et}}, \quad (3.13)$$

note that this relation does not depend on the electron effective mass m^* .

In Figure 3.10 we plot the measured source-drain current together with the fit (3.12). We find that the best fit to the data is obtained with $\eta = 4$. Using this exponent, the scattering

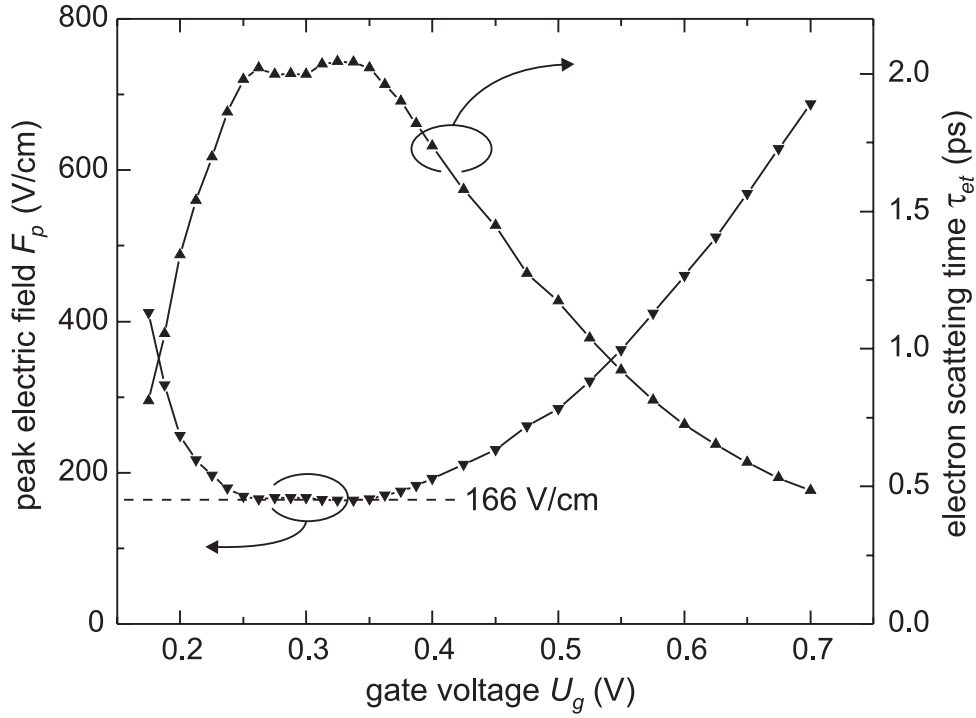


Figure 3.11: Peak electric field and electron scattering time

time τ_{et} is given by the peak electric field F_p through

$$\tau_{et} = \frac{\hbar}{edF_p\sqrt{3}}. \quad (3.14)$$

For a peak electric field of $F_p = U_p/L = 28.5 \text{ mV}/1.5\mu\text{m} = 190 \text{ V/cm}$ in this experiment we thus find $\tau_{et} = 1.8 \text{ ps}$.

We want to point out an interesting coincidence of the scattering time τ_{et} determined in the Esaki-Tsu model, and the quantum scattering time τ_q as determined from the onset of the magnetoresistance oscillations at the field B_c through $\tau_q = m_c/eB_c$, see Chapter 2. There we have found the cyclotron effective mass $m_c = 0.12m_0$ and $B_c = 0.3 \text{ T}$. The resulting quantum scattering time is $\tau_q = 2.3 \text{ ps}$. This similarity of both scattering times indicate, that the relevant scattering events for the Bloch-oscillating electrons are the ones that are phase-breaking.

In Figure 3.11 we plot the density dependence of the electron scattering time τ_{et} as evaluated from peak position of the source-drain current. For gate voltages between $U_g = 0.25 \text{ V}$ and $U_g = 0.35 \text{ V}$ the peak electric field is only $F_p = 166 \text{ V/cm}$, and the electron scattering

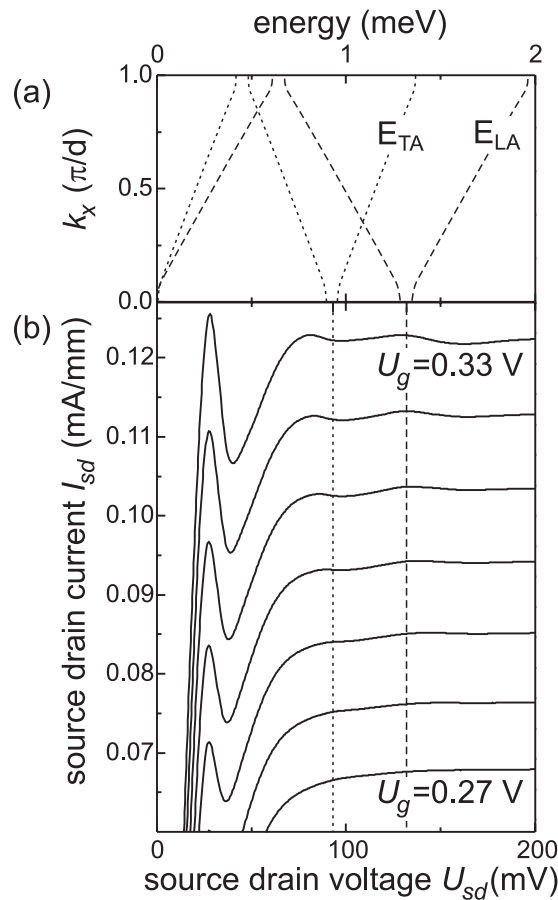


Figure 3.12: (a) Phonon dispersion relation, the minigaps are schematically drawn, (b) Bloch-phonon resonances observed in the source-drain current.

time exhibits a maximum at 2 ps. For larger gate voltages, when the Fermi energy enters the minigap, the electron scattering time decreases.

3.3.3 Bloch - phonon resonances

In this section we want to introduce a scattering mechanism that explains the increasing source-drain current beyond the negative differential resistance region, as clearly seen in Figure 3.9. In the Esaki-Tsu picture, one expects that the electrons localize more and more, once the peak electric field is reached. This localization would result in an ever decreasing macroscopic current. In the case of the SLFET, however, it seems that starting with an electric field of about $F = U_{sd}/L = 50$ mV/ $1.5 \mu\text{m}$ some scattering mechanisms takes effect, that

lifts the electron localization so that the source-drain current increases again for increasing source-drain voltage.

Our model consists of two ingredients. First, we ask about low energy electron scattering mechanisms. Conduction electron scattering may occur by acoustic waves through the deformation potential [Bar50]. Additionally, if a semiconductor crystal consists of dissimilar atoms such as in GaAs, where the bonds are partly ionic, and the unit cell does not contain a center of symmetry, as in the zincblende lattice, carriers may be scattered by longitudinal acoustic waves due to piezoelectric scattering [See88]. Second, we realize that the superlattice not only affects the electronic structure through the periodicity of the potential energy, but also the phonon energy spectrum by means of the different elastic constants of GaAs and AlGaAs. Therefore the linear acoustic phonon spectrum is folded back at Brillouin zone boundary $k_0 = \pi/d$, as shown in Figure 3.12(a). Using the TA and LA sound velocities for GaAs $v_{GaAs}^{TA} = 3.34 \times 10^5$ cm/s, $v_{GaAs}^{LA} = 4.73 \times 10^5$ cm/s and Al_{0.32}Ga_{0.68}As $v_{AlGaAs}^{TA} = 3.51 \times 10^5$ cm/s, $v_{AlGaAs}^{LA} = 4.98 \times 10^5$ cm/s [Ins93], we calculate the low-energy dispersion relation for the TA and LA phonons using the mean sound velocity in the GaAs well and AlGaAs barrier of the superlattice

$$\begin{aligned} \overline{v_{TA}} &= \frac{l_w v_{GaAs}^{TA} + l_b v_{AlGaAs}^{TA}}{l_w + l_b} = 3.38 \times 10^5 \text{ cm/s} \\ \overline{v_{LA}} &= \frac{l_w v_{GaAs}^{LA} + l_b v_{AlGaAs}^{LA}}{l_w + l_b} = 4.78 \times 10^5 \text{ cm/s.} \end{aligned} \quad (3.15)$$

The phonon energies at $k = 0$ are $E_{TA}^0 = \hbar \overline{v_{TA}} 2\pi/d = 0.93$ meV and $E_{LA}^0 = \hbar \overline{v_{LA}} 2\pi/d = 1.32$ meV. Folded phonons have been observed experimentally by raman spectroscopy [Col85], but never in transport experiments.

For electric fields $F > F_p$ the majority of the electrons are performing Bloch oscillations with Bloch energy $E_B = edF = edU_{sd}/L$. The source-drain voltage axis therefore directly corresponds to an energy axis. In Figure 3.12(b) the source-drain current exhibits maxima at energies E_{TA}^0 and E_{LA}^0 , where also the density of states of the phonon spectra have maxima. Localization due to Bloch oscillation is lifted, when Bloch oscillating electrons resonantly emit TA or LA phonons. These electrons contribute to the drift current, and the source-drain current increases. For low gate voltages when the negative differential resistance is first observed, the subsequent increase of the source-drain current coincides with the energy scale of E_{TA}^0 and E_{LA}^0 .

In Figure 3.13 we present an overview of the maxima (red) and minima (blue) of the source-drain current in the (U_{sd}, U_g) parameter space. The $I_{sd}(U_{sd}, U_g)$ data was processed

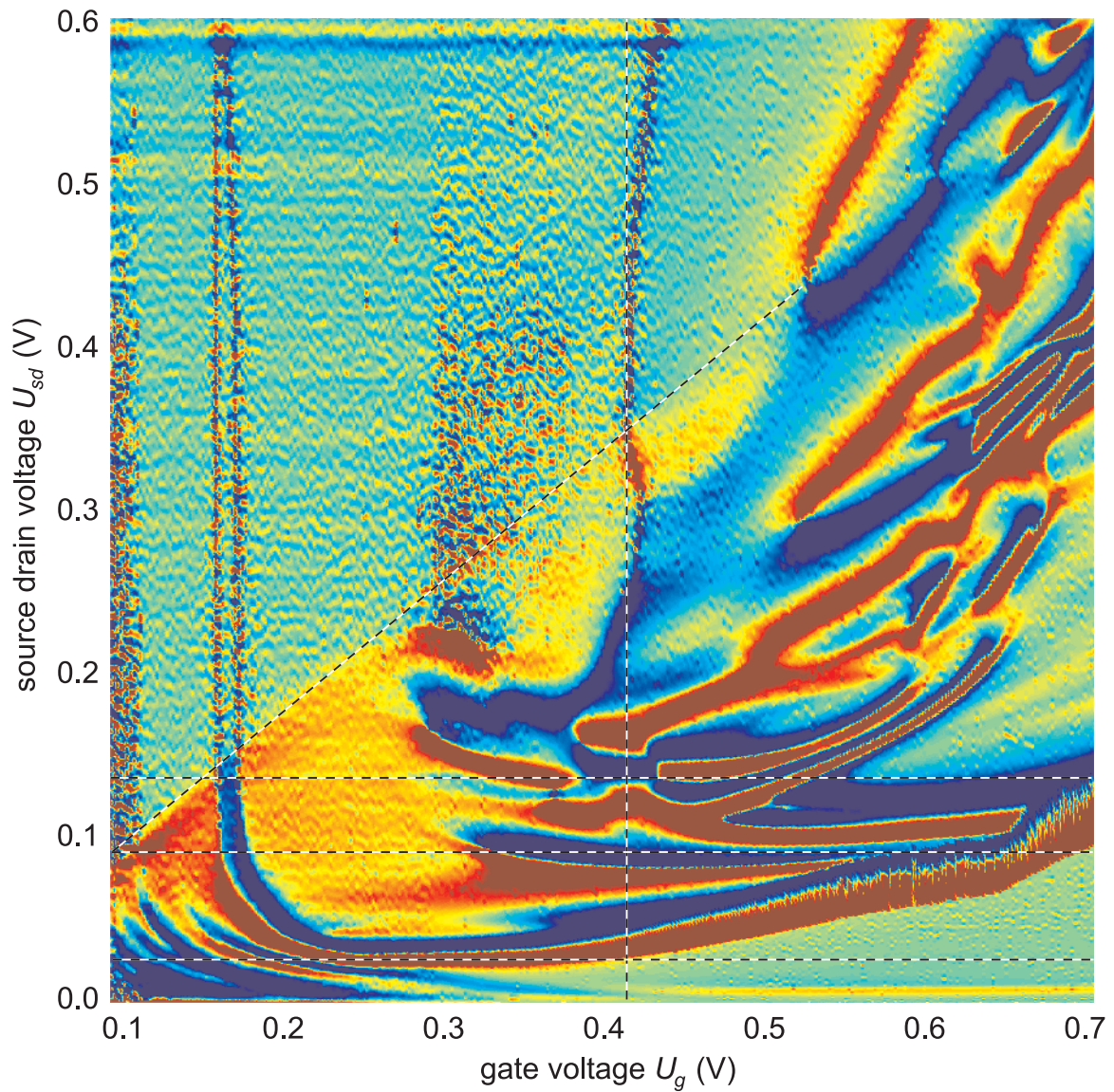


Figure 3.13: Color-scale coded source-drain current maxima (red) and minima (blue) in the (U_{sd}, U_g) plane.

to obtain a value V

$$V = -\frac{\partial^2 I_{sd} / \partial U_{sd}^2}{|\partial I_{sd} / \partial U_{sd}|} \quad (3.16)$$

which is large at extremal points if I_{sd} by means of the vanishing first derivative, the second derivative then determines the sign of the extremum. The horizontal dashed line at $U_{sd} = 25$ mV represents the negative differential resistance peak. Energies E_{TA}^0 and E_{LA}^0

are indicated by the horizontal dashed lines at $U_{sd} = 93$ mV and $U_{sd} = 132$ mV for the Bloch-phonon resonances. The diagonal dashed line indicates the SLFET pinch-off point. The electron density dependence of the resonances is not explained by our model, neither is the complicated resonance structure for gate voltages $U_g > 0.42$ V, indicated by the vertical dashed line, corresponding to Fermi energies in the minigap. We point out the symmetry in the resonance structure with respect to this gate voltage, which is strikingly close to the gate voltage marking a filling of the lowest miniband.

3.4 Experimental results: All SLFETs

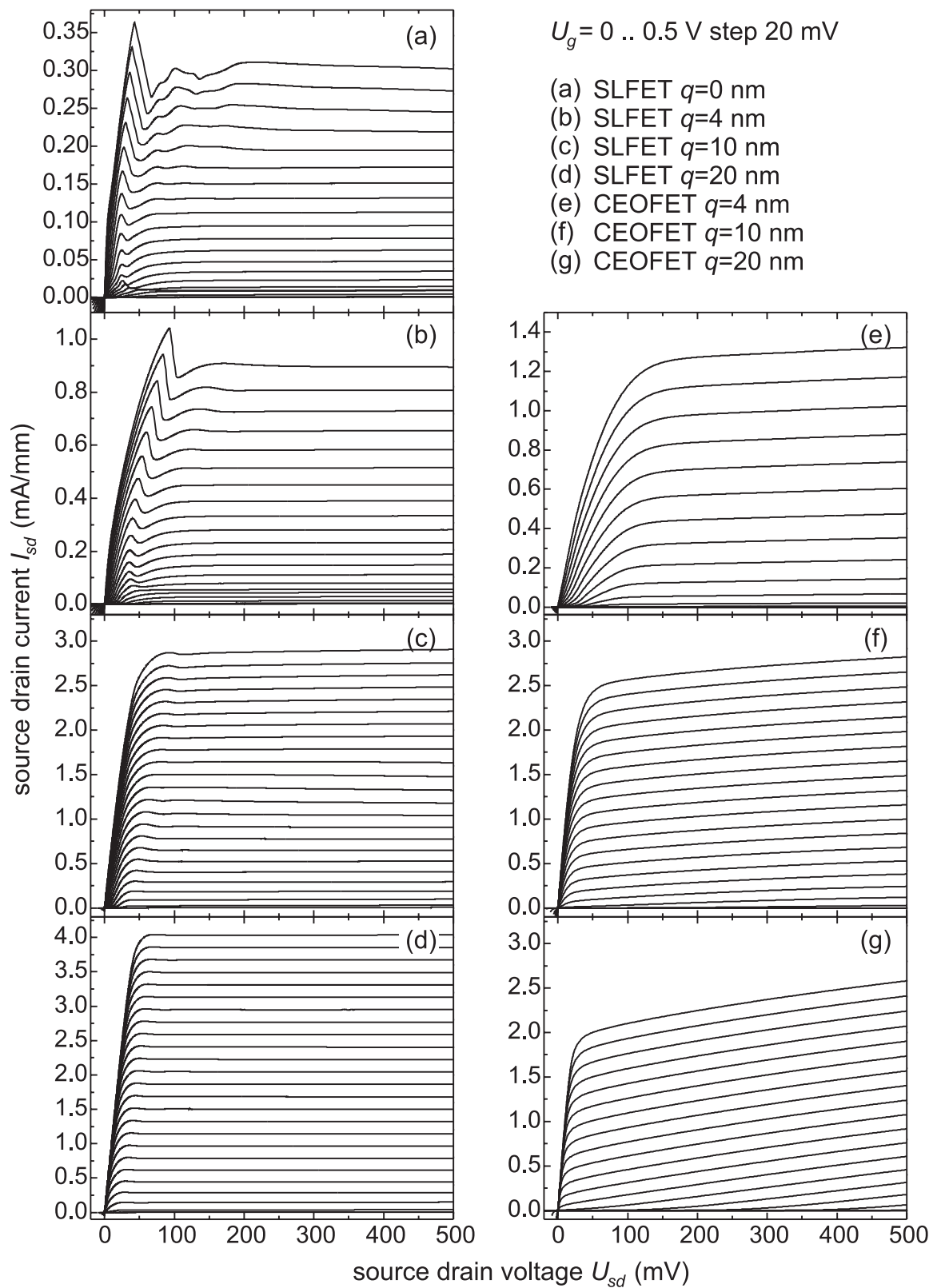
In this section we systematically study the influence of the miniband width on the physical properties of the SLFET. Four SLFETs and three reference CEOFETs with the following parameters are investigated at $T = 0.8$ K.

type	q (nm)	Δ (meV)	L (μm)
SLFET	0	3.3	1.5
SLFET	4	5.2	3
SLFET	10	12.2	3
SLFET	20	21.2	3
CEOFET	4	-	1.5
CEOFET	10	-	1.5
CEOFET	20	-	1.5

In the reference samples the superlattice has been replaced by an $\text{Al}_x\text{Ga}_{1-x}\text{As}$ layer with aluminum content $x = 6.7\%$ equal to the mean aluminum content in the superlattice. The reference samples are therefore vertical field effect transistors, we call them CEOFETs.

3.4.1 Current-voltage relation of SLFETs and CEOFETs

In Figure 3.14(a)-(g) the current-voltage relation of all samples is summarized. As the miniband width is increased from (a) to (d), the strength of the negative differential resistance decreases, the peak current and saturation current increases. We note that even the SLFET (d) with only very weakly modulated two-dimensional electron system, exhibits negative



R. A. Deuschmann *Two dimensional electron systems in atomically precise periodic potentials* (2001)
 Ph.D. Dissertation. Selected Topics of Semiconductor Physics and Technology, ISBN 3-527-40421-1

differential resistance. The $q = 0$ nm SLFET in (a) is identical to the SLFET presented in the first section of this chapter. The traces of the reference samples are shown on the right side of Figure 3.14 from (e) to (g). As can be seen, none of the CEOFETs exhibits negative differential resistance, and the saturation region is less flat. The saturation current from (e) to (f) increases, but decreases from (f) to (g). If corresponding SLFETs and CEOFETs are compared, it appears that the saturation current for the $q = 4$ nm devices is larger in the CEOFET, while it is smaller for the $q = 10$ nm and $q = 20$ nm CEOFET.

3.4.2 Peak current and transconductance

In Figure 3.15(a) we plot the peak current I_p in dependence of the gate voltage U_g for all four SLFETs. For the $q = 0$ nm SLFET the $I_p(U_g)$ relationship is super-linear for $U_g < 0.5$ V and sub-linear for larger gate voltages. This is not in agreement with calculations by Sakaki [Sak76], that predict a decreasing peak electron velocity v_p when increasing the electron density n_s , and thus a sub-linear increase of the peak current $I_p = n_s e v_p$. It must be borne in mind that these calculations were performed in the Esaki-Tsu model using a constant electron scattering time, and a more rigorous treatment is necessary for quantitative agreement. For larger miniband widths the peak-current to gate voltage relation is more and more linear, indicating that the linearly increasing electron density is responsible. From this representation of the data it can be seen, that the predicted increasing peak-current with increasing miniband width relation (3.10) is qualitatively reproduced.

In Figure 3.15(b) we plot the transconductance g_m

$$g_m = \left. \frac{\partial I_{sd}(U_{sd}, U_g)}{\partial U_g} \right|_{U_{sd}} \quad (3.17)$$

evaluated for a source-drain voltage $U_{sd} = 0.4$ V in the saturation regime. A logarithmic scale is used to make visible the small features for the $q = 0$ nm and the $q = 4$ nm SLFETs. In these devices the transconductance exhibits a small maximum for gate voltages below $U_g = 0.18$ V. This corresponds to the electron density region where no negative differential resistance is observed. For larger gate voltages g_m increases non-linearly. The sharp features above $U_g = 0.6$ V may be due to electrons being accelerated into the second miniband, as already mentioned in Section 3.3.1. Both SLFETs $q = 10$ nm and $q = 20$ nm exhibit a constant transconductance for $U_g > 0.1$ V. The independence of I_{sd} on U_{sd} in these devices is a sign for velocity saturation of the electrons in the channel.

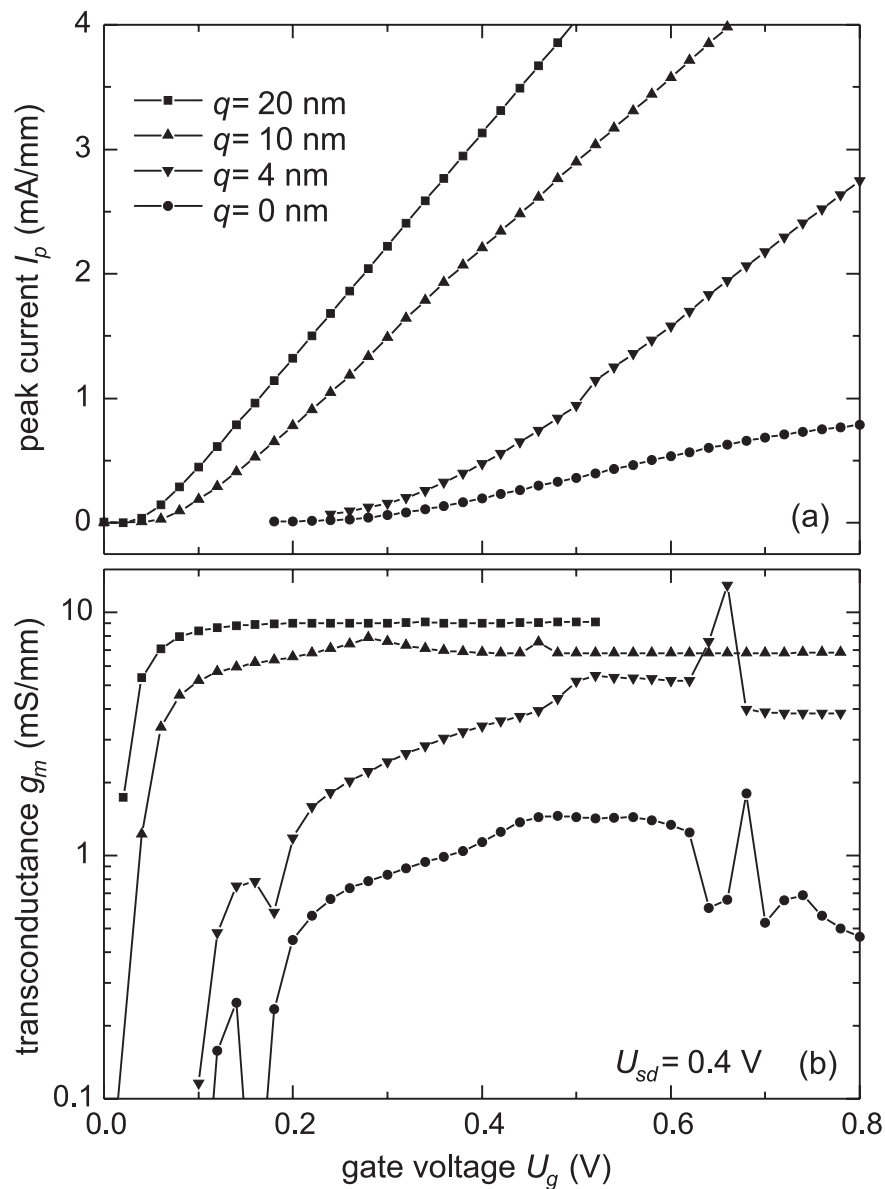


Figure 3.15: (a) Peak current and (b) transconductance. The lines are plotted as guide for the eye.

In Figure 3.16(a) we plot the peak current I_p versus the calculated miniband width for different electron densities n_s . The relation between gate voltage and electron density has separately been determined by evaluation of magnetoresistance data. As can be seen, the peak current I_p linearly increases with miniband width Δ for the SLFETs with $q = 0$ nm, $q =$

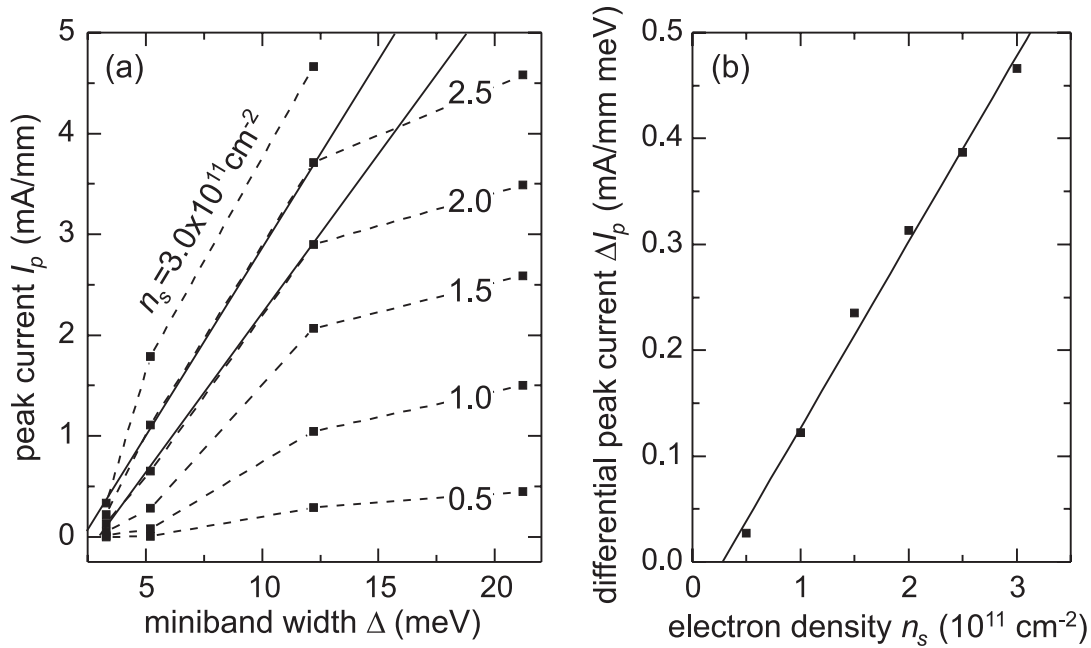


Figure 3.16: (a) Peak current versus miniband width for different electron densities. (b) Differential peak current versus electron density.

4 nm and $q = 10$ nm. Additionally the increase is stronger for large electron densities. This confirms the Esaki-Tsu result (3.10) predicting a linear relationship between peak velocity v_p and miniband width Δ . In Figure 3.16(b) we plot the differential peak current $\Delta I_p = \partial I_p / \partial \Delta$, obtained from the linear fit in (a). ΔI_p is the peak current normalized by the miniband width, and should increase linearly with electron density because $I_p = n_s e v_p$. As can be seen, this linearity is well confirmed by the experimental data.

In this discussion we have disregarded the data obtained from the $q = 20$ nm SLFET. As can be seen in Figure 3.16(a) the peak current in this device does not increase with the miniband width as strong as expected. The reason lies in the SLFET sample geometry, in which a potential barrier exists between the n+ GaAs contact layers and the two-dimensional electron gas for thick (110) GaAs layers ($q \geq 20$ nm), acting as an additional series resistor. This effect is also observed in the CEOFET reference sample when comparing the $q = 10$ nm and the $q = 20$ nm devices. In the latter the saturation current is even smaller than in the former. A more detailed discussion of this matter is given in Section 3.6 on the ultra-short channel CEOFETs.

3.4.3 Ruling out other mechanisms for negative differential resistance

In the following we discuss and rule out other possible reasons besides Bloch localization that could theoretically lead to NDR.

- (I) *Inter-subband scattering* might occur since U_p is comparable to the subband separation, and for $q > 10$ nm the subbands even overlap. For $q > 0$ nm Δ_2 is always smaller than Δ_1 and due to the heavier electron mass in the upper band, NDR could be expected. However, this picture is not applicable to the $q = 0$ nm case, where both subbands have the same width and mass, and the mobility in the higher subband will even be larger due to the larger distance of the electrons from the interface. Therefore the NDR of this sample cannot be explained by inter-subband scattering. Additionally, the strength of the NDR decreases with increasing q , even though the difference in effective mass of both subbands increases, which also rules out such an explanation for the NDR.
- (II) *Intervalley scattering* can be excluded because the energy separation between the Γ and L minima in GaAs is much larger than the energy even of ballistic electrons at U_p .
- (III) *Real space transfer* across the gate barrier can be ruled out because the gate current is orders of magnitude smaller than the source-drain current.
- (IV) *Breakdown of the electric field* in NDR devices into high field and low field domains may be a major obstacle for operating bulk SL devices beyond U_p . In our SLFETs, however, no sudden jumps in the current at voltages $U_{sd} > U_p$ are observed. Additionally both sweep directions yield identical traces (no hysteresis), almost identical traces are also obtained for both current directions and even from different samples. Sudden jumps observed only at high current levels in the $q = 0$ nm and $q = 4$ nm SLFETs are solely due to the external load resistance. We are therefore certain that no sudden breakdown of the electric field occurs in our SLFETs. Reasons why the charge distribution in our devices is stabilized even at the presence of NDR are discussed in the next Section 3.4.4.
- (V) We can rule out NDR due to *breakdown of the miniband picture* and sequential resonant tunneling because even for the narrowest miniband width of $\Delta_1 = 3.3$ meV the localization length $\lambda = \Delta L / eU_p$ at the NDR is more than 13 periods of the SL.

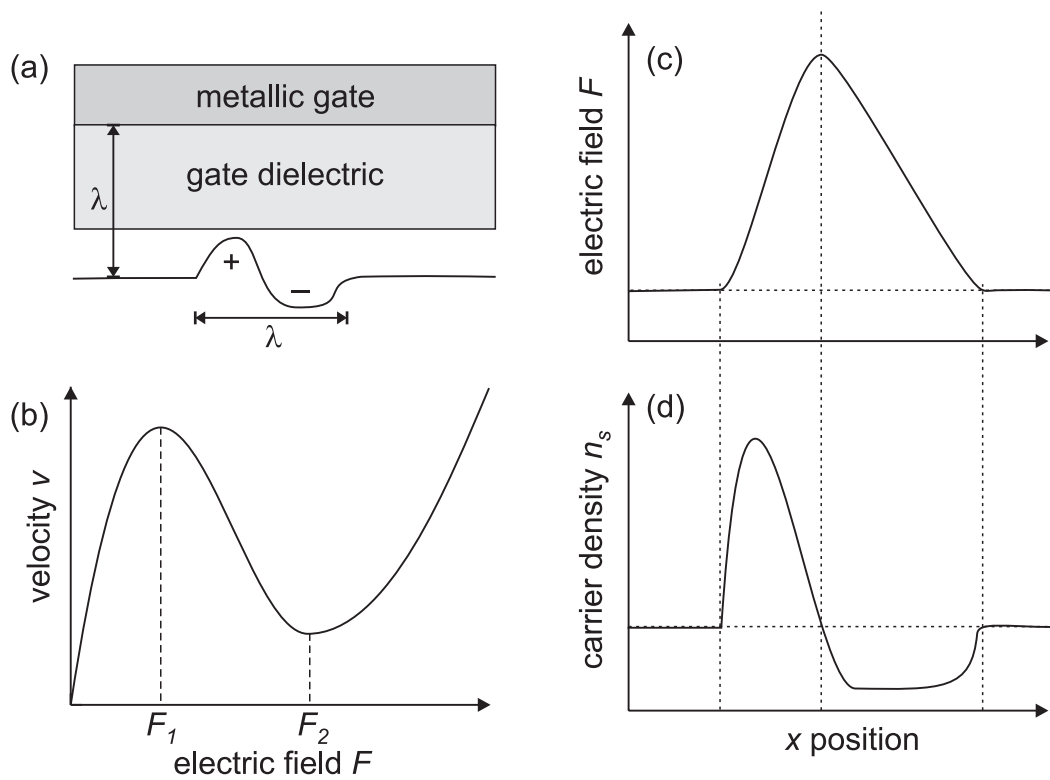


Figure 3.17: Charge instability and charge stabilization at the presence of NDR. (a) In a gated device charge instabilities are damped with a damping length λ similar to the distance between the metallic plane and the carrier system. (b) Velocity-field relation exhibiting NDR between the field F_1 and F_2 . (c) Electric field distribution with high-field domain. (d) Charge inhomogeneity that will grow over time due to the NDR.

3.4.4 Stabilization of the charge distribution

The physics of instabilities in solid state materials with mobile charge carriers and non-linear velocity-field relation has been an active field of research, for example for understanding Gunn oscillations, and, very recently, static and travelling domains in semiconductor superlattices [Mou01]. Here we merely want to point out the basic origin of an instability in a carrier system exhibiting negative differential resistance, and we qualitatively discuss reasons why in a low-dimensional superlattice, such as the SLFET, instabilities can be suppressed. An excellent theoretical text book about the physics of instabilities in solid state electron devices is [Sha92]. Recent articles about dynamic properties of superlattices can be found

in the book edited by Schöll, see especially the treatment by A. Wacker [Wac98a]. We point out that low-dimensional systems, such as the SLFET, have much less been investigated in this context to date.

We illustrate the consequences of a small charge inhomogeneity, as shown in Figure 3.17 (d), in a device that exhibits negative differential velocity (b), assuming positively charged free carriers. If the device is biased such that the electric field outside the instability is in the ohmic regime (c), the peak electric field, however, is between F_1 and F_2 , then the charge instability will grow over time. This happens because the higher upstream field in the center of the domain results in carriers moving more slowly than those at the edges, where the field is lower. Charge will therefore deplete on the right (leading) edge of the domain, and accumulate at the left (trailing) edge. This charge will add to what is already there, increasing the field in the domain. If the device is part of a resistive circuit, the increasing voltage across the domain will decrease the current in the circuit and lower the field outside the domain. In the case of a mobile domain, this process will continue until the domain velocity is equal to the velocity of the carriers outside of the domain, or the domain reaches the end of the device, at which instant a new domain may form, resulting in a periodic current oscillation [Gun64].

A full fledged analysis of mobile carriers with non-ohmic velocity-field relation may be obtained based on the continuity equation and Poisson's equation, or with more detailed models using the non-equilibrium Green function formalism, as well as semiclassical Boltzmann or balance equations supplemented by Monte Carlo simulations. Here we merely want to point out qualitatively reasons, why by means of a reduced dimensionality of the problem, the charge distribution in our devices is stabilized even at the presence of NDR, all related to electrostatic screening. First, as schematically shown in Figure 3.17(a), the presence of a metallic sheet close by the carrier system electrostatically prevents any major charge accumulation over length-scales larger than the distance between the gate and the carrier system. Second, in a two-dimensional electron system a possible charge accumulation is one-dimensional, and its resulting electric field decays inversely proportional with distance, while in bulk superlattices the field caused by a *plane* charge is independent of the distance. Third, the damping length in a system of mobile carriers decreases with increasing carrier density. As the local carrier density in the SLFETs is higher than in normal undoped or weakly doped bulk superlattices, possible instabilities will be damped on shorter length scales. Fourth, charge inhomogeneities are thought to preferentially occur at doping fluctuations. Since the SLFET devices are undoped, this source of charge inhomogeneity is to a

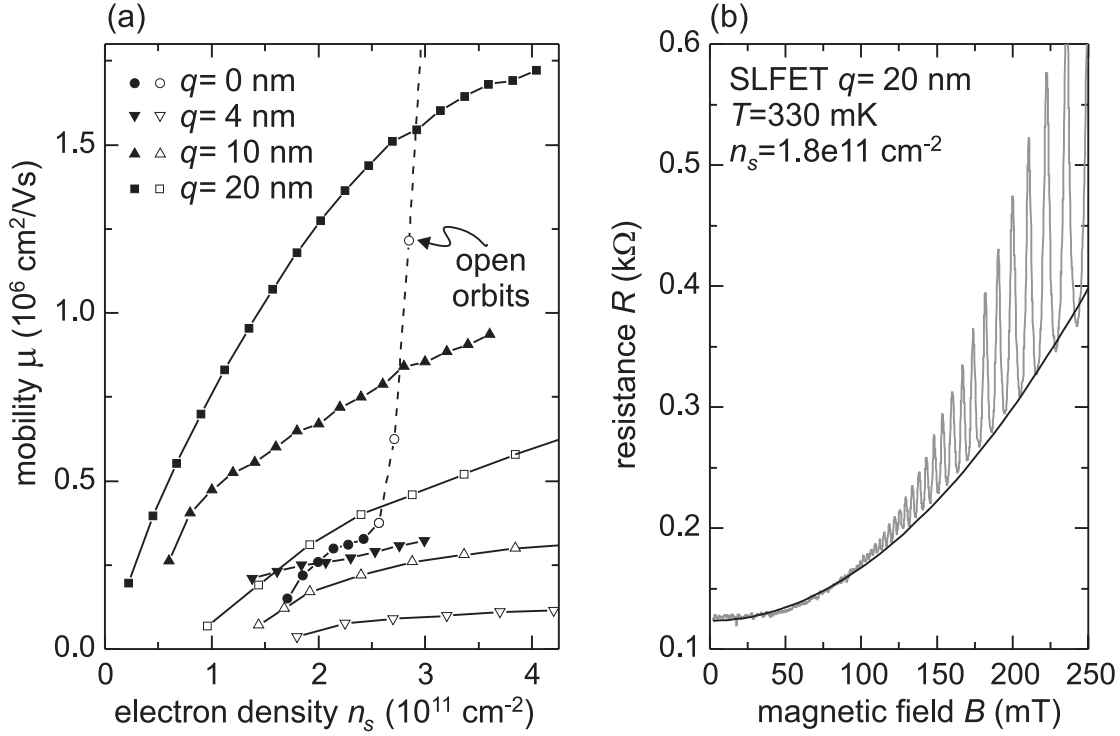


Figure 3.18: (a) Electron mobility determined from the low-field magnetoresistance. Solid symbols: SLFET, hollow symbols: reference CEOFET. Hollow circle: regime of open electron orbits in the $q = 0 \text{ nm}$ SLFET. (b) Example of the low-field magnetoresistance of the $q = 20 \text{ nm}$ SLFET. The black line represents the fit to the low-field resistance, the measurement is shown in gray.

large extent suppressed.

3.4.5 Electron mobility

Rather than determining the electron mobility from the zero-field resistance, which is bound to contain unknown series resistances R_s , we extract the electron mobility from the low-field magnetoresistance. We use the result for the measured magnetoresistance derived in Section 2.3.5, and rewrite Equation (2.48) for the classical regime $\omega_c \tau < 1$

$$R = \frac{1 + (\mu B)^2}{\sigma_0(W/L + \mu B)} + R_s. \quad (3.18)$$

For the SLFET samples the width to length ratio W/L is much larger than 1, and $\sigma_0 = n_s e \mu$, therefore the low-field magnetoresistance is given by

$$R \approx \text{const} + \frac{L}{W} \frac{\mu}{n_s e} B^2, \quad (3.19)$$

from which the mobility μ can be extracted directly using the known sample geometry and electron density n_s . The same procedure has previously been used by Tsui and coworkers [Maj00] for similar samples.

In Figure 3.18(b) we show an example of the low-field resistance for one of the SLFETs, in this case the $q = 20$ nm device. The magnetoresistance increases quadratically with increasing magnetic field, as predicted by Equation 3.19. The magnetoresistance oscillations commence at a field of about $B = 100$ mT, thus the best fit is taken between $B = 0$ T and $B = 100$ mT in this case. In Figure 3.18(a) the resulting electron mobility is displayed for all SLFETs, in dependence of the electron density n_s . In the low density regime, the mobility is almost proportional to the electron density, indicating that the mobility is limited by background impurity scattering [And82]. For higher densities, the increase in mobility starts to saturate, suggesting a contribution from interface-roughness scattering. The dependence of the mobility determined by interface roughness μ_{it} on electron density n_s is $\mu_{it} \propto n_s^{-2}$ [And82] [Wei91a]. Similar electron mobilities as determined for the $q = 20$ nm SLFET have been found in back-gated undoped (001) heterostructures [Hir98]. The strong increase in mobility for increasing (110) GaAs layer thickness q is consistent with a decreasing electron mass for increasing miniband widths, and a decreasing influence of surface-roughness scattering. The hollow circles in Figure 3.18(a) are not to be taken as real mobilities. For electron densities $n_s > 2.3 \times 10^{11} \text{ cm}^{-2}$ open electron orbits prevail in the $q = 0$ nm SLFET, which results in a strong quadratic increase of the low-field magnetoresistance (see Chapter 2). In this regime our evaluation of the electron mobility is not valid any more.

Reference CEOFETs are shown in hollow symbols. Their mobilities are significantly smaller than the mobilities obtained for the SLFETs. Since samples with the same (110) GaAs layer thickness have been overgrown in the same run on the same sample holder, differences in growth conditions can be excluded as an explanation. A possible reason for the high mobilities obtained with the SLFETs may be that the growth kinetics is favorable on a substrate that consists of alternating layers of GaAs and AlGaAs, as is the case with the SLFET superlattice substrates, and not with the reference sample substrates. Alloy scattering in the substrate AlGaAs should be comparable between SLFET and reference sample since the Al content for both is the same. The high mobilities obtained with the SLFET samples

make them ideal candidates for electron density dependent investigations in the fractional quantum Hall regime, as will be demonstrated in Chapter 6.

3.5 Transport in magnetic field

Non-equilibrium transport through SLFETs in magnetic fields can principally be studied in three different magnetic field orientations. In bulk SLs the two orientations parallel to the SL layers are equivalent, whereas in SLFETs all three magnetic field orientations are different. In this section we concentrate on crossed electric and magnetic fields, where the magnetic field is applied in z direction perpendicular to the 2DES. We demonstrate current-voltage traces in dependence of magnetic field strength, with a focus on the behavior of the negative differential resistance peak. All data are obtained on the $q = 0$ nm SLFET, which exhibits the strongest negative differential resistance peak. In a brief theory section we take on two different perspectives to interpret the results.

3.5.1 Experiment

In Figure 3.19 we show the evolution of the current-voltage relation in the $q = 0$ nm SLFET when the perpendicular magnetic field is increased from zero to $B = 14$ T. The negative differential resistance peak rapidly disappears, the low-field ohmic resistance increases, and the saturation current increases, until the saturation is quenched due to the high ohmic resistance. As can be seen in the enlargement in Figure 3.19(b), the negative differential resistance peak does not exhibit a pronounced shift, but merely quenches at about $B = 1$ T.

At gate voltage above about $U_g = 0.3$ V a very different behavior is observed. In Figure 3.20 we show data obtained for $U_g = 0.4$ V. The negative differential resistance peak does not quench with increasing magnetic field, it rather shifts to larger source-drain voltages. Peak positions are marked by downward pointing triangles. Additionally, the peak current first decreases, has a minimum at about $B = 1$ T, and subsequently increases. As before, the saturation current increases with increasing magnetic field, and the low-field ohmic resistance increases.

We summarize the peak voltages and peak currents obtained for gate voltages between $U_g = 0.3$ V and $U_g = 0.5$ V in Figure 3.21. In Figure 3.21(a) the peak voltage positions U_p versus magnetic field B are fitted by the quadratic function

$$U_p(B) = U_p^0 + c_p B^2, \quad (3.20)$$

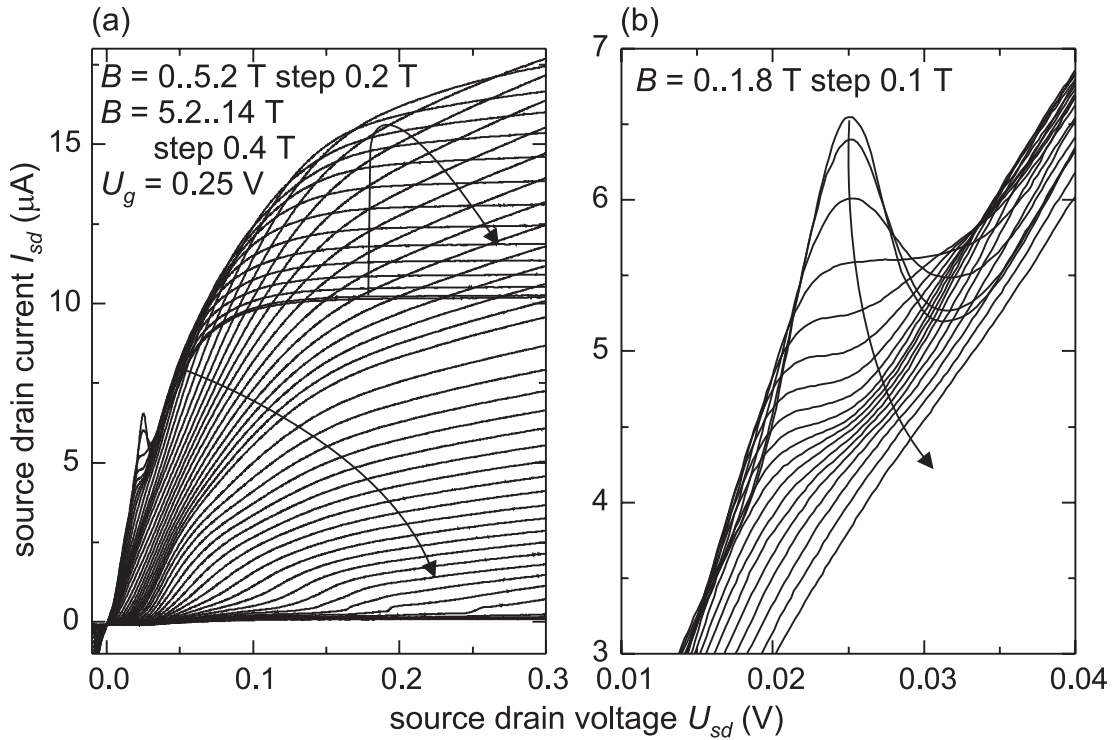


Figure 3.19: (a) Current-voltage relation for the $q = 0$ nm SLFET at a gate voltage of $U_g = 0.25$ V, obtained in perpendicular magnetic fields between 0 and 14 T. (b) The negative differential resistance peak is quenched when increasing the magnetic field from zero to above 1 T.

where U_p^0 is the peak voltage at zero magnetic field, and c_p is the fit parameter. As can be seen, the data is well approximated by this quadratic dependence on the magnetic field, no linear term is required. In the inset the value of the fit parameter c_p is plotted vs. gate voltage. At a gate voltage of $U_g = 0.35$ V, for example, $c_p = 0.031 \text{ V/T}^2$. In Figure 3.21(b) the peak current I_p is plotted against magnetic field for different gate voltages. The peak current at zero magnetic field I_p^0 has been subtracted to plot the data on the same axis. The peak current exhibits a minimum at magnetic fields of about $B = 1$ T. The increase of I_p corresponds to the increase in the saturation current observed in the current-voltage data.

3.5.2 Theory: Miniband transport

In this section we derive the magnetic-field dependent current-voltage relation in a simple, semiclassical miniband picture. When an electric field $F \parallel \hat{x}$ and a magnetic field $B \parallel \hat{z}$ are to

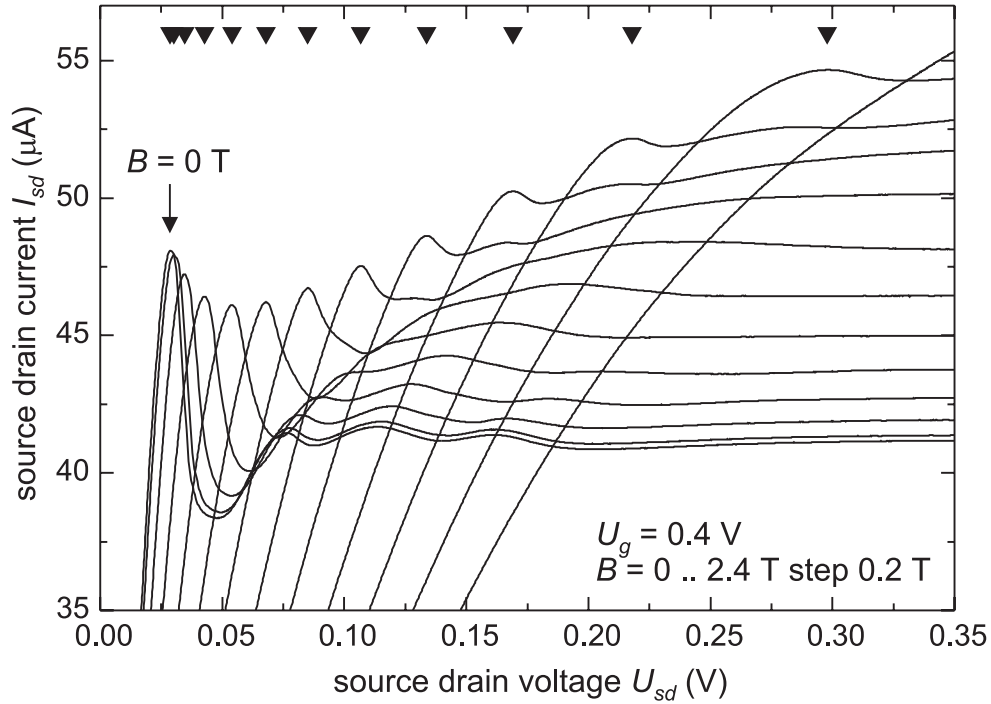


Figure 3.20: Current-voltage relation for $U_g = 0.4$ V for magnetic fields between $B = 0$ T and $B = 2.4$ T. Negative differential resistance peak positions are marked by downward pointing triangles.

be considered, the one-dimensional Esaki-Tsu model obviously has to be extended to more spatial dimensions in order to take into account electron motion perpendicular to F and B due to the Lorentz force, which couples the miniband motion to motion in the free \hat{y} direction. Using the dispersion relation

$$E(x, y) = \frac{\Delta}{2}(1 - \cos(k_x d)) + \frac{\hbar^2 k_y^2}{2m^*} \quad (3.21)$$

the equations of motion are

$$\begin{aligned} \frac{dk_x}{dt} &= -\frac{e}{\hbar}(F + v_y B), & \frac{dk_y}{dt} &= \frac{e}{\hbar}v_x B, & \frac{dk_z}{dt} &= 0 \\ v_x &= v_m \sin(k_x d), & v_y &= \frac{\hbar k_y}{m^*}, & v_z &= \frac{\hbar k_z}{m^*}. \end{aligned} \quad (3.22)$$

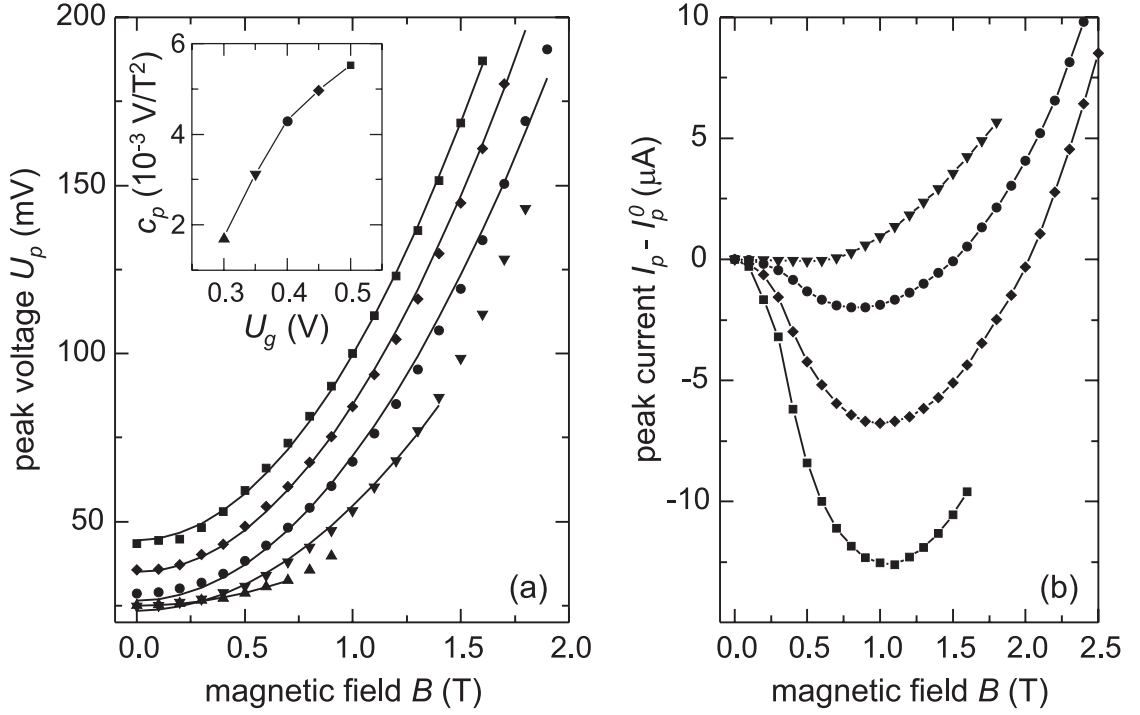


Figure 3.21: (a) Peak voltage U_p versus magnetic field B evaluated for gate voltages between $U_g = 0.3$ V and $U_g = 0.5$ V. Solid symbols are experimental values, the solid line is the best quadratic fit to the data. The inset shows the quadratic fit parameter c_p in dependence of the gate voltage. The shape of the symbols defines the gate voltages in the main plot. (b) Peak current I_p versus magnetic field for the gate voltages defined in the inset of (a). The solid lines are drawn to guide the eye.

where $v_m = \Delta d / (2\hbar)$ is the drift velocity at zero magnetic field. The resulting coupled differential equations

$$\frac{dk_x}{dt} = -\frac{e}{\hbar} \left(F + \frac{\hbar k_y}{m^*} B \right) \quad (3.23)$$

$$\frac{dk_y}{dt} = \frac{e}{\hbar} v_m B \sin(k_x d) \quad (3.24)$$

are solved by numerical integration. The mean drift velocity is then obtained by

$$\langle v_x(F, B) \rangle = \frac{v_m}{\tau} \int_0^\infty \exp(-t/\tau) \sin(k_x(F, B)d) dt \quad (3.25)$$

and displayed for different magnetic fields in Figure 3.22. Parameters used for this calculation are: superlattice period $d = 15$ nm, electron scattering time $\tau = 1$ ps, critical electric

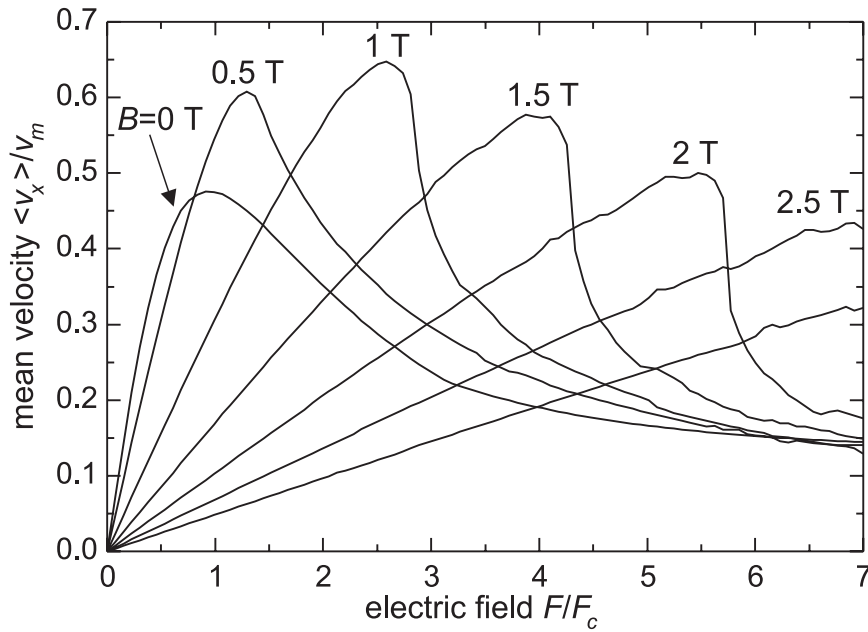


Figure 3.22: Mean electron velocity vs. electric field calculated for different magnetic field strengths using an extended Esaki-Tsu model.

field at zero magnetic field $F_c = 4.4 \times 10^4$ V/m, and drift velocity at zero magnetic field $v_m = 3.4 \times 10^4$ m/s.

As shown in Figure 3.23, in this model the peak velocity first increases, then decreases, and its position linearly shifts to larger electric fields for increasing magnetic field strength above a magnetic field of about $B = 0.3$ T. The fact that the peak electric field increases with magnetic field strength is consistent with the experimental data, the functional dependence, however, is linear in this model, but quadratic in the experiment. Additionally, the behavior of the peak current, which here shows a maximum, is not consistent with the experimental observation, where the peak current exhibits a minimum. The experimentally observed quenching of the negative differential resistance peak for low gate voltages is not reproduced by this calculation.

3.5.3 Theory: Resonant tunneling

In this section the superlattice transport is treated as a resonant tunneling process rather than in the miniband conduction picture. The problem of a particle tunneling between two adjacent quantum wells in crossed electric and magnetic fields can be treated quantum me-

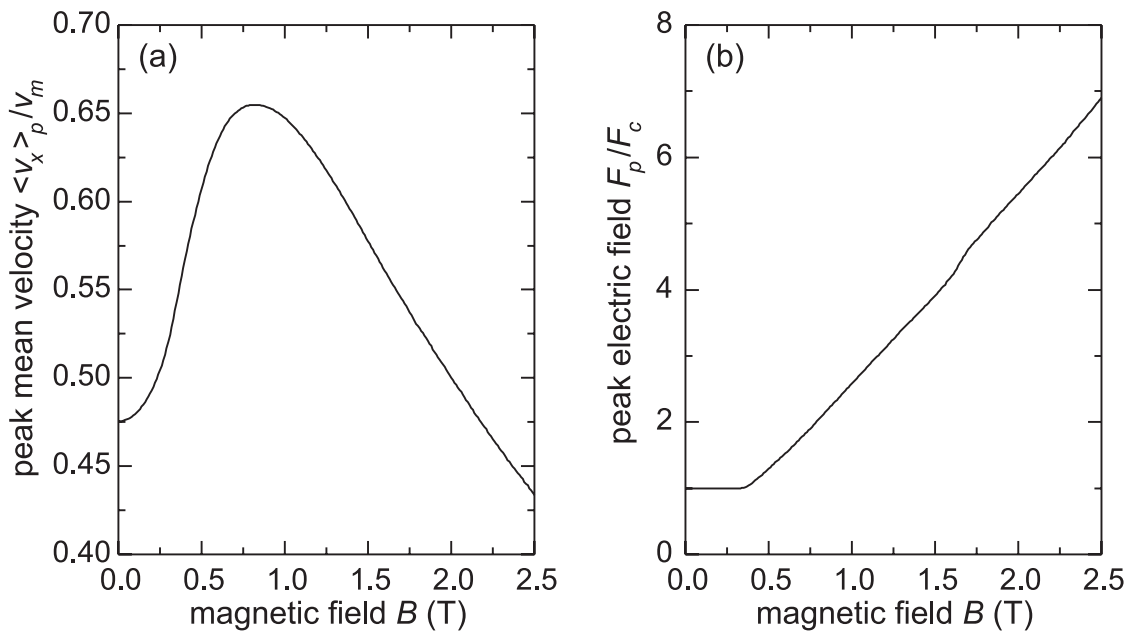


Figure 3.23: (a) Calculated peak mean velocity $\langle v_x \rangle_p$ and (b) peak electric field F_p vs. magnetic field B .

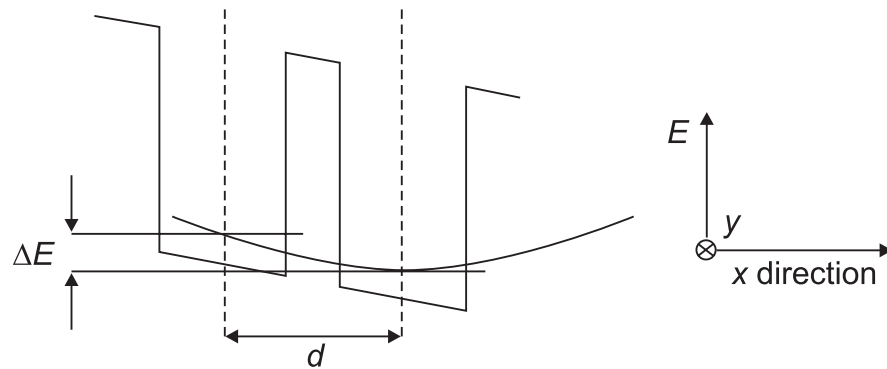


Figure 3.24: Electron tunneling in crossed electric and magnetic fields. The energy scale and real space distances are drawn not to scale.

chanically in first order perturbation theory [Maa87] [Bas88]. It is found that the energy levels are modified by a diamagnetic shift, and, most importantly, that the magnetic field induces an energy term parabolic in superlattice direction, the minimum of which depends on the electron momentum in the free electron direction. If the diamagnetic shift, and the polarization of the wave functions due to the quantum confined Stark effect are neglected,

the energy difference ΔE of an electron when tunneling between two neighboring quantum wells, is given by

$$\Delta E = \frac{e^2 B^2 d^2}{2m_y}, \quad (3.26)$$

where m_y is the electron mass in the free y direction.

Semiclassically, this energy difference can be understood as a result of the momentum transfer $\hbar k_y = eBd$ from the (tunneling) x direction to the free y direction induced by the Lorentz force, where d is the tunneling distance. Experimentally, relation (3.26) has been tested in weakly coupled bulk superlattices for tunneling processes from the lowest to the first excited subband [Mue93]. For the SLFET at hand, however, we consider electron motion between the lowest minibands of adjacent quantum wells. The superlattice is hardly biased, therefore neglecting the diamagnetic shift and the quantum confined Stark effect is a good approximation.

The tunneling process is schematically drawn in Figure 3.24. An electron, that has relaxed to the energy minimum in the left quantum well, can resonantly tunnel to the right quantum well only if the parabolic dispersion of this well intersect its energy level. This condition can be met when an additional electric field $\Delta F = \Delta E/(ed)$ with respect to the zero-magnetic field case is applied. If a constant electric field across the superlattice of length L is assumed, the magnetic field dependent peak voltage U_p is given by

$$U_p = U_p^0 + \frac{edL}{2m_y} B^2, \quad (3.27)$$

where U_p^0 is the peak voltage at zero magnetic field.

Relation (3.27) predicts a quadratic increase of the peak voltage with increasing magnetic field, exactly as observed in the experiment. Quite surprisingly, the prefactor $c_p = edL/(2m_y)$, which contains no free parameter, is given by $c_p = 0.03$, when we use the free GaAs electron mass. This is exactly the value obtained from the fit to the experimental data in Figure 3.21 for a gate voltage of $U_g = 0.35$ V. Even though the experimentally obtained prefactors were gate voltage dependent, all observed values are consistent with this model by order of magnitude. A density dependence is not included in this model.

3.5.4 Discussion

Main features observed in the transport experiment in crossed electric and magnetic fields were a quenching of the negative differential resistance peak at low gate voltages, for $U_g >$

0.3 V a quadratic shift of this peak to higher source-drain voltages with magnetic field, and a minimum in the peak current. A semiclassical miniband transport model predicted an increase in the peak voltage, but the functional dependence was incorrect. When the transport was modelled as electron tunneling process between adjacent wells, a quantitatively correct functional dependence was found for $U_g > 0.3$ V.

Both models are to be considered as limiting cases to the true transport physics. The Esaki-Tsu model in a miniband of width Δ is only valid for electric field strengths smaller than $\Delta/(ed)$, while for $F > \Delta/(ed)$ electron states are localized by the electric field. In this regime electron transport occurs by sequential tunneling between Wannier-Stark states, and the resonant tunneling model may more favorably be applied, which correctly predicts the quadratic increase of the peak voltage. This model, however, does not predict the quenching of the negative differential resistance peak, and it does not include any density dependence. Full energy relaxation and loss of phase information of the electron is assumed, which is incorrect in the transition regime between miniband transport and resonant tunneling. More sophisticated transport models must be developed here.

3.6 Towards ultra short channel vertical transistors

In May 2000 Infineon Technologies AG was celebrating the groundbreaking of the world's first 300 mm high-volume production facility in Dresden/Germany. Total investment is an estimated 1.1 Billion Euro over the following three years. Technology will be 0.14 μm and smaller, targeted product will be up to the 1Gbit DRAM. 42 million 0.18 μm MOSFETs run at a frequency of 1.5 GHz in INTEL's recent Pentium-4 microprocessor, in 2005 this company plans to use a 0.07 μm technology. The INTEL founder himself, G. Moore, originally expected his famous law to only hold until the quarter micron technology.

In view of these enormous technological advances on the one side, and of the high investments necessary on the other side, we wonder about the fundamental limits of the scaling law. In this Section we briefly highlight possible extensions of the CEOFET for fabricating ultra-short channel devices. These results have been obtained in collaboration with F. Ertl and T. Asperger. Our two devices can be considered as atomically precise counterparts of the two main recent developments in ultra-short channel silicon FETs. Both devices are vertical structures, critical dimensions are lithography independent, and they differ in the way how the source-drain isolation is achieved.

In Figure 3.25(a) we schematically show the first type of ultra-short channel CEOFET,

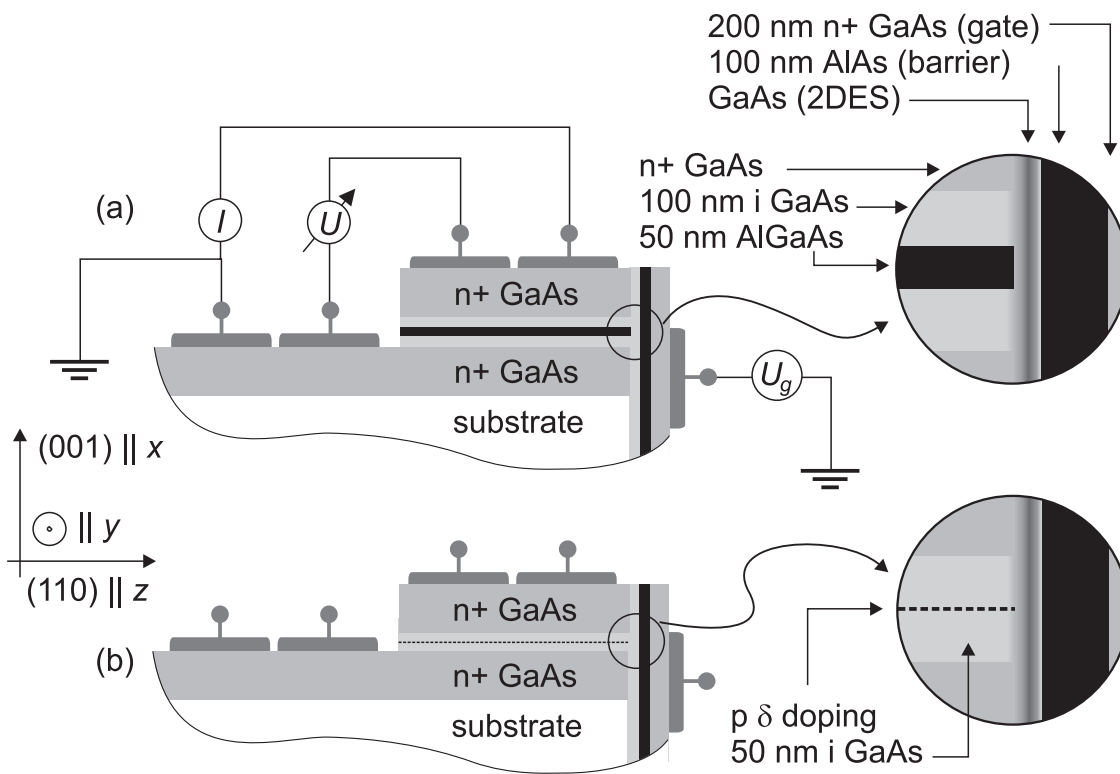


Figure 3.25: (a) Schematic sample design of the heterobarrier CEOFET. (b) Schematic sample design of the planar doped CEOFET.

the heterobarrier CEOFET. The channel length is determined by the thickness of the Al-GaAs barrier between source and drain. Intrinsic GaAs layers were added to avoid diffusion of dopants into the barrier. The (110) overgrown GaAs layer defines the geometrical channel thickness q . We study devices with source-drain barrier thickness of 50 nm and q between 20 nm and 40 nm. In some aspects a similar device has been developed by the Bell laboratories at Lucent Technologies. They have recently demonstrated a fully CMOS compatible 50 nm device, called the vertical replacement-gate MOSFET [Her00].

Our second type of CEOFET, the planar doped CEOFET, is shown in Figure 3.25(b). In this case the source-drain barrier is replaced by a planar p-type doped layer. This modification buys the advantage of improved source-drain isolation. Planar doped MOSFETs in silicon technology have been extensively investigated by the Eisele group of the University of the Armed Forces in Munich [Kae98].

Soon after they invented the cleaved-edge overgrowth technique, Stormer *et al.* have

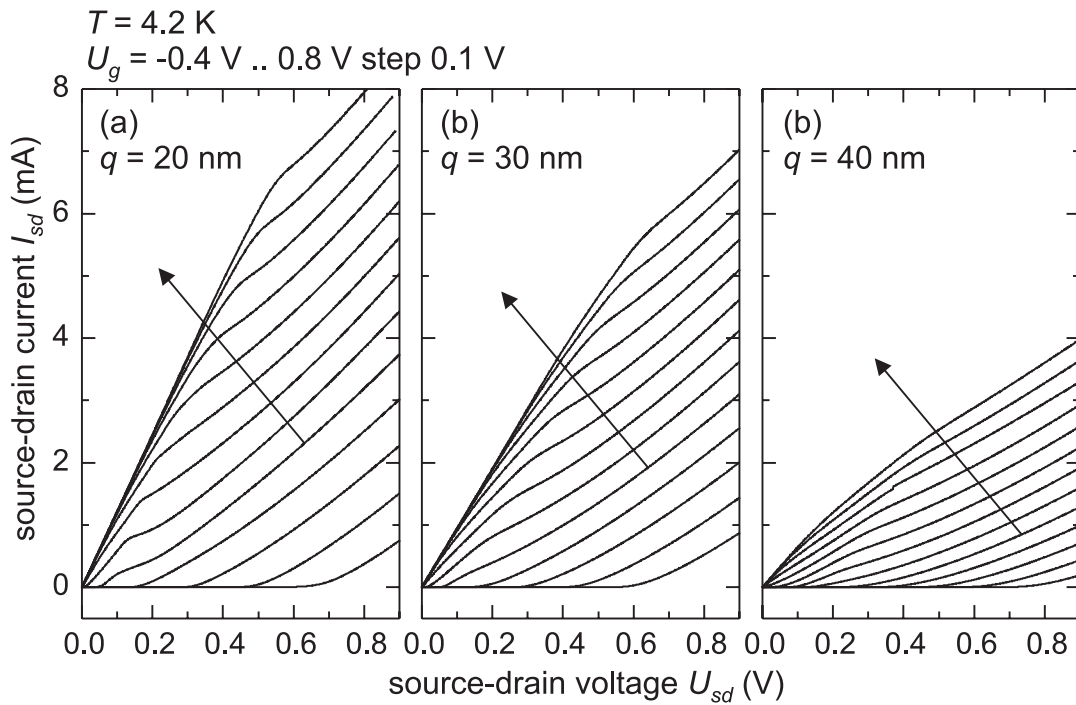


Figure 3.26: Current-voltage relation of heterobarrier CEOFETs. (a) $q = 20 \text{ nm}$, (b) $q = 30 \text{ nm}$, (c) $q = 40 \text{ nm}$.

demonstrated a field-effect transistor fabricated by this method [Sto91a]. In their device, a (001) GaAs quantum well acts as a gate to a (110) oriented two-dimensional electron system. Processing this device requires lithography on the (110) face of a $100 \mu\text{m}$ thick sample, which is, according to the authors, "challenging but feasible". The shortest gate length to date realized by a conventional architecture has been presented by a French group of the LETI lab in Grenoble [Del00]. Their n channel MOSFET has a 20 nm finished gate length, fabricated on 200 mm silicon wafers with 1.2 nm silicon dioxide as gate insulator.

3.6.1 Heterobarrier CEOFET

In Figure 3.26 we present current-voltage data of heterobarrier CEOFETs with (110) GaAs thickness of $q = 20 \text{ nm}$, $q = 30 \text{ nm}$ and $q = 40 \text{ nm}$, taken at $T = 4.2 \text{ K}$. The electron channel can be accumulated and depleted by applying positive and negative gate voltages. At this temperature, leakage between source and drain is negligible. At room temperature, however, the heterobarrier becomes transparent, and the gate leakage is intolerable. Some saturation

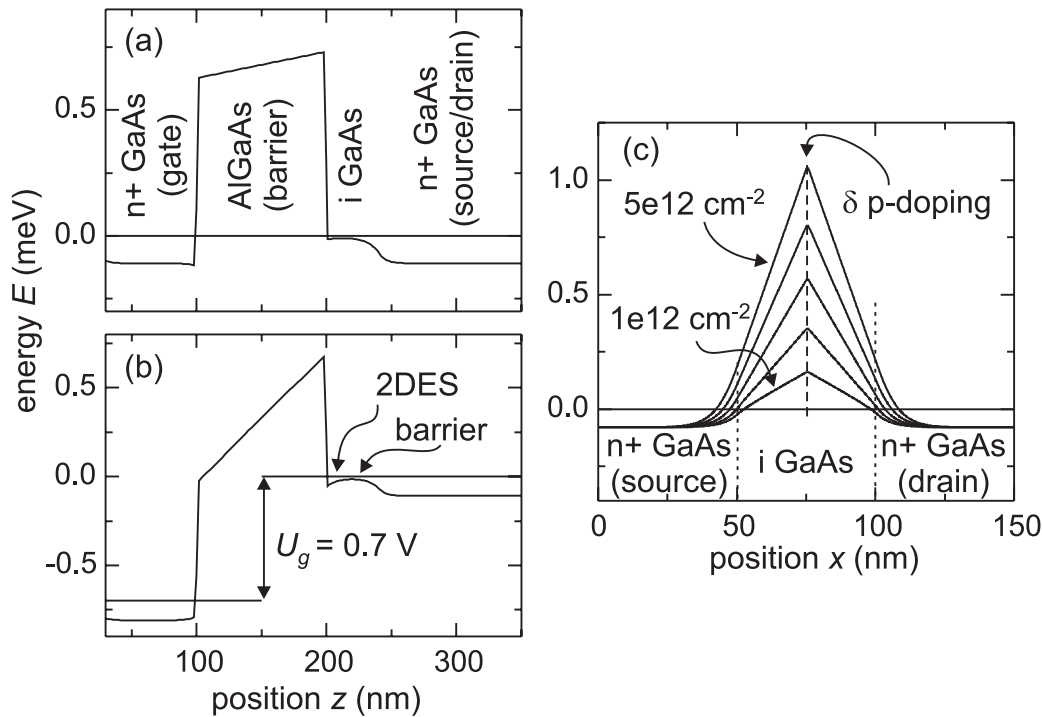


Figure 3.27: (a) Calculated conduction band profile for the unbiased CEOFET, cut in z direction from the n^+ GaAs gate through the gate barrier and the i GaAs channel into the n^+ GaAs source/drain contacts. (b) Conduction band profile for the CEOFET with applied gate voltage of $U_g = 0.7$ V. A barrier exists between the source/drain contacts and the two-dimensional electron gas. (c) Conduction band profile for the unbiased planar doped CEOFET, cut in x direction from the n^+ GaAs source contact through the source-drain barrier into the n^+ GaAs drain contact, calculated for different δ p-doping concentrations.

of the source-drain current can be observed. When comparing the three devices, the current level decreases with increasing channel thickness. This is contrary to our intuition, and contrary to the SLFET presented in Section 3.4, where the current level was increasing with increasing (110) GaAs layer thickness.

The decreasing current level with increasing intrinsic GaAs layer thickness is explained in Figure 3.27. In (a) we have calculated the conduction band profile for the unbiased device, a cut from the gate contact in z direction through the gate barrier, the intrinsic GaAs and into the n^+ GaAs contact is shown. As can be seen, an upward band bending occurs at the interface between i GaAs and n^+ GaAs. When a positive gate voltage is applied, as expected a two-dimensional electron gas is field-induced at the interface between gate barrier and

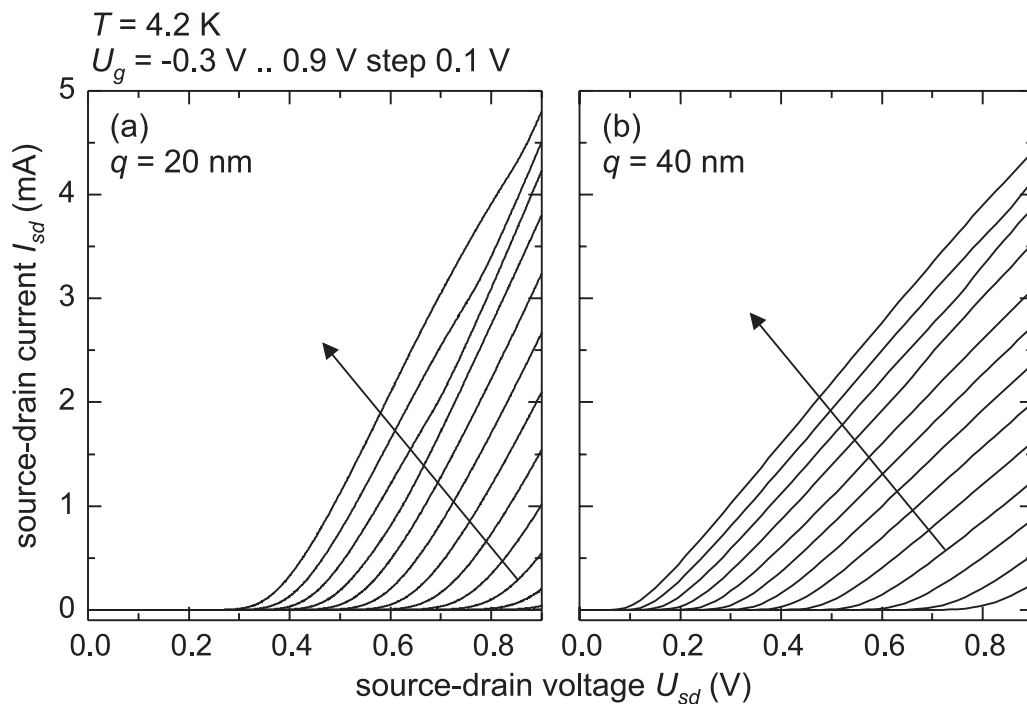


Figure 3.28: Current-voltage relation of planar-doped CEOFETs. (a) $q = 20$ nm, (b) $q = 40$ nm.

i GaAs. There is, however, a barrier between the two-dimensional electron system and the sourcing n+ GaAs contact, which has to be overcome by the electrons. This barrier becomes significant for $q > 30$ nm and then causes an additional resistance, and the observed drop of the current level for wide i GaAs layers.

3.6.2 Planar doped CEOFET

Current-voltage results obtained from the planar doped CEOFET at low temperatures are shown in Figure 3.28. As with the heterobarrier CEOFET, the source-drain current can be controlled both up and down by the gate. But even for large gate voltages of $U_g = 0.9$ V, an ohmic behavior for low source-drain voltages cannot be achieved. Remarkably, the $q = 40$ nm device comes closer to an ohmic trace than the device with narrower electron channel. This can be understood using Figure 3.27(c). There we have calculated the conduction band profile between the source and the drain contacts, across the planar doped source/drain barrier. As can be seen, depending on the p doping concentration, a rather high

source-drain barrier is obtained. This is the reason that these devices can be operated even at room temperature. On the other hand, the high conduction band energy between source and drain depletes the electron channel, which leads to the observed high resistance for small source-drain voltages. Only at large U_{sd} the barrier in the channel can be overcome and current flows. The barrier height is lowered by increasing the gate voltage.

3.7 Conclusion

In this chapter we have gathered strong evidence for the existence of Bloch localization in SLFETs, using non-equilibrium transport experiments. We have found negative differential resistance in SLFETs with miniband widths between 3.3 meV and 21.2 meV, most strongly pronounced in the device with the narrowest miniband. The peak voltage was shown to be independent of electron density over a certain range, in agreement with the Esaki-Tsu model. Further we demonstrated that the peak current linearly increases with miniband width, again in good agreement with the theory. Other possible reasons for negative differential resistance are discussed and can be excluded, and reasons for stabilization of the charge density in devices exhibiting a negative differential velocity relation are developed.

Additional current maxima beyond the negative differential resistance regime are explained by resonant emission of folded phonons by Bloch-oscillating electrons. Reference samples did not exhibit negative differential resistance and were well-behaved vertical field-effect transistors. Electron mobilities in the SLFETs were found to be high compared to the reference samples, and even compared to the best modulation doped heterostructures grown on (110) GaAs substrates. This fact makes them ideal candidates for electron density dependent investigations in the fractional quantum Hall regime, as we will show in Chapter 6.

Non-equilibrium transport has been studied also in crossed electric and magnetic fields. The observed shift of the negative differential resistance peak was discussed in a miniband picture and in using a resonant tunneling model. Finally we have given a preview on possible extensions of the CEOFET concept to ultra-short channel field-effect transistors. First devices with channel lengths of 50 nm were fully operable.

Chapter 4

Transport in the Resonant Tunneling Regime

Resonant tunneling is governed by the simultaneous conservation of energy and momentum. These conservation laws depend on the dimensionality of the source and drain reservoirs, and are fulfilled only for certain combinations of the Fermi energy, the applied electric field, and the direction and strength of an applied magnetic field. Transport through resonant tunneling occurs in weakly coupled multi-quantum well systems, and represents the opposite regime to miniband transport in strongly coupled superlattices.

In this chapter we study a superlattice of weakly coupled quantum wires by means of measuring the transverse tunneling current. Our SLFET offers the unparalleled opportunity to gain direct insight into the tunneling transport between identical wires in the absence of contact effects, which greatly influence the characteristics of few-barrier systems, such as resonant tunneling diodes. In our coupled one-dimensional system, the conservation rules are particularly simple. Quantizing magnetic fields perpendicular to the wires and the current result in both spatial splitting of forward and backward moving electrons, and in a distortion of the electron tunneling path, effects which leave their fingerprints on the current-voltage characteristics. A magnetic field parallel to the current direction changes the subband energies and results in a complex tunneling pattern. The additional control over the Fermi energy in the quantum wires makes our SLFET an ideal device to explore hitherto undisclosed tunneling regimes.

4.1 Review on low dimensional resonant tunneling

Early tunneling experiments were concerned with 3D-2D, 2D-2D and 2D-1D tunneling. Experiments to study tunneling between quantum wires have been studied much less. A review on resonant tunneling experiments and theory up to the year 1991 can be found in [Cha91]. Up to now to our knowledge no studies have been reported on tunneling experiments between an array of parallel quantum wires.

In a pioneering experiment Smoliner and coworkers studied the tunneling between two separately contacted 2DEGs in transverse magnetic fields (magnetic field orientation parallel to the tunneling barrier) [Smo89]. The two 2DEGs form at both sides of a modulation doped AlGaAs barrier. They observe peaks in the first derivative of the tunneling current that split and shift with increasing magnetic field. Classically the Lorentz force couples both components of the momentum perpendicular to the magnetic field orientation. Quantum mechanically this corresponds to the conservation of the canonical momentum. For an electron travelling a distance d through the barrier in x direction, the wave vector is changed in y direction by (see Equation (3.26))

$$\Delta k_y = \frac{eBd}{\hbar} \quad (4.1)$$

The fact that the resonances split into two peaks is due to the fact that electrons with positive and negative parallel Fermi wave vector contribute to the tunneling current.

Later Eisenstein and coworkers measured on a similar coupled 2DEG system equilibrium tunneling as a function of in-plane magnetic field and sheet density [Eis91]. For equal 2DEG densities the tunneling current is sharply peaked around zero magnetic field, but varies slowly at intermediate fields. Around 6 Tesla the conductance exhibits a weaker peak followed by an abrupt drop to zero. A simple and very intuitive model of two displaced, but intersecting, Fermi circles explains these results. As the magnetic field is increased, according to Equation 4.1 the two Fermi circles shift across each other, and simultaneous conservation of energy and momentum is possible only at certain values of magnetic field and electron density.

Tarucha and coworkers were the first to study the effect of resonant tunneling through one- and zero-dimensional states [Tar90]. Their device was a conventional resonant tunneling diode, which they confined laterally by focused ion-beam implantation. They observed a series of resonant tunneling current peaks corresponding to the one dimensional levels superimposed on the ground state confined by the heterojunction.

Dignam *et al.* investigated 2D-1D-2D tunneling without magnetic field in a sample prepared by cleaved-edge overgrowth [Dig94]. Their device was similar to the device studied in our work, except that in their device only one quantum wire was involved. Tunneling proceeds, in a planar geometry, from the edge of a 2DEG source through the bound states of the quantum wire into the edge of a 2DEG drain. The barriers are 6 nm and 7.5 nm AlGaAs, the wire width in between is only 5 nm. They find resonance peaks in the tunneling current, which they attribute to a resonance between the edge bound states in the 2D system and the first three bound states in the wire.

Wang and coworkers were the first group to study tunneling via 1D states in magnetic field [Wan94]. Their wires, though, were fabricated by conventional lateral etching, and thus rather wide (more than 100 nm). Experiments with magnetic field orientation parallel and perpendicular to the wire are interpreted in the framework of the transfer Hamiltonian formalism [Mor95]. They point out that at high magnetic fields oriented in z direction a weak modulation of the tunneling current arises from the formation of 1D subbands in the emitter.

Other examples of tunneling structures fabricated by the cleaved-edge overgrowth technique include 3D-2D (1D) tunneling into the fractional quantum Hall edge [Cha96], 2D-1D-2D, 2D-2D, and 2D-3D tunneling [Gra96], 1D-1D tunneling between two asymmetric quantum-wires [Wan99], and, very recently, tunneling between the edges of two lateral (integral) quantum Hall systems [Sto00].

Resonant tunneling in coupled quantum systems has been studied in doped and undoped superlattices. Undoped superlattices are usually embedded in a p-i-n diode in order to achieve a homogenous field, and transport is investigated either by photocurrent-voltage characteristics, or by time-of-flight experiments, while the diode is operated in reverse-bias [Mue93]. For electrical transport experiments, carriers must be introduced into the superlattice, usually by a fixed doping. This method, however, does not offer the same flexibility as the SLFET, where we are able to tune the electron density by means of the gate, and much higher (sheet) electron densities can be achieved.

Esaki and Chang were the first to observe current oscillations in a doped superlattice [Esa74]. They already hypothesized that these oscillations were due to an expanding high field domain. Their superlattice, however, was strongly coupled, and the low-field transport occurred in the lowest minibands rather than by resonant tunneling. Only more than ten years later, Choi and coworkers first investigated resonant tunneling in a weakly coupled superlattice, and found very regular negative conductance oscillations resulting from a periodic alignment of the two lowest quantum well states and an expanding high-field do-

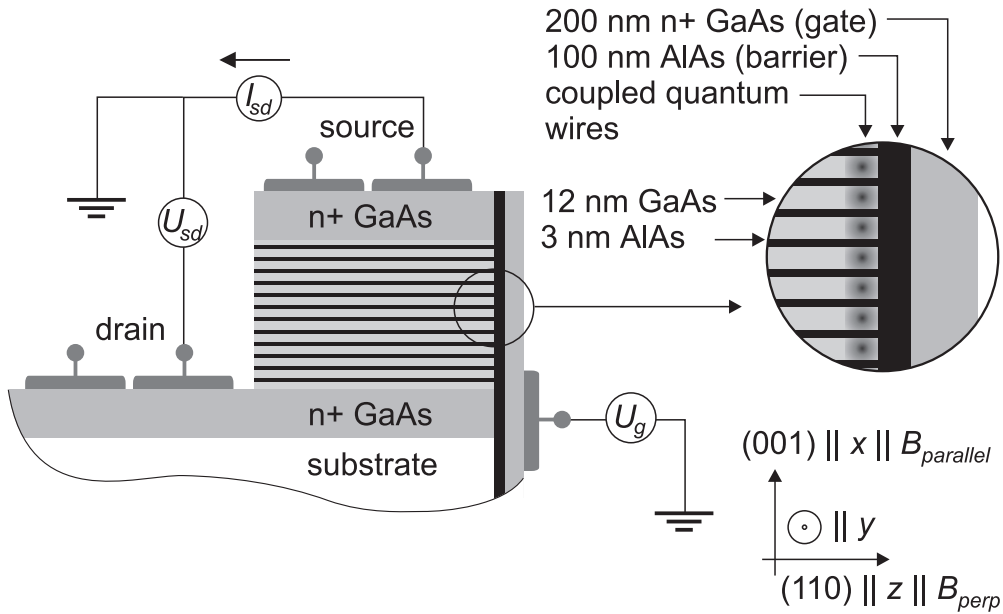


Figure 4.1: Resonant tunneling SLFET sample design.

main [Cho87]. Much theoretical and experimental work has been performed on these weakly coupled superlattices since. Grahn *et al.* found an increasing plateau current and a shift of the current resonances to higher electric fields in a magnetic field parallel to the superlattices layers [Gra91]. In Section 4.4 we perform a similar experiment for coupled quantum wires. Kastup *et al.* observed hysteresis between up- and down sweeps of the source-drain voltage due to the charge trapped in one quantum well at the boundary between the high- and the low-field domain [Kas94]. Recently, weakly coupled superlattices are much discussed in relation to self-sustained current oscillations [Wac97], as well as driven and undriven chaos [Luo00].

4.2 Sample design and band structure calculation

The sample structure of the resonant tunneling SLFET is shown in Figure 4.1. It is based on the SLFET discussed in Chapters 2 and 3, only the AlGaAs superlattice barriers were replaced by AlAs barriers to increase the barrier height, thus decreasing the coupling strength between the quantum wells to generate weakly interacting quantum wires. On the semi-insulating (001) GaAs substrate the layer sequence is $1 \mu\text{m}$ n+ GaAs (doped to $n = 2 \times 10^{18} \text{ cm}^{-3}$), 50 periods of 11.9 nm GaAs and 3.1 nm AlAs (period length $d = 15 \text{ nm}$), $1 \mu\text{m}$ n+ GaAs (doped to $n = 2 \times 10^{18} \text{ cm}^{-3}$). After the cleave the regrowth consists of 100 nm

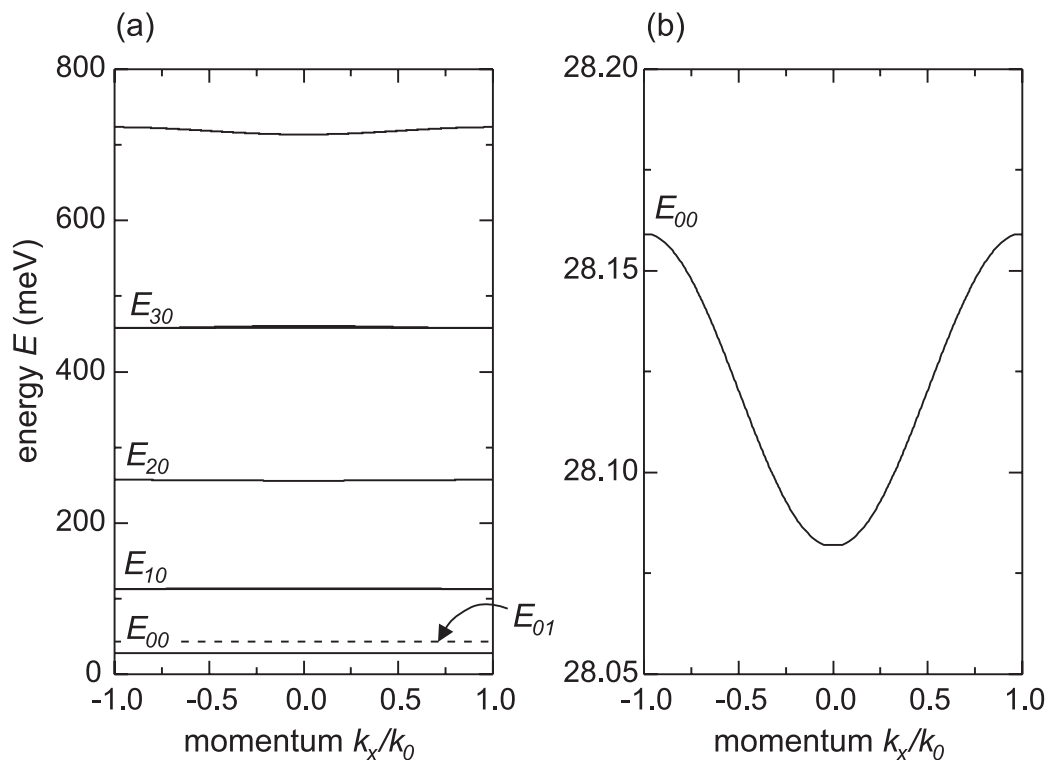


Figure 4.2: (a) Band structure calculated in the Kronig-Penney model. The bands are labelled according to the quantization index in the x and z direction E_{xz} . (b) Enlargement of the lowest subband.

AlAs, and 200 nm n^+ GaAs (doped to $n = 2 \times 10^{18} \text{ cm}^{-3}$). The (001) doped layers serve as source and drain contacts, while the (110) doped layer is used in the usual way as a gate. The channel length, i.e. the total distance travelled by the electrons from source to drain through the coupled quantum wires, is $L = 750 \text{ nm}$.

The calculated (Kronig-Penney) band structure is shown in Figure 4.2. We label the bands according to the quantization index in the x and z direction E_{xz} . As a result of the small overlap of the wave functions between two adjacent quantum wells, minibands are very narrow. For the present superlattice we retrieve much rather the quantum well energy levels. The broadening of the lowest level due to this overlap, enhanced in Figure 4.2(b), is less than 0.1 meV. This band width is comparable to the thermal broadening, and additionally we expect the broadening due to impurities and interface roughness to be at least of the same order. The first excited quantum well level lies $E_{10} - E_{00} = 85 \text{ meV}$ above the ground state. In the experiment we will be concerned with the lowest energy level E_{00} . In addition to

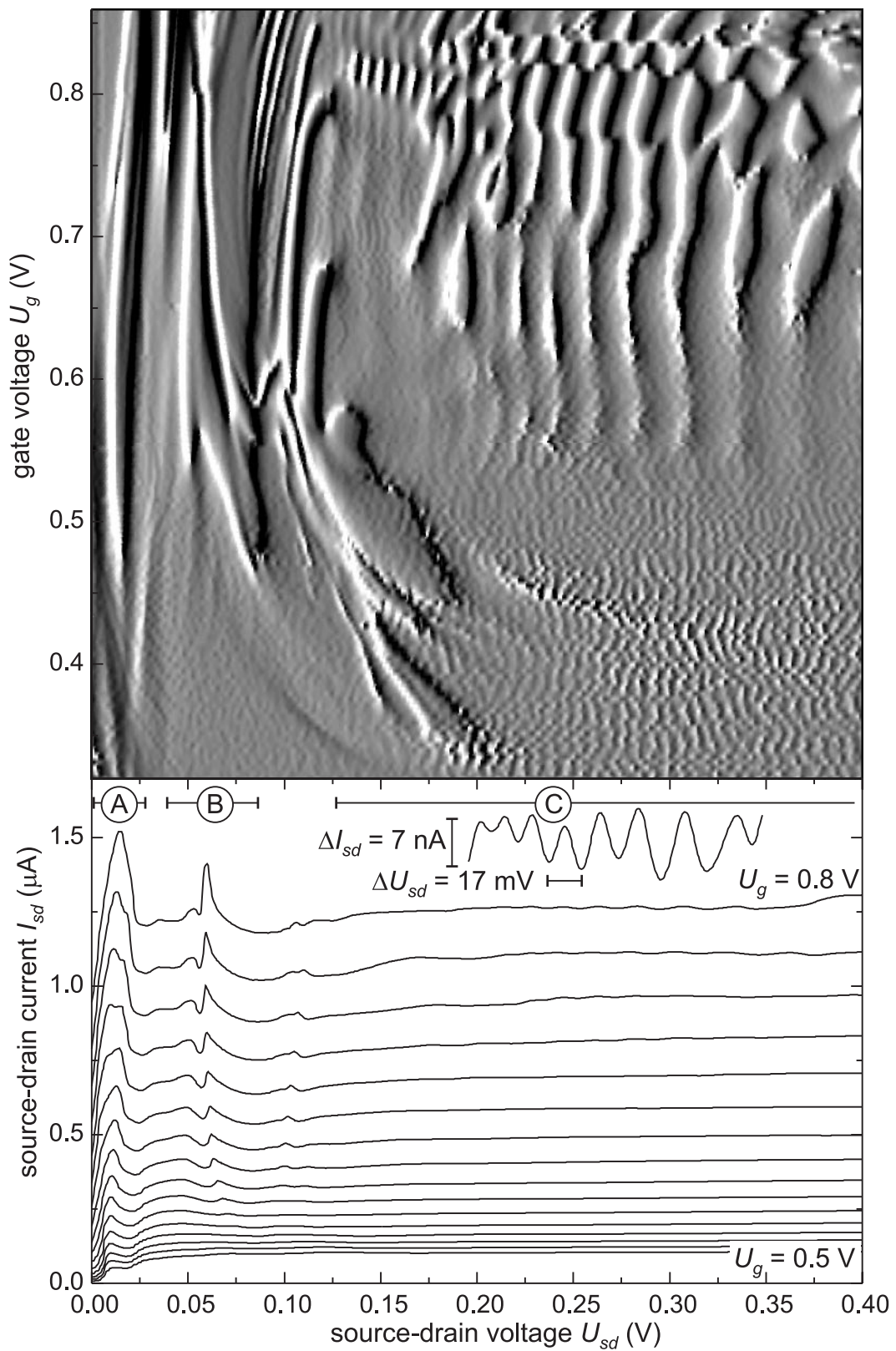
the quantum well energy levels, determined by this Kronig-Penney calculation, we have previously found by self-consistent two-dimensional calculations in Chapter 2 the presence of excited states due to the confinement in the z direction. Owing to the wider extent of the wave functions in z direction, the subband spacing between the lowest and the first excited level in z direction is only about $E_{01} - E_{00} = 15$ meV, and thus much smaller than the quantum well subband spacing. In Figure 4.2(a) the level E_{01} is drawn with a dashed line. In the experiment we are concerned with these lowest energy states of the system E_{00} and E_{01} .

4.3 Resonant tunneling in zero magnetic field

In this section we present current-voltage measurements, obtained at zero-magnetic field for different gate voltages. Additional information is gathered in the two following sections by applying a magnetic field perpendicular to the wire direction, either perpendicular or parallel to the current flow. All experiments are performed at temperatures between $T = 330$ mK and $T = 4.2$ K, the results are found to be insensitive to temperature in this range. The measurements are obtained by keeping the upper (source) contact grounded, while applying the positive source-drain voltage U_{sd} to the lower (drain) contact. The gate potential U_g is defined with respect to ground.

4.3.1 Experimental current-voltage traces

In Figure 4.3 we show gate voltage dependent current-voltage traces. The gray value picture is intended to demonstrate source-drain current maxima (white) and minima (black), that are otherwise difficult to see in the current-voltage traces due to their small amplitude. It has been obtained by dividing the second derivative of the source-drain current with respect to the source-drain voltage by the negative first derivative. Below a gate voltage of $U_g = 0.3$ V the SLFET is insulating, indicating that the Fermi energy in the supplying contact is below the lowest energy state in the quantum wire system. For gate voltages up to $U_g = 0.51$ V the current increase at small U_{sd} is diode like, as a result of the exponential dependence of the tunneling current on the lowered barriers with increasing bias. An ohmic behavior at small source-drain voltages is observed above $U_g = 0.52$ V, at which point the contact Fermi energy matches the lowest energy state in the quantum wire system. The fact that this condition can be met is a unique feature of the SLFET, and makes possible the observation of current features at very small bias voltages, that would otherwise be masked by the current



R. A. Deutschmann *Two dimensional electron systems in atomically precise periodic potentials* (2001) Ph.D. Dissertation. Selected Topics in Condensed Matter Physics and Technology, ISBN 3-932749-42-1

suppression due to the barrier.

Starting at a gate voltage of $U_g = 0.48$ V a pronounced negative differential resistance peak at $U_{sd} = 11$ mV appears (region A), which only slightly shifts to $U_{sd} = 18$ mV for the largest gate voltages of $U_g = 0.86$ V. For larger U_{sd} the current saturates. The current level, however, is two orders of magnitude smaller than typical saturation currents obtained with SLFET of identical period length, see Chapter 3. The reason is the much weaker wire to wire coupling in the present SLFET, which results in tunneling transport rather than miniband transport.

As the gate voltage is raised, other features besides the negative differential resistance peak are observed at larger U_{sd} . In the quadrant ($U_{sd} > 125$ mV, $U_g > 0.55$ V), small amplitude current oscillations appear (region C), the positions of which are gate voltage independent. The current oscillation amplitude is below 1% of the source-drain current, and their period at $U_{sd} = 0.25$ V is about $\Delta U_{sd} = 17$ mV, and increases for larger source-drain voltages. A magnification of these oscillations for $U_g = 0.8$ V is shown in Figure 4.3. At intermediate source-drain voltages (region B), another current feature is observed as peak and double-peak maximum at $U_{sd} = 56$ mV.

4.3.2 Resonant tunneling model

We explain the current-voltage relation using Figure 4.4. The dispersion of the two lowest energy levels is shown for two adjacent quantum wires. In this low energy regime, the dispersion in the free y direction is parabolic. As shown in Figure 4.4(a), at very small bias, tunneling proceeds for electrons originating in the lowest energy level of the left quantum wire E_{00} to empty states in the lowest level of the right quantum wire. Simultaneous energy and momentum conservation is only guaranteed for a small bias region around zero bias corresponding to the width of the energy levels. The current peak in region A thus results from ground state to ground state tunneling. The width of this current peak $\Delta U_{sd} = 10$ mV is remarkably small. The resulting width of one energy level $\Delta E = 10$ meV/50 periods=0.2 meV/period corresponds to the thermal energy at $T = 4.2$ K. This indicates that at this temperature the level width is not limited by the finite electron lifetime in one quantum wire, or by scattering, but rather by temperature. The current peak itself occurs at a very small electric field $F_{peak} = U_{peak}/L = 145$ V/cm, which is smaller than the peak electric field observed in miniband transport, see Chapter 3. For larger source-drain voltages the ground state to ground state resonance condition is destroyed, and the source-drain current decreases beyond the

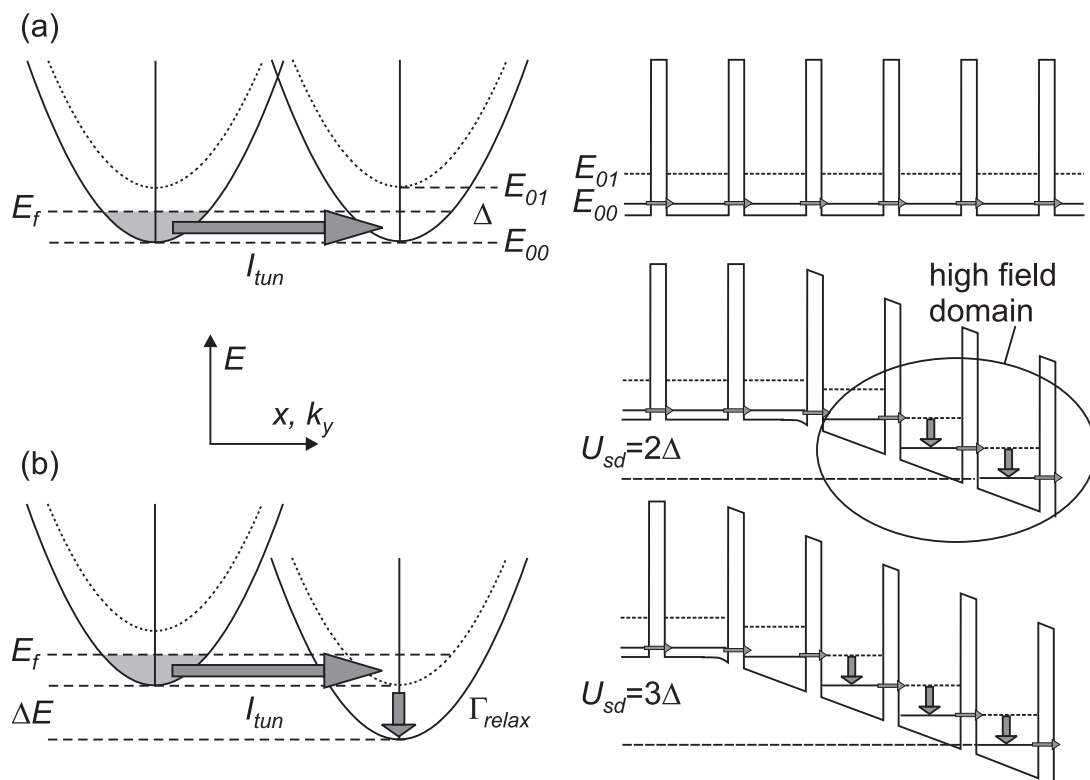


Figure 4.4: Resonant tunneling model. Energies are not drawn to scale, only the two lowest energy levels are shown. (a) Ground state to ground state tunneling at almost zero bias. (b) Ground state to first excited state tunneling. The superlattice is drawn for two different resonance conditions.

first peak. The valley current is determined by non-resonant tunneling events.

For larger source-drain voltages, the current peak observed in region *B* is explained by a resonant tunneling process between the ground states of two adjacent quantum wires under the emission of a longitudinal optical phonon. The voltage difference between the pronounced current maximum at $U_{sd}=56$ meV and the ground state to ground state current maximum at $U_{sd}=18$ meV matches nicely the GaAs LO phonon energy of $E = 36$ meV [Ins90].

A genuine effect of the coupled quantum wire system, however, are the current oscillations observed at even larger U_{sd} in region *C*. As shown in Figure 4.4(b), we assert that a resonance condition can be met in the superlattice for tunneling between the ground state E_{00} of one quantum wire to the first excited state E_{01} of the adjacent wire. The excited state considered here results from the quantization in z direction, and is offset from the ground state,

as mentioned before, by $\Delta = 15$ meV. As the source-drain voltage is increased, a periodic increase of the source-drain current is expected, as the resonance condition is periodically met. The periodicity ΔU_{sd} is given by the energy difference between the participating energy states Δ , which is in fact observed in the experiment. Under bias, the wire system consists of two domains with different electric field. The low field domain is characterized by ground state to ground state tunneling, while in the high field domain ground state to excited state tunneling prevails. The current is limited by the domain boundary, which is formed by a negative charge accumulation within one quantum wire. The high field domain grows at the cost of the low field domain for increasing U_{sd} . The fact that ground state to excited state tunneling is observable only above a gate voltage of $U_g = 0.55$ V is explained by the fact that a certain minimum electron density is required to account for the change in electric field between the high-field and the low-field domain. Furthermore, as U_{sd} is increased, the relative drain to gate voltage decreases, and the electron density in the high-field domain gradually decreases. With the corresponding decrease in the local Fermi level of the ground states in the high-field domain, the resonance condition is reached at larger fields. Therefore we expect the period of the current oscillations to increase with increasing source-drain voltage, which is in fact observed in the experiment. In this model we neglect the energy level shift due to the quantum-confined Stark effect, which is a good approximation for the small electric fields and small well widths in our experiment.

The intersubband scattering time τ_{relax} depends on the availability of relaxation processes. For an intersubband spacing larger than the optical phonon energy in GaAs $\hbar\omega = 36$ meV, τ_{relax} can be below 1 ps. In our case the intersubband spacing Δ is much smaller, and large scattering times may be expected. However, in superlattices intersubband scattering may also be mediated by folded acoustic phonons (see Section 3.3.3).

4.4 Resonant tunneling in a perpendicular magnetic field

In this section we discuss current-voltage traces obtained in a magnetic field B_{perp} , defined in Figure 4.1, for fixed gate voltages. The magnetic field is oriented perpendicular to the quantum wires and the current direction. First we present experimental data, which we subsequently explain by a semiclassical model.

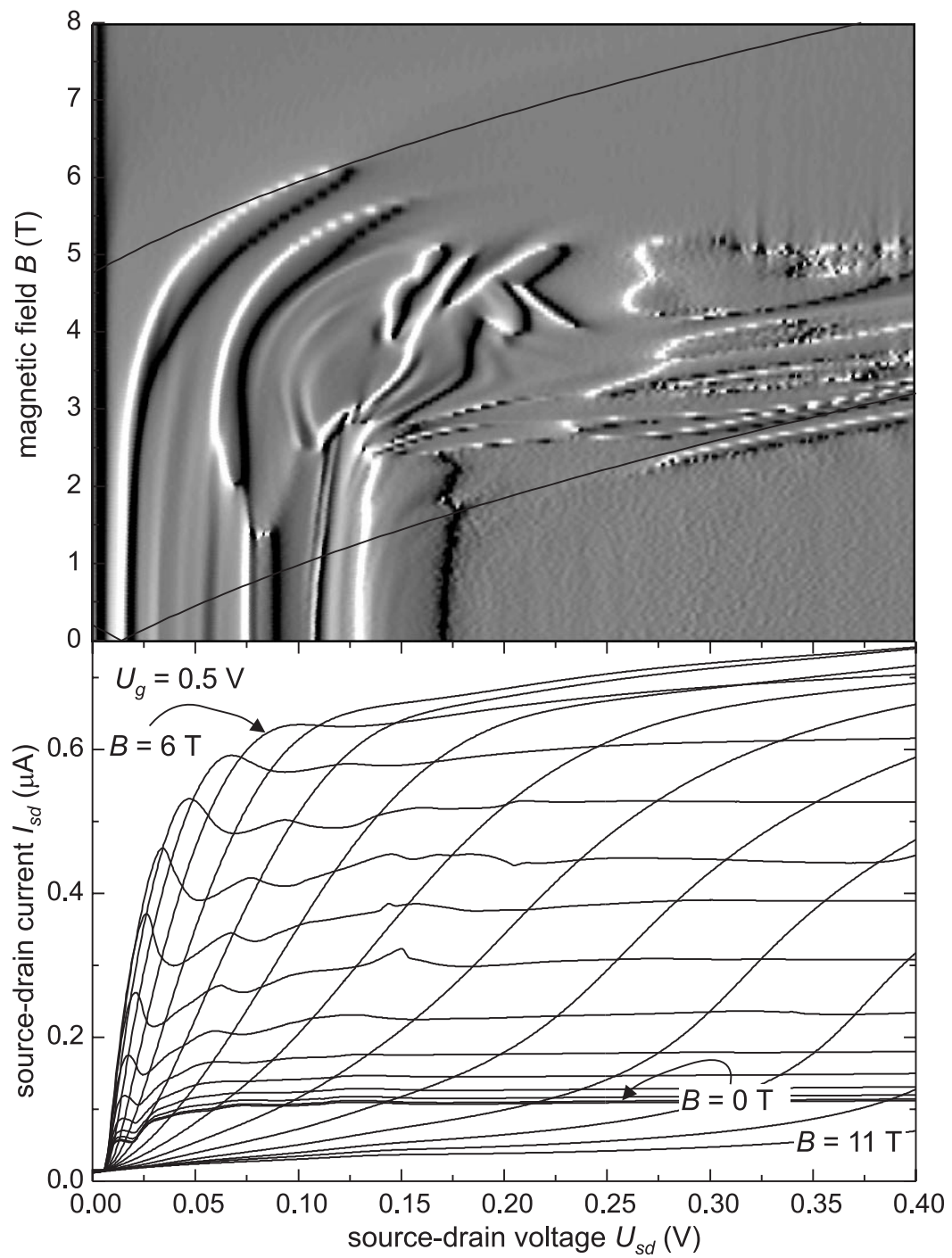


Figure 4.5: Current-voltage relation in perpendicular magnetic field at $U_g = 0.5$ V.

4.4.1 Experimental current-voltage traces

In Figure 4.5 the current-voltage relation for a gate voltage of $U_g = 0.5$ V in a perpendicular magnetic field between $B = 0$ T and $B = 8$ T is shown. The current-voltage data has been processed in the aforementioned way to obtain the gray value plot, which shows the evolution of the current maxima (white) and minima (black) in the covered parameter space. The peak current of the ground state to ground state resonance drastically increases with increasing magnetic field, in sharp contrast to the behavior in the miniband transport regime (see Section 3.5). Furthermore, the peak voltage remains at about $U_{sd} = 14$ mV for magnetic fields up to $B = 3$ T. For larger fields, the peak voltage increases rapidly. For $B > 6$ T, a sharp transition is observed, characterized by a simultaneous quenching of the source-drain current and the negative differential resistance peak. For large magnetic fields, the source-drain current is suppressed at low bias, and increases super-linearly with the source-drain voltage.

For a larger gate voltage of $U_g = 0.7$ V, we observe similar overall behavior, (see Figure 4.6), characterized by a drastic increase of the peak current, and a positive shift of the peak voltage. The quenching of the source-drain current occurs at the same magnetic field as for the lower gate voltage. In this measurement, however, we additionally observe a significant increase in the peak-to-valley ratio of the ground state to ground state tunneling peak with increasing magnetic field. The negative differential resistance part of the current-voltage relation beyond the peak even becomes steeper than the external lead resistance, resulting in a discontinuous current drop. Additionally, at this gate voltage the ground state to first excited state resonances are observed. We find that below a magnetic field of $B = 2$ T their position does not change, while above $B = 2$ T they are interrupted by a current feature that rapidly moves to larger source-drain voltages with increasing magnetic field.

4.4.2 Theory for the ground state to ground state resonance shift

In Section 2.4 we have derived the Schrödinger equation for a superlattice electron in a perpendicular magnetic field (see Equation (2.61))

$$\left(\frac{1}{2m^*} p_x^2 + \frac{1}{2m^*} (\hbar k_y + eBx)^2 + V(x) \right) \psi(x) = E(k_y) \psi(x). \quad (4.2)$$

For all relevant magnetic fields, the quantum well subband spacing is much smaller than the magnetic energy, therefore the first order correction to the ground state energy caused by the

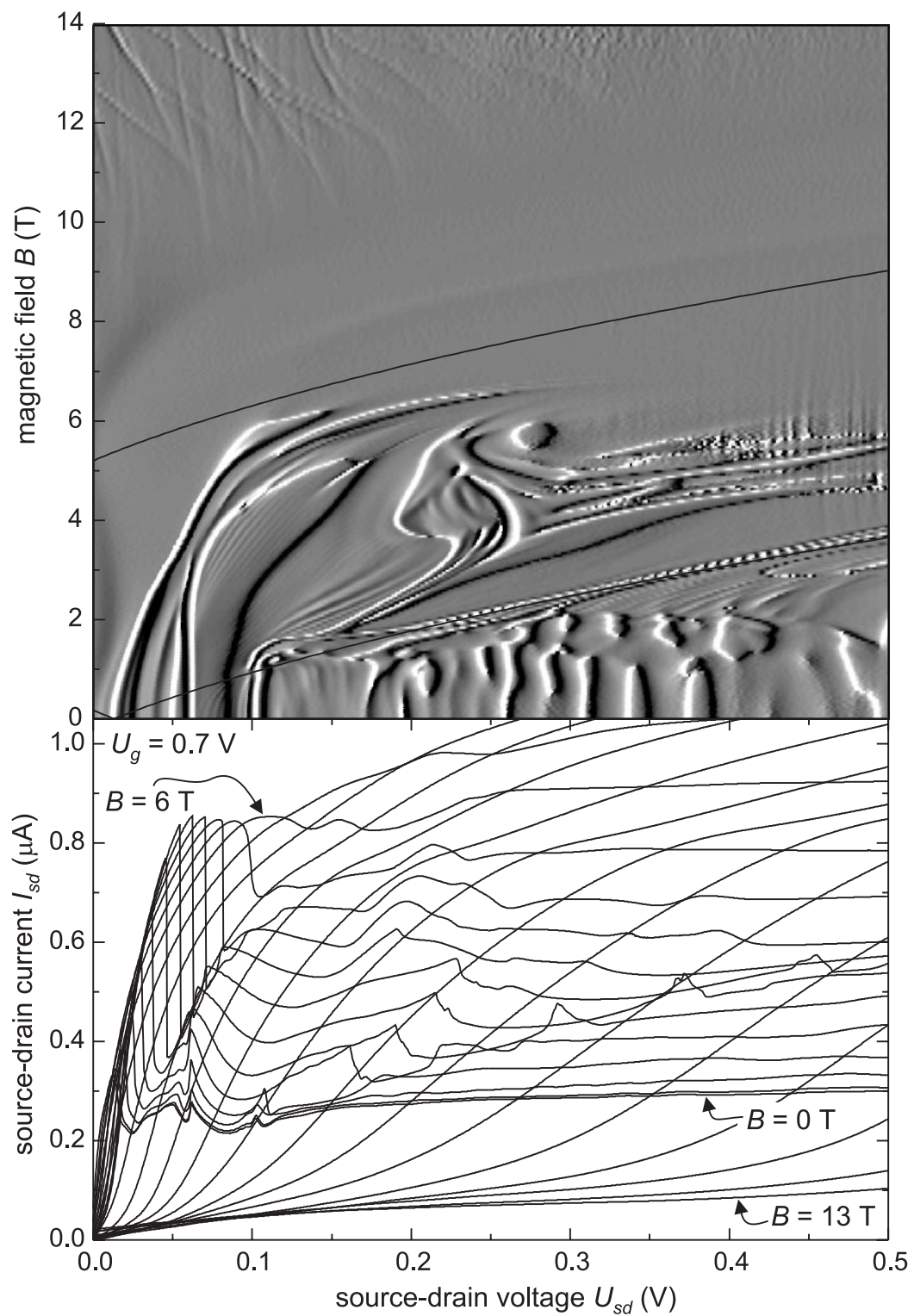


Figure 4.6: Current-voltage relation in perpendicular magnetic field at $U_g = 0.7$ V.

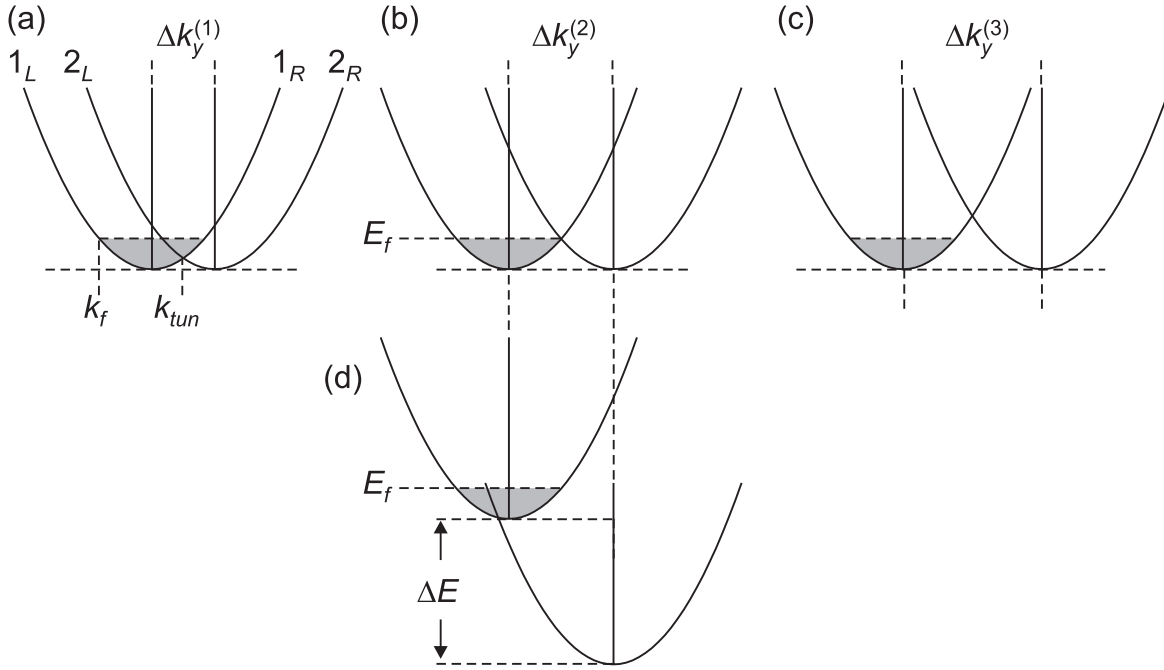


Figure 4.7: Back and forward scattering conservation conditions between adjacent wires. (a)-(c) Back scattering resonance condition for increasing magnetic field at vanishing bias. In (a) resonance is achieved below the Fermi energy, in (b) at the Fermi energy, and in (c) above the Fermi energy. At this high field tunneling is only possible for a bias $\Delta E > 0$. (d) represents the forward scattering condition at the same magnetic field as in (b).

presence of the magnetic field is given by [Maa87]

$$E = \frac{\hbar^2}{2m^*} \left(k_y + \frac{eB\langle x \rangle}{\hbar} \right)^2 + \frac{e^2 B^2}{2m^*} (\langle x^2 \rangle - \langle x \rangle^2), \quad (4.3)$$

where $\langle x \rangle = \langle \psi_0 | x | \psi_0 \rangle$ and $\langle x^2 \rangle = \langle \psi_0 | x^2 | \psi_0 \rangle$. The last term represents the diamagnetic shift of the ground state energy, while the first term can semiclassically be interpreted as due to the Lorentz force acting along the free y direction, changing the electron momentum k_y upon tunneling across the barrier in x direction by the amount $\Delta k_y = eB\langle x \rangle / \hbar$.

In Figure 4.7 we show the dispersion relation of a tunneling electron relative to the target dispersion, which is shifted by Δk_y . The magnetic field strength determines the offset between both parabolas. As can be seen, due to this shift, states in different wires with the same k_y are generally no longer degenerate in energy, and elastic tunneling between these states is forbidden. For any given bias there are, however, points of intersection between

the two parabolas, at which energy and momentum conserving tunneling is allowed. If the corresponding state in parabola 1 is occupied, but empty in parabola 2, tunneling can occur.

The relation between the momentum k_y , the momentum change Δk_y , and the energy difference ΔE at resonance, is given by

$$\Delta E_{\pm} = \frac{\hbar^2 \Delta k_y^2}{2m^*} \pm \frac{\hbar^2 k_y \Delta k_y}{m^*} \quad (4.4)$$

For any combination of k_y and Δk_y there are two possible energy differences. Concerning states at the Fermi energy $k_y = k_F$, we realize, that for any combination of k_F and Δk_y there are positive solutions ΔE_+ . Solutions $\Delta E_- > 0$, however, can only be obtained for large enough magnetic fields, such that $\Delta k_y > 2k_F$. Scattering events corresponding to ΔE_+ occur between the leftward moving branches of the dispersion parabolas $1_L \rightarrow 2_L$, whereas scattering events corresponding to $\Delta E_- > 0$ occur between the rightward moving branch and the leftward moving branch of the parabolas $1_R \rightarrow 2_L$. These are back scattering events which require a momentum change $2k_F$.

In the gray value parts of the Figures 4.5 and 4.6 we have plotted the calculated voltage drop $\Delta U_{sd} = N\Delta E_{\pm}/e$ for both forward and backward scattering events, using $N = 50$ periods, a line density of $n_{1D} = 1.2 \times 10^{15} \text{ d 1/m}$ and $n_{1D} = 1.3 \times 10^{15} \text{ d 1/m}$, respectively, resulting in Fermi vectors $k_F = \pi n_{1D} = 5.65 \times 10^7 \text{ 1/m}$ and $k_F = \pi n_{1D} = 6.13 \times 10^7 \text{ 1/m}$, respectively. The momentum change $\Delta k_y = eBd/\hbar$ was calculated using the superlattice period $d = 15 \text{ nm}$ as tunneling distance.

Comparing the experimental data with the calculation, the sudden increase of the ground state to ground state tunneling peak coincides with the calculated back scattering resonance position. Surprisingly, the current maxima, that rapidly shift to larger source-drain voltages with increasing magnetic field, seem to correspond to the forward scattering resonance condition. In Figure 4.6 the fact that the ground state to first excited state resonance peaks cease to exist at around $B = 1 \text{ T}$ is therefore explained by the fact that forward scattering becomes more favorable at these fields.

4.4.3 Theory for the tunneling current increase

In Figure 4.8 we explain why the tunneling current is increasing with increasing magnetic field. Forward and backward moving electrons are shifted to opposite sides of the wire due to the Lorentz force. In single ballistic quantum wires this effect has been found to

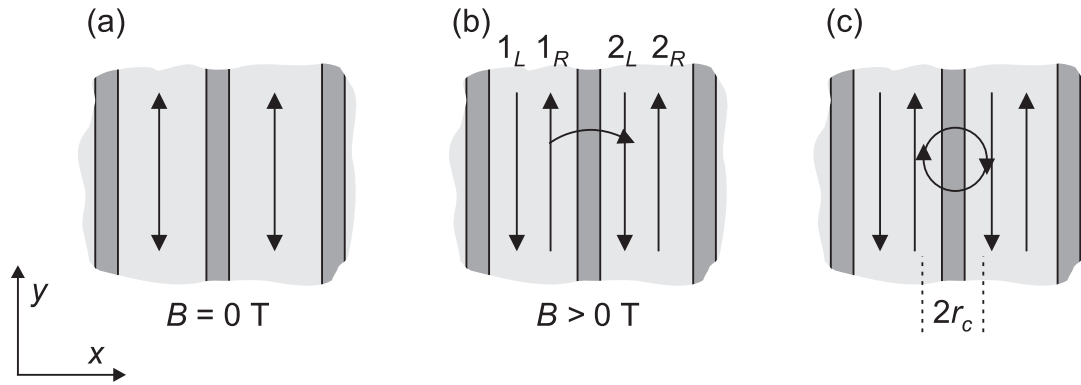


Figure 4.8: Tunneling probability and cyclotron radius.

result in a suppression of the back scattering probability and an increase of the wire conductivity [Rot00]. For our experiment it is important to realize that as the magnetic field is increased, the effective tunneling distance between the forward moving electrons 1_R and the backward moving electrons 2_L decreases, and the tunneling probability thus increases. This effect explains our experimental observation of an increasing source-drain current with increasing magnetic field. Eventually, for magnetic fields so large that the cyclotron radius of the tunneling electron $r_c = \hbar k_F / (eB)$ becomes smaller than half the period of the superlattice, tunneling is effectively quenched. For the Fermi vector $k_F = 5.65 \times 10^7$ 1/m used before, the critical magnetic field is $B = 5$ T, in nice agreement with the experimental observation of a quenching of the tunneling current for $B > 6$ T.

Interestingly, the quenching of the source-drain current at high magnetic fields is relieved by a sufficiently large source-drain voltage. This observation is reminiscent to the tunneling experiment by H. Stormer, W. Kang *et al.* between the edges of a quantum Hall system [Sto00]. The parabolic magnetic confinement potential of both neighboring systems overlap in the superlattice barrier, and an applied electric field results in an effective barrier lowering, and thus an increasing source-drain current.

4.5 Resonant tunneling in a parallel magnetic field

In this section we discuss current-voltage traces obtained in a magnetic field $B_{parallel}$ parallel to the tunneling current, and perpendicular to the quantum wires, as defined in Figure 4.1. We present experimental data for a fixed gate voltage, and qualitatively explain the results.

4.5.1 Experimental current-voltage traces

In Figure 4.9(b) we plot the $B = 0$ T trace (black) and the $B = 14$ T trace (gray), obtained for a fixed gate voltage $U_g = 0.75$ V. The traces have manually been offset by $\Delta I_{sd} = 50$ nA for clarity. As can be seen, the ground state to ground state peak barely shifts between $B = 0$ T and $B = 14$ T, and also the double peak at $U_{sd} = 56$ mV remains unchanged. As expected for a magnetic field parallel to the current, the tunneling current level I_{sd} in the plateau region is also unchanged. When we trace the ground state to first excited states in the gray value plot, however, a quite complicated behavior is found. In region *A* for fields between $B = 0$ T and $B = 2$ T, the positions of these current peaks orderly increase with increasing magnetic field. In region *B* we observe a rather linear increase of current maxima, whereas in the high-field region *C* these maxima become magnetic field independent. In addition, at the beginning of region *C* diamond-shaped anticrossing features are observed. The $B = 14$ T trace has additionally been expanded by a factor of 10 in the current-voltage plot to make visible the current oscillations. The period of the current oscillations at this field is $\Delta U_{sd} = 30$ mV.

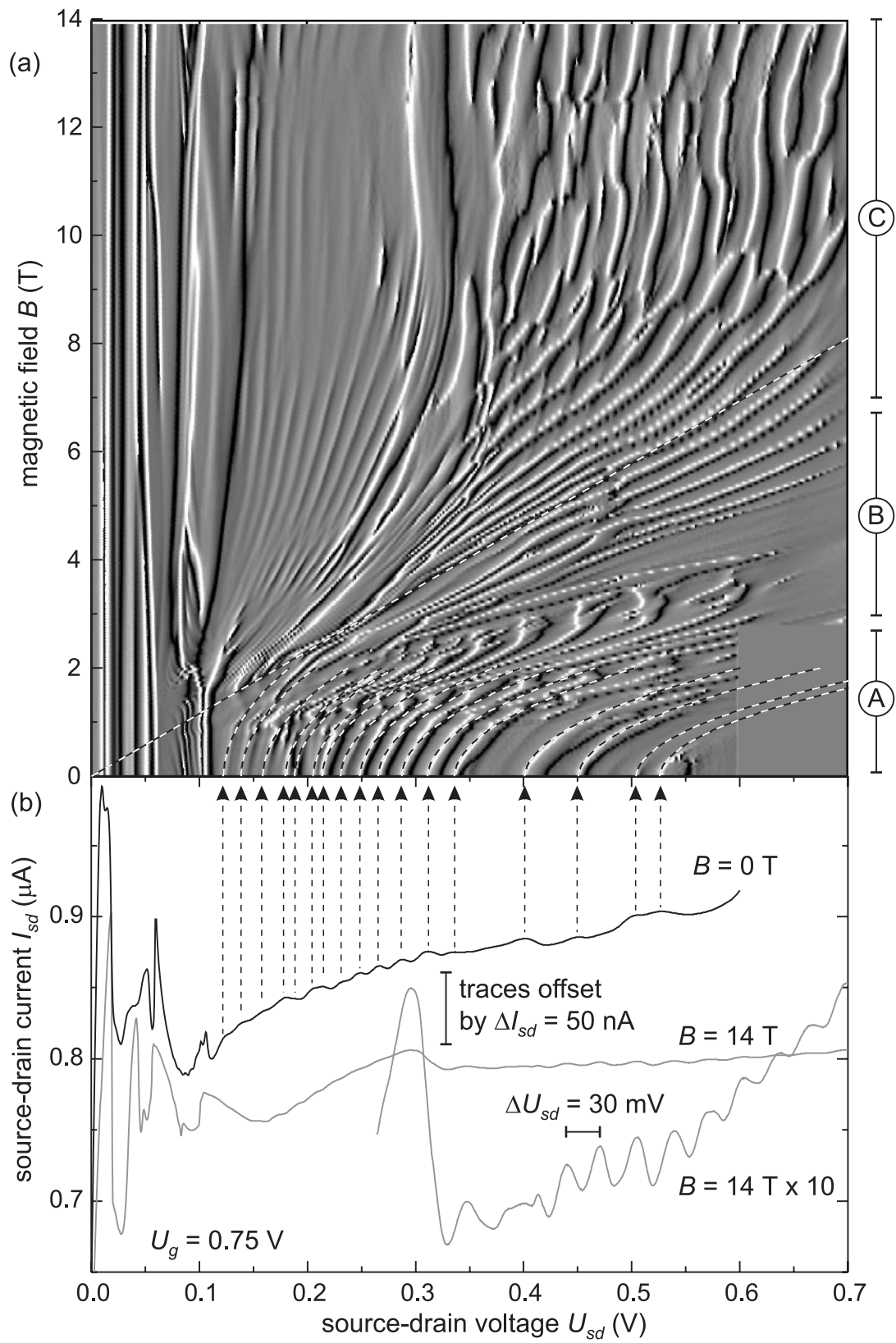
4.5.2 Qualitative model

A magnetic field applied parallel to the current direction does not exert a Lorentz force on the tunneling electrons, the tunneling path is therefore independent on the magnetic field strength. The energy levels, however, are still changed by the field. The ground state to ground state tunneling will be unaffected by this change, since the ground states of all wires are changed in the same manner. This explains our experimental observation of a constant position for the ground state to ground state tunneling peak. The relative energy difference Δ between the ground and the first excited level, however, will depend on the magnetic field. As long as B can be treated as perturbation to the energy levels, i.e. $\hbar\omega_c < \Delta = 15$ meV, or $B < 8$ T, the first order correction to Δ will be quadratic in B . Any given wire will contribute an energy shift quadratic in B to the total voltage drop U_{sd} across the superlattice, which for wire n can therefore be written as

$$U_{sd}^{(n)}(B) = n\Delta(1 + cB^2) \quad (4.5)$$

In Figure 4.9(a) we have plotted the resulting parabolas, using $c = 0.12$ as fit parameter. As can be seen, in region *A* this theory results in an excellent fit.

In order to explain our observation of a linear shift of the current maxima in region *B*, we assert that in this regime we observe inter-Landau level tunneling between quantum



R. A. Deutschmann *Two dimensional electron systems in atomically precise periodic potentials* (2001)
 Ph.D. Dissertation, Selected Topics of Semiconductor Physics and Technology, ISBN 3-932749-42-1
 Figure 4.9: Current-voltage relation in parallel magnetic field at $U_g = 0.75$ V.

wires. Inter-Landau level tunneling has been observed between the quantum wells of a bulk superlattice [Hig89]. In ideal systems, inter-Landau level tunneling is forbidden since harmonic oscillator eigenfunctions are orthogonal. This selection rule, however, is relaxed by variations in the z direction electric field between adjacent wires, as well as any scattering processes, such as interface roughness and impurity scattering (elastic), or phonon emission (inelastic). Can we speak about Landau levels in a one-dimensional system? If the magnetic field is strong enough, and the magnetic length becomes comparable to the quantized wire dimensions (the z direction in our case), the system is no longer strictly one-dimensional, so that the formation of Landau levels is perceivable. In order to find the energy scale for inter-Landau level tunneling, we calculate the expected voltage drop across the superlattice if all wires were tunneling from the lowest to the first Landau level

$$U_{sd}(B) = N \frac{\hbar}{m^*} B, \quad (4.6)$$

where $N = 50$ is the amount of quantum wires in the superlattice. The resulting resonance condition is plotted in Figure 4.9(a) as a straight line from point $(B, U_{sd}) = (0 \text{ T}, 0 \text{ V})$ to $(B, U_{sd}) = (8.1 \text{ T}, 0.7 \text{ V})$. As can be seen, the prevailing tunneling mechanism in region B in fact is consistent with inter-Landau level tunneling. To our knowledge, inter-Landau level tunneling between one-dimensional systems has not been observed to date.

In the high-field region C for fields $B > 8 \text{ T}$, the magnetic field cannot be treated as a perturbation to the zero-field eigenstates. We observe magnetic field independent current maxima with a period larger than the zero-field oscillation period. For this regime we do not have a theory at present.

4.6 Conclusion

In this chapter we have presented a superlattice consisting of weakly coupled quantum wires. The dominant transport mechanism was found to be resonant tunneling, rather than miniband transport as in previous chapters. We have identified two main tunneling processes. First, ground state to ground state tunneling occurred at electric fields close to zero. The observability of this process is possible in the SLFET because the Fermi level in the contacts can be raised to match the wire ground states by means of the gate. The second tunneling process occurred between the ground state and the first excited wire state, and resulted in a series of almost periodic current oscillations.

Transport through the superlattice was greatly affected by the application of magnetic fields perpendicular to the wires. A magnetic field applied perpendicular to the current di-

rection, in a simple picture, resulted in a distortion of the tunneling path, and in an effective splitting and shift of the resonance condition. We have found signatures of both forward and back scattering tunneling events. In a parallel magnetic field orientation a direct observation of the energy level change with magnetic field was possible. Furthermore, at higher magnetic fields, inter-Landau level tunneling between quantum wires may explain the observed linear shift of the resonances. Current oscillations in the high-field regime await an appropriate theory.

Although we have been able to account for most of the experimental findings, our theory can be quantified by a number of ways. Self-consistent and quantum mechanical calculations of the wire eigenstates without and with an applied magnetic field should be performed. The transport via resonant tunneling should be calculated self-consistently using Poisson and continuity equations with appropriate tunneling and relaxation times, and using the correct potential distribution in the channel. The tunneling process can be modelled more realistically, taking into account the finite Fermi energy, the magnetic field dependent transmission probability across the barrier, the change of the electron wave function and density distribution in the wires at an applied magnetic field, the density of states, and the finite temperature.

We remark that our SLFET may be considered as a model for coupled one-dimensional correlated electron systems, or Luttinger liquids. Luttinger liquids are quintessential scale-invariant non-Fermi liquids with correlation functions exhibiting power-law behavior, typically with anomalous exponents [Rot00]. In the past few years experimental evidence has been gathered for static or dynamic charge inhomogeneity in several strongly correlated electronic systems, such as high-temperature superconductors, and quantum Hall systems. In two dimensions these structures are linear and are known as stripes. Stripe phases may be insulating or conducting. Kivelson and coworkers [Car00] have recently proposed that quite generally the quantum mechanical ground states, and the thermodynamic phases which emerge from them, can, on the basis of broken symmetries, be characterized as electronic liquid crystal states. In their theory, a conducting stripe ordered phase is an electronic smectic state, while a state with only orientational stripe order (such as is presumably observed in quantum Hall systems) is an electronic nematic state. In their recent analysis [Eme00], which is asymptotically exact in the limit of weak interstripe coupling, they find that in addition to an insulating stripe crystal phase, a variant of a Wigner crystal, there exist stable smectic phases, one of which is a stripe ordered smectic superconductor. We suggest that the SLFET may serve as an ideal device to test these theories in an array of weakly interacting Luttinger liquids.

Chapter 5

Quantum interference in artificial band structures

The fundamental understanding of solid state physics greatly gained from the study of metals. In 1930 people like Landau, Shubnikov, de Haas and van Alphen inaugurated the rise of Fermiology, which culminated in an explanation of magnetoresistance oscillations from the metallic band structure by Onsager, Lifshitz, Shoenberg, Pippard and others in the '50 and '60. With the invention of the semiconductor superlattice in 1969 by Esaki and Tsu, artificial band structures could be designed and have extensively been studied until today.

In this chapter we try to complete the circle to the metals by making visible hitherto undisclosed band structure effects, and quantum interference phenomena previously observed in metals. First, within the previously fabricated lateral surface superlattices (LSSLs) we position our cleaved-edge overgrowth superlattice field-effect transistor (SLFET) and point out its peculiar features. Then our experimental results are presented, together with our semiclassical model for their explanation, and the relation to metal physics is established. In a trailing section we present another novel type of LSSL fabricated using a focused laser beam.

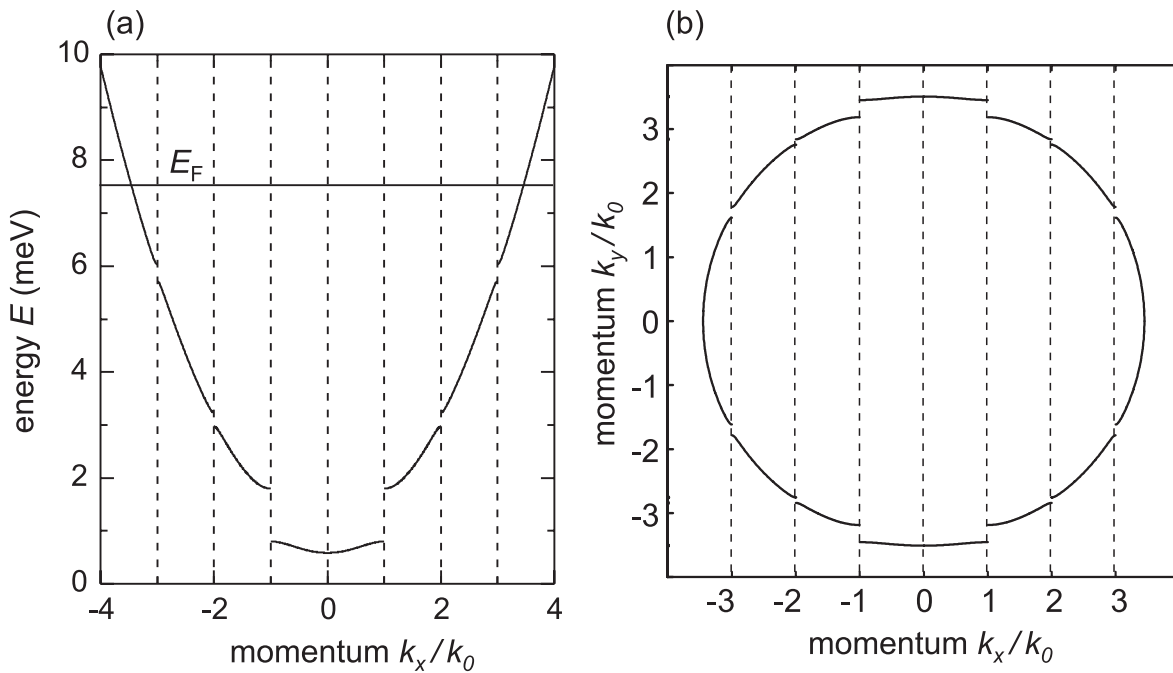


Figure 5.1: (a) Band structure of a periodically modulated system in the extended zone scheme. The Brillouin zone boundary is $k_0 = \pi/d$, where d is the modulation period. (b) Fermi contour of the modulated system.

5.1 Artificial band structures

In this chapter we are interested in studying weakly modulated electron systems. The term 'weakly' refers to the fact that the amplitude of the perturbing potential V_0 is much smaller than the Fermi energy E_F of the system. Equivalently, the electron density modulation amplitude is much smaller than the electron density. When a perturbing potential of period d in x direction is applied to a two-dimensional electron system, the parabolic dispersion relation of the free system is modified mainly at the Brillouin zone boundaries $k_x = nk_0$, $n = \pm 1, \pm 2, \dots$; $k_0 = \pi/d$, where small energy gaps open up. This situation is shown in Figure 5.1(a), where we have calculated the dispersion relation using the Kronig-Penney model with a modulation amplitude $V_0 = 1.6$ meV.

Since we are only concerned with one-dimensional modulation patterns, in a two-dimensional electron system the electrons can move freely in y direction, where the dispersion is parabolic. The resulting Fermi contour for Fermi energy $E_F = 7.5$ meV is shown in Figure 5.1(b). The contour resembles the known Fermi circle for undisturbed two-

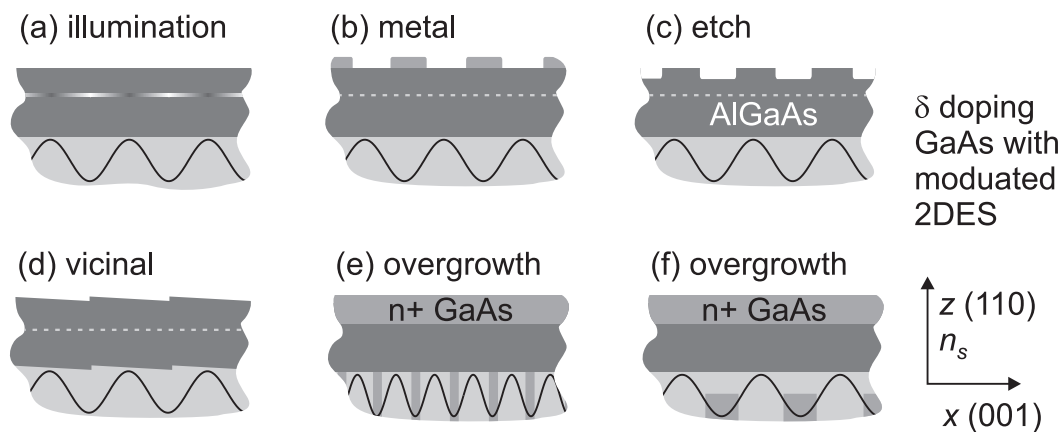


Figure 5.2: Overview of lateral superlattice patterning methods. Shown is the heterostructure, the density $n_s(x)$ of the modulated electron gas, and relevant patterning features. (a) Holographic illumination. The DX centers in the donor layer are partially ionized. (b) Metallic top gates. (c) Shallow etching. (d) Growth on vicinal surfaces. (e) Cleaved-edge overgrowth. (f) Cleaved-edge overgrowth with set back superlattice, represents the SLFET investigated in this chapter.

dimensional systems, only at the Brillouin zone boundaries the closed contour is interrupted. In the following we will learn about the consequences of this change in topology on the magnetotransport of electrons.

How can such model systems actually be fabricated? Two classes of fabrication methods can be distinguished, and we have summarized the most prominent methods schematically in Figure 5.2. The first class modifies surface properties of a two-dimensional electron gas to achieve a periodic density modulation. A special type of magnetoresistance oscillations, the Weiss oscillations, have first been observed in devices fabricated by holographic illumination of a modulation doped heterostructure [Wei89] [Ger89], see Figure 5.2(a). These Weiss oscillations will be discussed in more detail in Section 5.3.7. The fringe pattern of two interfering laser beams locally ionizes the DX centers at low temperatures to produce one-dimensional or two-dimensional density modulations. This *in situ* method is of great versatility, as different superlattices can be fabricated on the same sample in different cool-downs. It is, however, limited to weak potential modulations, and period lengths only down to $d = 265$ nm have been reported [Wei92], naturally limited by the wavelength of the used laser. Many groups have resorted to using metallic top-gates to locally deplete the underlying electron gas [Win89], see Figure 5.2(b). Although the electron density can be varied

by changing the gate voltage, at the same time the potential modulation amplitude is altered. Additionally, a contribution to the electron density modulation results from the strain caused by the different thermal expansion constants of the metal and GaAs [Lon99]. Strain is avoided by shallow etching a modulation doped heterostructure, which due to surface depletion results in the desired electron density modulation [Mue94], see Figure 5.2(c). High electron mobilities are pertained such that even composite Fermions could be studied in these samples [Sme98], and evidence of Hofstadter's fractal energy spectrum in the quantized Hall conductance has been gathered [Alb01]. Generally, with methods that modify the sample surface properties, period lengths not much below the distance between the surface and the two-dimensional electron gas can be achieved.

A second class of patterning methods modifies the very vicinity of the electron gas, and uses self-organized growth methods rather than lithography. This way much shorter period lengths can be obtained. One exploits the corrugated growth on high-index surfaces and the fact that atomic steps modify the electrostatic potential in a two-dimensional electron gas, see Figure 5.2(d). Experiments were performed using metal-oxide-semiconductor structures prepared on high-index silicon [Col77] [Mat82], and p InSb [Eve86] surfaces. On vicinal (111)B GaAs surfaces multi-atomic steps with a periodicity of a few tens of nanometers were generated [Nak98] [Sak99], similar devices were fabricated on GaAs (001) vicinal planes [Fuk88] [Mot89] [Tsu90]. All these structures have the advantage of small period modulations, but due to the self-organized growth, the superlattices are irregular and fine structures, such as narrow minigaps in the artificial band structure, are smeared out.

With the cleaved-edge overgrowth technique the best of both worlds can be combined. The electron gas is directly accessed to generate a short period potential modulation, and the preciseness of molecular beam epitaxy growth guarantees highly regular superlattices. The first such superlattice, invented by Stormer et al. [Sto91b], was very strongly modulated, and no superlattice effect was reported. Magnetotransport on similar samples revealed the formation of one-dimensional subbands [Ohn95] and an enhancement of the effective electron mass in the lowest miniband [Maj00]. Our SLFETs, investigated in Chapter 2, 3 and 4, are modified with respect to these devices, and schematically shown in Figure 5.2(e). A two-dimensional electron gas is field-induced within a perpendicularly oriented a superlattice. SLFETs combine high electron mobility, atomically precise potential modulation, and electron density tunability. The SLFET investigated in this chapter is schematically shown in Figure 5.2(f). A weak potential modulation is obtained by a set back superlattice. Period lengths are comparable to the shortest period lengths reported in the literature on lateral sur-

face superlattices, while the preciseness is unprecedented. This device will be discussed in detail in the following section.

Other methods have been developed for the fabrication of special superlattices, which include laser interference melting of the heterostructure surface [Neb97], and surface oxidation of the sample surface by the conductive tip of an atomic force microscope [Hel98]. In Section 5.4 of this chapter we demonstrate the successful fabrication of lateral surface doped superlattices using a focused laser beam.

The theoretical understanding of the experimental results on the SLFET, presented in this chapter, was developed in collaboration with C. Albrecht and J. Smet, Max-Planck-Institut für Festkörperforschung, Stuttgart. In an independent work they observed different electron orbits in lateral surface superlattices with two-dimensional modulation [Alb98a] [Alb98b]. Our work represents the first demonstration of different electron orbits in the textbook one-dimensional case. Part of this work has previously been published in [Deu00b] and [Deu01c]. The work on the superlattices fabricated by focused laser beam induced doping was done in collaboration with C. Stocken and has previously been published in [Deu01a].

5.2 Self-consistent calculation

The vast majority of studies on low-dimensional electronic structures is performed using gated heterostructures. The calculation of the electron density in dependence of the gate geometry, the gate voltage and the distance between the gate and the two-dimensional electron system requires the correct modelling of mechanical strain due to the different elastic constants of the gate metal and the superlattice material. The electronic structure in the SLFET can be calculated using the layer thicknesses and material composition, which are defined to atomic precision by the molecular epitaxy beam growth. Comparable calculations [Tok89] [Tok90] have only been performed for fractional layer superlattice devices which cannot be applied to the present case because of the different geometry. In this section we present calculations of the electron density, the electrostatic potential and the band structure obtained with a two-dimensional Poisson-Schrödinger solver [Rot99a][Rot00]. We demonstrate that it is crucial to consider the two-dimensionality of the problem, as the electron density is found to be modulated not only laterally in the plane of the two-dimensional electron gas, but also in the z direction, contrary to what is commonly assumed for gated structures.

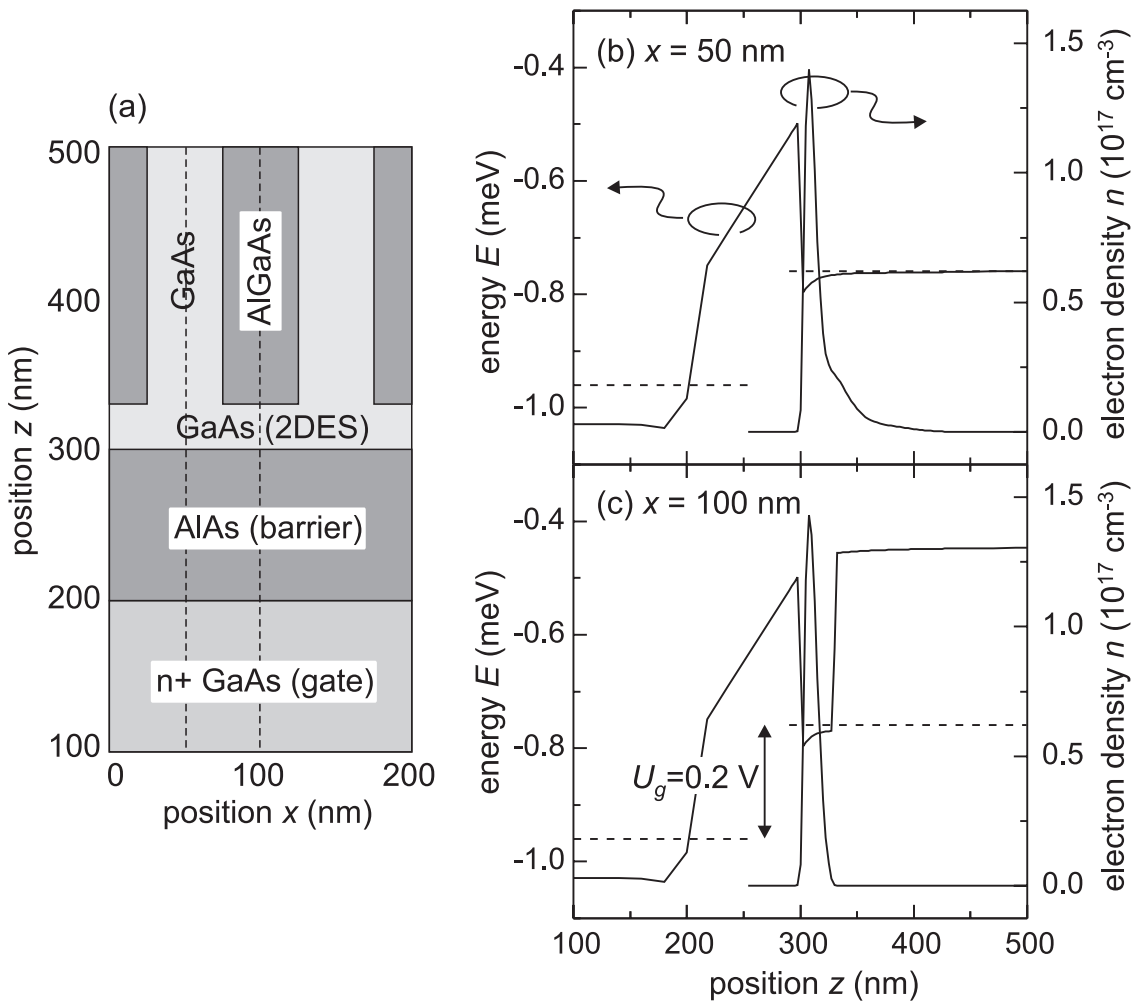


Figure 5.3: (a) Part of the SLFET structure, schematically drawn to scale. (b),(c) Self-consistently calculated conduction band profile and electron density, shown is a cut in z direction at superlattice well position $x = 50$ nm (b) and at superlattice barrier position $x = 100$ nm (c).

5.2.1 SLFET structure and electron density

The superlattice field effect transistors (SLFETs) under investigation in this chapter consist of a 30 period 50 nm GaAs/50 nm $\text{Al}_{0.3}\text{Ga}_{0.7}\text{As}$ superlattice grown in (001) direction, sandwiched between two n^+ GaAs contacts. In (110) direction the layer sequence consists of q nm GaAs, a 100 nm AlAs barrier, and a 200 nm n^+ GaAs gate contact. We investigate SLFETs with q between 10 nm and 40 nm. In reference samples the superlattice was re-

placed by a $3\mu\text{m}$ AlGaAs layer with reduced aluminum content of only 5%. For the present calculation we consider an SLFET with $q = 30$ nm.

The SLFET is simulated in the (x, z) plane, and part of the simulated structure is shown in Figure 5.3(a). Two Fermi systems are defined, one includes the gate contact, the other the two-dimensional electron gas. The gate voltage is defined as the potential difference between these two Fermi systems. In Figures 5.3(b) and (c) one-dimensional cuts through the two-dimensionally calculated conduction band and electron density are displayed for $x = 50$ nm (through the superlattice well) and $x = 100$ nm (through the superlattice barrier). A gate voltage of $U_g = 0.2$ V is assumed here. The electron gas is localized close to the gate barrier at $z = 300$ nm, and extends to larger distances towards the z direction for the case of the superlattice well. For the case of the superlattice barrier, the electrons are entirely confined in the (110) GaAs well.

The calculated three-dimensional electron density distribution is shown in Figure 5.4(a). The electron gas is localized close to the gate barrier, but as can be seen from the contour lines, it extends into the superlattice wells. The density modulation becomes apparent when the electron density is integrated over the z direction to obtain the two-dimensional density n_s , as shown in Figure 5.4(b). At x positions of the superlattice well, n_s is increased with respect to the mean density. In Figure 5.4(c) we show cuts through the three-dimensional electron density in x direction for different z positions. As expected, in or close by the superlattice, the electron density is enhanced in the well region. Even at $z = 350$ nm, far within the superlattice, a significant electron density is observed. More counterintuitive, within the (110) GaAs region between $z = 315$ nm and $z = 305$ nm, the electron density is enhanced in the barrier region at $x = 0, 100, 200$ nm.

5.2.2 Potential modulation

In accord with the three-dimensional electron density the potential distribution in Figure 5.5(a) is found. The overall potential drops towards the gate due to the applied gate voltage, resulting in the two-dimensional electron gas at the gate barrier. In Figure 5.5(b) we show cuts of the potential distribution in x direction for different z positions. In the superlattice well region the potential is enhanced, and the potential equals the Fermi energy $\Phi = 0$ V at about $z = 400$ nm.

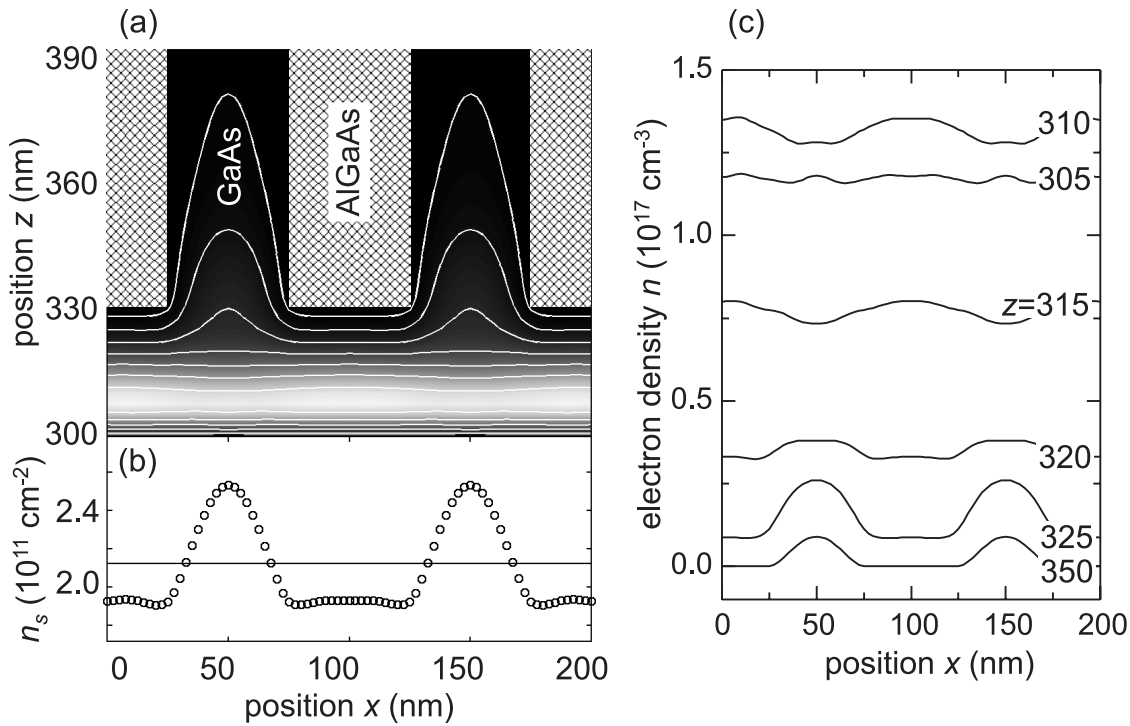


Figure 5.4: (a) Self-consistently calculated three-dimensional electron density distribution for a (110) GaAs layer of thickness $q=30$ nm (gray scale coded). (b) Electron density integrated over the z direction to obtain the sheet electron density $n_s(x)$. The mean two-dimensional electron density is $n_s = 2.1 \times 10^{11} \text{ cm}^{-2}$. (c) Cuts of the calculated three-dimensional electron distribution in x direction for different z positions.

5.2.3 Potential modulation amplitude

In the literature on surface lateral superlattices, it is customary to consider the electron density variation Δn_s in superlattice direction, and the potential modulation amplitude V_0 as proportional values,

$$\Delta n_s = D_0 V_0, \quad (5.1)$$

where $D_0 = m^*/\pi\hbar^2$ is the constant density of states for a two-dimensional electron system in GaAs. V_0 can then be used as input parameter for a band structure calculation. For the SLFET, the situation is more complicated, because of the variation of the electron density and the potential in z direction, as discussed in the previous two sections. We derive a potential modulation amplitude V_0 for the SLFET by weighting the potential modulation amplitude evaluated at a fixed z position with the electron density at that z position. By way of this

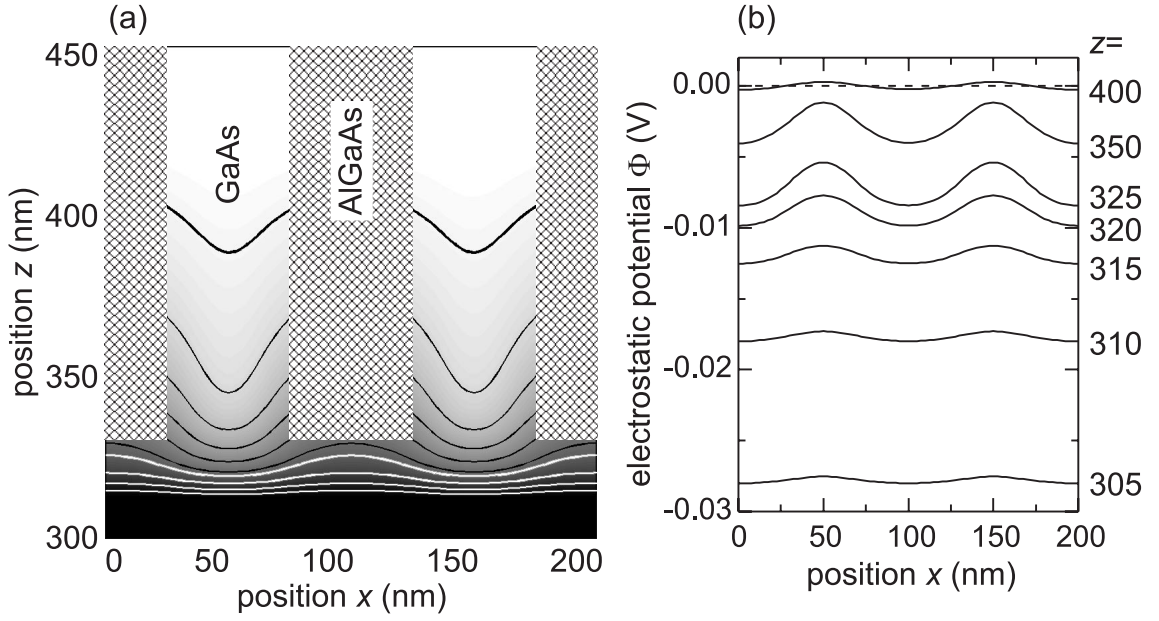


Figure 5.5: (a) Self-consistently calculated potential distribution, corresponding to the electron density distribution shown of Figure 5.4 with mean two-dimensional electron density of $n_s = 2.1 \times 10^{11} \text{ cm}^{-2}$. The potential is plotted gray scale coded, and the contour lines are displayed in black and white for better visibility. The Fermi line at around $z = 400 \text{ nm}$ is plotted thicker. (b) Cuts through the potential distribution in x direction for different z locations. The Fermi energy is plotted as a dashed line at $\Phi = 0 \text{ V}$.

method, we take into account that the potential modulation in superlattice direction is smaller at z positions with high three-dimensional electron density. In Figure 5.6(a) in solid symbols we plot V_0 in dependence of the electron density, calculated for the SLFET with (110) GaAs layer thickness of $q = 30 \text{ nm}$. On the right axis V_0 is expressed as a percentage of the Fermi energy. The potential modulation is on the order of 1 meV , or between 5 and 10 percent of the Fermi energy. For comparison in open symbols we also show the potential amplitude evaluated according to relation (5.1). V_0 is much larger in this case. In Figure 5.6(b) we calculate V_0 for constant electron density of $n_s = 2.1 \times 10^{11} \text{ cm}^{-2}$ in dependence of q . The potential modulation decreases exponentially with increasing q , and the interesting region, investigated in this chapter, is underlaid with gray.

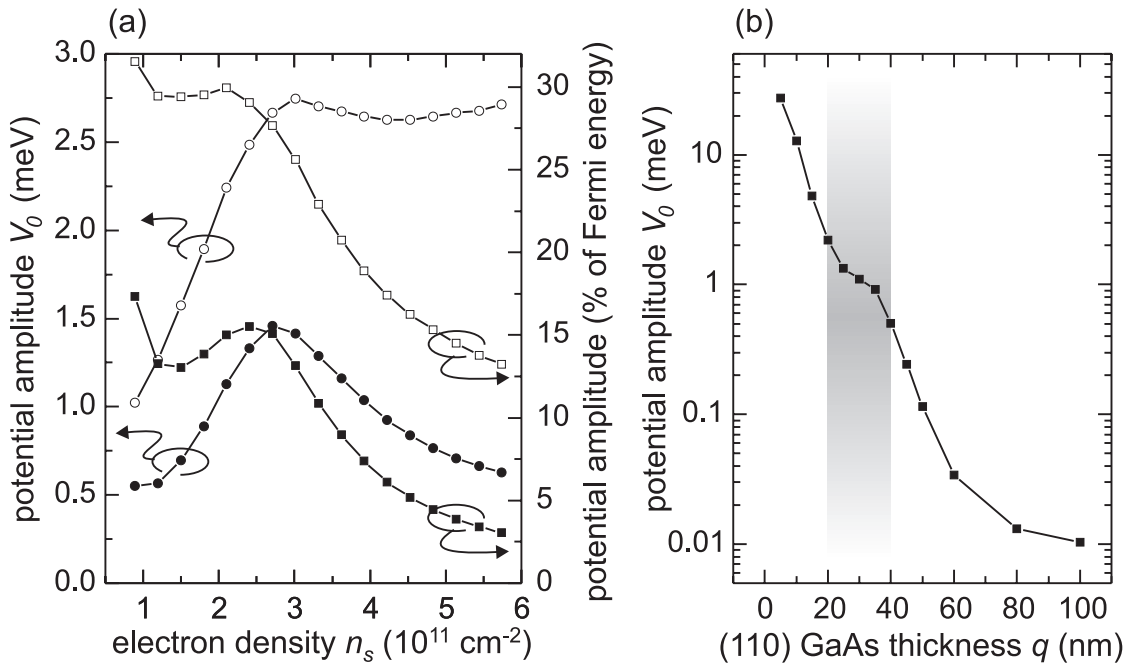


Figure 5.6: Calculated potential modulation amplitude V_0 . (a) V_0 versus electron density, calculated for $q = 30$ nm. Solid symbols: weighted average, open symbols: V_0 calculated directly from the electron density variation, circles: V_0 plotted on an energy axis, square: V_0 expressed as a percentage of the Fermi energy. (b) V_0 for constant electron density $n_s = 2.1 \times 10^{11} \text{ cm}^{-2}$ versus (110) GaAs layer thickness q .

5.3 Magnetotransport experiments

The experiments in this chapter are performed in the measurement scheme shown in Figure 5.7. The lock-in oscillator output drives an AC current $I = 10$ nA (rms) through the superlattice, one of the lower n+ GaAs contacts is grounded, and the gate voltage U_g is applied with respect to ground. The voltage drop across the SLFET is measured with the lock-in between the second pair of contacts to avoid contact resistances and the voltage drop across the leads. All measurements are performed in liquid ^3He at the base temperature of $T = 330$ mK. The field of a superconductive 14 T magnet is oriented perpendicular to the two-dimensional electron system in z direction, a sweep rate of 35 mT/min is used.

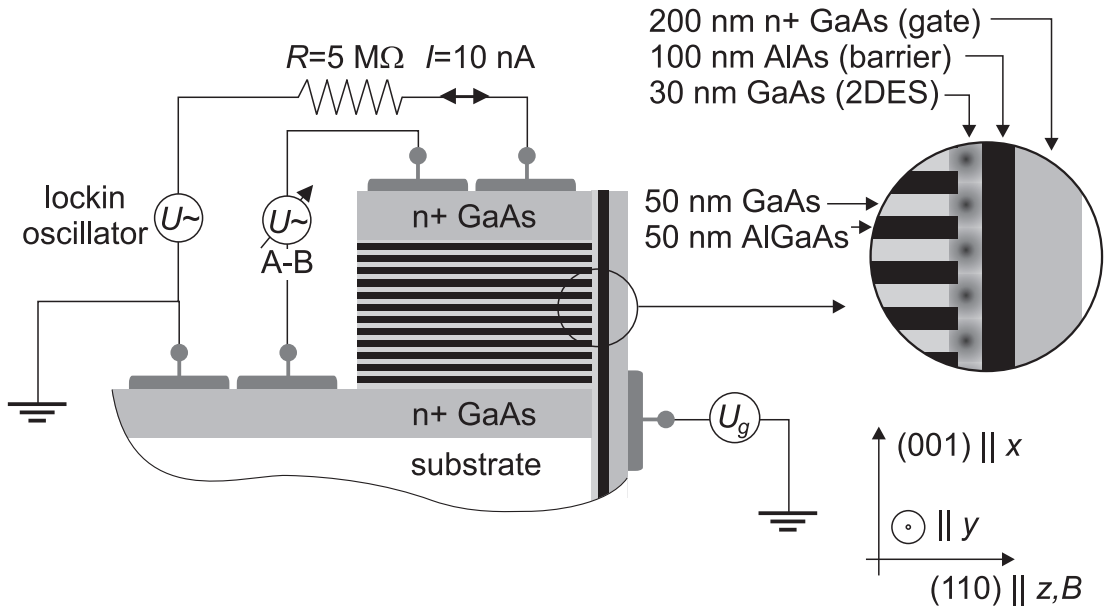


Figure 5.7: Sample structure and measurement scheme.

5.3.1 Magnetoresistance traces

In Figure 5.8 we show the magnetoresistance $R(B)$ of the $q = 40$ nm SLFET and the corresponding $q = 40$ nm CEOFET reference sample, for magnetic fields between $B = 0$ T and $B = 0.5$ T. The resistance $R(B)$ increases quadratically, and oscillations commence at around $B = 90$ mT. In Section 2.3.5 this overall behavior of the magnetoresistance is explained. There it is found that resistance maxima occur at integer filling factors. For the present measurement, however, the SLFET trace seems more complex than the reference sample, oscillation amplitudes vary with magnetic field, and are generally smaller in magnitude.

In order to gain insight into the frequency spectrum of the magnetoresistance, we subtract the non-oscillating background and plot the data versus inverse magnetic field. To make visible the small amplitude oscillations at small magnetic fields, additionally we multiply the data by the inverse magnetic field. This operation only affects the amplitudes, but leaves their frequency unchanged. In Figure 5.9 we show a resulting trace, obtained with the $q = 30$ nm SLFET at a density of $n_s = 1.9 \times 10^{11} \text{ cm}^{-2}$. Three different frequencies can be distinguished even by eye in this presentation of the data. Quantitatively, two of the frequencies are found by a Landau plot, where the minima are indexed. To very good approximation, the minima (or maxima) lie on a straight line, and the magnetoresistance frequency

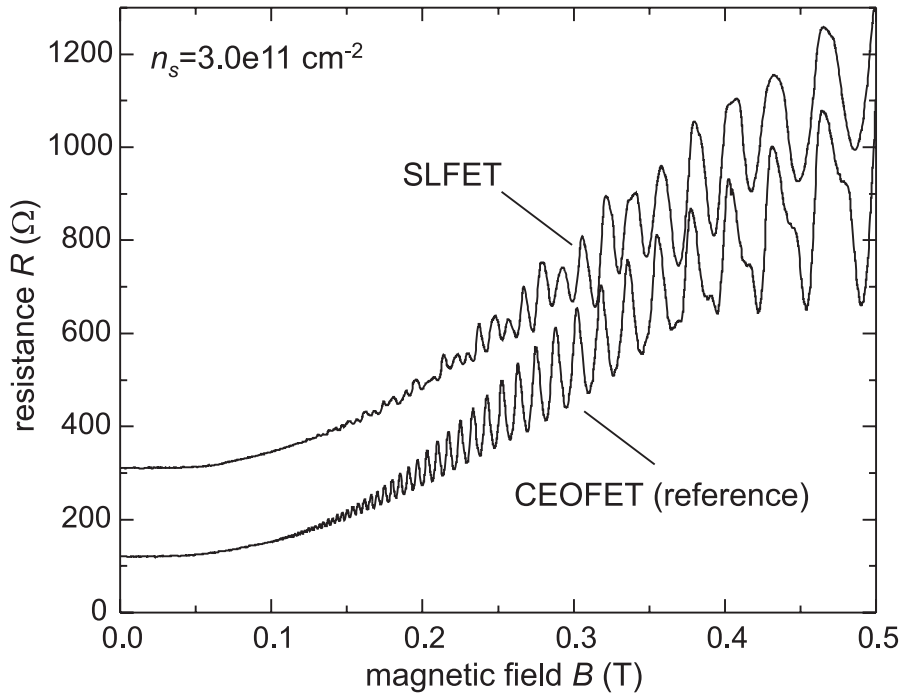


Figure 5.8: Magnetoresistance of the $q = 30$ nm SLFET and CEOFET, recorded for an electron density of $n_s = 3.0 \times 10^{11} \text{ cm}^{-2}$ and plotted versus magnetic field. The SLFET trace has been shifted by $R = 100 \text{ } \Omega$ to make the two traces, that would otherwise overlay on top of each other, distinguishable.

$\Delta^{-1} \equiv (1/B_i - 1/B_{i-1})^{-1}$ for $B > 200$ mT (region A) is $\Delta^{-1} = 3.97$ T, while for $B < 200$ mT (region B) we find $\Delta^{-1} = 2.72$ T. The third frequency component is also $1/B$ -periodic, and appears in the envelope of the magnetoresistance trace for $B > 140$ mT. For better visibility we have traced the envelope of this beating pattern by a dotted line. Maxima and minima of this beating pattern appear at the same magnetic field strengths, we have marked their position by downward pointing triangles. The corresponding frequency is smaller than both of the other frequencies with $\Delta^{-1} = 1.44$ T.

At a different electron density of $n_s = 3.1 \times 10^{11} \text{ cm}^{-2}$, the frequency spectrum is even more complex, as shown in Figure 5.10. Besides the frequency $\Delta^{-1} = 8.41$ T for $B > 167$ mT (region A), the frequency $\Delta^{-1} = 4.9$ T for $167 \text{ mT} > B > 104$ mT (region B), and the beating pattern with $\Delta^{-1} = 1.84$ T, a fourth frequency appears at very small magnetic field $B < 104$ mT (region C) with a frequency of $\Delta^{-1} = 3.18$ T.

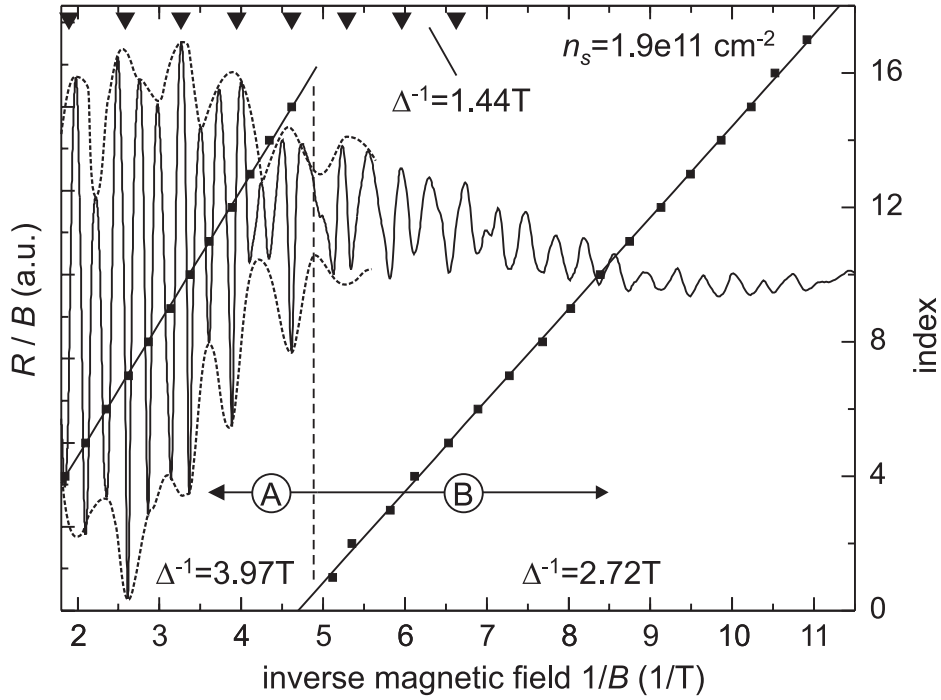


Figure 5.9: Magnetoresistance $R(B)$ of the $q = 30$ nm SLFET at $n_s = 1.9 \times 10^{11} \text{ cm}^{-2}$.

5.3.2 Density dependent study

We have systematically measured the magnetoresistance between $B = 0$ T and $B = 1.4$ T for fixed electron densities between $n_s = 0.45 \times 10^{11} \text{ cm}^{-2}$ and $n_s = 4.6 \times 10^{11} \text{ cm}^{-2}$. Each curve is then Fourier transformed with respect to the inverse magnetic field to obtain the frequency components Δ^{-1} of the magnetoresistance oscillations. The resulting Fourier spectrum is shown in Figure 5.11, where we plot the data on a logarithmic color scale. A quite complex density dependent frequency spectrum is found. The most prominent peak, labelled by A_F^0 , exhibits a linear dependence on electron density. The peak labelled by A_D^1 shows a very different n_s -dependence. The labelling will be used in the following Sections 5.3.5 and 5.3.6, where we explain all frequencies and calculate the lines shown in black and white.

In Figure 5.12 we show the data of the SLFET with (110) GaAs layer thickness $q = 40$ nm, which therefore exhibits a weaker electron density modulation. The evaluation and representation of the data is the same as for Figure 5.11. Both measurements yield the same overall result. It appears, however, that features denominated by A_F^2 and A_D^2 do not show up in the $q = 40$ nm SLFET, where feature A_D^1 is more strongly expressed.

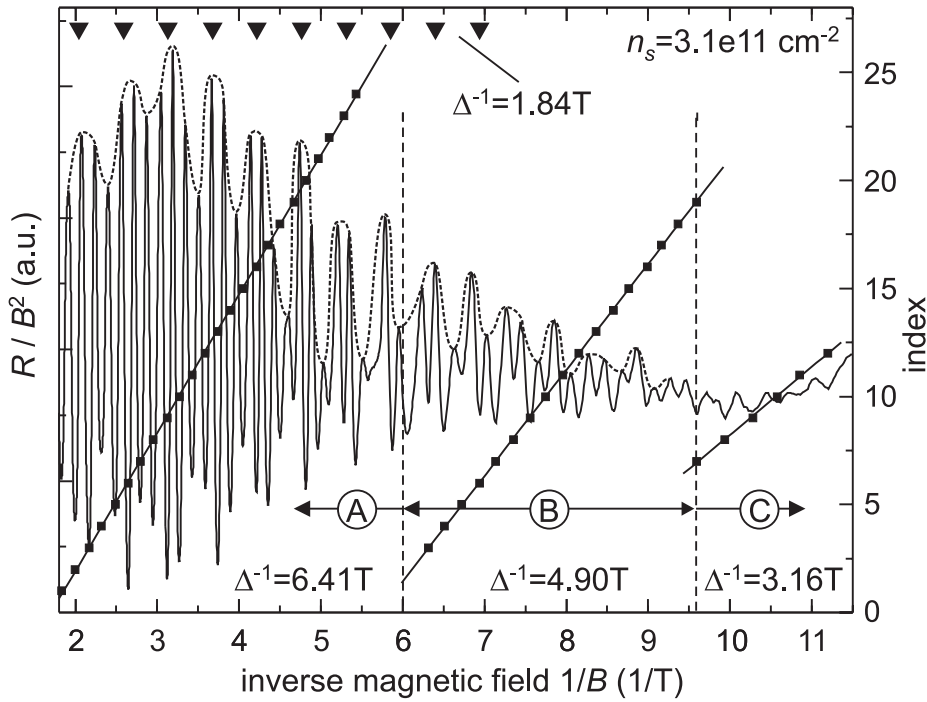


Figure 5.10: Magnetoresistance $R(B)$ of the $q = 30$ nm SLFET at $n_s = 3.1 \times 10^{11} \text{ cm}^{-2}$. $R(B)$ has been multiplied by $1/B^2$ to make visible the small amplitude oscillations at low magnetic fields $B < 100$ mT.

In contrast to the SLFETs, both reference samples exhibit only the single frequency A_F^0 , as shown in Figure 5.13 for the $q = 40$ nm CEOFET. The plot for the $q = 30$ nm device looks identical. Multiples iA_F^0 of the fundamental frequency are introduced by the Fourier transformation, and do not correspond to a frequency in the resistance data.

5.3.3 Electron orbits in a multi-band structure, magnetic breakdown

We analyze the transport data semiclassically using the zero-field band structure, which is a good approximation for the small magnetic fields in this experiment. From the self-consistent quantum mechanical calculations, reported in Section 5.2, we have found that the modulation amplitude V_0 is about 1 meV, and the band structure corresponds to the free electron dispersion, with gaps of below 0.5 meV at the Brillouin zone boundaries. In Figure 5.14(a) we plot the band structure calculated in the Kronig-Penney model using a larger modulation amplitude $V_0 = 1.6$ meV in order to make visible the minigaps in the band structure. We

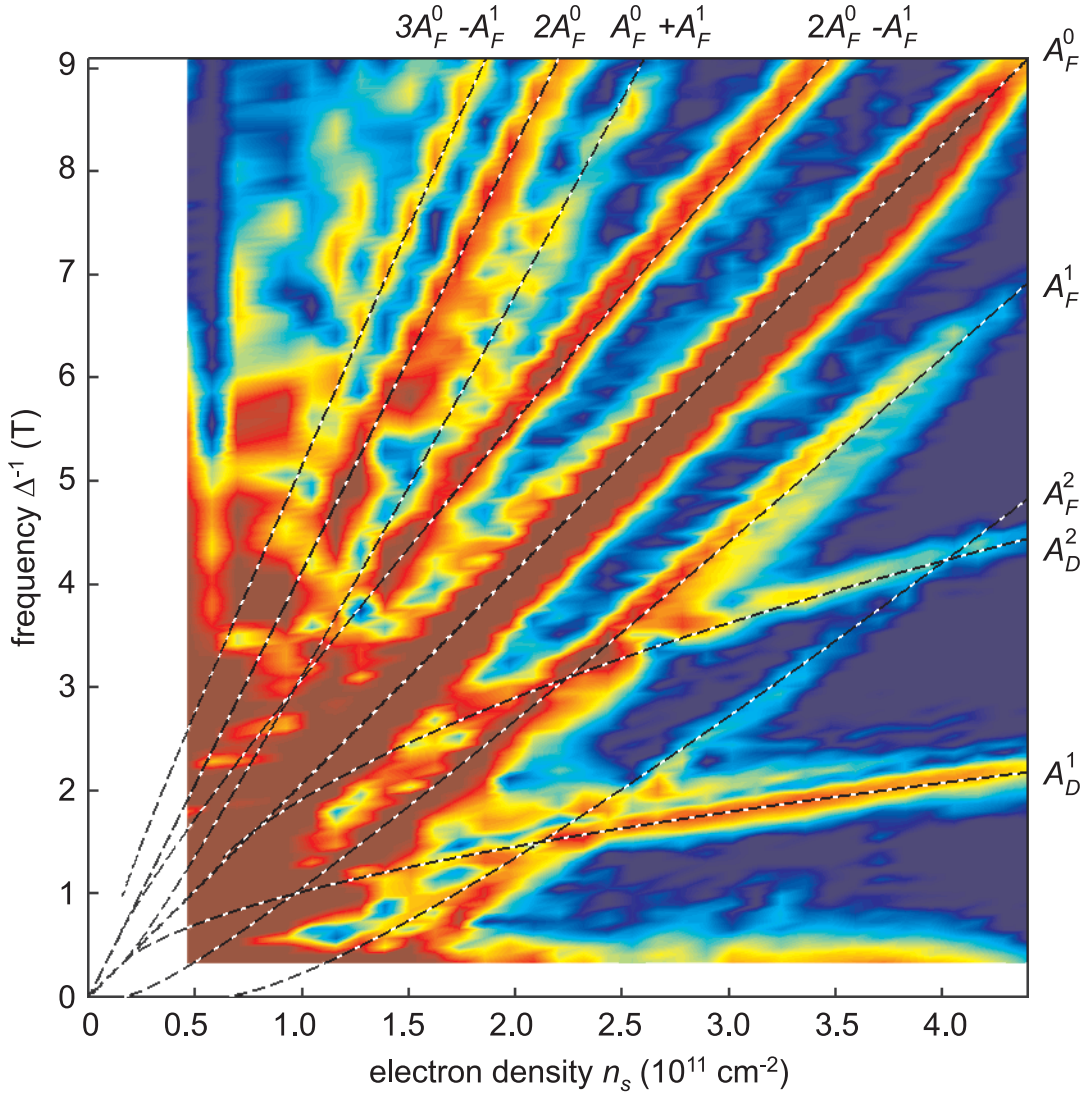


Figure 5.11: Magnetoconductance Fourier spectrum for the $q = 30$ nm SLFET (color scale coded). Large frequency components are shown in red, in blue areas no corresponding frequency is found in the data. The dashed lines are calculated in Sections 5.3.5 and 5.3.6, the indicated labels will be defined there as well.

plot the contours of constant energy E_F of the modulated 2DES using this band structure and the free electron dispersion along the y-direction in Figure 5.14(b). Minibands are assigned an index n that runs from 0 for the energetically lowest lying miniband to N for the last, partially filled miniband. The minibands with index n and $n + 1$ are separated by the minigap denoted as E_n at $k_x = \pm\pi/d$ or $k_x = 0$. For the density range covered in this experiment three

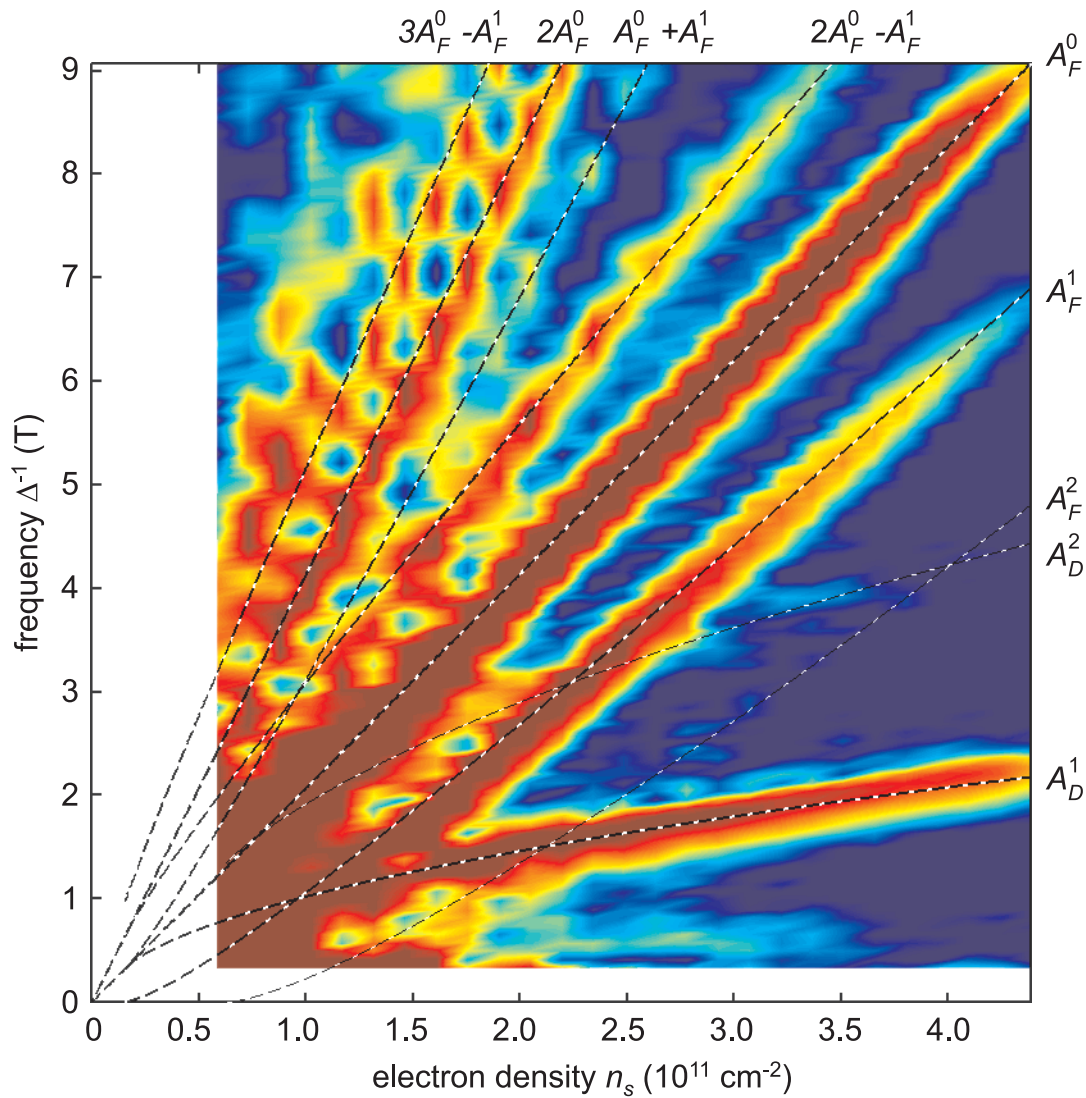


Figure 5.12: Magnetoconductance Fourier spectrum for the $q = 40$ nm SLFET. The same color scale as in Figure 5.11 is used. The dashed lines are calculated in Sections 5.3.5 and 5.3.6.

to six minibands are occupied, and the case of four minibands ($n = 0, \dots, 3; N = 3$) is shown in Figure 5.14. The Fermi contours are drawn in black lines and indexed according to the miniband they are associated with. In general, Fermi contour N is closed, whereas all other contours ($0, \dots, N - 1$) describe open electron trajectories. The electrons trace these contours in a direction fixed by the sign of the magnetic field.

A transition from contour n to its neighbor $n + 1$ entails quantum mechanical tunneling

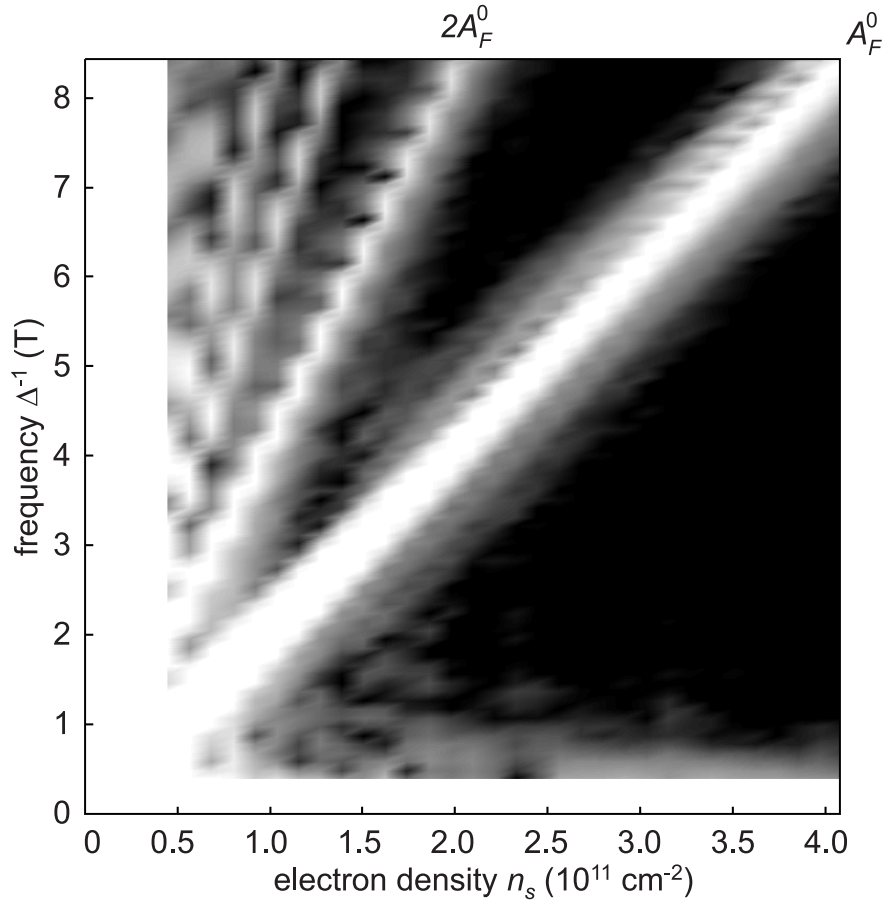


Figure 5.13: Magnetoconductance Fourier spectrum for the $q = 40$ nm reference CEOFET (gray scale coded).

across the gap of size E_n , a process referred to as magnetic breakdown [Coh61] [Blo62]. We have described this mechanism in Section 2.2.8, where we have also used it to remedy the lack of quantum mechanics in the semiclassical description of electron motion, which would entirely be confined to the zero-field Fermi contours. The tunneling probability $p_n(B)$ depends on the Fermi energy E_F , the minigap E_n , and the magnetic field B . It vanishes at $B = 0$ and increases exponentially with B [Sta67]

$$p_n(B) = \exp(-B_n/B), \quad (5.2)$$

where B_n is the critical magnetic field (see Equation (2.28))

$$\hbar\omega_c E_F = E_n^2 \quad \Rightarrow \quad B_n = \frac{E_n^2 m^*}{E_F \hbar e} \quad (5.3)$$

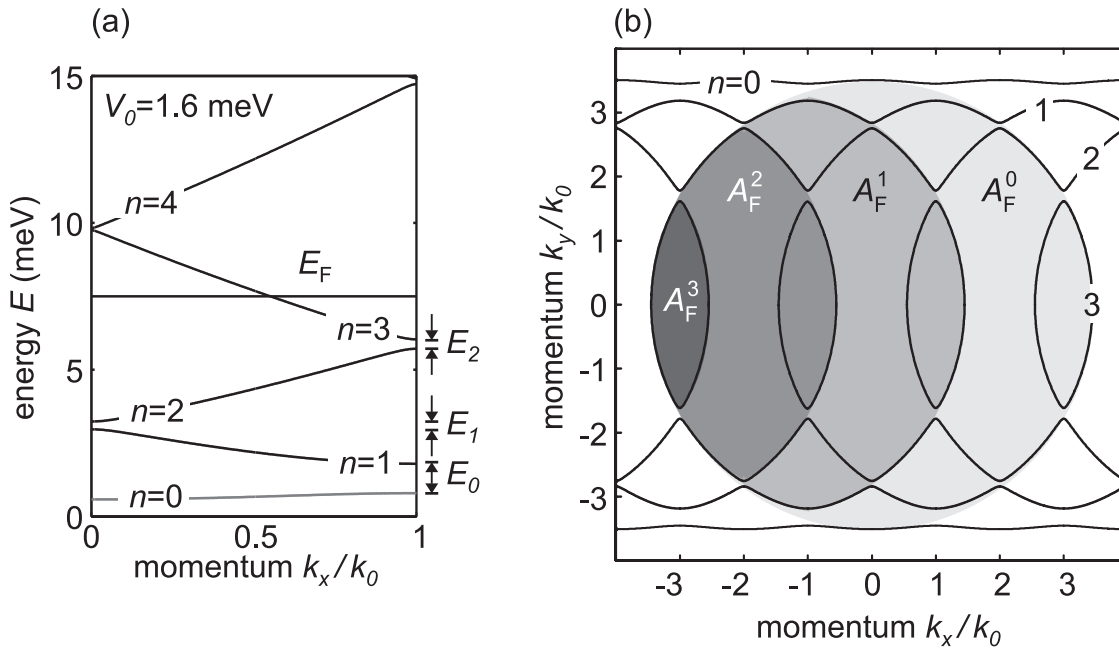


Figure 5.14: Band structure and Fermi contours.

At the lowest B -values, all tunneling probabilities p_n are close to zero, and the only possible closed electron orbit is along contour N . As B is raised though, tunneling probabilities p_n increase, and other closed orbits, composed of segments of contour N as well as segments of open contours with lower index, become possible by virtue of magnetic breakdown. In particular the orbit (hereafter classified according to the lowest contour index n involved), that descends from the closed Fermi contour associated with miniband n before the Fermi energy was raised from miniband n into miniband N , is reactivated. This closed electron path n shares segments of contours n to N and requires a total of $4 \times (N - n)$ tunneling events across gaps of size E_n to E_{N-1} . The product of the corresponding $p_n(B)$ factors determines its probability [Pip62]. This orbit encloses an area A_F^n that can be calculated to a very good approximation in the limit $V_0 \rightarrow 0$:

$$A_F^n = 2k_F^2 \left(\arccos n \frac{k_0}{k_F} - n \frac{k_0}{k_F} \sqrt{1 - (n \frac{k_0}{k_F})^2} \right), \quad (5.4)$$

where k_F is the Fermi wave number and $k_0 = \pi/d$. In Figure 5.14(b), the closed orbit $n = 1$ contains sections of contours $n = 1, 2$ and 3 , involves tunneling across E_1 and E_2 and encircles the light gray area A_F^1 . Orbits $n = 2$ $n = 3$, with corresponding A_F^2 and A_F^3 , drawn in dark gray, cover part of this area.

5.3.4 Probability of electron orbits

The probability p of an electron orbit, that encounters a series of tunneling gaps, is determined by the product of the probability p_i for tunneling across gaps E_i , and the probability $1 - p_j$ for remaining on the the same contour at the junction of gaps E_j [Pip62]

$$p = \prod_{i \in \text{tunnel}} p_i \prod_{j \in \neg \text{tunnel}} (1 - p_j). \quad (5.5)$$

We find for the contours around areas A_{F}^0 , A_{F}^1 , A_{F}^2 and some more complex contours

$$\begin{aligned} p(A_{\text{F}}^0) &= p_1^4 p_2^4 p_3^4 \\ p(A_{\text{F}}^1) &= (1 - p_1)^2 p_2^4 p_3^4 \\ p(A_{\text{F}}^2) &= (1 - p_2)^2 p_3^4 \\ p(A_{\text{F}}^0 - A_{\text{F}}^1) &= (1 - p_1)^2 p_1^4 p_2^4 p_3^4 \\ p(2A_{\text{F}}^0 - A_{\text{F}}^1) &= (1 - p_1)^2 p_1^4 p_2^4 p_3^4 \\ p(A_{\text{F}}^0 + A_{\text{F}}^1) &= (1 - p_1)^2 p_1^4 p_2^8 p_3^8 \end{aligned} \quad (5.6)$$

In Figure 5.15 we have calculated these probabilities in dependence of the magnetic field, using the gap energies $E_1 = 1.3$ meV, $E_2 = 0.8$ meV and $E_3 = 0.4$ meV, and electron densities $n_s = 1.9 \times 10^{11} \text{ cm}^{-2}$ in (a) and $n_s = 3.1 \times 10^{11} \text{ cm}^{-2}$ in (b). At the smallest magnetic fields, the orbit around A_{F}^2 has the largest probability, followed by the orbit around A_{F}^1 for intermediate fields, and the orbit around A_{F}^0 for large fields. The respective magnetic field ranges are shaded in different gray values. Figure 5.15(b) compares to the magnetoresistance trace presented in Figure 5.10. There we have found a switching between different magnetoresistance frequencies at magnetic fields of $B = 104$ mT and $B = 167$ mT. This switching is reproduced in the probability calculation as a shift of the maximum probability for electrons orbiting around A_{F}^2 , A_{F}^1 and A_{F}^0 . The dependence of the critical magnetic field on the Fermi energy, or, similarly, on the electron density, is manifested in a shift of the probability maxima to smaller magnetic fields when increasing the electron density, cf. Figures 5.15(a) and (b). This is also consistent with the experimental observation in Figures 5.9 and 5.10, where for the smaller electron density $n_s = 1.9 \times 10^{11} \text{ cm}^{-2}$ the transition between orbits around A_{F}^1 and A_{F}^0 occurs at a smaller magnetic field. The dependence of the switching magnetic field on the electron density is summarized in Figure 5.15(c). The different gray shaded regions indicate the dominance of the different orbits in the (B, n_s) parameter space. The higher

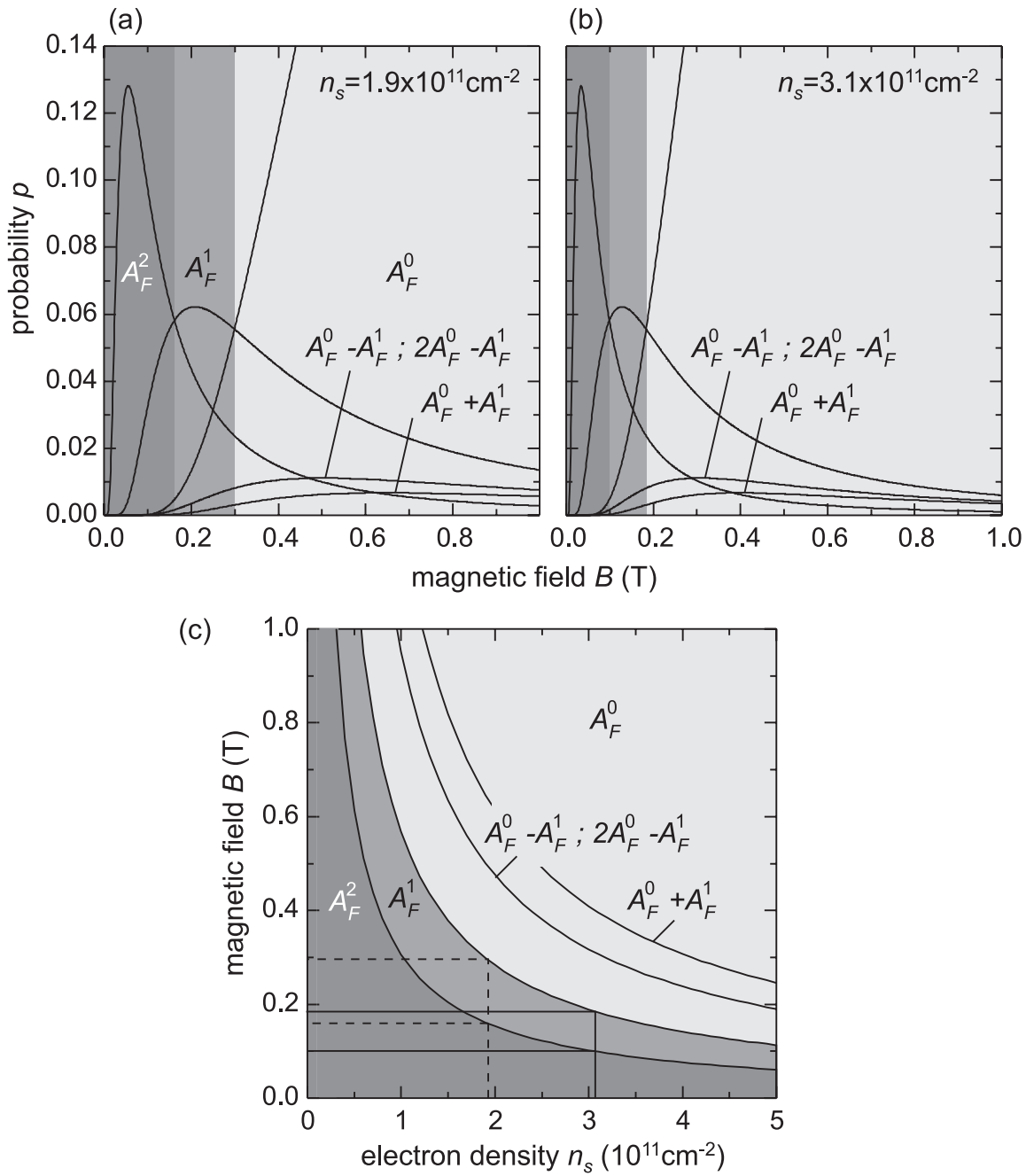


Figure 5.15: Calculated probabilities for closed orbits in a multi-band structure. (a) $n_s = 1.9 \times 10^{11} \text{ cm}^{-2}$. (b) $n_s = 3.1 \times 10^{11} \text{ cm}^{-2}$. (c) Phase space diagram in the (B, n_s) parameter space, within which the different electron orbits have the largest probability of all probabilities (for A_F^0 , A_F^1 and A_F^2), or their maximum probability (for $A_F^0 - A_F^1$, $2A_F^0 - A_F^1$ and $A_F^0 + A_F^1$).

the electron density is, the lower the magnetic fields are at which the switching from orbits around smaller areas to orbits around larger areas occurs.

In this framework it also becomes clear why in the $q = 40$ nm SLFET, with weaker density modulation, and therefore smaller energy gaps, the orbit around A_F^2 cannot be measured (see Figure 5.12). The reason is, that for smaller gaps E_i the critical magnetic field for the orbit around A_F^2 shifts to a field so small that quantum oscillations are inhibited by scattering.

5.3.5 Quantum interference in closed orbits

In the last section, based on the magnetic field dependence of the tunneling probabilities, different electron orbits were found to dominate in different magnetic field regions. These regions correspond to the experimentally determined regions A, B, and C in Figures 5.9 and 5.10. In this section we gather further evidence for this interpretation by directly calculating the magnetoresistance frequencies associated with the different electron orbits.

According to Onsager [Ons52], electrons that orbit around an arbitrarily shaped Fermi surface A_F give rise to $1/B$ -periodic oscillations in the magnetoresistance with a frequency Δ^{-1} ,

$$\Delta^{-1} = \frac{\hbar}{2\pi e} A_F. \quad (5.7)$$

In a semiclassical picture, this expression originates from the fact that a stationary state on a closed orbit must fulfil the Bohr-Sommerfeld quantization condition. The phase of the electron wave function φ is given by the integral over the canonical momentum $\vec{p} = \hbar\vec{k} - e\vec{A}$, where \vec{A} is the vector potential [Lan76]

$$\varphi = \frac{1}{\hbar} \oint (\hbar\vec{k} - e\vec{A}) d\vec{r} + \frac{\pi}{2} C. \quad (5.8)$$

C is a magnetic field independent constant, which in some cases is referred to as the Maslov index, and counts the amount of turning points in a closed orbit [Bra97]. Using the equation of motion of the electron in a magnetic field, and applying Stokes theorem to the contour integral [Kit96], we impose the condition for a stationary state on the phase (the phase accumulated around a closed orbit equals an integer multiple of 2π)

$$\varphi = l_B^2 A_F + \frac{\pi}{2} C = 2\pi i, \quad i = 1, 2, \dots \quad (5.9)$$

where $l_B^2 = \hbar/eB$ is the magnetic length. From this equation Onsager's relation (5.7) follows immediately. As a side product we find the constant C by comparing Equation (5.9) to the

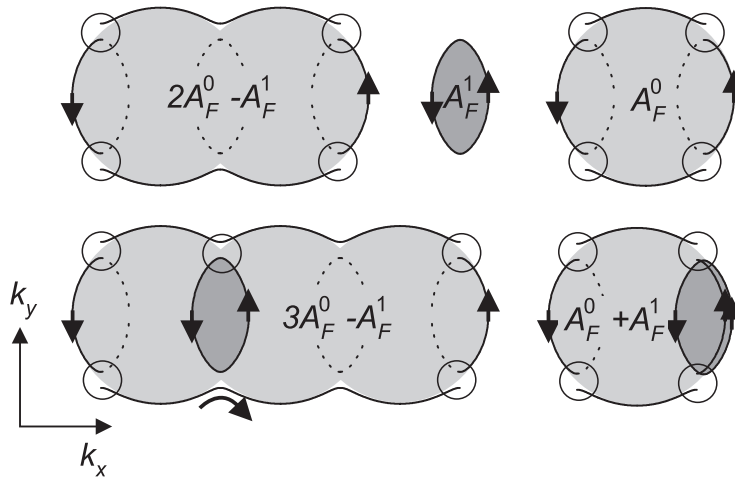


Figure 5.16: Possible closed electron orbits in reciprocal space. The small circles indicate the location of the tunneling junctions, the arrows point in the direction of the electron motion.

quantum mechanical result for the position of the Landau levels

$$E_F = \hbar\omega_c(i - 1/2), \quad i = 1, 2, \dots \quad (5.10)$$

Using $n_s = D_0 E_F$, $D_0 = m^*/(\pi\hbar^2)$ and $n_s = 2A_F/(2\pi)^2$, we find $C = 2$, corresponding to the two turning points at a 'soft' potential wall (the two-dimensional cyclotron motion can be reduced to the one-dimensional harmonic oscillator) [Bra97].

Our density dependent study in Figures 5.11 and 5.12 of the frequency components contained in the magnetoresistance together with Equations (5.4) and (5.7) now enables us to identify the maxima marked A_F^0 , A_F^1 and A_F^2 as caused by electrons performing closed orbits $n = 0, 1$ and 2 . The switching from lower to higher frequency near $B = 104\text{mT}$ and $B = 167\text{mT}$ in Figure 5.10 results from the transition of electrons orbiting predominantly around the area A_F^2 to orbits around A_F^1 and A_F^0 , respectively. In the intermediate B -field regime multiple closed paths may simultaneously have a significant probability. Eventually all tunneling probabilities approach unity for sufficiently large fields and the orbit with area A_F^0 , equivalent to the cyclotron orbit of the unmodulated 2DES that brings about the commonly known Shubnikov-de Haas oscillations, is restored and prevails. The orbits with area A_F^n are the most obvious closed trajectories, however more complicated closed paths with these simple surfaces as constituents are illustrated in Figure 5.16 and are in fact resolved in the experimental data (for example $A_F^0 + A_F^1$ and $2A_F^0 - A_F^1$).

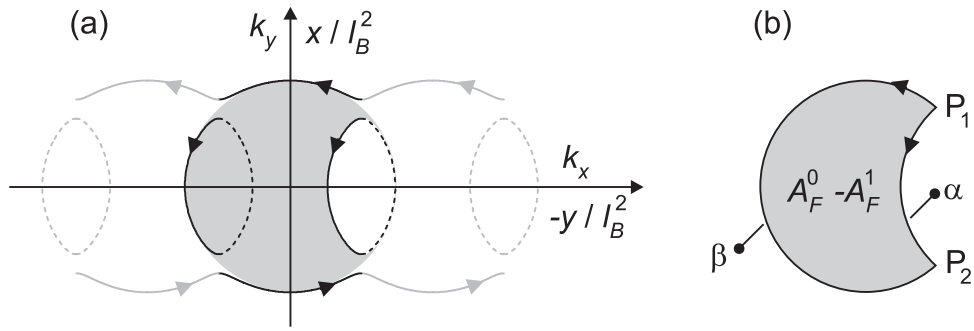


Figure 5.17: Quantum interference between open orbits. (a) At intermediate magnetic field strengths electrons travelling in negative k_x direction can either tunnel backwards into the opposite direction, or remain on the open orbit. This model bears some similarity to the edge channel picture used to describe the quantum Hall effect. (b) Quantum interference between electrons passing from $P_1 \rightarrow P_2$ either along path α or along path β , schematically drawn for the limit $V_0 = 0$ of vanishing energy gaps.

5.3.6 Quantum interference between open orbits

Hitherto, the discussed oscillations were a direct consequence of the constructive self-interference of the electron wave function along *closed* orbits and the subsequent quantization in a magnetic field. This mechanism leaves unexplained our observation of the frequency components determined by the surfaces $A_D^1 = A_F^0 - A_F^1$ and $A_D^2 = A_F^0 - A_F^2$ in Figures 5.11 and 5.12, since an electron circling along the closed boundary of this surface would violate the chirality imposed by the B -field along part of the perimeter. We assert that oscillations with such frequencies originate from the $1/B$ -periodic modulation of the backscattering probability due to quantum-mechanical interference between two open trajectories with common start and end points, as illustrated in Figure 5.17 for surface A_D^1 . Electrons travelling in negative k_x direction from point P_1 follow either path α or β , depending on whether they do or do not tunnel at this starting point, and rejoin at point P_2 . Constructive interference of the coherent superposition of both paths maximizes the backscattering probability and consequently the conductivity σ_{yy} approaches a minimum. By tensor inversion this implies a minimum in the longitudinal resistivity ρ_{xx} as well. In the case of destructive interference, the electron will effectively proceed along the open Fermi contour and thus σ_{yy} and ρ_{xx} reach their maximum value. This qualitatively different interference phenomenon reminds of an Aharonov-Bohm interferometer with the important disparity that in the case at hand the area

in real space enclosed by the interfering paths scales with B^{-2} , since real space orbits have the same shape apart from a $\pi/2$ -rotation as their counterparts in reciprocal space but are scaled with the square of the magnetic length, $l_B^2 = \hbar/(eB)$. As a result, one anticipates a $1/B$ -periodic rather than a B -periodic phase difference between the interfering trajectories.

Similar to the last section, we calculate the electron phase accumulated along its trajectory semiclassically. Unlike before, where only closed electron orbits were to be considered, here we need the phase φ_i of an electron travelling from point P_1 to point P_2 along open orbits $i = \alpha$ and $i = \beta$, given by

$$\varphi_i^{P_1 \rightarrow P_2} = \frac{1}{\hbar} \int_i (\hbar \vec{k} - e \vec{A}) \cdot d\vec{r} + \frac{\pi}{2} C_i. \quad (5.11)$$

The C_i are magnetic field independent constants, which depend on the particular path of integration. The phase difference

$$\Delta\varphi^{P_1 \rightarrow P_2} = \varphi_\alpha^{P_1 \rightarrow P_2} - \varphi_\beta^{P_1 \rightarrow P_2} = \varphi_\alpha^{P_1 \rightarrow P_2} + \varphi_\beta^{P_2 \rightarrow P_1} \quad (5.12)$$

between the two paths is obtained by simultaneously reversing the sign and the direction of integration of one of the contour integrals. By this mathematical trick the two formerly open orbits have been joined to one 'virtual' closed orbit. The phase difference evaluates to

$$\Delta\varphi^{P_1 \rightarrow P_2} = \frac{1}{\hbar} \oint_{\alpha-\beta} (\hbar \vec{k} - e \vec{A}) \cdot d\vec{r} + \frac{\pi}{2} \Delta C = l_B^2 A_D^{\alpha-\beta} + \frac{\pi}{2} \Delta C, \quad (5.13)$$

where $\Delta C = C_\alpha - C_\beta$. The relevant reciprocal space area $A_D^{\alpha-\beta}$ is bounded by a pair of paths α and β , and is nothing but the difference between surfaces A_F^i and A_F^j , that have common borders except for path α and β . The alternation frequency of the backscattering probability is then obtained from the condition

$$\Delta\varphi^{P_1 \rightarrow P_2} = l_B^2 A_D^{\alpha-\beta} + \frac{\pi}{2} \Delta C = 2\pi i, \quad i = 1, 2, \dots \quad (5.14)$$

which translates to a relation similar to Onsager's relation (5.7)

$$\Delta^{-1} = \frac{\hbar}{2\pi e} A_D^{\alpha-\beta} \quad (5.15)$$

with the difference area $A_D^{\alpha-\beta}$ in place of the closed orbit area. The features denominated by A_D^1 and A_D^2 in Figures 5.11 and 5.12 have been calculated according to Equation (5.15). The

relation between A_{D}^i and the electron density is obtained via Equation (5.4). The correspondence between our quantum interference model and the experiment is excellent.

In Section 5.3.4 we have calculated the probability of the orbit around A_{D}^1 . As can be seen in Figure 5.15, the probability of this orbit is nowhere dominant over the closed orbits A_{F}^i , but nevertheless has a finite value over a wide range of magnetic fields. This is the reason why the corresponding magnetoresistance oscillations are visible as a beating pattern overlaid to the oscillations due to closed orbits.

5.3.7 Commensurability oscillations

In 1989 Weiss and coworkers [Wei89] reported on the observation of a new type of magnetoresistance oscillation periodic in $1/B$ in weakly 1D modulated two-dimensional electron systems. Phenomenologically they were attributed to Shubnikov-de Haas oscillations where only the electrons within the first Brillouin zone contribute. The position of the magnetoresistance minima is given by the condition

$$2r_c = d(i - 1/4), \quad i = 1, 2, \dots, \quad (5.16)$$

indicating a commensurability effect between the electron cyclotron radius $r_c = \hbar k_{\text{F}}/(eB)$ and the superlattice period d . The resulting frequency of the commensurability (Weiss) oscillations is

$$\Delta_{\text{CO}}^{-1} = \frac{2\hbar\sqrt{2\pi n_s}}{ed} \quad (5.17)$$

with the characteristic square root dependence on the electron density. Soon after, these Weiss oscillations were attributed in a quantum mechanical picture to an oscillating band width of modulation broadened Landau bands [Ger89] [Win89] [Zha90]. These calculations use Landau states, and consider the modulation potential as a weak perturbation under the conditions $V_0 \ll E_{\text{F}}$ and $V_0 \ll \hbar\omega_c$. We remark that in Section 2.4 of this work we calculate quantum mechanically the Landau band spectrum in a tight-binding model, where we do not need to impose these weak perturbation conditions. Beenakker showed that the conductivity related to the Landau band dispersion can also be explained in a classical picture as a guiding center drift resonance [Bee89]. Weiss oscillations have also been explained in the high-field magnetic breakdown regime [Str90]. Even though quite some theoretical and experimental work has been done since, a direct theoretical relationship between the Weiss oscillations and the band structure had been elusive to this date.

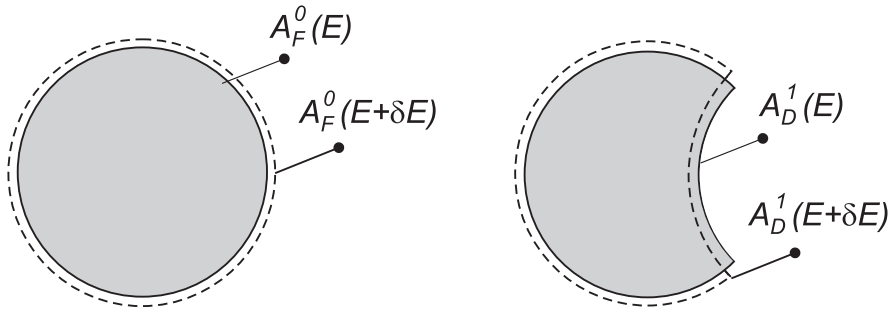


Figure 5.18: Temperature dependence of quantum interference oscillations. (a) Quantum interference in closed orbits. (b) Quantum interference between open orbits.

We show that the Weiss oscillations can be explained as special case within our semiclassical model of quantum interference between open orbits, directly related to the artificial band structure. Expanding Equation (5.4) for large Fermi wave numbers $k_F \gg k_0$, the difference area is given by $A_D^1 = 4k_F\pi/d$. This is a very good approximation for the electron density range of the present experiments, and exact in the high density limit. Inserting this difference area into our semiclassically derived Onsager type relation (5.15), quite surprisingly the magnetoresistance frequency (5.17) of the Weiss oscillations is found.

Under the assumption, that the orbit A_D^1 gives rise to the Weiss oscillations, we are able to derive the value for the difference of the Maslov indices ΔC defined in Equation (5.14) by comparing this equation to Equation (5.16), where the factor $1/4$ fixes the absolute position of the magnetoresistance minima on the magnetic field axis. We find $\Delta C = 1$, in contrast to the previously derived $C = 2$ for the Shubnikov-de Haas oscillations. Since the topology of the imaginary closed orbit around A_D^1 is different from the free cyclotron orbit around A_F^i , the difference in their Maslov indices does not come as a surprise. It has, however, been impossible for us to directly calculate the Maslov index ΔC for the open orbits.

5.3.8 Temperature dependence

To provide further support for the relationship between the Weiss oscillations and the special case of quantum interference between open orbits bounding area A_D^1 , it is instructive to derive the temperature scale up to which this interference phenomenon persists. To this end, the energy variation δE at fixed B inducing a phase change of 2π is calculated,

$$\delta E = \frac{2\pi eB}{\hbar} \left(\frac{\partial A}{\partial E} \right)^{-1} = 2\pi\hbar\omega_c k_F \left(\frac{\partial A}{\partial k_F} \right)^{-1}, \quad (5.18)$$

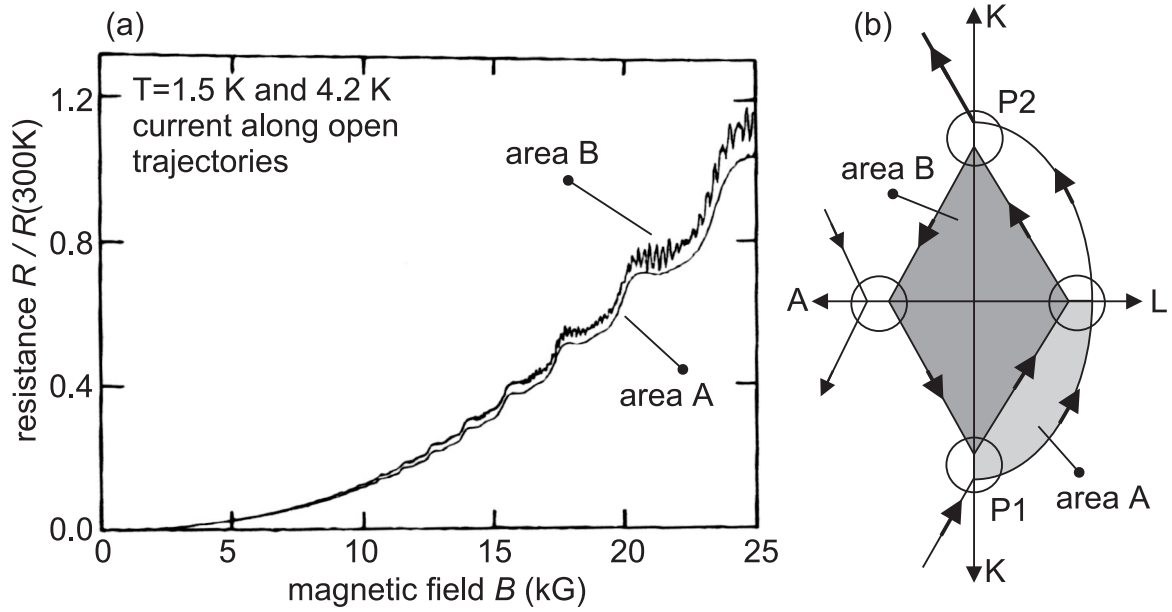


Figure 5.19: (a) Quantum interference oscillations in the transverse magnetoresistance of a pure magnesium crystal for B along $[10\bar{1}0]$ and current along $[11\bar{2}0]$. The upper curve is for $T = 1.5\text{ K}$, the lower curve for $T = 4.2\text{ K}$ (data plot modified from [Sta74]). (b) Stark quantum interferometer as part of the magnesium band structure (schematically drawn).

where $\hbar\omega_c$ is the free electron cyclotron energy and A the relevant k -space area. For the free electron cyclotron orbit with area $A_F^0 = \pi k_F^2$ the familiar condition $k_B T < \delta E_0 = \hbar\omega_c$ is retrieved from this formula. In Figure 5.18(a) we schematically show the area $A_F^0(E)$ for energy E . For temperatures $T > 0$ electrons occupy also states with $E + \delta E$, and circle a larger area $A_F^0(E + \delta E)$. If the phase difference between the two corresponding orbits is larger than 2π , quantum interference effects will be washed out. In contrast, a much weaker temperature dependence is predicted for the interfering open orbits bordering A_D^1 , and the oscillations survive as long as $k_B T < \hbar\omega_c k_F d/2$. This situation is shown in Figure 5.18(b). As can be seen, the areal difference between energy E and $E + \delta E$ is much weaker, as part of the higher energy orbit is contracting. This weak temperature dependence is in fact also found in the conventional commensurability oscillation picture [Bet90].

5.3.9 Quantum interference in metal physics

In 1930 Landau [Lan30] predicted that the magnetization of metallic free electrons at low temperatures should oscillate as the magnetic field varies. Incidentally, within only months, the oscillatory magnetic behavior was experimentally discovered in single crystal bismuth by de Haas and van Alphen [dH30], and Shubnikov and de Haas [Shu30]. In the following decades the study of the magnetization and the magnetoresistance lead to the understanding of many metallic band structures. Especially fruitful was the classic three page paper by Onsager [Ons52], relating the oscillation frequency to the Fermi surface in a semi-classical treatment based on the Bohr-Sommerfeld condition to quantize the electron motion. This physics can be compared to the cyclotron orbit of unmodulated two-dimensional electrons in a semiconductor. In our work this corresponds to the limit $V_0 \rightarrow 0$ with the area A_F^0 .

In the 1960s Cohen, Falicov [Coh61] and Blount [Blo62] introduced the notion of magnetic breakdown to explain Fermi surface extremal areas much larger than expected from the zero-field band structure. This could explain Priestley's observation of high-frequency oscillations in magnesium. In our work, the relevant counterpart to this metallic physics are the magnetoresistance oscillations due to orbits around areas A_F^1 and A_F^2 . As we have shown, these orbits become possible by electron tunneling in reciprocal space across energy gaps of the artificial band structure. The excellent agreement of the concepts previously developed for metals with the experimental data on our superlattices shows, that they really can be considered as artificial crystals.

A decade later, Stark and Friedberg [Sta71] [Sta74] reported on the observation of a magnetoresistance frequency smaller than the frequency expected from zero-field orbits. Within the known band structure of magnesium, they explained these oscillations as resulting from a quantum interference effect between electrons travelling on two different paths. We reproduce their experimental data, and the so-called Stark interferometer, in Figure 5.19. At a temperature of $T = 1.4$ K they observe two frequencies, the larger one of both is quenched at a temperature of $T = 4.2$ K. The high frequency oscillation is attributed to a closed electron orbit around area B , and the low frequency component corresponds to an area A . This area, however, is not traced by the electron in a closed orbit, but rather passed by two open orbits in the same direction. The temperature dependence of the latter oscillations is much weaker. Within our work, we claim that the physics of this Stark quantum interferometer corresponds to the quantum interference between open orbits as described in Section 5.3.6 for areas A_D^i . The Weiss oscillations as a special case of this quantum interference phenomenon with area

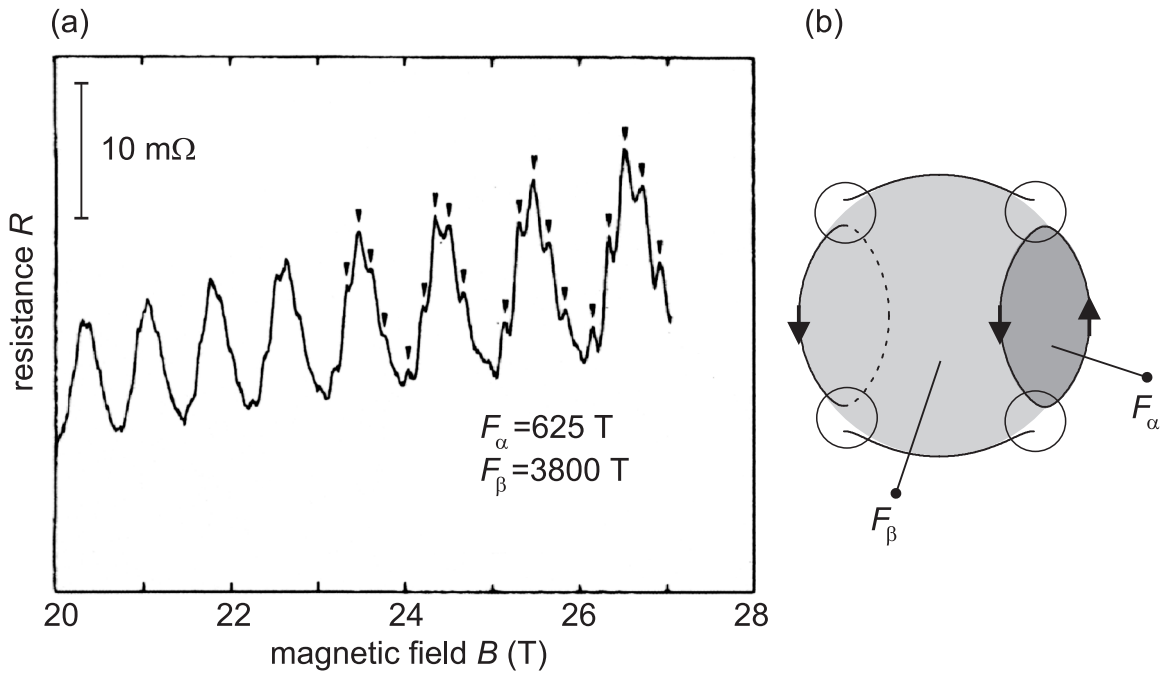


Figure 5.20: Magnetic breakdown in the organic superconductor κ -(BEDT-TTF) $_2$ Cu(NCS) $_2$ (data plot modified from [Sas90]).

A_D^1 have therefore been observed in metals at a time when the semiconductor superlattice was just about to be born.

5.3.10 Quantum interference in organic superconductors

Recently, an increasing interest has been paid to magnetic oscillations in two-dimensional organic materials. Especially the band structure of the superconductor κ -(BEDT-TTF) $_2$ Cu(NCS) $_2$ bears great similarity to the band structure of the SLFET in our work. As shown in Figure 5.20(b), the Fermi contour consists of a closed orbit circling area α , and an open orbit. In the experiment [Sas90], a switching from a low frequency oscillation F_β to a high frequency oscillation F_α is observed. The reason is magnetic breakdown across the gap, making the large area β dominant for electron orbits. In our work, we have observed this switching behavior at much lower fields in Section 5.3, when electrons orbiting predominantly around area A_D^i switched to a larger orbit around area A_D^{i-1} .

In addition to this well understood switching behavior in the superconductor, some groups have observed also sum and difference frequencies $F_\beta \pm F_\alpha$ [Har96] [Mey95]. This

observation is currently subject of theoretical discussions [For98b] [For98a]. These frequencies may be understood in the framework of quantum interference between open orbits, as described in Section 5.3.6.

In summary we think that our work bridges the gap between quantum interference phenomena observed in semiconductor superlattices, in metals, and in organic superconductors. These systems have in common a band structure with narrow gaps, allowing for different electron trajectories at finite magnetic field. The large body of theoretical work developed for semiconductor superlattices may favorably be applied also to the latter two systems. In particular at high magnetic fields even in these systems the lattice potential may be regarded as a perturbation to the free electron gas in magnetic field.

5.4 Commensurability effects in focused laser beam diffused structures

In parallel to the cleaved-edge overgrowth technique we have developed a different method to fabricate density-modulated two-dimensional electron systems. We demonstrate for the first time lateral surface *doped* superlattices (LSDSLs), which we obtain by local and shallow compensation doping the silicon donor layer of an GaAs/Al_xGa_{1-x}As heterostructure. The versatility of this method is demonstrated by three different examples of commensurability effects in two-dimensional electron systems. First in weak one-dimensional LSDSLs the known Weiss oscillations [Wei89] [Ger89] [Win89] at low magnetic fields are recovered, a fact which provides evidence of the high homogeneity of the laser doped lines. At increased compensation doping concentrations in two-dimensional LSDSLs typical antidot resonances [Wei91b] are found, demonstrating that high electron mobilities are preserved. In magnetic focusing experiments elongated lines in this high compensation doping regime are shown to be specular reflecting, which further confirms their quality.

5.4.1 Method of fabrication

Our samples were MBE grown GaAs/Al_{0.3}Ga_{0.7}As modulation doped heterostructures with the 2DES 60 nm below the surface. The electron density could be varied between $n_s = 3.5 \times 10^{11} \text{ cm}^{-2}$ and $n_s = 6.1 \times 10^{11} \text{ cm}^{-2}$ by successive illumination with a red light emitting diode, electron mobility at the latter density was $\mu = 1.6 \times 10^6 \text{ cm}^2/\text{Vs}$. All experi-

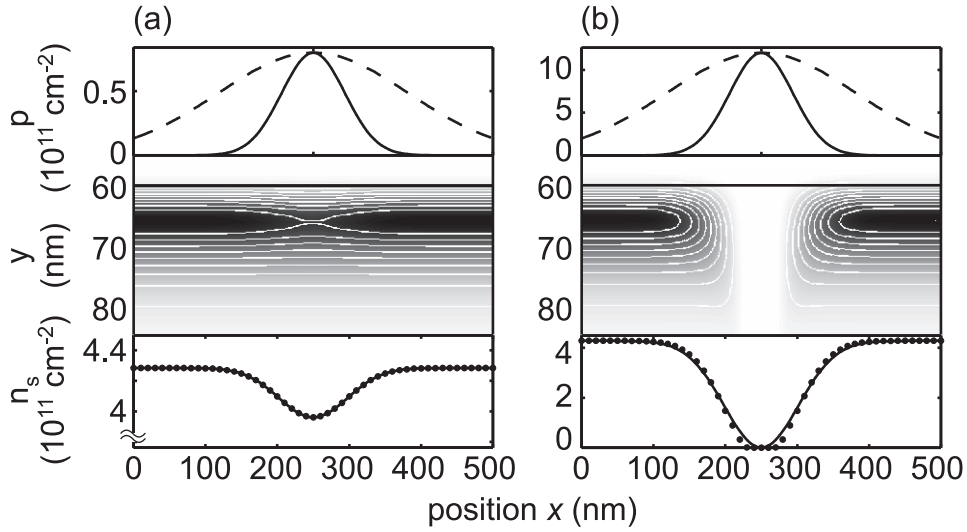


Figure 5.21: Top: scaled laser beam profile (dashed) and doping concentration (solid); middle: calculated electron concentration gray scale encoded (black: $3.57 \times 10^{17} \text{ cm}^{-3}$, white: $0 \times 10^{17} \text{ cm}^{-3}$); bottom: integrated 2D charge density n_s (circles) and gaussian fit (solid line). (a) small laser power, $p_0 = 8 \times 10^{10} \text{ cm}^{-2}$; (b) large laser power, $p_0 = 1.2 \times 10^{12} \text{ cm}^{-2}$.

ments were performed at liquid helium temperatures using four point lock-in measurement technique with a measurement current of $I = 1 \mu\text{A}$. Compensation doping was achieved by heating the Zn:SiO₂ capped sample surface with the highly focused beam of an Ar⁺ laser (wavelength 458 nm, laser power 1-100 mW). A non-linear thermally activated diffusion process results in local compensation doping of the initial n-type silicon doping layer by p-type zinc atoms, and, most importantly, in a significant narrowing of the lateral doping profile as compared to the initial laser spot profile [Bg97]. Calculated diffusion depths of the zinc atoms are between a few nm and 20 nm, depending on the used laser power [Bau94]. It is therefore expected that ionized impurity scattering is hardly increased after laser patterning. This method was developed by Baumgartner *et al.* [Bg97], who have previously fabricated in-plane-gated devices such as quantum-point contacts, single-electron transistors and Aharonov-Bohm rings [Bau97] [Bau98].

5.4.2 Self-consistent calculation

In order to determine possible period lengths and modulation amplitudes in our LSDSLs we have performed self-consistent Poisson/Schrödinger calculations of the 2DES at the presence

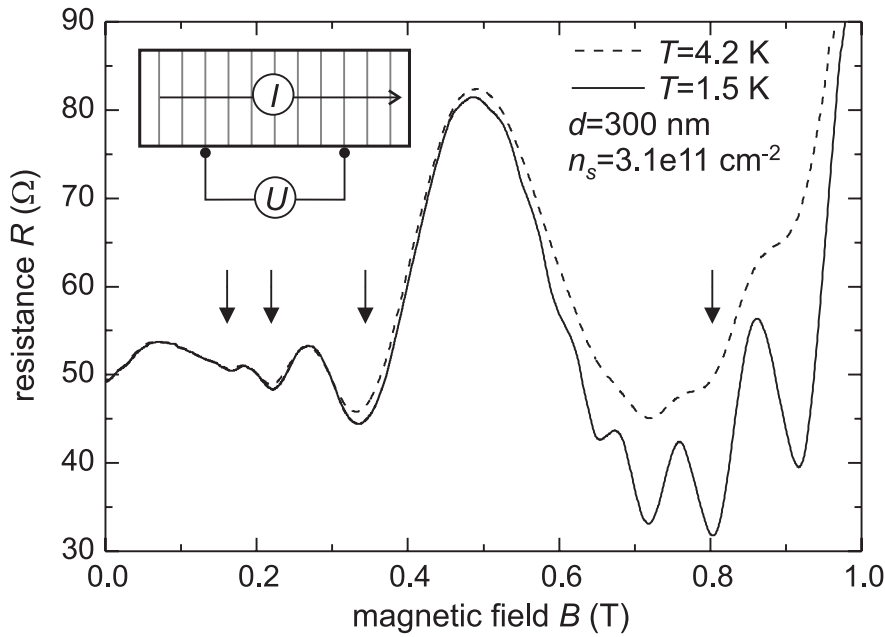


Figure 5.22: Commensurability oscillations in a one-dimensional LSDSL with period $d = 300$ nm at $n_s = 3.1 \times 10^{11} \text{ cm}^{-2}$ for two different temperatures. The inset schematically shows the measurement scheme for the longitudinal magnetoresistance. Arrows indicate the theoretically expected location of resistance minima. Shubnikov-de Haas oscillations appear as $1/B$ periodic features above $B = 0.6$ T.

of compensation doping in the initial n-type doping layer. At a measured laser spot full width at half maximum (FWHM) of 315 nm the calculated resulting doping profile is gaussian shaped with a FWHM of 105 nm [Bau94], and the maximum p-doping concentration in the center p_0 depends on the laser power. We find that for $n_s = 4.3 \times 10^{11} \text{ cm}^{-2}$ and $p_0 = 8 \times 10^{10} \text{ cm}^{-2}$ the potential modulation is 7% of the Fermi energy with a FWHM of 112 nm, while for $p_0 = 1.2 \times 10^{12} \text{ cm}^{-2}$ at the same electron density the 2DES is depleted, but the FWHM is hardly increased to 122 nm, see Figure 5.21. Depending on the laser power small and large potential modulations can be fabricated, while the width of the electron depletion zone remains almost constant, and much below the laser spot size. These results indicate that LSDSL with periods even below the laser spot size should be achievable.

5.4.3 One-dimensional surface lateral superlattice

In a first set of experiments we have successfully fabricated LSDSLs with one-dimensional modulation and periods between $d = 500$ nm and $d = 200$ nm by laser writing an array of $10 \mu\text{m}$ long lines across a small Hall bar. The same laser power as used for the calculation shown in Figure 5.21(a) was chosen. Measurement results of a sample with $d = 300$ nm are shown in Figure 5.22 for two different temperatures $T = 4.2$ K and $T = 1.5$ K. At magnetic fields below $B = 1$ T Weiss oscillations with their typical weak temperature dependence are clearly resolved as $1/B$ periodic oscillations in the longitudinal magnetoresistance. We have discussed Weiss oscillations in Section 5.3.7. Given the period and electron density, which we determine from the high field Shubnikov-de Haas oscillations, the expected positions B_i of the resistance minima $i = 1, 2, \dots$ (see Equation (5.16))

$$B_i = \frac{2\hbar\sqrt{2\pi n_s}}{ed(i - 1/4)}, \quad (5.19)$$

marked by arrows in Figure 5.22, coincide well with the experimental data. Potential modulation amplitudes evaluated both using the semiclassical model [Bee89] and the magnetic breakdown picture [Bet91] mutually agree well with a magnitude of 7% of the Fermi energy.

5.4.4 Two-dimensional antidot superlattice

In a second set of experiments two-dimensional LSDSLs were fabricated by laser writing a $10 \mu\text{m} \times 10 \mu\text{m}$ square array of dots in a small hall bar at a laser power corresponding to Figure 5.21(b). Clear resistance maxima are found at magnetic field strengths corresponding to electron cyclotron orbits around one and four antidots with $d = 500$ nm as indicated by arrows in Figure 5.23, in agreement with a simple electron pinball model [Wei91b]. The small dips α and β in the Shubnikov-de Haas maxima at smaller filling factors were reproducible in different cool-downs and different samples. Their position forbids the trivial explanation by spin splitting, for example the dip denoted by β lies between filling factors three and four.

5.4.5 Magnetic focussing structure

In addition to the first set of experiments, where the presence of Weiss oscillations indicated highly homogenous laser written lines in the weak potential modulation regime, a third set of experiments was set up to determine the quality of laser written lines in the strong potential modulation regime. For that reason we have performed magnetic focusing experiments in

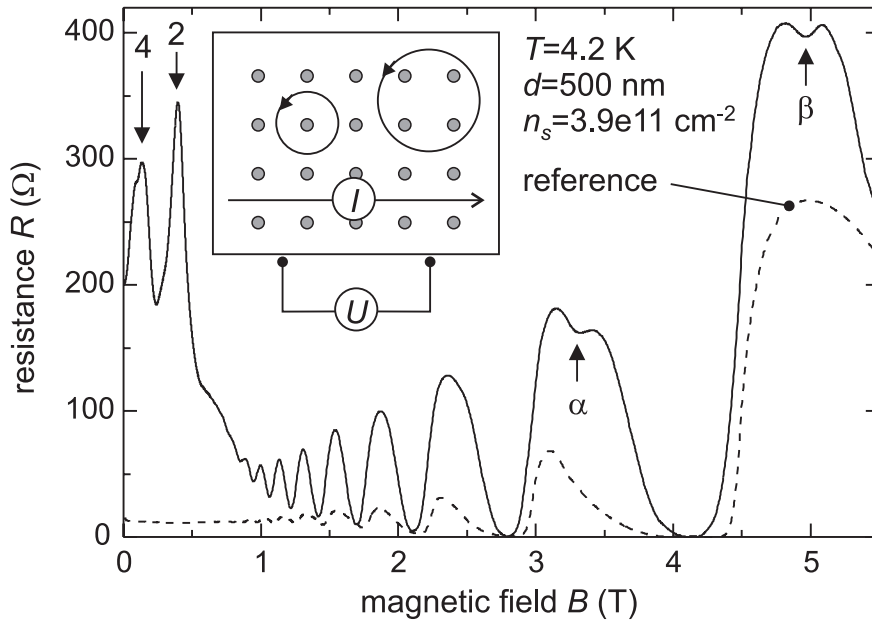


Figure 5.23: Commensurability oscillations in rectangular two-dimensional LSDSL at $n_s = 3.9 \times 10^{11} \text{ cm}^{-2}$. Resistance resonances originate from electron localization around one and four antidots, as indicated by the arrows and shown schematically in the inset. Features marked by α and β cannot easily be explained by semiclassical orbits.

a $10 \mu\text{m} \times 10 \mu\text{m}$ square of electrically isolating laser written lines with small openings at the corners, as shown in Figure 5.24. Clear magnetoresistance oscillations periodic in magnetic field B are caused by electrons that are specularly reflected at the boundary up to 5 times [vH89]. We have experimentally confirmed the expected length dependence of the resonances in a structure with side wall length of $5 \mu\text{m}$, where resonances appeared at double the magnetic field strengths. The result of this experiment further demonstrates the smoothness of the laser generated potential modulation.

5.4.6 Summary

In summary we have fabricated lateral surface doped superlattices by selectively p-type doping an initially n-type GaAs/Al_{0.3}Ga_{0.7}As heterostructure with down to sub-laser wavelength periods. Lateral regularity and homogeneity of the laser written structures were confirmed by magnetotransport measurements on one-dimensional and two-dimensional LSDSLs. In

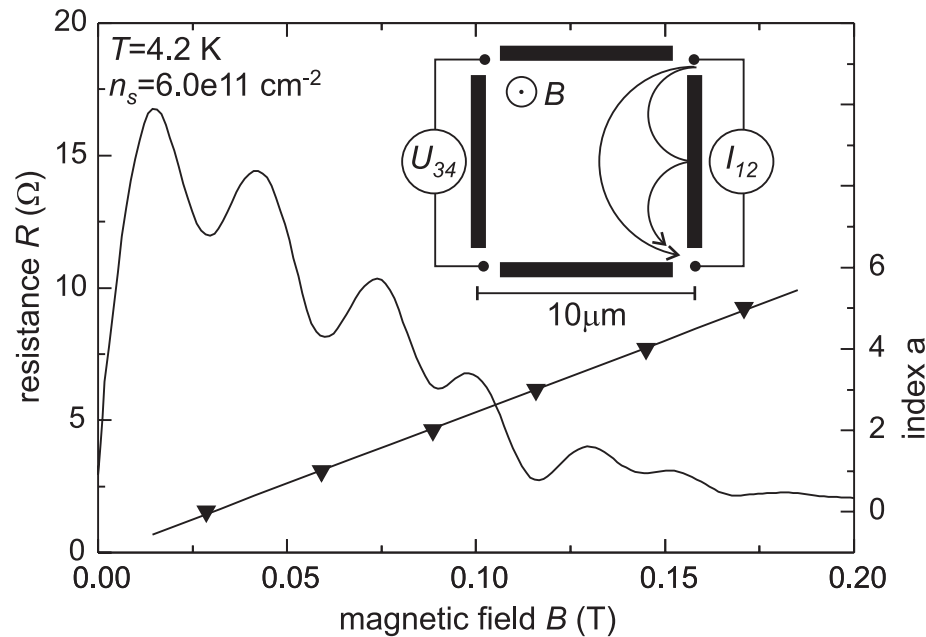


Figure 5.24: Magnetic focussing resistance oscillations (left axis), the resistance minima lie on a straight line (right axis). The inset shows the focussing structure and the measurement geometry. Observed resistance oscillations demonstrate the commensurability between the electron cyclotron radius and the $10\ \mu\text{m}$ sidewall where the electron bounces an integer number of times a , as schematically shown in the inset for $a = 0$ and $a = 1$.

the former case Weiss oscillations were observed, whereas in the latter case typical antidot resonances appeared. The high quality of the laser written lines was further demonstrated by magnetic focusing experiments, showing specular reflection of electrons of up to 5 times. In contrast to other conventional patterning methods with our method of compensation doping almost arbitrary lateral potential landscapes may be fabricated. This is simply achieved by adjusting the laser power during the patterning process. LSDSLs with complex unit cells not only in lateral shape but also in electron density should be feasible. We have demonstrated two particular examples of weak and strong modulation strengths. With our method little or no crystal damage occurs during patterning, and mechanical strain, which often interferes with the electrostatic modulation using other methods, is avoided. Our LSDSLs may additionally be gated for further flexibility.

5.5 Conclusion

In this chapter we have demonstrated the rich physics arising out of the combination of an artificial band structure and quantum interference effects. We distinguish two physically different interference effects. First, quantum interference of electrons travelling on closed orbits, and second quantum interference between two open electron orbits.

In the simplest case, quantum interference in an unmodulated two-dimensional electron system results in magnetoresistance oscillations due to electrons orbiting on cyclotron orbits. When a perturbing periodic potential is added, as in the SLFET, the zero-field band structure falls apart in a series of open Fermi contours, and one closed orbit enclosing a much smaller reciprocal space area. At the smallest magnetic fields, this orbit produces magnetoresistance oscillations with small frequency. As the magnetic field is raised, however, the process of magnetic breakdown couples previously unconnected trajectories, and closed orbits around larger reciprocal space areas become dominant. In the experiment, higher magnetoresistance frequencies are then observed. As the breakdown probability approaches unity for large fields, the cyclotron orbit encountered in the unperturbed electron system is reinstalled.

In addition to these closed orbit phenomena, at intermediate magnetic fields, where the breakdown probability is about 50 %, we have discovered a process in reciprocal space reminiscent to the Aharonov-Bohm effect in real space. Forward moving electrons can reverse direction by taking two different paths, and the resulting backscattering probability is modulated by the magnetic flux threading the enclosed area. We have discovered that the resulting magnetoresistance frequency for the lowest order of such processes is identical to the well known Weiss oscillations. This sheds new light on their understanding, and in particular established for the first time a direct relation between their magnetoresistance frequency and the band structure. We think that quantum interference phenomena observed in metallic systems, and in organic superconductors, may be treated on a similar footing as the commensurability effects investigated in superlattices.

Chapter 6

Phase Transition at Fractional Filling

Ultra-clean two-dimensional electron systems in a strong perpendicular magnetic field condense by virtue of the Coulomb interaction at particular rational values of the filling factor into incompressible fractional quantum Hall states. In GaAs-based systems, the Zeeman splitting is so small, that at low electron densities it becomes comparable to the Coulomb energy, and spin is turned into an important extra dynamical internal degree of freedom. Spin reversal then occurs at little or no energetic cost.

Owing to the unparalleled combination of high electron mobility and electron density tunability in the SLFET, we are able to investigate the rich phase transition physics resulting from competing ground states with different spin orientations. This phase transition is accompanied by hysteresis, ascribed to 2D-Ising ferromagnetism with easy axis anisotropy, by a temperature activated amplitude, and by a peculiar non-monotonic temporal behavior, reminiscent of the Barkhausen effect. Furthermore, resistively detected nuclear magnetic resonance suggests an intricate domain morphology and dynamics, that partly involves the nuclear spin system of the host semiconductor. Even though our experiment and theory quite generally apply to two-dimensional systems, the superlattice in the SLFET seems to offer periodic pinning centers for the spin domains, thus intensifying hysteretic effects.

6.1 Review

For a two-dimensional electron system of density n_s in a perpendicular magnetic field B , the Landau level filling is given by $\nu = n_s h / (eB)$. Unlike the integer quantum Hall effect, which occurs at integer filling factors, under favorable conditions the two-dimensional system condenses into a new many-body ground state at fractional filling factors, characterized, as in the integer case, by a quantized Hall and vanishing longitudinal conductance. Some good reviews on the quantum Hall effects include [Pra87], [Cha95] and [Sar96]. At very strong fields, all electron spins are aligned and the spin degree of freedom is effectively frozen out, since the Coulomb interaction scales with \sqrt{B} , whereas the Zeeman splitting rises linearly. However, in GaAs-based two-dimensional electron systems the Zeeman splitting is so small, that by lowering n_s the fractional quantum Hall regime can be shifted to fields, where spin is turned into an important extra dynamical internal degree of freedom [Hal83] [Xie89] [TC90]. Spin reversal then occurs at little or no energetic cost and rich phase transition physics ensues, since multiple fractional quantum Hall ground states that differ mainly in their spin configuration compete. Signatures for phase transitions at $\nu = 2/3$ and $\nu = 2/5$ between distinct spin-unpolarized and fully spin-polarized FQHE states that occupy the same filling factor were uncovered in transport experiments [Eis90] [Eng92] [Kan97] [Kro99]. A recent photoluminescence study even gained direct access to the degree of spin polarization [Kuk99].

In the integer quantum Hall regime, the correlation between two macroscopically degenerate Landau levels, that are brought energetically close to alignment, can result in a transition of the electronic system to ordered many-particle ground states similar to those of familiar low dimensional ferromagnets [Jun98] [Pia99] [Mac99]. To benefit from this analogy, the Landau level degree of freedom is assigned a pseudospin and the problem is analyzed in terms of the anisotropy energy for a particular pseudospin orientation. The competition between exchange and Coulomb interaction energies controls the most favorable orientation. In cases where electrostatic energy contributions are negligible, exchange energy costs dictate that the pseudospin either points up or downwards characteristic of a ferromagnet with easy axis anisotropy [Jun98]. Integer quantum Hall states at even integer filling near the coincidence of two spin-resolved Landau levels with different index and opposite spin constitute examples. In the fractional quantum Hall regime, a rigorous physical description of ferromagnetism has not been put forward. Because the ground state spin transition physics at filling factors $\nu = 2/3$ and $\nu = 2/5$ can be rephrased in the composite fermion [Sar96]

language as occurring at even composite fermion filling factor $\nu_{\text{CF}} = 2$ from the coincidence of the spin-down state of the lowest composite fermion Landau level with the spin-up state of the second Landau level, it is natural to pursue whether these phase transitions too fall within the realm of ferromagnetism. In such ferromagnets disorder should introduce a random component into the effective field strength that aligns the pseudospin [Jun98]. Moreover, it may pin and nucleate domains of opposite pseudospin orientation. Large energy barriers between adjacent domains then are bound to promote hysteresis in physical properties. From its observation Ising ferromagnetism has been inferred [Pia99] [Cho98]. The domain morphology, dynamics and microscopic mechanisms for transport through such a ferromagnet have not been addressed to date.

In this chapter, we exploit high electron mobility and density tunability of the SLFET to investigate the ground state spin transition near $\nu = 2/3$ in dependence of electron density n_s , magnetic field strength and sweep direction, temperature T , modulation strength, and radio frequency irradiation. We find that the spin transition following the line $\nu = 2/3$ occurs at different values of the carrier density depending on whether n_s is gradually lowered or raised, as one would anticipate for a ferromagnet with easy axis anisotropy broken up in domains. To improve our comprehension of the physical mechanisms responsible for hysteresis, the time behavior of the resistance is examined. It exhibits sudden jumps akin to the Barkhausen effect in the magnetization of conventional ferromagnets [Ber98], where it is ultimately assigned to the energy landscape in which the system evolves with a huge number of local minima and saddle points that reflect the unavoidable presence of structural disorder in a macroscopic magnetic system. On longer time scales, the resistance reveals that equilibrium is progressively approached in a logarithmic fashion, typical for systems characterized by a wide distribution of energy barriers or time constants [Ber98]. Finally, the response to radio frequency irradiation in the resistance is investigated. Its correlation with the sign and size of the hysteresis supports the assertion that the nuclear spin system affects transport through this peculiar ferromagnet. All these observations are intimately connected with domain morphology.

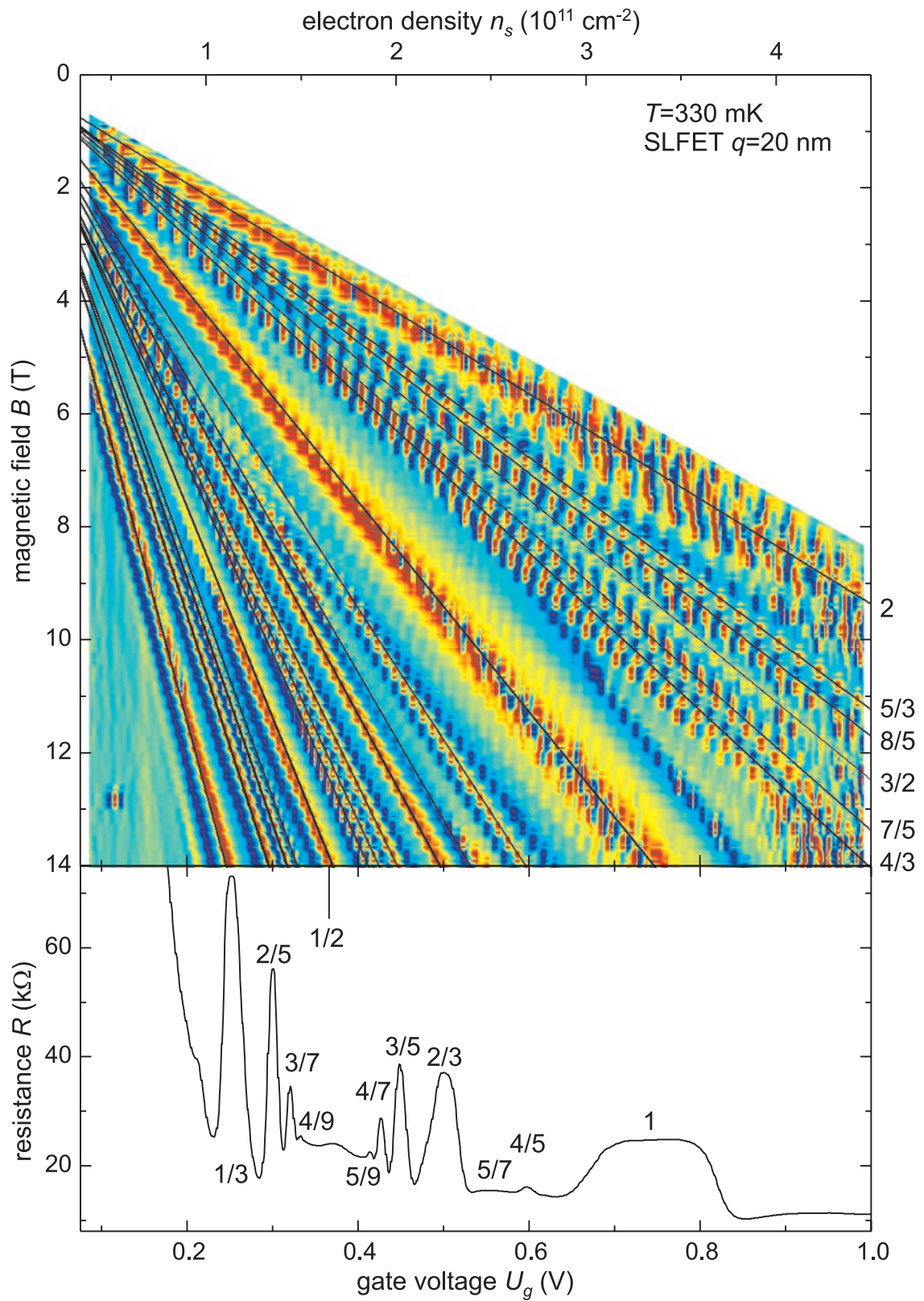
The work reported here is the result of a collaboration with J. Smet of the K. v. Klitzing group, Max-Planck-Institut für Festkörperforschung, Stuttgart. All $T = 50$ mK measurements were performed in their dilution refrigerator, and J. Smet contributed the major part of the understanding of our results. Two of the SLFETs described in Chapter 3 are used in this study. Both have a superlattice period of $d = 15$ nm, a channel length of $L = 3$ μm , but differ in the modulation strength. As calculated in Section 3.2, the SLFET with (110) GaAs

layer thickness $q=10$ nm exhibits a significant periodic electron density modulation, while the $q = 20$ nm SLFET much rather resembles a free two-dimensional electron system with only very weak modulation. Most of the results presented in this chapter have previously been published in [Sme01].

6.2 Overview

In Figure 6.1 we present an overview of the magnetoresistance, obtained with the $q = 20$ nm SLFET at a temperature of $T = 330$ mK. This measurement was obtained by sweeping the electron density for fixed magnetic field. In the color coded plot the measured magnetoresistance was processed to make visible the maxima (red) and the minima (blue). As we have discussed in Section 2.3.5, for the given short and wide sample geometry, resistance *maxima* are observed at integer (fractional) filling factors. We concentrate on the density and magnetic field range for filling factors smaller than $\nu = 2$. As can be seen, a variety of fractional filling factors are observed even at remarkably small electron densities. We point out that it is generally difficult to measure the fractional quantum Hall effect in the low density regime $n_s < 1 \times 10^{11} \text{ cm}^{-2}$, first because reduced screening of ionized impurities is detrimental to high electron mobilities, and second because ohmic contacts to a low density system are difficult to fabricate. In the SLFET, ionized impurity scattering is to a large extent reduced as no modulation doping is employed, and because of the special contacting scheme via n+ GaAs layers, even very low electron density systems are reliably contacted. Yet the observation of the fractional quantum Hall effect in the SLFET is somewhat surprising because of the close proximity of the metallic gate electrode to the two-dimensional electron system, as a result of which long range correlations required for the fractional quantum Hall states should be screened out. The bottom trace in Figure 6.1 is obtained for $B = 14$ T and serves as example for an unprocessed measurement. To our knowledge fractional quantum Hall traces of similar quality on (110) GaAs have not been published to date, and even in our molecular beam epitaxy machine we have not been able to grow similar quality material on bulk (110) GaAs wafers.

In Figure 6.2 we compare the magnetoresistance of the $q = 10$ nm SLFET and the corresponding reference CEOFET, obtained for a fixed electron density of $n_s = 1.6 \times 10^{11} \text{ cm}^{-2}$ at $T = 330$ mK. As can be seen, even in the significantly modulated electron system of the $q = 10$ nm SLFET the fractional quantum Hall state is developed, most clearly seen for the $\nu = 2/3$ state. The reference CEOFET, in contrast, exhibits a quite low electron mobility,



R. A. Deuschmann *Two dimensional electron systems in atomically precise periodic potentials* (2001)
 Ph.D. Dissertation, Selected Topics of Semiconductor Physics and Technology ISBN 3-932749-42-1

Figure 6.1: Fractional quantum Hall effect in the $q=20 \text{ nm}$ SLFET.

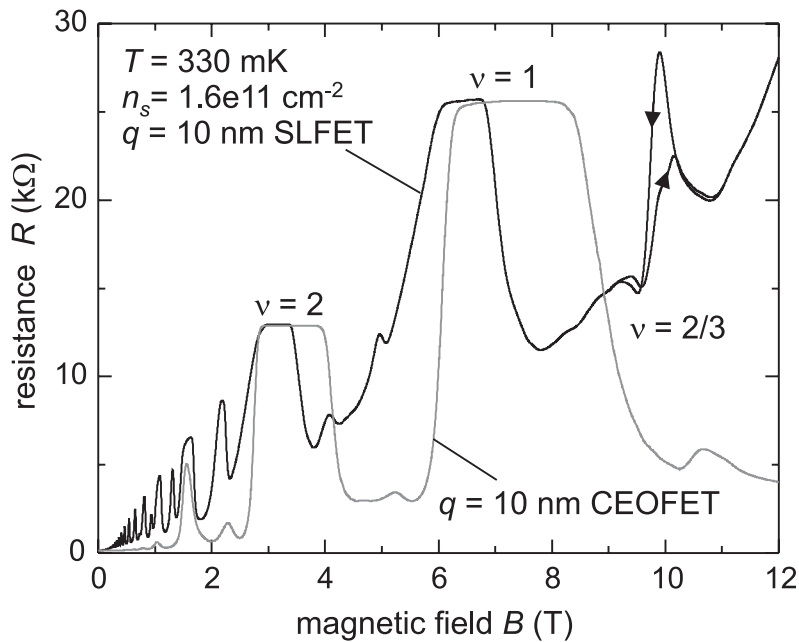


Figure 6.2: Magnetoresistance of the $q = 10$ nm SLFET (black line) and CEOFET (gray line).

manifested in an almost complete loss of the $\nu = 2/3$ state, and an onset of magnetoresistance oscillations at a large magnetic field. The reason for this discrepancy is unclear to date. Possibly the (110) growth kinetics on a cleaved GaAs/AlGaAs superlattice substrate is favorable to the growth on homogenous GaAs.

A significant feature is observed in the SLFET at the $\nu = 2/3$ filling factor. The resistance exhibits a strong dependence on the magnetic field sweep direction. During the upward sweep, the resistance peak is almost quenched, and rejoins the trace obtained during the downward sweep beyond the $\nu = 2/3$ filling factor. Only during the downward sweep this fractional state seems fully developed. This hysteretic behavior is the main focus of this chapter.

A low-temperature measurement ($T = 50$ mK) of the $q = 20$ nm SLFET in the vicinity of half-filling is shown in Figure 6.3. The $\nu = 2/3$, $\nu = 3/5$, $\nu = 2/5$ and $\nu = 1/3$ states are fully developed, and fractions up to $\nu = 5/9$ and $\nu = 4/9$ are resolved. This is to demonstrate the high quality of this SLFET. In the inset we show the resistance for a smaller electron density of $n_s = 0.94 \times 10^{11} \text{ cm}^{-2}$, measured around the $\nu = 2/3$ state magnetic fields between $B = 5$ T and $B = 7$ T. The trace has been shifted vertically for clarity. At this density a

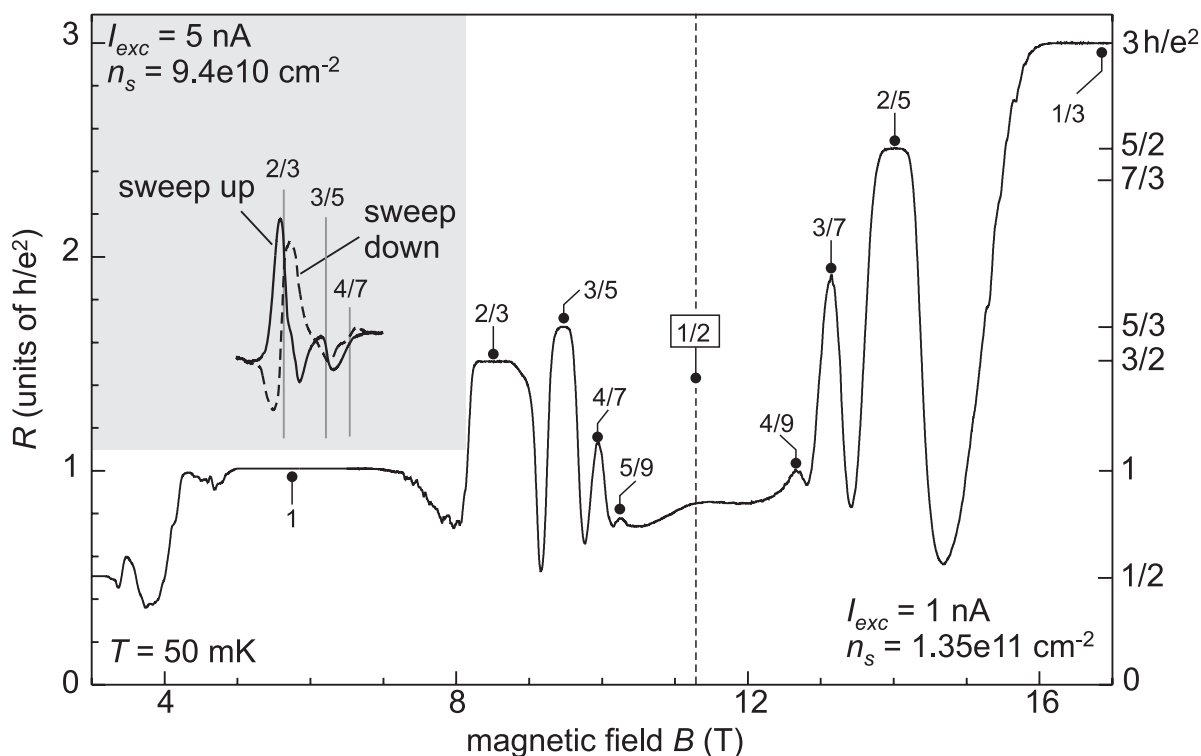


Figure 6.3: Magnetoresistance of the $q = 20$ nm SLFET.

pronounced hysteresis between upward and downward sweep is observed. In Section 6.4 the dependence of this hysteresis on the electron density is studied in detail. It is interesting to note that at a temperature of $T = 330$ mK, the same sample did not exhibit any hysteresis. In the next section we therefore look at the temperature dependence of this hysteresis.

6.3 Temperature dependence

We investigate the temperature dependence of the $\nu = 2/3$ resistance maximum of the $q = 10$ nm SLFET between $T = 350$ mK and $T = 700$ mK. As can be seen in Figure 6.4(b), the resistance maximum at down sweep orderly quenches with increasing temperature. The maximum at up sweep, however, first increases and shifts on the magnetic field axis, and then decreases, see Figure 6.4(a). In Figure 6.4(c) the drop of the resistance down sweep maximum is found to be linear. Strikingly, the amplitude of the hysteresis, defined as the difference between the up sweep and the down sweep resistance maxima, exhibits an expo-

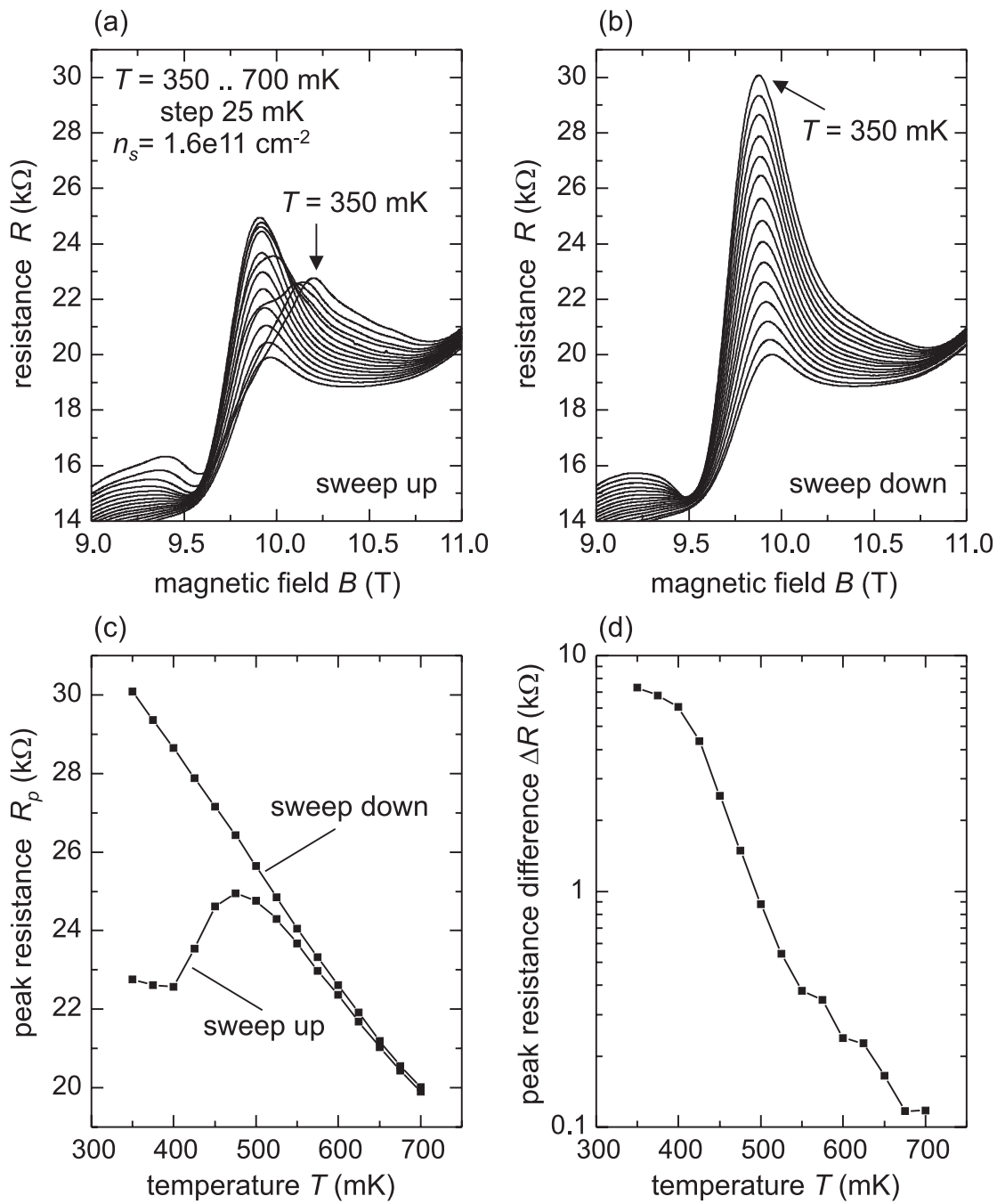


Figure 6.4: Temperature dependence of the $\nu = 2/3$ hysteresis in the $q = 10$ nm SLFET.

ponential drop, see Figure 6.4(d). This type of quenching of the hysteresis indicates that the underlying physics is characterized by an activation process. In conjunction with our observation, that no hysteresis is found in the $q = 20$ nm SLFET at $T = 330$ mK, but clearly at $T = 50$ mK, we speculate that the potential modulation induced by the superlattice serves to increase the cause for the hysteretic behavior.

6.4 Hysteresis at filling factor $\nu=2/3$

In Figure 6.5 we present a complete scan of the hysteretic region, obtained with the $q = 20$ nm SLFET at a temperature of $T = 50$ mK. Figure 6.5(a) displays the magnetoresistance R in the $(1/\nu, n_s)$ -plane for $\nu < 1$ for negative sweep direction. Following the line of constant filling $\nu = 2/3$ as n_s (or equivalently the field B) is lowered, the resistance maximum collapses and subsequently reemerges at a slightly offset filling factor. This reentrant behavior is the signature in transport for the transition between the spin-unpolarized ($\uparrow\downarrow$) to the spin-polarized ($\uparrow\uparrow$) ground states [Eis90] [Eng92] [Kan97]. Inverting the field sweep direction for recording the resistance in the $(1/\nu, n_s)$ -plane unveils hitherto undisclosed aspects of this $\nu = 2/3$ phase transition. When acquiring the data during upward sweeps in Figure 6.5(b), the spin transition is postponed to higher electron densities n_s (i.e. magnetic fields B) in comparison with data collected during downward sweeps. Accordingly, the electronic spin polarization γ along the lines of constant filling factor $\nu = 2/3$ will exhibit hysteretic behavior, as schematically shown in the inset of Figure 6.5(b). These observations are congruous with an Ising ferromagnetic phase transition, if the unpolarized and fully polarized ground states are mapped onto states of opposite pseudospin orientation. The drop in the resistance in the vicinity of the phase transition may then reflect the dissipative current, that originates from the eventual backscattering of charge-carrying quasi-particles that suffer reflections off energy barriers separating disorder-induced domains of distinct pseudospin.

6.5 Resistance time dependence

The ferromagnetic nature of the domains is indirectly confirmed by the introduction of time as a parameter. It allows to corroborate on the importance of domains and their boundaries and sheds light on their dynamics. The resistance in the hysteretic region manifests a strong dependence on both the field sweep rate and the time following a change in an ap-

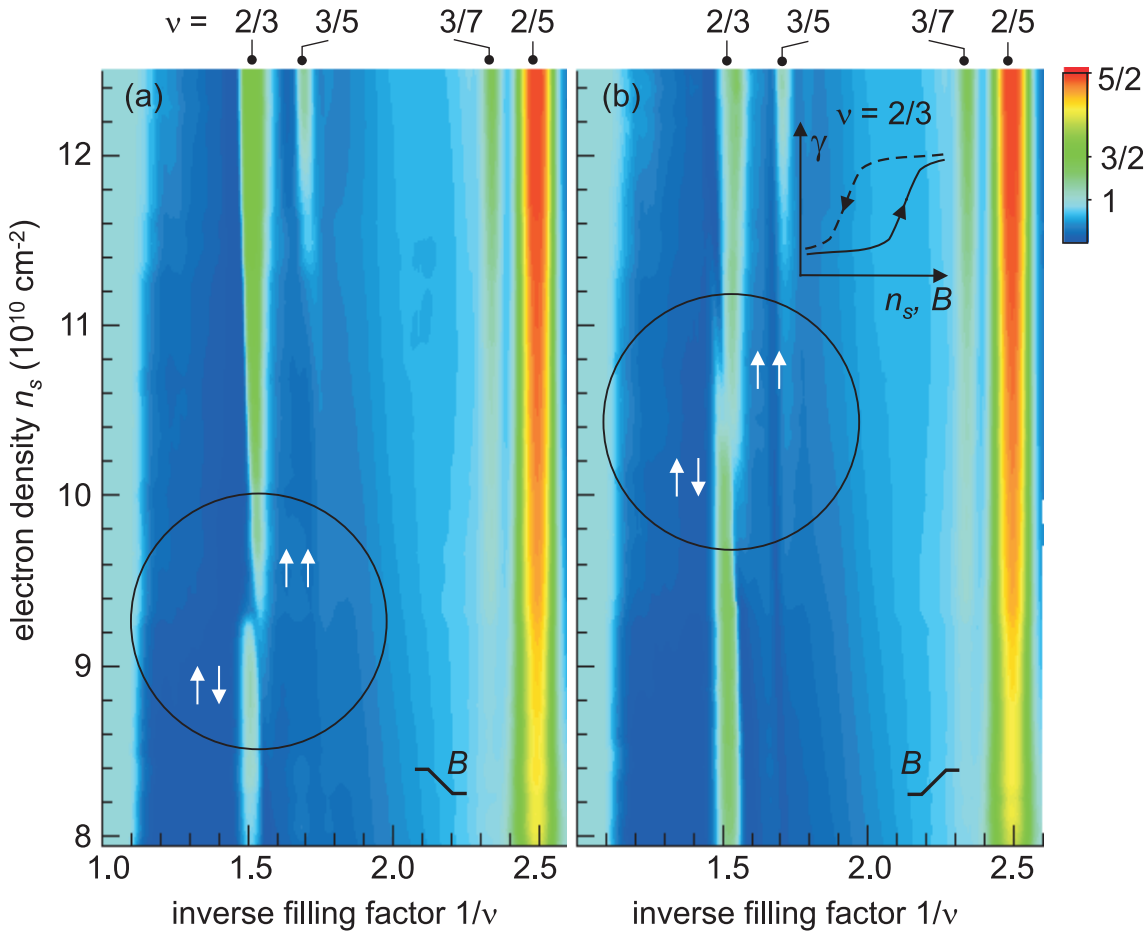


Figure 6.5: Color map of the source-drain resistance R in units of h/e^2 in the $(1/\nu, n_s)$ -plane when the field or carrier density is swept (a) downwards or (b) upwards. The inset schematically indicates the degree of electron spin polarization along the line $\nu = 2/3$ when the carrier density or field is increased (solid line) or lowered (dashed line) (modified from [Sme01]).

plied field. One example is depicted in Figure 6.6. In this experiment on the $q = 20$ nm SLFET at $T = 50$ mK, the resistance was recorded while sweeping from $\nu = 2/3$ downward to $\nu = 1$, and upward back to $\nu = 2/3$, see Figure 6.6(a). While the magnetic field was held constant, the resistance was then recorded over time, see Figure 6.6(b). As can be seen, R decreases over time, and exhibits sudden drops. After almost one hour the resistance has drastically dropped by $\Delta R = 10$ k Ω , or 40% of h/e^2 . When the magnetic field is then increased, the resistance entirely recovers, see Figure 6.6(c). Phenomenologically, this time dependent behavior invariably reminds of the Barkhausen- and magnetic after-effects in

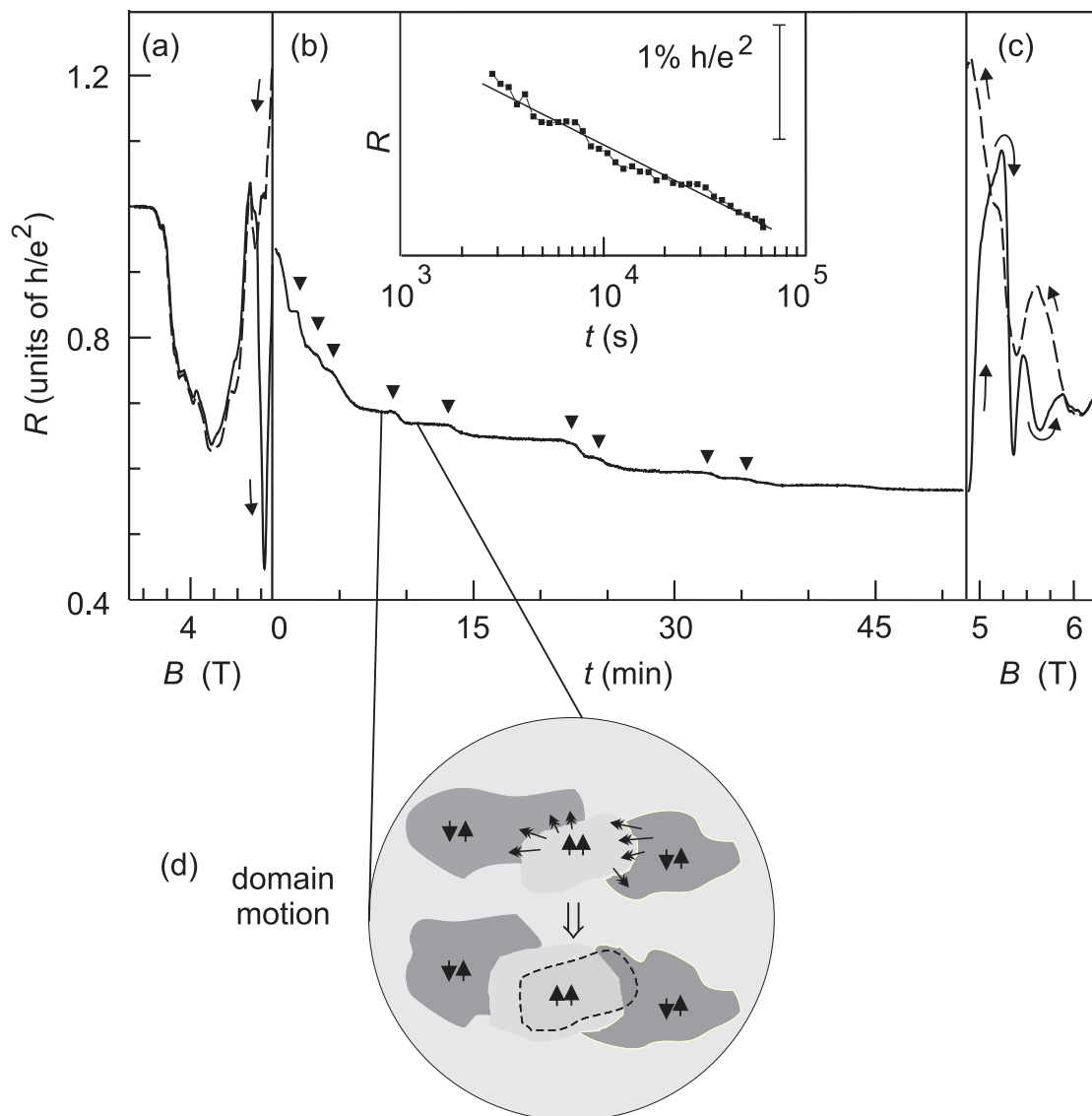


Figure 6.6: Time evolution of the $\nu = 2/3$ resistance (modified from [Sme01]), and one snapshot of a domain wall motion event (schematically drawn).

familiar ferromagnetic materials [Ber98] [Pro99]. Their hallmarks are abrupt, mostly non-reproducible jumps in the magnetization and a time lag on the scale of minutes, hours or even days between the sudden change in applied field and the equilibrium of the magnetization in a specimen. Here, in an analogous fashion, impediments to free domain wall motion, caused by any imperfections or irregularities that render the wall energy position-dependent, may make wall motion in our system proceed by a series of Barkhausen jumps between energy

minima. These jumps may be due to thermal agitation or external field driven. Surges in R proclaim these prompt rearrangements of domains, that reshape the potential landscape for backscattering of the mobile charge-carrying quasi-particles near domain walls held responsible for the dissipative current. One particular example of a domain wall motion incident is schematically shown in Figure 6.6(d). Here the spin-polarized ground state domain grows on the cost of the neighboring domains being in the spin-unpolarized ground state.

Using the same experimental procedure that led to Figure 6.6(b), we have monitored R over long time frames (> 10 hours). We find that the resistance R does not settle and its overall trend follows a time-logarithmic function, as shown in the insert to Figure 6.6. In common ferromagnetic materials, described by a wide spread of time constants because of the heterogeneous domain shapes and barriers, the thermal relaxation and magnetic viscosity indeed only accomplish a logarithmic approach of the magnetization to the equilibrium state [Ber98] [Pro99]. Keeping in mind that here a resistance is measured, the analogies are extraordinary. Even though only one specific example is shown, the time-logarithmic relaxation and the "resistive Barkhausen jumps" are pervasive in the entire phase transition region. We interpret them as additional evidence for domain morphology.

6.6 Nuclear magnetic resonance

For a system partitioned in domains, domain growth or transport across domains with different spin configuration demands electron spin flips. Besides spin-orbit coupling and acoustic phonon emission, the contact hyperfine interaction is a possible candidate to mediate electron spin reversal via flip-flop scattering events, the simultaneous flip of an electron and nuclear spin [Wal94]. As a consequence, the nuclear spin polarization of the host semiconductor is modified. This process, referred to as dynamic nuclear spin polarization (DNP), conversely will affect the electron transport in the following ways, if the net nuclear spin polarization is substantial:

1. The altered number of nuclear partners with the appropriate spin modulates the flip-flop scattering rate.
2. A net nuclear spin polarization represents an effective nuclear field to be considered for the electronic Zeeman splitting. Depending on whether at the domain wall the transition occurs from an unpolarized to a spin polarized domain or vice versa, the nuclear field will either enhance or lower the Zeeman splitting as the net nuclear spin

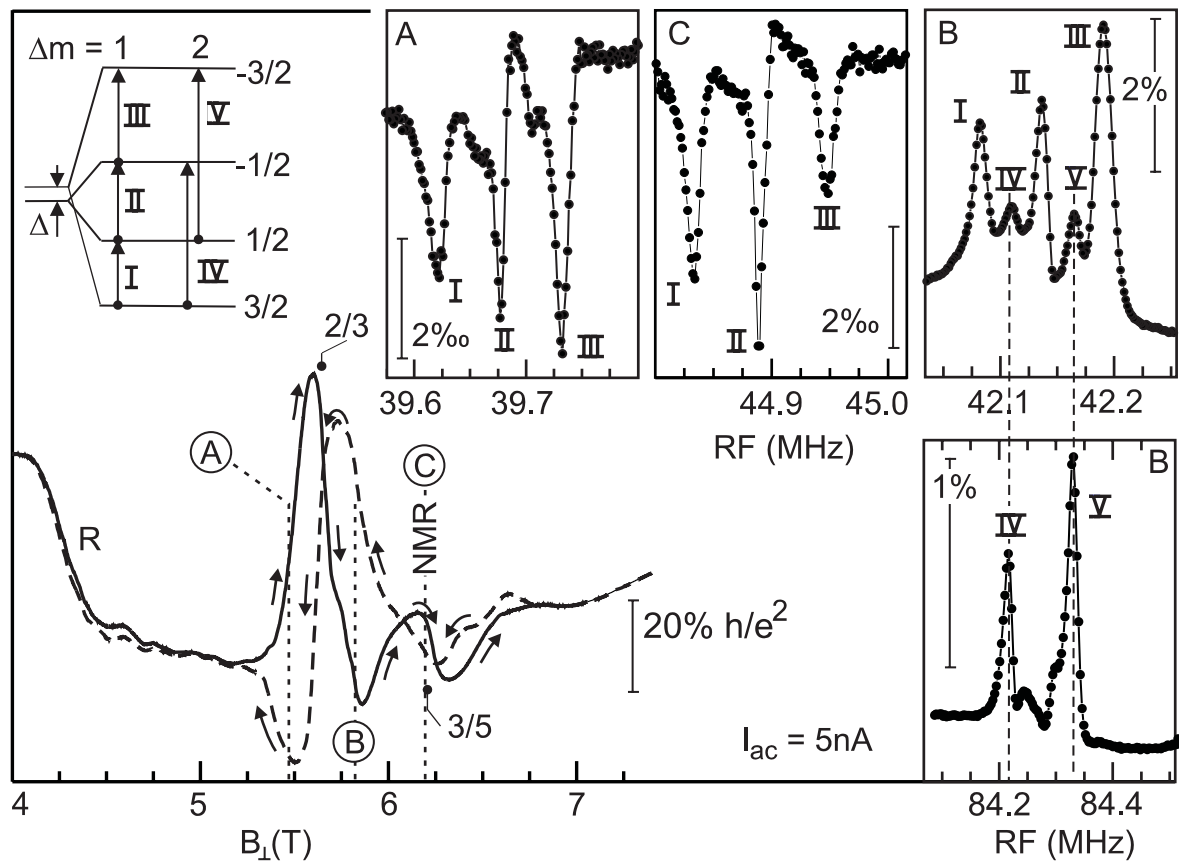


Figure 6.7: Resistively detected NMR for As^{75} at different fields (A,B,C) around filling factor $\nu = 2/3$ indicated on the R vs. B curves. The transitions between the nuclear energy levels are depicted in the insert (from [Sme01]).

polarization grows and subsequently in turn suppress or promote additional spin flips. This effective field lays out modified energy barriers between domains of opposite electronic spin configuration.

3. Due to nuclear spin diffusion, the net nuclear spin polarization is not localized to the domain walls and ‘cross-talk’ will further complicate the picture.

The standard approach in transport to highlight the influence of the nuclear spin system consists of irradiating the sample with narrow-band radio frequency, while simultaneously monitoring the resistance of the 2DES [Wal94] [Kro99]. Radio frequency in resonance with a transition between the Zeeman split nuclear energy levels, impairs the net nuclear spin polarization and reverses the effects of the DNP. Nuclear magnetic resonance spectra for

As^{75} are plotted in Figure 6.7. The resonance lines show a three-fold splitting, ascribed to the interaction of the quadrupole moment of these $I = 3/2$ -nuclei with intrinsic electric field gradients induced by stress and/or the broken cubic symmetry near the interface of the slightly lattice-mismatched GaAs and AlAs layers in the SLFET. Two additional peaks in between the dominant triplet, are identified as $\Delta m = 2$ -transitions triggered by the unintentionally generated second-harmonic of the incident radio frequency. By virtue of the quadrupole interaction, these transitions are no longer forbidden and saturable because of the long T_1 -relaxation time. Data taken at double the frequency (bottom right panel) confirm this assertion.

These nuclear magnetic resonance results support the importance of DNP for transport across this ferromagnetic phase, since magnitude and sign of the radio frequency response correlate with the difference in R between up and down sweeps. Quadrupole splitting accounts for the resonance substructure. It is difficult to unravel in this nuclear magnetic resonance set-up whether the nuclear spin polarization is the sole consequence of current flow. However, other potential sources are difficult to reconcile with the large number of nuclear spin flips required to have an observable impact in comparison with the insignificant number of electrons involved. DNP and nuclear spin diffusion will bring in a slow time dependence and should themselves be — besides the very presence of domains due to the exchange interaction and disorder — an *additional* source for hysteresis. Granting that current flow is responsible for the nuclear spin polarization, this assertion is supported by systematically lowering the excitation current over three orders of magnitude (5 nA down to 5 pA), while keeping the sweep rate constant, and studying the hysteresis along $\nu = 2/3$. The contribution of DNP should dwindle. Indeed, at 5 pA dramatic hysteresis remains. It is only altered in shape for currents above 0.5 nA and the transitions shift to different densities with increasing excitation current.

6.7 Conclusion

Substantial evidence has been gathered for ferromagnetic ordering and domain morphology in the fractional quantum Hall regime. Intricate, possibly unique, microscopic mechanisms for magnetism and transport through this peculiar ferromagnet are at work. The time-dependent interplay of the domain structure, thermal relaxation and the role of nuclear spins turns the microscopic description of transport through this ferromagnet in the fractional quantum Hall regime into a tremendous challenge. In nominally isotropic two-dimensional

electron systems, the domain formation is disorder-induced. In the SLFET, however, we have evidence that the potential modulation plays an intensifying role to domain formation. The study of samples with artificially created boundary between both phases of opposite pseudospin should be promising to isolate the various mechanisms pointed out here. Using the SLFET, further studies could be dedicated to changing the superlattice period and modulation strength. Eventually, local probes may then be put to work. Generally, the unrivalled controllability, through patterning and gating among others, inherent to the GaAs-based two-dimensional electron systems is then likely to render it into a profitable test vehicle for the general study of low dimensional magnetism, macroscopic quantum tunnelling and non-equilibrium thermodynamics.

Chapter 7

Conclusion

In this work we have introduced a new semiconductor device, the superlattice field effect transistor (SLFET). This device is a combination of a two-dimensional electron system and a superlattice. We were able to explore the wide range of physics between one- and two-dimensional electron systems because of the fact that several controllable energy scales could be brought into the same order of magnitude. In Figure 7.1 we summarize some of the interrelations between the different regimes and their dependence on the experimentally controllable parameters. Two-dimensional physics was characterized by magneto-quantum oscillations, and miniband transport. As we have increased the Fermi energy, or, equivalently, the electron density by means of the gate, we entered the one-dimensional world, characterized in magnetotransport by open electron orbits. We were then able to travel back to the two-dimensional world by increasing the magnetic field, thus invoking magnetic breakdown, and recovered closed electron orbits. Tweaking the coupling strength, we found that with increasing overlap of the wave functions in adjacent quantum wires, we left the regime of resonant tunneling, characteristic of separate quantum wires, and entered the regime of miniband transport, characteristic of modulated two-dimensional electron systems. On yet another axis of this parameter space, when increasing the superlattice period length at constant Fermi energy, more than one miniband became occupied, and we were faced with a multi-band structure, perfectly suited for studying quantum interference effects. At very small magnetic fields, only the electron orbit with the smallest reciprocal space area was dominant and observed as characteristic magnetoresistance frequency. For larger magnetic fields, however, by virtue of magnetic breakdown, quantum interference in several different closed orbits and between different open orbits became possible, all marking the magnetore-

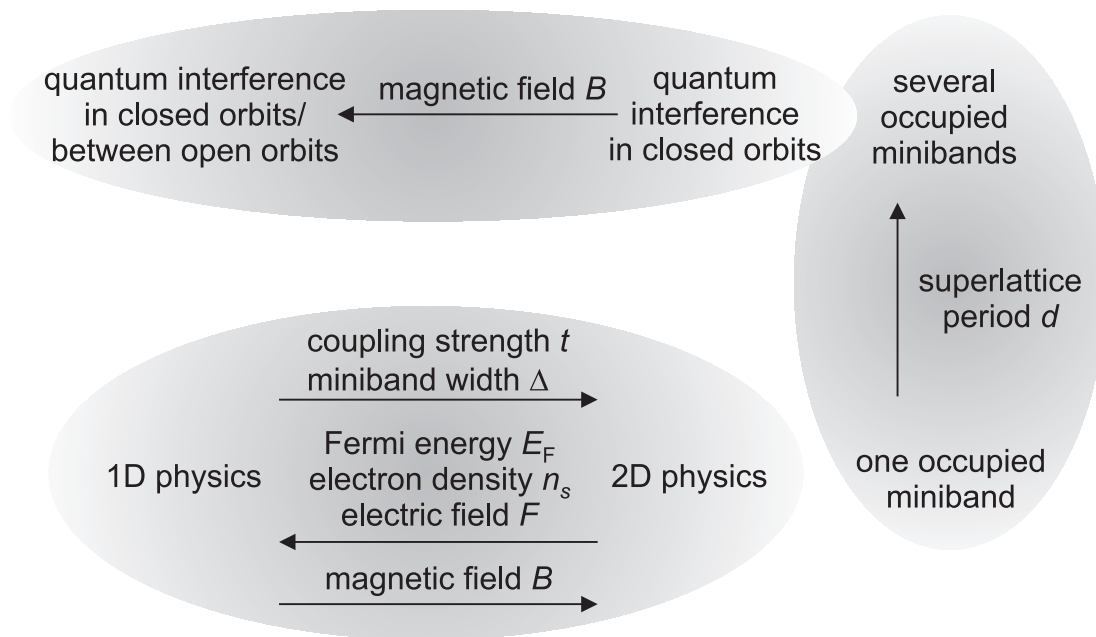


Figure 7.1: Parameter space.

sistance frequency spectrum with their own frequency. Finally, weakly modulated SLFETs were found to be an ideal testbed for studies in the fractional quantum Hall regime.

The main **technological advance** of this work is the development of the superlattice field effect transistor, which offers the unparalleled combination of flexibility in band structure engineering, high electron mobility, and electron density tunability.

The main **experimental advances** of this work are

- the discovery of negative differential resistance due to Bloch localization of miniband electrons
- the observation of the transition from closed to open electron orbits when raising the Fermi energy from within the miniband into the minigap
- the first experimental confirmation of the magnetic breakdown formula in an artificial band structure
- the first observation of resonant tunneling between an array of identical quantum wires

- the direct visualization of the artificial multi-band structure of a one-dimensionally modulated two-dimensional electron system
- the first complete mapping of the ferromagnetic phase transition in the fractional quantum Hall regime

The main **theoretical advances** of this work are

- the numerical calculation of the SLFET band structure
- the semiclassical model for transport in weakly modulated two-dimensional electron systems, in particular the quantum interference between open electron orbits
- the discovery that the Weiss oscillations represent a special case of this semiclassical theory, and their explanation based on the artificial band structure

We think that our work offers the potential for a variety of future projects, of both theoretical and experimental nature. Transport calculations using the Kubo formula should be able to quantitatively explain our magnetoresistance data in Chapter 2. Spin effects are observed in experiment, and also need to be included in the theory. Non-equilibrium transport calculations, already well established for bulk superlattices, are required for quantitative explanation of the miniband transport data in Chapter 3. Of particular interest here is the question of charge stability in the regime of negative differential velocity, qualitatively postulated in our model. Can travelling charge waves even exist in this low-dimensional superlattice system? Our resonant tunneling model in Chapter 4 may be quantified, and the periodic current resonances at high magnetic fields remained unexplained in our model. In Chapter 5 with our semiclassical theory we were able to explain the frequency of the magnetoresistance oscillations due to quantum interference, the resistance amplitudes await a quantitative explanation. Certainly, the ferromagnetic phase transition observed in the fractional quantum Hall regime (see Chapter 6) is only quite phenomenologically described in our model. And in particular, the intricate, time-dependent interplay of the disorder-induced domain structure, thermal relaxation, and the role of nuclear spins turns the microscopic description of transport through this ferromagnet into a tremendous challenge.

On the experimental side, further magnetotransport studies of the type presented in Chapter 2 should be dedicated to spin effects. As already mentioned in Section 2.3.8, there has been increasing theoretical interest in the ground state of a two-dimensional electron gas in

a short-period lateral potential in magnetic field, with the Coulomb electron-electron interaction included in the Hartree-Fock approximation. It is found that for a sufficiently short period the dominant Coulomb effects are determined by the exchange interaction, and hysteretic behavior is predicted when the magnetic field is tilted and increased, such that the perpendicular component is always constant [Man00]. This behavior is a result of the interplay of the exchange interaction with the energy dispersion and the spin splitting. Hysteresis effects of this type should be observable in magnetotransport experiments in tilted magnetic fields using the SLFET.

Regarding non-equilibrium transport, a definitive goal must be the fabrication of the Bloch oscillator. Although we have not been successful to detect Bloch emission from the SLFET, neither using a photoconductive InSb, nor a second identical SLFET, as detector, the observation of Bloch-phonon resonances (Section 3.3.3) is a first indication that with more sensitive detectors Bloch emission should be seen. Under irradiation with the Bloch frequency the SLFET should exhibit a current resonance effect (inverse Bloch oscillator). CEOFETs have been found to operate at room temperature, but the high-temperature behavior of the SLFETs, and in particular the temperature dependence of the negative differential resistance, is yet to be measured. Further studies could be dedicated to non-equilibrium transport in crossed and parallel electric and magnetic fields. With respect to the recent theoretical studies of coupled Luttinger liquids, equilibrium (magneto)transport experiments may reveal interesting aspects using the weakly coupled array of quantum wires (Chapter 4). At finite bias, voltage-controlled lasing has been proposed in a weakly coupled superlattice [Kaz71]. The problem of instabilities may be solved by using coupled one-dimensional wires as in the SLFET instead of quantum wells. Our work on weakly modulated electron systems (Chapter 5) may be extended to even smaller period lengths, such that only two or three minibands are occupied, in which case the quantum interference phenomena should be most clearly seen. Some attention should also be paid to the region around half filling, as we can expect similar quantum interference phenomena also for composite fermions. Finally, our studies in the fractional quantum Hall regime presented in Chapter 6 represent only the beginning of an understanding of the phenomena. A further increase of the electron mobility would be desired, and the influence of the potential modulation should be clarified. The SLFET concept may be extended by a second cleave and overgrowth to fabricate a Mott wire, that could be tuned in and out of the Mott gap by means of the gate.

Acknowledgements

I am indebted to many people that directly or indirectly contributed to realizing this work, in particular I want to thank

- Prof. Dr. Gerhard Abstreiter. You gave me all the freedom and support I needed to develop and realize my own ideas. I am proud of the confidence I received.
- Prof. Dr. Werner Wegscheider. You are a constant source of inspiration and good mood. It was great to work with you.
- Max Bichler. Thanks for all the great samples, and the good time we had even in tough situations, for example after the heated window in our MBE cracked while Werner was surfing in Hawaii.
- Dr. Martin Rother. You introduced me to the art of cleaved-edge overgrowth, you were an enjoyable office mate, always open for discussions, and you wrote the great software tools *Auriga* which I used for all my measurements, and *Aquila* to calculate my SLFETs. Thanks for all that! (and sorry for my undocumented modifications).
- My Diploma students Andreas Krammer, Michael Huber and Christian Stocken. You have done a great job!
- Frank Ertl. Most of my measurements were performed in the excellent He3 magnet system you have built together with Martin Rother.
- Dr. Matthew Grayson. Discussions with you were always enjoyable, and you contributed, amongst other topics, to my understanding of the coupled quantum wire system.
- Dr. Jurgen Smet. Thanks for your great hospitality, which led to an ongoing excellent collaboration and great results.

- Christian Albrecht for our collaboration to solve the mysteries of quantum interference in artificial band structures.
- Prof. Dr. Axel Lorke for help in the early stages of my work, when first faced with the term "magnetic breakdown", and our Sonderforschungsbereich partner Dr. Robert Blick (I bet your dots are good Bloch frequency detectors).
- Prof. Dr. Peter Vogl. It was a great pleasure to discuss various aspects critical to my work with you. Thanks that you *always* had time for me. Christian Strahberger and Jazec Majewski for discussions.
- Prof. Dr. Ludvik Smrcka and Karel Vyborny. Our collaboration regarding magneto-transport in the lowest miniband was most pleasant and fruitful.
- Dr. Andreas Wacker and Dr. E. Schomburg for your help with transport in superlattices. Thanks Andreas for the preprint of your habilitation.
- Prof. Dr. Werner Dietsche. You pointed out the possible influence of folded acoustic phonons on the electronic transport.
- Prof. Dr. Sackmann, Dr. Adnane Abdelghani, and Dr. Motomo Tanaka for a good collaboration in the exciting field of bio-organic surface functionalization. This work is not included in this thesis.
- Dr. Karl Unterrainer and Reinhard Zobl for your hospitality and help with the Bloch emission measurement. I am glad we tried!
- Prof. Brack and Christian Amann for discussions about the Maslov index of electrons in a magnetic field.
- The scientific, technical and support staff of the Walter Schottky Institute. You made the institute a great place to work. In particular I want to thank Dr. Artur Zrenner for competent help with scientific and technical questions, how will the Institute survive when you are gone northwards; Markus Arzberger together we have discovered the "art of coffee", thanks for the numerous chats, and also for occasional RIE; Dr. Gert Schedelbeck for helping me with cleaved-edge overgrowth problems; Dr. Karl Brunner and Robert Neumann for help with our silicon-on-insulator project (work not included in this thesis); Matthias Herbst we were a good bonder-team; Gerhard

Böhm you contributed the substrates for the short channel CEOFETs; Uli Gürster, Reiner Schneider, Gabi Ebert and Edith Sckopke for help with sample processing; Fritz Sedlmeir and Wolfgang Bendak for help in the machine shop; Maria Manhart, Irmgard Neuner and Regina Huber for secretarial help; Dr. Martin Rother, Stefan Sedlmaier, Angelika Paassen, Olav Jaeger, Michael Huber and Dr. Matthew Grayson we had a good time in our (sometimes crowded) office; the Pizza service 3262175 that saved us from starving, thanks for coming even at the worst weather.

- Kruder & Dorfmeister.
- My friends Oliver Wenisch and Frank Hille.
- My parents Heidi and Günter Deutschmann. You always believed in me, and you made possible my physics studies.
- My wife Annike.

This work was supported by the Deutsche Forschungsgemeinschaft via Sonderforschungsbereich 348, and by the German Bundesministerium für Bildung, Wissenschaft, Forschung und Technologie under contract No. 01BM912.

List of Figures

1.1	Modulation doped heterostructure	4
1.2	Natural and artificial band structures	8
1.3	Fabrication of the superlattice field-effect transistor	9
1.4	Cleaved-edge overgrowth technique	10
1.5	Thesis outline	12
2.1	SLFET sample structure	18
2.2	Calculated band structure in the Kronig-Penney model	19
2.3	Self-consistently calculated electron density distribution	21
2.4	Self-consistently calculated band structure	22
2.5	Fermi contours for different Fermi energies	23
2.6	Calculated density of states and electron density	24
2.7	Fermi contours for different Fermi energies in k space	26
2.8	Landau level spacing vs. energy and electron density	28
2.9	Fermi contours for different Fermi energies in real space	30
2.10	Electron orbits in the regime of magnetic breakdown	31
2.11	Electron trajectory 'phase diagram' in the (n_s, B) plane	33
2.12	Magnetoresistance for gate voltage $U_g = 0.25$ V	34
2.13	Magnetoresistance for gate voltage $U_g = 0.4$ V	35
2.14	Magnetoresistance for gate voltage $U_g = 0.5$ V	36
2.15	Magnetoresistance for gate voltage $U_g = 0.6$ V	37
2.16	Overview of magnetoresistance traces for $E_F > \Delta$	38
2.17	Relation between gate voltage and electron density	39
2.18	Magnetoresistance maxima and minima in the (U_g, B) plane.	40
2.19	Sample geometry and definitions for calculating the magnetoresistance	41
2.20	Calculated and experimental magnetoresistance for $U_g = 0.4$ V	45

2.21	Calculated and experimental magnetoresistance for the reference CEOFET at $U_g = 0.4$ V	46
2.22	Calculated and experimental magnetoresistance for $U_g = 0.275$ V	47
2.23	Comparison of calculated and experimental breakdown magnetic field	48
2.24	Spin-polarized state at high magnetic fields	49
2.25	Electron density dependence of the zero magnetic field resistance	51
2.26	Model for explaining the zero-field resistance	52
2.27	High-frequency magnetoresistance oscillations at commensurate superlattice period and magnetic length	53
2.28	Calculated low-field band structure and density of states	57
2.29	Calculated medium-field band structure and density of states	58
2.30	Calculated high-field band structure and density of states	59
2.31	Experimental and calculated magnetoresistance maxima and minima in the (U_g, B) plane	61
3.1	Electron velocity and electron effective mass in the Esaki-Tsu model	65
3.2	Wave function and mean electron velocity in tilted superlattice	67
3.3	Different regimes of superlattice transport	69
3.4	Self-consistently calculated electron density distribution	72
3.5	Calculated electron wave functions	73
3.6	Calculated miniband structure	75
3.7	Calculated miniband width and electron density variation	76
3.8	Current-voltage relation of the $q = 0$ nm SLFET.	77
3.9	Current-voltage relation for small source-drain voltages	78
3.10	Esaki-Tsu fit to the source-drain current.	79
3.11	Peak electric field and electron scattering time	80
3.12	Phonon dispersion relation and current Bloch-phonon resonances	81
3.13	Resistance maxima and minima in the (U_{sd}, U_g) plane	83
3.14	Current-voltage relations for SLFETs and reference CEOFETs	85
3.15	Peak current and transconductance	87
3.16	Peak current versus miniband width	88
3.17	Charge instability at the presence of NDR	90
3.18	Electron mobility determined from the low-field magnetoresistance	92
3.19	Current-voltage traces in magnetic field for $U_g = 0.25$ V.	95

3.20	Current-voltage traces in magnetic field for $U_g = 0.4$ V.	96
3.21	Peak voltage and peak current for different gate voltages versus magnetic field.	97
3.22	Calculated mean electron velocity-field relation	98
3.23	Calculated peak mean velocity and peak electric field vs. magnetic field.	99
3.24	Electron tunneling in crossed electric and magnetic fields.	99
3.25	Sample design of the heterobarrier and planar doped CEOFETs.	102
3.26	Current-voltage relation of heterobarrier CEOFETs.	103
3.27	Band structure calculation for CEOFET and planar doped CEOFET	104
3.28	Current-voltage relation of planar-doped CEOFETs.	105
4.1	Resonant tunneling SLFET sample design	110
4.2	Kronig-Penney band structure calculation	111
4.3	Current-voltage relation	113
4.4	Resonant tunneling model	115
4.5	Current-voltage relation in perpendicular magnetic field at $U_g = 0.5$ V	117
4.6	Current-voltage relation in perpendicular magnetic field at $U_g = 0.7$ V	119
4.7	Back and forward scattering conservation conditions	120
4.8	Tunneling probability and cyclotron radius	122
4.9	Current-voltage relation in parallel magnetic field	124
5.1	Artificial band structure	128
5.2	Lateral superlattice patterning methods	129
5.3	SLFET structure and calculated electron density	132
5.4	Calculated electron density distribution	134
5.5	Calculated potential distribution	135
5.6	Calculated potential modulation amplitude	136
5.7	Sample structure and measurement scheme	137
5.8	SLFET and CEOFET magnetoresistance at $n_s = 3 \times 10^{11} \text{ cm}^{-2}$	138
5.9	Magnetoresistance at $n_s = 1.9 \times 10^{11} \text{ cm}^{-2}$	139
5.10	Magnetoresistance at $n_s = 3.1 \times 10^{11} \text{ cm}^{-2}$	140
5.11	Magnetoresistance Fourier spectrum for the $q = 30$ nm SLFET	141
5.12	Magnetoresistance Fourier spectrum for the $q = 40$ nm SLFET	142
5.13	Magnetoresistance Fourier spectrum for the $q = 40$ nm CEOFET	143
5.14	Band structure and Fermi contours	144
5.15	Probability of electron orbits in a multi-band structure	146

5.16	Closed electron orbits	148
5.17	Quantum interference between open orbits	149
5.18	Temperature dependence of quantum interference oscillations	152
5.19	Stark quantum interferometer	153
5.20	Magnetic breakdown in an organic superconductor	155
5.21	Self-consistent calculation of the laser-doped structure	157
5.22	Commensurability oscillations in a 1D LSDSL	158
5.23	Resistance resonances in a 2D antidot lattice	160
5.24	Magnetic focussing resistance oscillations	161
6.1	Fractional quantum Hall effect in the $q = 20$ nm SLFET	167
6.2	Magnetoresistance of the $q = 10$ nm SLFET and CEOFET	168
6.3	Magnetoresistance of the $q = 20$ nm SLFET	169
6.4	Temperature dependence of the $\nu = 2/3$ hysteresis	170
6.5	Hysteresis at filling factor $\nu = 2/3$	172
6.6	Time evolution of the $\nu = 2/3$ resistance	173
6.7	Nuclear magnetic resonance at filling factor $\nu = 2/3$	175
7.1	Parameter space	180

Bibliography

- [Abr65] M. Abramowitz and I. Stegun. *Handbook of mathematical functions*. Dover Publications, New York, 1965.
- [Alb98a] C. Albrecht, J. H. Smet, D. Weiss, K. v. Klitzing, V. Umansky, and H. Schweizer. *Novel magneto-resistance oscillations in short period lateral superlattices*. *Physica B* 249-251:914, 1998.
- [Alb98b] C. Albrecht, J. H. Smet, D. Weiss, K. von Klitzing, R. Hennig, M. Langenbuch, M. Suhrke, U. Ressler, V. Umansky, and H. Schweizer. *Fermiology of two-dimensional lateral superlattices*. *Phys. Rev. Lett.* 83:2234, 1998.
- [Alb01] C. Albrecht, J. H. Smet, K. v. Klitzing, D. Weiss, V. Umansky, and H. Schweizer. *Evidence of Hofstadter's fractal energy spectrum in the quantized Hall conductance*. *Phys. Rev. Lett.* 86:147, 2001.
- [All88] R. S. Allgaier. *Magneto-transport at high Hall angles: a comparison of the high-magnetic-field and high-mobility (quantum Hall effect) limits in the Hall bar and Corbino disc configurations*. *Semicond. Sci. Technol.* 3:306, 1988.
- [And82] T. Ando, A. B. Fowler, and F. Stern. *Electronic properties of two-dimensional systems*. *Rev. Mod. Phys.* 54(2):437, 1982.
- [Ash76] N. W. Ashcroft and N. D. Mermin. *Solid state physics*, chapter 10, page 175. Saunders College Publishing, 1976.
- [Bar50] J. Bardeen and W. Shockley. *Phys. Rev.* 80:72, 1950.
- [Bas81] G. Bastard. *Superlattice band structure in the envelope-function approximation*. *Phys. Rev. B* 24:5693, 1981.

- [Bas88] G. Bastard. *Wave mechanics applied to semiconductor heterostructures*, page 22. Les editions de physique, 1988.
- [Bau94] P. Baumgartner, K. Brunner, G. Abstreiter, G. Böhm, G. Tränkle, and G. Weimann. *Fabrication of in-plane-gate transistor structures by focused laser beam-induced Zn doping of a modulation-doped GaAs/AlGaAs quantum wells*. Appl. Phys. Lett. 64:592, 1994.
- [Bau97] P. Baumgartner, W. Wegscheider, M. Bichler, G. Schedelbeck, R. Neumann, and G. Abstreiter. *Single-electron transistor fabricated by focused laser beam-induced doping of a GaAs/AlGaAs heterostructure*. Appl. Phys. Lett. 70:2135, 1997.
- [Bau98] P. Baumgartner, W. Wegscheider, M. Bichler, G. Groos, and G. Abstreiter. *Direct writing of in-plane-gated nanostructures by focused laser beam-induced doping*. Physica E 2:441, 1998.
- [Bee89] C. W. J. Beenakker. *Guiding-center-drift resonance in a periodically modulated two-dimensional electron gas*. Phys. Rev. Lett. 62:2020, 1989.
- [Ber87a] G. Bernstein and D. K. Ferry. *Negative differential conductivity in lateral surface superlattices*. J. Vac. Sci. Technol. B 5:964, 1987.
- [Ber87b] G. Bernstein and D. K. Ferry. *Observation of negative differential conductivity in a FET with structured gate*. Z. Phys. B - Condensed matter 67:449, 1987.
- [Ber98] G. Bertotti. *Hysteresis in Magnetism*. Academic Press, San Diego, 1998.
- [Bet90] P. H. Beton, P. C. Main, M. Davison, M. W. Dellow, R. P. Taylor, E. S. Alves, L. Eaves, S. P. Beaumont, and C. D. W. Wilkinson. *Temperature dependence of magnetoresistance oscillations in a two-dimensional electron gas subjected to a periodic potential*. Phys. Rev. B 42:9689, 1990.
- [Bet91] P. H. Beton, M. W. Dellow, P. C. Main, E. S. Alves, L. Eaves, S. P. Beaumont, and C. D. W. Wilkinson. *Magnetic breakdown of a two-dimensional electron gas in a periodic potential*. Phys. Rev. B 43:9980, 1991.
- [Bg97] P. Baumgartner. *Optische und elektronische Eigenschaften lasergeschriebener GaAs Nanostrukturen*. Ph.D. thesis, Walter Schottky Institut, 1997.

- [Blo28] F. Bloch. *Über die Quantenmechanik der Elektronen in Kristallgittern*. Z. Phys. 52:555, 1928.
- [Blo62] E. I. Blount. Phys. Rev. 126:1636, 1962.
- [Bra72] W. Brauer. *Einführung in die Elektronentheorie der Metalle*. Akademische Verlagsgesellschaft, Leipzig, 1972.
- [Bra97] M. Brack and R. K. Bhaduri. *Semiclassical Physics*. Frontiers in Physics. Addison-Wesley Publishing Company, Inc., 1997.
- [Car00] E. W. Carlson, D. Orgad, S. A. Kivelson, and V. J. Emery. *Dimensional crossover in quasi-one-dimensional and high- T_c superconductors*. Phys. Rev. B 62:3422, 2000.
- [Cha90] R. G. Chambers. *Electrons in Metals and Semiconductors*. Physics and its applications. Chapman and Hall, 1990.
- [Cha91] L. L. Chang, E. E. Mendez, and C. Tejedor. *Resonant Tunneling in Semiconductors. Physics and Applications*. NATO ASI Series. Plenum Press, 1991.
- [Cha95] T. Chakraborty and P. Pietilainen. *The Fractional Quantum Hall Effects*. Solid-State Sciences. Springer, 2nd edition edition, 1995.
- [Cha96] A. M. Chang, L. N. Pfeiffer, and K. W. West. *Observation of chiral Luttinger behavior in electron tunneling into fractional quantum Hall edges*. Phys. Rev. Lett. 77:2538, 1996.
- [Cho87] K. K. Choi, B. F. Levine, R. J. Malik, J. Walker, and C. G. Bethea. *Periodic negative conductance by sequential resonant tunneling through an expanding high-field superlattice domain*. Phys. Rev. B 35:4172, 1987.
- [Cho98] H. Cho, J. B. Young, W. Kang, K. L. Campman, A. C. Gossard, M. Bichler, and W. Wegscheider. *Hysteresis and spin transitions in the fractional quantum Hall effect*. Phys. Rev. Lett. 81:2522, 1998.
- [Coh61] M. H. Cohen and L. M. Falicov. *Magnetic breakdown in crystals*. Phys. Rev. Lett. 7:231, 1961.

- [Col77] T. Cole, A. A. Amir, and P. J. Stiles. *Influence of a one-dimensional superlattice on a two-dimensional electron gas*. Phys. Rev. Lett. 38:722, 1977.
- [Col85] C. Colvard, T. A. Gant, M. V. Klein, R. Merlin, R. Fischer, H. Morkoc, and A. C. Gossard. *Folded acoustic and quantized optic phonons in (GaAl)As superlattices*. Phys. Rev. B 31:2080, 1985.
- [Dah96] M. B. Dahan, E. Peik, J. Reichel, Y. Castin, and C. Salomon. *Bloch oscillations of atoms in an optical potential*. Phys. Rev. Lett. 76:4508, 1996.
- [Dek96] T. Dekorsy and H. Kurz. *Bloch-Oszillationen in Halbleiter-Übergittern*. Phys. Bl. 52:1015–1017, 1996.
- [Del00] S. Deleonibus, G. Bertrand, G. Guegan, M. Heitzmann, P. Mur, D. Souil, and S. Tedesco. *20 nm MOS devices for the birth of the 21st century*. Extended abstracts of SSDM 2000 page 56, 2000.
- [Deu00a] R. A. Deutschmann, A. Lorke, W. Wegscheider, M. Bichler, and G. Abstreiter. *Breakdown of SdH oscillations in a short period 1D lateral superlattice*. Physica E (Amsterdam) 6:561–564, 2000.
- [Deu00b] R. A. Deutschmann, W. Wegscheider, C. Albrecht, J. H. Smet, M. Rother, M. Bichler, and G. Abstreiter. *Bridging the gap with cleaved edge overgrowth: on minigaps, magnetic breakdown and quantum interference in artificial band-structures*. Proc. 25th International Conference on the physics of semiconductors (ICPS 25) 2000.
- [Deu00c] R. A. Deutschmann, W. Wegscheider, M. Rother, M. Bichler, and G. Abstreiter. *Negative differential resistance of a 2D electron gas in a 1D miniband*. Physica E (Amsterdam) 7:294–298, 2000.
- [Deu01a] R. A. Deutschmann, C. Stocken, W. Wegscheider, M. Bichler, and G. Abstreiter. *Commensurability effects in lateral surface doped superlattices*. Appl. Phys. Lett. 78:2175, 2001.
- [Deu01b] R. A. Deutschmann, W. Wegscheider, M. Rother, M. Bichler, and G. Abstreiter. *Miniband transport in vertical superlattice field-effect transistors*. Appl. Phys. Lett. 79:1564, 2001.

- [Deu01c] R. A. Deutschmann, W. Wegscheider, M. Rother, M. Bichler, G. Abstreiter, C. Albrecht, and J. H. Smet. *Quantum interference in artificial band structures*. Phys. Rev. Lett. 86:1857, 2001.
- [dH30] W. J. de Haas and P. M. van Alphen. Proc. Netherlands Roy. Acad. Sci. 33:1106, 1930.
- [Dig94] M. M. Dignam, R. C. Ashoori, H. L. Stormer, L. N. Pfeiffer, K. W. Baldwin, and K. W. West. *One-dimensional quantum-wire states probed by resonant electron tunneling*. Phys. Rev. B 49:2269, 1994.
- [dLK31] R. de L. Kronig and W. G. Penney. Proc. Roy. Soc. (London) A 130:499, 1931.
- [Eis90] J. P. Eisenstein, H. L. Stormer, L. N. Pfeiffer, and K. W. West. *Evidence for a spin transition in the $\nu = 2/3$ fractional quantum Hall effect*. Phys. Rev. B 41:7910, 1990.
- [Eis91] J. Eisenstein, T. J. Gramila, L. N. Pfeiffer, and K. W. West. *Probing a two-dimensional Fermi surface by tunneling*. Phys. Rev. B 44:6511, 1991.
- [Eme00] V. J. Emery, E. Fradkin, S. A. Kivelson, and T. C. Lubensky. *Quantum theory of the smectic metal state in stripe phases*. Phys. Rev. Lett. 85:2160, 2000.
- [Eng92] L. W. Engel, S. W. Hwang, T. Sajoto, D. C. Tsui, and M. Shayegan. *Fractional quantum Hall effect at $\nu = 2/3$ and $3/5$ in tilted magnetic fields*. Phys. Rev. B 45:3418, 1992.
- [Esa70] L. Esaki and R. Tsu. *Superlattice and negative differential conductivity in semiconductors*. IBM J. Res. Dev. 14:61, 1970.
- [Esa74] L. Esaki and L. L. Chang. *New transport phenomenon in a semiconductor "superlattice"*. Phys. Rev. Lett. 33:495, 1974.
- [Eve86] T. Evelbauer, A. Wixforth, and J. P. Kotthaus. *One-dimensional minigaps in inversion layer subbands on high-index surfaces of InSb*. Z. Phys. B 64:69, 1986.
- [Fan83] F. F. Fang and P. J. Stiles. *Quantized magnetoresistance in two-dimensional electron systems*. Phys. Rev. B 27:6487, 1983.

- [Fel92] J. Feldmann, K. Leo, J. Shah, D. A. B. Miller, J. E. Cunningham, T. Meier, G. von Plessen, A. Schulze, P. Thomas, and S. Schmitt-Rink. *Optical investigation of Bloch oscillations in a semiconductor superlattice*. Phys. Rev. B 46:7252, 1992.
- [For98a] J.-Y. Fortin, J. Bellissard, M. Gusmao, and T. Ziman. *de Haas-van Alphen oscillations and magnetic breakdown: Semiclassical calculation of multiband orbits*. Phys. Rev. B 57:1484, 1998.
- [For98b] J.-Y. Fortin and T. Ziman. *Frequency mixing of magnetic oscillations: Beyond the Falicov-Stachowiak theory*. Phys. Rev. Lett. 80:3117, 1998.
- [Fow66a] A. B. Fowler, F. F. Fang, W. E. Howard, and P. J. Stiles. *Magneto-oscillatory conductance in silicon surfaces*. Phys. Rev. Lett. 16:901, 1966.
- [Fow66b] A. B. Fowler, F. F. Fang, W. E. Howard, and P. J. Stiles. *Oscillatory magneto-conductance in Si surfaces*. J. Phys. Soc. Japan 21:331, 1966.
- [Fuk88] T. Fukui and H. Saito. *(AlAs)_{1/2}(GaAs)_{1/2} fractional layer superlattices grown on (001) vicinal GaAs substrates by metal-organic chemical vapor deposition*. J. Vac. Sci. Technol. B 6:1373, 1988.
- [Ger89] R. R. Gerhardts, D. Weiss, and K. v. Klitzing. *Novel magnetoresistance oscillations in a periodically modulated two-dimensional electron gas*. Phys. Rev. Lett. 62:1173, 1989.
- [Gra91] H. T. Grahn, R. J. Haug, W. Müller, and K. Ploog. *Electric field domains in semiconductor superlattices: A novel system for tunneling between 2D systems*. Phys. Rev. Lett. 67:1618, 1991.
- [Gra95] H. Grahn. *Semiconductor superlattices. Growth and electronic properties*. World Scientific Publishing Co., Singapore, 1995.
- [Gra96] M. Grayson, C. Kurdak, D. C. Tsui, S. Parihar, S. Lyon, and M. Shayegan. *Novel cleaved edge overgrowth structures for tunneling into one- and two-dimensional electron systems*. Solid-State Electronics 40:233, 1996.
- [Gra98] M. Grayson. *Tunneling into the edge of a two-dimensional electron system*. Ph.D. thesis, Princeton University, 1998.

- [Gra01] M. Grayson. *personal communication*, 2001.
- [Gun64] J. B. Gunn. *IBM J. Res. Dev.* 8:141, 1964.
- [Hal83] B. I. Halperin. *Helv. Phys. Acta* 56:75, 1983.
- [Har96] N. Harrison, J. Caulfield, J. Singleton, P. Reinders, F. Herlach, W. Hayes, M. Kuumoo, and P. Day. *Magnetic breakdown and quantum interference in the quasi two-dimensional superconductor κ -(BEDT-TTF) $_2$ Cu(NCS) $_2$ in high magnetic fields*. *J. Phys.: Condens. Matter* 8:5415, 1996.
- [Hel98] R. Held, T. Vancura, T. Heinzel, K. Ensslin, M. Holland, and W. Wegscheider. *In-plane gates and nanostructures fabricated by direct oxidation of semiconductor heterostructures with an atomic force microscope*. *Appl. Phys. Lett.* 73:262, 1998.
- [Her00] J. Hergenrother and D. Monroe. *The vertical replacement-gate (VRG) MOSFET: A high performance vertical MOSFET with lithography-independent critical dimensions*. Extended abstracts of SSDM 2000 page 220, 2000.
- [Hig89] T. K. Higman, M. E. Favaro, L. M. Miller, M. A. Emanuel, and J. J. Coleman. *Observation of apparent inelastic tunneling between Landau levels in superlattices*. *Appl. Phys. Lett.* 54:1751, 1989.
- [Hir98] Y. Hirayama, K. Muraki, and T. Saku. *Two-dimensional electron gas formed in a back-gated undoped heterostructure*. *Appl. Phys. Lett.* 72:1745, 1998.
- [Ins90] Inspec. *Properties of Gallium Arsenide*. the Institution of Electrical Engineers, edited by S. Adachi, 2nd edition, 1990.
- [Ins93] Inspec. *Properties of Aluminum Gallium Arsenide*. the Institution of Electrical Engineers, edited by S. Adachi, 1993.
- [Ism88] K. Ismail, W. Chu, D. A. Antoniadis, and H. I. Smith. *Surface superlattice effects in a grating-gate GaAs/GaAlAs modulation-doped field-effect transistor*. *Appl. Phys. Lett.* 52:1071, 1988.
- [Jun98] T. Jungwirth, S. P. Shukla, L. Smrka, M. Shayegan, and A. H. MacDonald. *Magnetic anisotropy in quantum Hall ferromagnets*. *Phys. Rev. Lett.* 81:2328, 1998.

- [Kae98] F. Kaesen, C. Fink, K. G. Anil, W. Hansch, T. Doll, T. Grabolla, H. Schreiber, and I. Eisele. *Optimization of the channel doping profile of vertical sub-100 nm MOSFETs*. Thin Solid Films 336:309, 1998.
- [Kan97] W. Kang, J. B. Young, S. T. Hannahs, E. Palm, K. L. Campman, and A. C. Gosard. *Evidence for a spin transition in the $\nu = 2/5$ fractional quantum Hall effect*. Phys. Rev. B 56:12776, 1997.
- [Kas94] J. Kastrup, H. T. Grahn, K. H. Ploog, F. Prengel, A. Wacker, and E. Schöll. *Multistability of the current-voltage characteristics in doped GaAs-AlAs superlattices*. Appl. Phys. Lett. 65:1808, 1994.
- [Kas97] J. Kastrup, R. Hey, K. H. Ploog, H. T. Grahn, L. L. Bonilla, M. Kindelahn, M. Moscoso, A. Wacker, and J. Galan. *Electrically tunable GHz oscillations in doped GaAs-AlAs superlattices*. Phys. Rev. B 55:2476, 1997.
- [Kaz71] R. Kazarinov and R. Suris. *Possibility of the amplification of electromagnetic waves in a semiconductor with a superlattice*. Sov. Phys. Semicond. 5:707, 1971.
- [Kit96] C. Kittel. *Introduction to Solid State Physics*, chapter 9, pages 255–257. John Wiley & Sons, Inc., seventh edition edition, 1996.
- [Kro99] S. Kronüller. *Eigenschaften von Grund- und Anregungszuständen im FQHE-Regime*. Ph.D. thesis, Max-Planck-Institut für Festkörperforschung Stuttgart, 1999.
- [Kuk99] I. V. Kukushkin, K. v. Klitzing, and K. Eberl. *Spin polarization of composite fermions: measurements of the fermi energy*. Phys. Rev. Lett. 82:3665, 1999.
- [Kur95] C. Kurdak, A. Zaslavsky, D. C. Tsui, M. B. Santos, and M. Shayegan. *High field transport in an edge overgrown lateral superlattice*. Appl. Phys. Lett. 66:323, 1995.
- [Lan30] L. D. Landau. Z. Phys. 64:629, 1930.
- [Lan76] L. D. Landau and E. M. Lifshitz. *Lehrbuch der Theoretischen Physik*, volume 3. Akademie-Verlag, Berlin, 1976.

- [Lau83] R. B. Laughlin. *Anomalous quantum Hall effect: An incompressible quantum fluid with fractionally charged excitations*. Phys. Rev. Lett. 50:1395, 1983.
- [Leb70] P. A. Lebowitz and R. Tsu. *Electrical transport properties in a superlattice*. J. Appl. Phys. 41:2664, 1970.
- [Leo92] K. Leo, P. Haring-Bolivar, F. Brüggemann, R. Schwedler, and K. Köhler. Solid State Comm. 84:943, 1992.
- [Leo98] K. Leo. *Interband optical investigation of Bloch oscillations in semiconductor superlattices*. Semicond. Sci. Technol. 13:249–263, 1998.
- [Lif56] I. M. Lifshitz, M. I. Azbel, and M. I. Kaganov. *On the theory of galvanomagnetic effects in metals*. Soviet Phys. JETP 3:143, 1956.
- [Lif57] I. M. Lifshitz, M. I. Azbel, and M. I. Kaganov. *The theory of galvanomagnetic effects in metals*. Soviet Phys. JETP 4:41, 1957.
- [Lif59] I. M. Lifshitz and V. G. Peschanskii. *Galvanomagnetic characteristics of metals with open Fermi surfaces. I*. Soviet Phys. JETP 8:875, 1959.
- [Lif60] I. M. Lifshitz and V. G. Peschanskii. *Galvanomagnetic characteristics of metals with open Fermi surfaces. II*. Soviet Phys. JETP 11:137, 1960.
- [Lon99] A. R. Long, E. Skuras, S. Vallis, R. Cusc, I. A. Larkin, J. H. Davies, and M. C. Holland. *Potential modulation by strain in lateral surface superlattices*. Phys. Rev. B 60:1964, 1999.
- [Luo00] K. J. Luo, K.-J. Friedland, H. T. Grahn, and K. H. Ploog. *Magnetic field effects on undriven chaos in a weakly coupled GaAs/AlAs superlattice*. Appl. Phys. Lett. 76:2913, 2000.
- [Lys97] V. G. Lyssenko, G. Valusis, F. Löser, T. Hasche, K. Leo, M. M. Dignam, and K. Köhler. *Direct measurement of the spatial displacement of Bloch-oscillating electrons in semiconductor superlattices*. Phys. Rev. Lett. 79:301, 1997.
- [Lys98] V. G. Lyssenko, M. Sudzius, F. Löser, G. Valusis, T. Hasche, K. Leo, M. M. Dignam, and K. Köhler. *Bloch oscillations in semiconductor superlattices*. Festkörperprobleme/Advances in Solid State Physics 38:225–249, 1998.

- [Maa87] J.-K. Maan. *Magnetic quantization in superlattices*, volume 27 of *Festkörperprobleme/Advances in Solid State Physics*, page 137. Vieweg, Braunschweig, 1987.
- [Mac99] A. H. MacDonald, R. Rajaraman, and T. Jungwirth. *Broken-symmetry ground states in $\nu = 2$ bilayer quantum Hall systems*. Phys. Rev. B 60:8817, 1999.
- [Maj00] A. Majumdar, L. Rokhinson, D. C. Tsui, L. N. Pfeiffer, and K. W. West. *Effective mass enhancement of two-dimensional electrons in a one-dimensional superlattice potential*. Appl. Phys. Lett. 76:3600, 2000.
- [Man95] A. Manolescu and R. R. Gerhardt. *Exchange-enhanced spin splitting in a two-dimensional electron system with lateral modulation*. Phys. Rev. B 51:1703, 1995.
- [Man00] A. Manolescu and V. Gudmundsson. *Hysteresis effect due to the exchange Coulomb interaction in short-period superlattices in tilted magnetic fields*. Phys. Rev. B 61:R7858, 2000.
- [Mat82] T. Matheson and R. J. Higgins. *Tunneling in tilted Si inversion layers*. Phys. Rev. B 25:2633, 1982.
- [Men88] E. E. Mendez, F. Agullo-Rueda, and J. M. Hong. *Stark localization in GaAs-GaAlAs superlattices under an electric field*. Phys. Rev. Lett. 60:2426, 1988.
- [Mey95] F. A. Meyer, E. Steep, W. Biberacher, P. Christ, A. Lerf, A. G. M. Jansen, W. Joss, P. Wyder, and K. Andres. *High-field de Haas-van Alphen studies of κ -(BEDT-TTF)₂Cu(NCS)₂*. Europhys. Lett. 32:681, 1995.
- [Mor95] N. Mori, P. H. Beton, J. Wang, and L. Eaves. *Theory of resonant tunneling through a quantum wire*. Phys. Rev. B 51:1735, 1995.
- [Mot89] J. Motohisa, M. Tanaka, and H. Sakaki. *Anisotropic transport and nonparabolic miniband in a novel in-plane superlattice consisting of a grid-inserted selectively doped heterojunction*. Appl. Phys. Lett. 55:1214, 1989.
- [Mou01] L. G. Mouroukh, N. J. M. Horing, and A. Y. Smirnov. *Domain formation in a one-dimensional superlattice*. Appl. Phys. Lett. 78:1412, 2001.

- [Mue93] W. Mueller. *Transport durch GaAs-AlAs Übergitter in elektrischen und magnetischen Feldern*. Ph.D. thesis, Max-Planck-Institut für Festkörperforschung Stuttgart, 1993.
- [Mue94] G. Mueller, P. Streda, D. Weiss, K. v. Klitzing, and G. Weimann. *Giant magnetoresistance in lateral surface superlattices*. Phys. Rev. B 50:8938, 1994.
- [Nak98] Y. Nakamura, T. Inoshita, and H. Sakaki. *Novel magnetoresistance oscillations in laterally modulated two-dimensional electrons with 20 nm periodicity formed on vicinal GaAs (111)B surfaces*. Physica E 2:944, 1998.
- [Neb97] C. E. Nebel, J. Rogg, M. K. Kelly, B. Dahlheimer, M. Rother, M. Bichler, W. Wegscheider, and M. Stutzmann. *Realization of AlGaAs antidot arrays by pulsed laser interference gratings*. J. Appl. Phys. 82:1497, 1997.
- [Ohn95] Y. Ohno, Y. Nakamura, M. Foley, T. Someya, T. Noda, and H. Sakaki. *Magnetoresistance oscillations in 50 nm wide GaAs/Al_xGa_{1-x}As multiple-edge quantum wires*. Phys. Rev. B 52:R11619, 1995.
- [Ons52] L. Onsager. *Interpretation of the Haas-van Alphen Effect*. Philos. Mag. 43:1006, 1952.
- [Pea90] S. J. Pearton and N. J. Shah. *High-Speed Semiconductor Devices*, chapter 5: Heterostructure field-effect transistors, page 283. John Wiley & Sons, edited by S. M. Sze, 1990.
- [Pet97] F. Petit, L. Sfaxi, F. Lelarge, A. Cavanna, M. Hayne, and B. Etienne. *High-field spin-polarization transition in the Landau bands of quasi-2D electron gases with strong lateral modulation*. Europhys. Lett. 38:225, 1997.
- [Pfe90] L. Pfeiffer, K. W. West, H. L. Stormer, J. P. Eisenstein, K. W. Baldwin, D. Gershoni, and J. Spector. *Formation of a high-quality electron gas on cleaved GaAs*. Appl. Phys. Lett. 56:1697, 1990.
- [Pia99] V. Piazza, V. Pellegrini, F. Beltram, W. Wegscheider, T. Jungwirth, and A. H. MacDonald. *First-order phase transitions in a quantum Hall ferromagnet*. NATURE 402:638, 1999.

- [Pip62] A. B. Pippard. *Quantization of coupled orbits in metals*. Proc. Roy. Soc. (London) A 270:1, 1962.
- [Pip65] A. B. Pippard. *The dynamics of conduction electrons*. Documents on modern physics. Science Publishers, 1965.
- [Pra87] R. E. Prange and S. M. Girvin. *The Quantum Hall effect*. Graduate texts in contemporary physics. Springer, 1987.
- [Pro99] R. Prozorov, Y. Yeshurun, T. Prozorov, and A. Gedanken. *Magnetic irreversibility and relaxation in assembly of ferromagnetic nanoparticles*. Phys. Rev. B 59:6956, 1999.
- [Rau97] C. Rauch, G. Stasser, K. Unterrainer, E. Gornik, and B. Brill. *Ballistic electron spectroscopy of vertical superlattice minibands*. Appl. Phys. Lett. 70:649, 1997.
- [Rot99a] M. Rother. *AQUILA - computer program for self-consistent calculation of semiconductor nanostructures*. Walter Schottky Institut, Technische Universität München, 1999.
- [Rot99b] S. Rott, P. Binder, N. Linder, and G. H. Döhler. *Combined description for semi-classical and quantum transport in superlattices*. Phys. Rev. B 59:7334, 1999.
- [Rot00] M. Rother. *Elektronische Eigenschaften von Halbleiternanostrukturen hergestellt durch Überwachsen von Spaltflächen*. Ph.D. thesis, Walter Schottky Institut, Technische Universität München, 2000.
- [Sak76] H. Sakaki, K. Wagatsuma, J. Hamasaki, and S. Saito. *Possible applications of surface corrugated quantum thin films to negative-resistance devices*. Thin Solid Films 36:497, 1976.
- [Sak99] H. Sakaki, Y. Nakamura, M. Yamauchi, T. Someya, H. Akiyama, and D. Kishimoto. *10 nm scale edge-and step-quantum wires and related structures: Progress in their design, epitaxial synthesis and physics*. Physica E 4:56, 1999.
- [Sar96] S. D. Sarma and A. Pinczuk. *Perspectives on Quantum Hall Effects*. Wiley, New York, 1996.

- [Sas90] T. Sasaki, H. Sato, and N. Toyota. *Magnetic breakdown effect in organic superconductor κ -(BEDT-TTF) $_2$ Cu(NCS) $_2$* . Solid State Comm. 76:507, 1990.
- [Sch98a] G. Schedelbeck. *Optische Eigenschaften von Halbleiternanotrukturen hergestellt durch Überwachsen von Spaltflächen*. Ph.D. thesis, Walter Schottky Institut, Technische Universität München, 1998.
- [Sch98b] E. Schomburg, T. Blomeier, K. Hofbeck, J. Grenzer, S. Brandl, I. Lingott, A. A. Ignatov, and K. F. Renk. *Current oscillation in superlattices with different miniband widths*. Phys. Rev. B 58:4035, 1998.
- [See88] K. Seeger. *Semiconductor physics: An introduction*, volume 40 of *Springer Series in Solid-State Sciences*. Springer Verlag, 4th edition, 1988.
- [Sha92] M. P. Shaw, V. V. Mitin, E. Schöll, and H. L. Grubin. *The physics of instabilities in solid state electron devices*. Plenum Press, New York, 1992.
- [Sho84] D. Shoenberg. *Magnetic oscillations in metals*. Cambridge University Press, 1984.
- [Shu30] L. W. Shubnikov and W. J. de Haas. Proc. Netherlands Roy. Acad. Sci. 33:130, 1930.
- [Sib89] A. Sibille, J. F. Palmier, F. Molloy, H. Wang, and J. C. Esnault. *Negative differential conductance in GaAs/AlAs superlattices*. Phys. Rev. B 39:6272, 1989.
- [Sib90] A. Sibille, J. F. Palmier, H. Wang, and F. Molloy. *Observation of Esaki-Tsu negative differential velocity in GaAs/AlAs superlattices*. Phys. Rev. Lett. 64:52, 1990.
- [Sme98] J. H. Smet, K. v. Klitzing, D. Weiss, and W. Wegscheider. *DC transport of composite fermions in weak periodic potentials*. Phys. Rev. Lett. 80:4538, 1998.
- [Sme01] J. H. Smet, R. A. Deutschmann, W. Wegscheider, G. Abstreiter, and K. von Klitzing. *Ising ferromagnetism and domain morphology in the fractional quantum Hall regime*. Phys. Rev. Lett. 86:2412, 2001.
- [Smo89] J. Smoliner, W. Demmerle, G. Berthold, E. Gornik, G. Weimann, and W. Schlapp. *Momentum conservation in tunneling processes between barrier-separated 2d-electron-gas systems*. Phys. Rev. Lett. 63:2116, 1989.

- [Sta67] R. W. Stark and L. M. Falicov. *Magnetic breakdown in metals*. Prog. Low Temp. Phys. 5:235–286, 1967.
- [Sta71] R. W. Stark and C. B. Friedberg. *Quantum interference of electron waves in a normal metal*. Phys. Rev. Lett. 26:556, 1971.
- [Sta74] R. W. Stark and C. B. Friedberg. *Interfering quantum electron states in ultrapure magnesium*. J. Low Temp. Phys. 14:111–146, 1974.
- [Sti78] P. J. Stiles. *The artificial superlattice in a two-dimensional system*. Surf. Sci. 73:252, 1978.
- [Sto91a] H. L. Stormer, K. W. Baldwin, L. N. Pfeiffer, and K. W. West. *GaAs field-effect transistor with an atomically precise ultrashort gate*. Appl. Phys. Lett. 59:1111, 1991.
- [Sto91b] H. L. Stormer, L. N. Pfeiffer, K. W. Baldwin, K. W. West, and J. Spector. *Atomically precise superlattice potential imposed on a two-dimensional electron gas*. Appl. Phys. Lett. 58:726, 1991.
- [Sto00] H. L. Stormer, L. N. Pfeiffer, K. W. Baldwin, K. W. West, and W. Kang. *Tunneling between the edges of two lateral quantum Hall systems*. Nature 403:59, 2000.
- [Str90] P. Streda and A. H. MacDonald. *Magnetic breakdown and magnetoresistance oscillations in a periodically modulated two-dimensional electron gas*. Phys. Rev. B 41:11892, 1990.
- [Tar90] S. Tarucha, Y. Hirayama, T. Saku, and T. Kimura. *Resonant tunneling through one and zero dimensional states constricted by AlGaAs/GaAs/AlGaAs heterojunctions and high-resistance regions induced by focused Ga ion-beam implantation*. Phys. Rev. B 41:5459, 1990.
- [TC90] P. P. T. Chakraborty. *Spin-reversed excitations in the fractional quantum Hall effect*. Phys. Rev. B 41:10862, 1990.
- [Tok89] Y. Tokura, K. Tsubaki, and N. Susa. *Electronic states in lateral structures on modulation doped heterointerfaces*. Appl. Phys. Lett. 55:1403, 1989.

- [Tok90] Y. Tokura and N. Susa. *Electron effective-mass modulation transistor*. J. Appl. Phys. 67:2171, 1990.
- [Tsu73] R. Tsu and L. Esaki. *Tunneling in a finite superlattice*. Appl. Phys. Lett. 22:562, 1973.
- [Tsu75] R. Tsu and G. Döhler. *Hopping conduction in a "superlattice"*. Phys. Rev. B 12:680, 1975.
- [Tsu82] D. C. Tsui, H. L. Stormer, and A. C. Gossard. *Two-Dimensional Magnetotransport in the Extreme Quantum Limit*. Phys. Rev. Lett. 48:1559, 1982.
- [Tsu90] K. Tsubaki, Y. Tokura, and N. Susa. *Density of states of an AlAs/GaAs fractional superlattice in a modulation-doped structure*. Appl. Phys. Lett. 57:2101, 1990.
- [Unt96] K. Unterrainer, B. J. Keay, M. C. Wanke, S. J. Allen, D. Leonard, G. Medeiros-Ribeiro, U. Bhattacharya, and M. J. W. Rodwell. *Inverse Bloch oscillator: Strong THz photocurrent resonances at the Bloch frequency*. Phys. Rev. Lett. 76:2973, 1996.
- [vH89] H. v. Houten, C. W. J. Beenakker, J. G. Williamson, M. E. I. Broekaart, P. H. M. v. Loosdrecht, B. J. v. Wees, J. E. Mooij, C. T. Foxon, and J. J. Harris. *Coherent electron focusing with quantum point contacts in a two-dimensional electron gas*. Phys. Rev. B 39:8556, 1989.
- [vK80] K. v. Klitzing, G. Dorda, and M. Pepper. *New method for high-accuracy determination of the fine-structure constant based on quantized Hall resistance*. Phys. Rev. Lett. 45:494, 1980.
- [Wac97] A. Wacker, M. Moscoso, M. Kindelan, and L. L. Bonilla. *Current-voltage characteristic and stability in resonant tunneling n-doped semiconductor superlattices*. Phys. Rev. B 55:2466, 1997.
- [Wac98a] A. Wacker. *Vertical transport and domain-formation in multiple quantum wells*, volume 4 of *Electronic materials series*, chapter 10, pages 321–352. Chapman&Hall, edited by E. Schöll, 1998.
- [Wac98b] A. Wacker and A.-P. Jauho. *Quantum transport: the link between standard approaches in superlattices*. Phys. Rev. Lett. 80:369, 1998.

- [Wac00] A. Wacker. *Semiconductor superlattices: A model system for nonlinear transport*. Habilitationsschrift TU Berlin, 2000.
- [Wal94] K. R. Wald, L. P. Kouwenhoven, P. L. McEuen, N. C. van der Vaart, and C. T. Foxon. *Local dynamic nuclear polarization using quantum point contacts*. Phys. Rev. Lett. 73:1011, 1994.
- [Wan94] J. Wang, P. H. Beton, N. Mori, L. Eaves, H. Buhmann, L. Mansouri, P. C. Main, T. J. Foster, and M. Henini. *Resonant magnetotunneling via one-dimensional quantum confined states*. Phys. Rev. Lett. 73:1146, 1994.
- [Wan99] Y. Wang, Q. Huang, and J. Zhou. *1D to 1D electron resonant tunneling in a double asymmetric quantum-wire structure*. Appl. Phys. Lett. 74:1412, 1999.
- [Was93] C. Waschke, H. Roskos, R. Schwedler, K. Leo, H. Kurz, and K. Köhler. *Coherent submillimeter-wave emission from Bloch oscillations in a semiconductor superlattice*. Phys. Rev. Lett. 70:3319, 1993.
- [Weg97] W. Wegscheider, G. Schedelbeck, G. Abstreiter, M. Rother, and M. Bichler. *Atomically precise GaAs quantum dots fabricated by twofold cleaved edge overgrowth*. Phys. Rev. Lett. 79:1917, 1997.
- [Wei89] D. Weiss, K. v. Klitzing, K. Ploog, and G. Weimann. *Magnetoresistance oscillations in a two-dimensional electron gas induced by a submicrometer periodic potential*. Europhys. Lett. 8:179, 1989.
- [Wei91a] C. Weisbuch and B. Vinter. *Quantum Semiconductor Structures: Fundamentals and Applications*. Academic Press, Inc., 1991.
- [Wei91b] D. Weiss, M. L. Roukes, A. Menschig, P. Grambow, K. v. Klitzing, and G. Weimann. *Electron pinball and commensurate orbits in a periodic array of scatterers*. Phys. Rev. Lett. 66:2790, 1991.
- [Wei92] D. Weiss. *Kommensurabilitätseffekte in lateralen Übergittern*. Habilitationsschrift Max-Planck-Institut für Festkörperforschung, Stuttgart, 1992.
- [Win89] R. W. Winkler, J. P. Kotthaus, and K. Ploog. *Landau-band conductivity in a two-dimensional electron system modulated by an artificial one-dimensional superlattice potential*. Phys. Rev. Lett. 62:1177, 1989.

- [Xie89] X. C. Xie, Y. Guo, and F. C. Zhang. *Fractional quantum Hall effect with spin reversal*. Phys. Rev. B 40:R3487, 1989.
- [Yac96] A. Yacoby, H. L. Stormer, N. S. Wingreen, L. N. Pfeiffer, K. W. Baldwin, and K. W. West. *Nonuniversal conductance quantization in quantum wires*. Phys. Rev. Lett. 77:4612, 1996.
- [Zen34] C. Zener. Proc. Roy. Soc. (London) A 145:523, 1934.
- [Zha90] C. Zhang and R. R. Gerhardts. *Theory of magnetotransport in two-dimensional electron systems with unidirectional periodic modulation*. Phys. Rev. B 41:12850, 1990.

R. A. Deutschmann *Two dimensional electron systems in atomically precise periodic potentials* (2001)
Ph.D. Dissertation. Selected Topics of Semiconductor Physics and Technology, ISBN 3-932749-42-1

Publications

1. K. Adlkofer, M. Tanaka, H. Hillebrandt, G. Wiegand, E. Sackmann, T. Bolom, R. A. Deutschmann, and G. Abstreiter. *Electrochemical passivation of gallium-arsenide surface with organic self-assembled monolayers in aqueous electrolytes*. Appl. Phys. Lett. 76:3313–3315, 2000.
2. R. A. Deutschmann, M. Huber, R. Neumann, K. Brunner, and G. Abstreiter. *Direct sub- μm lateral patterning of SOI by focused laser beam induced oxidation*. International Journal of Microelectronic Engineering 48:367–370, 1999.
3. R. A. Deutschmann, A. Lorke, W. Wegscheider, M. Bichler, and G. Abstreiter. *Breakdown of SdH oscillations in a short period 1D lateral superlattice*. Physica E (Amsterdam) 6:561–564, 2000.
4. R. A. Deutschmann, W. Wegscheider, C. Albrecht, J. H. Smet, M. Rother, M. Bichler, and G. Abstreiter. *Bridging the gap with cleaved edge overgrowth: on minigaps, magnetic breakdown and quantum interference in artificial bandstructures*. Proceedings of the 25th International Conference on the Physics of Semiconductors, Editors: N. Miura and T. Ando, Springer Proceedings in Physics Vol. 87, 2001 (invited talk).
5. R. A. Deutschmann, W. Wegscheider, M. Rother, M. Bichler, and G. Abstreiter. *Negative differential resistance of a 2D electron gas in a 1D miniband*. Physica E (Amsterdam) 7:294–298, 2000.
6. R. A. Deutschmann, C. Stocken, W. Wegscheider, M. Bichler, and G. Abstreiter. *Commensurability effects in lateral surface doped superlattices*. Appl. Phys. Lett. 78:2175–2177, 2001.
7. R. A. Deutschmann, W. Wegscheider, M. Rother, M. Bichler, G. Abstreiter, C. Albrecht, and J. H. Smet. *Quantum interference in artificial band structures*. Phys. Rev.

- Lett. 86:1857–1859, 2001.
8. R. A. Deutschmann, W. Wegscheider, M. Rother, M. Bichler, and G. Abstreiter. *Mini-band transport in vertical superlattice field-effect transistors*. Appl. Phys. Lett. 79:1564–1566, 2001
 9. E. F. Duijs, F. Findeis, R. A. Deutschmann, M. Bichler, A. Zrenner, G. Abstreiter, K. Adlkofer, M. Tanaka, and E. Sackmann. *Influence of thiol coupling on photoluminescence of near surface InAs quantum dots*. Phys. Stat. Sol. (B) 224:871–875, 2001.
 10. F. Ertl, M. Rother, W. Wegscheider, R. A. Deutschmann, M. Bichler, and G. Abstreiter. *Investigation of conductance fluctuations in quantum wires fabricated by cleaved edge overgrowth*. Proceedings of the 25th International Conference on the Physics of Semiconductors, Editors: N. Miura and T. Ando, Springer Proceedings in Physics Vol. 87, pp. 1027, 2001.
 11. F. Ertl, T. Asperger, R. A. Deutschmann, W. Wegscheider, M. Bichler, G. Bhm, and G. Absteiter *Vertical field-effect transistors realized by cleaved-edge overgrowth*. Physica E (Amsterdam), 2001
 12. F. Ertl, R. A. Deutschmann, D. Schuh, M. Bichler, and G. Absteiter *Device characteristics of vertical field effect transistors with ultra-short InGaAs/GaAs channels*. Compound Semiconductors, Institute of Physics Publishing Bristol, 2001
 13. J. Hntschel, R. Stenzel, W. Klix, F. Ertl, T. Asperger, R. A. Deutschmann, M. Bichler, and G. Abstreiter *Simulation of vertical CEOFETs by a coupled solution of the Schrödinger equation with a hydrodynamic transport model*. in: Simulation of Semiconductor Processes and Devices 2001, Editors: D. Tsoukalas and C. Tsamis, Springer Berlin, pp. 222, 2001
 14. M. Huber, R. A. Deutschmann, R. Neumann, K. Brunner, and G. Abstreiter. *Local laser induced rapid thermal oxidation of SOI substrates*. Appl. Surf. Sci. 168:204–207, 2000.
 15. R. Meisels, K. Dybko, F. Ziouzia, F. Kuchar, R. A. Deutschmann, G. Hein, and K. Pierz. *Millimeter wave and DC investigations of spin effects in the 2DES of AlGaAs/GaAs*. Physica E (Amsterdam) 10:57, 2001.

16. M. Rother, R. A. Deutschmann, W. Wegscheider, M. Bichler, and G. Abstreiter. *Evidence for Luttinger Liquid Behavior in Cleaved Edge Overgrowth GaAs/AlGaAs Quantum Wires*. *Physica E* 6:551–554, 2000.
17. J. H. Smet, R. A. Deutschmann, W. Wegscheider, G. Abstreiter, and K. von Klitzing. *Ising ferromagnetism and domain morphology in the fractional quantum Hall regime*. *Phys. Rev. Lett.* 86:2412–2414, 2001.
18. W. Wegscheider, M. Rother, F. Ertl, R. A. Deutschmann, M. Bichler, and G. Abstreiter. *Quantum wires as Luttinger Liquids: Experiment*. Volume 40 of *Festkörperprobleme/Advances in Solid State Physics*, edited by B. Kramer, pages 97–116, 2000.